

Computational Study of Vortex Pair Dynamics

Computational study of vortex pair dynamics
R. Steijl

Thesis University of Twente, Enschede - With ref. - With summary in Dutch.
ISBN 90-365-1696X

Copyright ©2001 by R. Steijl, Hengelo, The Netherlands

COMPUTATIONAL STUDY OF VORTEX PAIR DYNAMICS

PROEFSCHRIFT

ter verkrijging van
de graad van doctor aan de Universiteit Twente,
op gezag van de rector magnificus,
prof.dr. F.A. van Vught,
volgens besluit van het College voor Promoties
in het openbaar te verdedigen
op vrijdag 14 december 2001 te 13:15 uur.

door

René Steijl

geboren op 29 juli 1974
te Rotterdam

Dit proefschrift is goedgekeurd door de promotor:
prof. dr. ir. H. W. M. Hoeijmakers

TABLE OF CONTENTS

1	Introduction	1
1.1	Basic relations concerning vortices and vorticity	4
1.2	Vortex wake formation	6
1.2.1	Roll-up of near-wake	6
1.2.2	Axial velocity in trailing vortices	9
1.3	Cooperative instabilities in vortex pairs	9
1.3.1	Long-wavelength instability	9
1.3.2	Short-wavelength instability	10
1.3.3	Interaction of short-wavelength and long-wavelength instabilities . .	12
1.4	Decay of an aircraft vortex wake	14
1.5	Scaling of decay process	15
1.6	Outline and objective of present study	16
2	Linear stability analysis	19
2.1	Review of stability analysis of Crow	21
2.2	Stability analysis for a pair of Rosenhead vortex filaments	31
2.3	Stability analysis of Widnall	40
2.4	Orr-Sommerfeld equations in Cartesian coordinates	43
2.4.1	Formulation in terms of a stream function	46
2.4.2	Normal mode analysis due to Sipp et al. (1998)	46
2.5	Isolated vortex in a plain strain field	47
2.6	Computation of Kelvin waves	50
2.7	Orr-Sommerfeld equations in cylinder coordinates	51
2.7.1	Kelvin modes computation from Orr-Sommerfeld equation	56
2.7.2	Computation of growth rate of short-wavelength instability	57
3	Description of numerical methods	59
3.1	Temporal integration of Navier-Stokes equations for incompressible flows . .	60
3.2	Fractional time-stepping method	62
3.3	Compact-difference low-pass filter	63
3.3.1	Filtering data on a one-dimensional domain	63
3.3.2	General non-periodic domain boundary	66
3.3.3	Sub-domain interface boundary condition	68

3.4	Parallelization techniques	71
3.5	Parallel compact finite-difference method	74
3.5.1	Collocated mesh formulation	75
3.5.2	Parallelization of the method	75
3.5.3	Implementation of spatial filter	80
3.6	Hybrid method	83
3.6.1	Implementation of spatial filter	85
3.7	Iterative solution methods for linear systems of equations	86
3.7.1	Direct and iterative methods for linear systems	86
3.7.2	The Conjugate Gradient method	88
3.7.3	The Bi-Conjugate Gradient method	89
3.7.4	Preconditioning	89
3.7.5	Implementation of matrix-vector multiplications	90
4	Spatial discretization methods	91
4.1	Spatial discretization of first-derivative	92
4.1.1	General non-periodic domain boundary	93
4.1.2	Sub-domain interface boundary condition	94
4.2	Spatial discretization of second-derivative	94
4.2.1	General non-periodic domain boundary	94
4.2.2	Sub-domain interface boundary condition	95
4.3	Spatial discretization of Laplace operator	95
4.4	Spatial discretization of 2D Laplace operator	97
4.5	Spatial discretization of 3D Laplace operator	98
4.6	Fast 2D Poisson/Helmholtz solver	100
4.6.1	Formulation of boundary conditions	101
4.6.2	Fast direct solution procedure	103
4.7	Iterative 3D Poisson/Helmholtz solver	104
4.7.1	Formulation of boundary conditions	105
4.7.2	Iterative solution procedure	108
4.8	Application to 3D model problem	108
5	Results for Crow instability	113
5.1	Review of previous work	114
5.2	Numerical results	119
5.3	Determination of initial condition	121
5.4	Numerical study of linear stage of the Crow instability	122
5.4.1	Exponential growth of perturbations	124
5.4.2	Rotational motion of perturbations	126
5.5	Nonlinear stage of the Crow instability	129
5.5.1	Theoretical analysis by Kida and Takaoka (1994)	129
5.5.2	Numerical analysis of vortex reconnection	130
5.6	Numerical study of the nonlinear stage of the Crow instability	138
5.7	Analysis of kinetic energy spectra	144
5.7.1	Decay of kinetic energy of vortex pair	144
5.7.2	Kinetic energy spectra for nonlinear stage	146

6	Short-wavelength instability	149
6.1	Determination of initial condition	150
6.1.1	Normal modes of linearized equations for Lamb-Oseen vortex	151
6.1.2	Boundary value problem for pressure	153
6.1.3	Chebyshev collocation discretization method	154
6.1.4	Computed Kelvin modes for Lamb-Oseen vortex	155
6.1.5	Initial perturbation of the vortex pair	155
6.2	Numerical results	157
6.2.1	Results for $k = 2.261$	157
6.2.2	Results for $k = 3.958$	159
7	Vortex-pair rebound from solid wall	165
7.1	Numerical method for two-dimensional flow	166
7.2	Summary of performed simulations	166
7.3	Vortex-pair interaction with wall in potential flow	167
7.4	Numerical results for vortex-pair rebound	168
8	Concluding remarks	175
8.1	Development of Navier-Stokes methods	176
8.2	Numerical study of long-wavelength instability	177
8.3	Numerical study of short-wavelength instability	178
8.4	Discussion	180
8.5	Recommendations for further study	180
	<i>References</i>	<i>183</i>
	<i>Summary</i>	<i>187</i>
	<i>Samenvatting</i>	<i>189</i>
	<i>Acknowledgment</i>	<i>191</i>
	<i>About the author</i>	<i>193</i>

INTRODUCTION

1 Chapter

The study of vortices and their motion forms an important topic in fluid dynamics. Vortices are compact and coherent regions of the flow with a predominant rotational or swirling motion. The rotation of a velocity field is typically referred to as *vorticity*. In a large number of problems in fluid mechanics, the dynamics of vorticity or the motion of vortices is dominating the flow. In turbulent flows, the dynamics of *coherent structures* (vortical structures) is believed to be one of the driving mechanisms of the complicated and chaotic motion of the fluid.

In aerodynamics, two well-documented problems related to the dynamics of vortices are the *vortex break-down* problem and the *wake-vortex hazard*. The vortex break-down problem studied in aerodynamic applications is usually the sudden break-down of the organized vortical structure of the flow that exists above a slender, delta-like, wing at a high angle of attack. This phenomenon was first observed by Peckham and Atkinson (1957) and is particularly relevant for aerodynamics of fighter aircraft which, at high angles of attack, rely on the lift force generated by the suction of the strong vortical system above the wing. The vortical flow over slender delta wings has received considerable attention in the last decades, both in experimental studies (Donohoe (1996), Verhaagen and van Ransbeeck (1990)) and numerical studies (Hoeijmakers (1989), Visbal (1996), van Noordenburg (1999)). A similar break-down phenomenon can occur in confined swirling flows, such as pipe flows or flows in combustion chambers.

The wake-vortex hazard forms the motivation of the present research project. The problem originates from the persistence of the trailing vortices in the far-wake of an aircraft. These trailing vortices are large masses of rotating air, which form a safety hazard for following aircraft. An aircraft in cruise flight may encounter trailing vortices of other aircraft. A distinction can be made between in-trail encounters and across-vortex encounters, see Rossow and James (2000). In-trail encounters occur when the flight path is (nearly) parallel to that of the aircraft which generated the wake and the following aircraft experiences either a rolling motion when it enters one of the vortices of the trailing vortex pair or a loss of altitude when entering the region of induced downward velocity between the trailing vortices. Across-vortex encounters occur when the flight path is (nearly) perpendicular to the wake-vortex pair. In that case, the aircraft experiences a series of successive vertical accelerations, which induce large structural loads on the aircraft. Near the ground, the resulting change in altitude is particularly hazardous.

The hazard posed by the persisting wake vortices is particularly severe during landing and, to a lesser extent, during take-off. One of the parameters for the severity of the hazard is the

strength of the vortices in the vortex-pair, which is directly proportional to the weight of the aircraft and inversely proportional to the velocity of flight. This means that during take-off and landing, with low flight speeds compared to the cruise phase of the flight, the generated vortices are particularly strong. Another factor is the low altitudes at which aircraft travel during take-off and landing, which make sudden rolling maneuvers or a loss of altitude more dangerous than at higher altitudes.

The wake-vortex hazard has received significant attention in the past, particularly since the introduction of the very large commercial jets in the early 1970s.

In commercial aircraft operation, it is current practice that air traffic control (ATC) prescribes the minimum separation that must be maintained between two aircraft. Air traffic control employs a system of empirically determined separation distances between aircraft in air corridors and near airports. These separation distances form the *matrix of separations*, giving the minimum separation distance as a function of the weights of the leading and the following aircraft. The minimum separation distances for commercial airliners during take-off and landing are shown in table 1.1 for the three weight classes that were introduced by the aviation authorities. A number of these separation distances originate from the wake-vortex

TABLE 1.1: *Separation distances [nautical miles] for commercial airliners*

following aircraft	leading aircraft		
	small	large	heavy
small	3	4	6
large	3	3	5
heavy	3	3	4

hazard. The time needed for sufficient decay or dispersal of the vortex wake of the leading aircraft to ensure a safe flight condition for the following aircraft determines these distances. Uncertainties in navigation, radar tracking, etc. determine the other distances.

The dynamics of the aircraft vortex wake is largely determined by three-dimensional instabilities which occur in the vortex system. The dynamics of these instabilities form the main subject of this thesis.

The occurrence and characteristics of the instabilities are strongly influenced by atmospheric conditions such as ambient turbulence and stratification. Ideally, the separation distances would be the absolute minimum for the specific conditions along the corridor or near the airport. Since this is not practical, the matrix of separations is constant and as a result conservative. One of the main objectives of the research effort devoted to this problem since the early 1970s is to determine a more accurate, and therefore more economical, set of separation distances. Despite the research performed during three decades, the matrix of separations is still unaltered.

Research related to the aircraft wake-vortex hazard includes both studies involving counter-rotating vortex pairs similar to the far wake of an aircraft and more fundamental studies concerning vortex dynamics and stability of vortex flows. Initially, this research effort was predominantly of analytical nature. An important study was presented by Crow (1970). This was the first study concerning three-dimensional instabilities that occur in counter-rotating vortex pairs. A linear stability analysis was performed predicting sinusoidal instabilities at wavelengths very similar to those observed in condensation trails of jet transport aircraft in

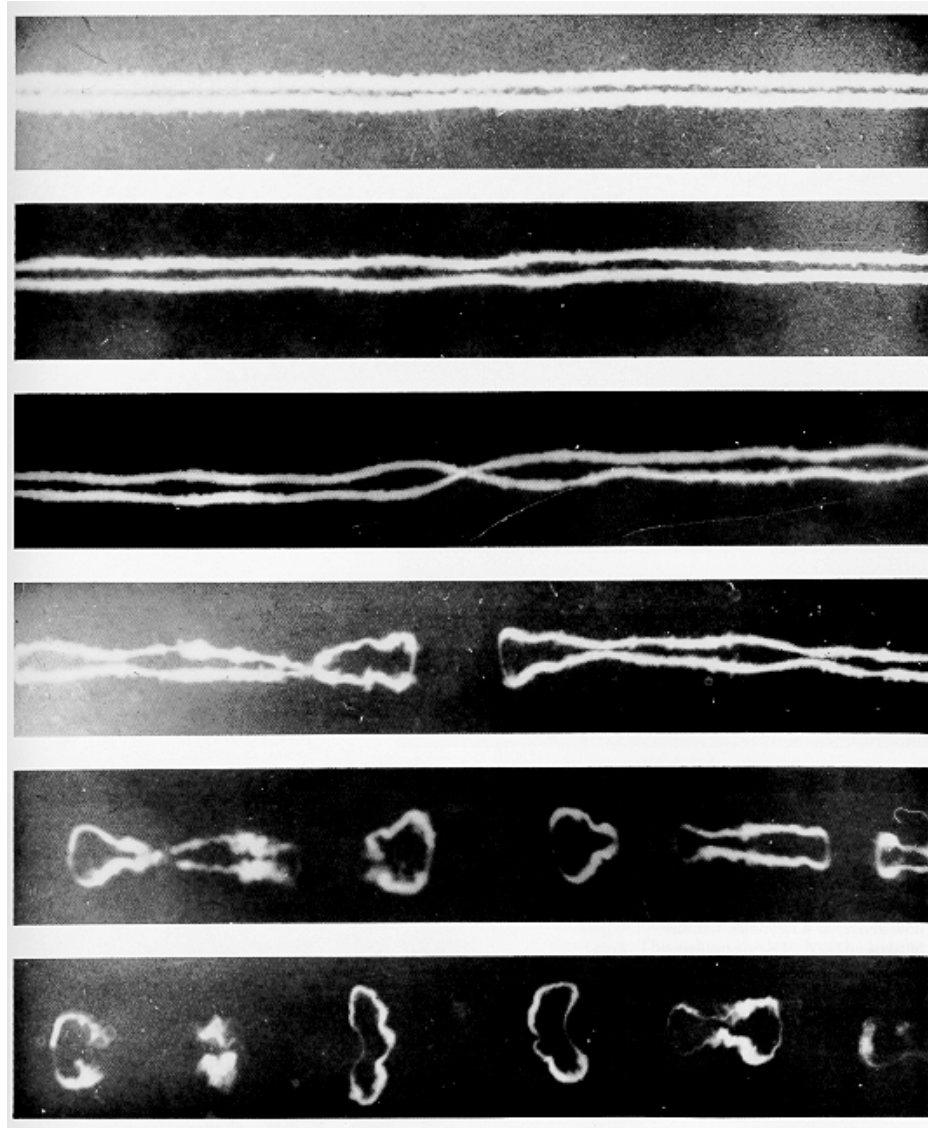


FIGURE 1.1: *Condensation trails of jet transport showing sinusoidal instabilities, with 15 s interval between the different pictures. (from Crow (1970))*

cruise flight. Figure 1.1 presents a sequence of photographs showing the condensation trails of a jet aircraft flying at high altitude. The trails are formed by the condensed water vapour from the engine exhausts that is entrained in the wing-tip vortices. The growth of sinusoidal disturbances is apparent. At later stages, the trailing vortices form vortex-ring structures. Following this landmark publication, more theoretical studies concerning instabilities of vortex flows were performed in the 1970s, for example Widnall et al. (1970), Widnall and

Bliss(1971), Widnall et al. (1974), Moore and Saffman (1975), Tsai and Widnall (1976). In recent years, wake vortex research is based mainly on large-scale numerical simulations of vortex pair dynamics based on the Navier-Stokes equations governing a viscous flow. A review of wake-vortex research was presented by Spalart (1998), including both a summary of earlier reviews and a review of selected numerical studies.

Before continuing the description of the problem related to aircraft wake vortices and the objective of the present study, some basic relations concerning vortices and vortex dynamics and some definitions are introduced in the next section.

1.1 Basic relations concerning vortices and vorticity

The motion of a fluid is usually described by a vector field $\underline{u}(\underline{x}, t)$. In a three-dimensional domain using a Cartesian coordinate system, the velocity vector \underline{u} has three components, i.e. $\underline{u}(\underline{x}, t) = u(\underline{x}, t)\underline{e}_x + v(\underline{x}, t)\underline{e}_y + w(\underline{x}, t)\underline{e}_z$. Here, \underline{e}_x , \underline{e}_y and \underline{e}_z denote the unit vectors in the three coordinate directions x , y and z , respectively, and the vector \underline{x} is the position vector of the fluid element considered. Vorticity $\underline{\omega}$ is defined as the curl of the velocity

$$\underline{\omega}(\underline{x}, t) = \nabla \times \underline{u} = \left(\frac{\partial w}{\partial y} - \frac{\partial v}{\partial z} \right) \underline{e}_x + \left(\frac{\partial u}{\partial z} - \frac{\partial w}{\partial x} \right) \underline{e}_y + \left(\frac{\partial v}{\partial x} - \frac{\partial u}{\partial y} \right) \underline{e}_z \quad (1.1)$$

The vorticity field satisfies a number of conservation equations and kinematic relations described in detail by Saffman (1992).

An important quantity in the description of vortical flow is the circulation Γ associated with a simply closed curve C , bounding surface S , defined as the line integral of the tangential velocity

$$\Gamma = \oint_{C=\partial S} \underline{u} \cdot d\underline{c} = \iint_S \underline{\omega} \cdot \underline{n} dS \quad (1.2)$$

One of the properties that makes circulation an important quantity is the direct relation of circulation of the velocity field around a body in a fluid flow and the lift force generated on this body. The special case of a three-dimensional wing is of particular interest here. In this case, the generated lift is directly related to the circulation that persists in the wake behind the wing. The wake of such a finite lifting surface is commonly modeled as a system of streamwise vortices, as described in the next section.

In an incompressible flow, vorticity and velocity are related through the kinematic relation:

$$\underline{u}(\underline{x}_0) = \frac{1}{4\pi} \int \int \int_V \frac{\underline{\omega}(\underline{x}) \times \underline{r}}{|\underline{r}|^3} dV(\underline{x}) \quad (1.3)$$

where the velocity is computed at an arbitrary point \underline{x}_0 and $\underline{r} = \underline{x}_0 - \underline{x}$. The vorticity distribution is denoted by $\underline{\omega}(\underline{x})$.

In case the vorticity is concentrated in a small number of discrete vortical structures, a more useful formulation of (1.3) can be used. An extreme situation is the situation in which all vorticity in the flow field is concentrated in a curve in space, such that the circulation of any closed contour around the curve is finite. This distribution is called a *line vortex* or *vortex filament* with Γ , the circulation around it, which is the strength of the filament.

In case the curve in space forming the vortex filament, at time t , is parameterized as $\underline{x} = \underline{x}(s)$, with s a monotonically increasing parameter specifying the position along the curve, the vorticity distribution can be expressed as

$$\underline{\omega} = \Omega(x', y'; s) \frac{d\underline{x}_v}{ds} / \left| \frac{d\underline{x}_v}{ds} \right| \quad (1.4)$$

with (x', y') local coordinates in the infinitesimal cross-section of the filament at $\underline{x}_v(s)$. Then with $dV(\underline{x}) = |d\underline{x}_v/ds|dsdS$, where dS denotes the cross-section of the filament C , relation (1.3) can be written as:

$$\underline{u}(\underline{x}_0) = -\frac{1}{4\pi} \int_C \frac{\underline{x}_0 - \underline{x}_v(s)}{|\underline{x}_0 - \underline{x}_v(s)|^3} \times \left\{ \frac{d\underline{x}_v}{ds} \int \int_S \Omega(x', y'; s) dS \right\} ds \quad (1.5)$$

The surface integral is the circulation $\Gamma(s)$ of the filament, so that

$$\underline{u}(\underline{x}_0) = -\frac{1}{4\pi} \int_C \Gamma(s) \frac{\underline{x}_0 - \underline{x}_v(s)}{|\underline{x}_0 - \underline{x}_v(s)|^3} \times \frac{d\underline{x}_v}{ds} ds \quad (1.6)$$

This expression is a singular integral for points \underline{x}_0 on the filament, with the induced velocity becoming unbounded. It is known as the Biot-Savart expression for the velocity induced by a vortex filament.

The special case of the infinitely long straight line vortex, the rectilinear line vortex, is of particular importance, see for example Saffman (1992). The streamlines of the induced velocity field are concentric circles with center on the line vortex, in planes perpendicular to the line vortex. The circumferential or azimuthal component of velocity induced in this case is given by: $u_\theta(r) = \Gamma/2\pi r$, with r the distance from the straight vortex. Using equation (1.6) for the evaluation of the velocity induced in a point \underline{x}_0 in the domain, a well-documented problem occurs in case the line vortex is curved. The Biot-Savart integral (1.6) leads to an infinite speed of the vortex filament, i.e. the induced velocity at the curved line vortex is singular. Various methods exist to regularize the induced velocity in practical applications of vortex filaments.

Furthermore, in practical applications it is often more useful to use vortices with a finite *vortex core* region. Examples of these vortices are:

- Rankine vortex. In this case

$$u_\theta(r) = \begin{cases} \frac{1}{2}\omega_0 r & \text{for } r < a \\ \frac{1}{2}\omega_0 \frac{a^2}{r} & \text{for } r \geq a \end{cases} \quad (1.7)$$

with ω_0 a constant and a the vortex core size. A vortex with velocity distribution (1.7) has a cylindrical region with constant vorticity in the core (commonly known as *solid body rotation*) and a vanishing vorticity outside the core ($r \geq a$);

- Lamb-Oseen vortex. This model arises as an exact axisymmetric solution of the Navier-Stokes equations for the initial condition consisting of a singular pointwise vorticity field: $\omega_z(r, \theta, z; t = 0) = \Gamma_0 \delta(r)$, with δ the Dirac delta function and ω_z the component of the vorticity in the (axial) z -direction.

The exact solution is then

$$\omega_z(r, \theta, z; t) = \frac{\Gamma}{4\pi\nu t} e^{-r^2/4\nu t} \quad (1.8)$$

$$u_\theta(r, \theta, z; t) = \frac{\Gamma}{2\pi r} (1 - e^{-r^2/4\nu t}) \quad (1.9)$$

with ν the (constant) kinematic viscosity of the viscous fluid. The expression for the azimuthal velocity (1.9) represents a profile that asymptotically approaches a potential

flow vortex for $r \gg \sqrt{\nu t}$ and has a smooth core region with a finite vorticity. In the present study, a Lamb-Oseen vortex is typically prescribed as vortex with the azimuthal velocity profile:

$$u_\theta(r) = \frac{\Gamma}{2\pi} \frac{[1 - \exp(-\gamma r^2/r_c^2)]}{r} \quad (1.10)$$

where r_c represents the vortex core radius.

The constant γ in the exponential function is chosen to position the maximum of azimuthal velocity at r_c (this leads to the constraint $(2\gamma + 1)e^{-\gamma} = 1 \rightarrow \gamma \cong 1.256$);

- Rosenhead vortex. For this vortex, the following azimuthal velocity profile is prescribed:

$$u_\theta(r) = \frac{\Gamma}{2\pi} \frac{r}{r^2 + \mu^2} \quad (1.11)$$

with μ a parameter that determines the dimension of the finite 'core region' of the Rosenhead vortex. At $r = \mu$, the azimuthal velocity has a maximum of $\Gamma/4\pi\mu$. For large r , the azimuthal velocity of the Rosenhead vortex shows a slower decay with increasing r than the Lamb-Oseen vortex.

In the numerical simulations of vortex pairs discussed in the present study, vortices are initialized with the Lamb-Oseen velocity profile (1.10).

1.2 Vortex wake formation

Figure 1.1 shows the trailing-vortex pair that forms the far-wake of an aircraft. The present study focuses on the dynamics of a counter-rotating pair as a model for the far-wake of an aircraft in cruise. This simple model assumes that all vortical structures present in the near-wake of an aircraft configuration *roll-up* into a single counter-rotating vortex-pair consisting of axisymmetric vortices. This *roll-up* of the near-wake is discussed in more detail in section 1.2.1 and the accompanying occurrence of an axial velocity component in the vortices in section 1.2.2.

1.2.1 Roll-up of near-wake

Figure 1.2 shows a visualization of wing-tip vortices in the near-wake of an aircraft without deflection of wing trailing-edges flaps. The smoke injected into the flow at the wing tips can be seen to convect into two vortices with a separation somewhat smaller than the wing span. This figure supports the view that the far wake of an aircraft in a cruise configuration can be treated as a single vortex pair.

Figure 1.3 shows a similar smoke visualization for an aircraft configuration with deflected trailing-edges flaps. This "high-lift" configuration, i.e. a configuration resulting in a high-lift coefficient, is representative for both take-off and landing configurations of any conventional airliner. The landing configuration differs from the take-off configuration in the larger angle of flap deflection. The figure shows three counter-rotating vortex pairs: a pair consisting of the wing-tip vortices, a pair formed by vortices emanating from the outer edge of the out-board flap on both sides of the aircraft and a similar pair formed by vortices emanating from the outer edge of the inner flaps. Figure 1.3 does not show the vortical structure formed at



Dryden Flight Research Center ECN 3831 Photographed 1974
B-727 vortex study NASA photo



FIGURE 1.2: *Visualization (injected smoke) of wing-tip vortex formation: without flap deflection*



Dryden Flight Research Center ECN 4242 Photographed 1974
B-747 vortex study NASA photo



FIGURE 1.3: *Visualization (injected smoke) of wing-tip vortex formation: with flap deflection*

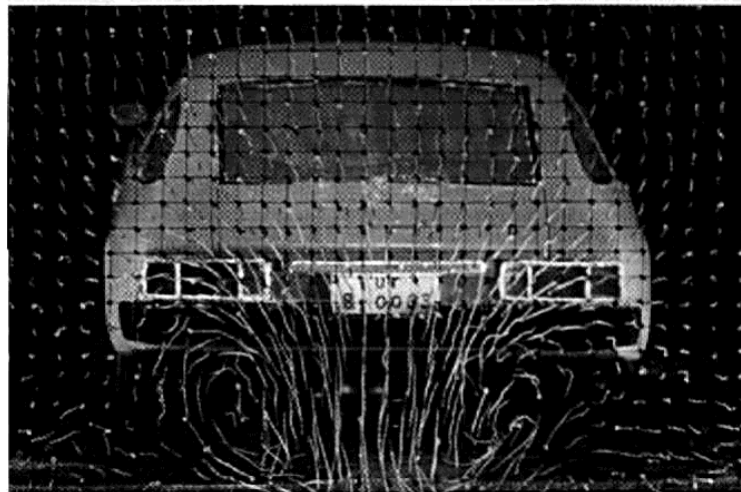


FIGURE 1.4: *Visualization of vortex-pair formation behind lift-generating car*

the sides of the fuselage at the junction between the wing and fuselage, which was shown in a visualization of a high-lift configuration in a wind tunnel, see De Bruin et al. (1996). From figure 1.3 it appears that the two inner vortices on each side of the aircraft merge within a distance of the order of a few wing spans. The figure does not show a merger of the newly-formed vortex pair with that of the wing-tip vortices, consistent with the visualization presented by De Bruin et al. (1996), which seems to indicate that the vortices remain separate until distances behind the wing, at which roll-up is completed in the situation without deflected flaps. This observation clearly undermines the use of the single counter-rotating vortex pair model when studying high-lift configurations. Furthermore, it must be remarked that condensation trails and trails of injected smoke are certainly not a direct visualization of the vorticity of the flow field.

As an aside, figure 1.4 shows a visualization of the near-wake of a car model in a wind tunnel. The figure illustrates that the formation of a trailing vortex pair is a general feature of a finite-span lift-generating body in a flow.

Accurate numerical simulation of the roll-up process of the near-wake of an aircraft configuration, employing computational methods based on the Euler or Navier-Stokes equations, is a challenging problem. Results published for this problem are typically obtained for coarse meshes, with a significant lack of resolution of the details within the vortex core. A numerical study using a highly accurate spatial discretization method was presented by Lockard and Morris (1998). The lack of adequate spatial resolution was immediately apparent as a too rapid diffusion of the vortex. Other attempts have been reported, based on either the inviscid flow assumption or crude turbulence modeling. A realistic simulation would need to include details of the aircraft configuration and fully resolve the transition to turbulence and the subsequent evolution of the turbulent flow. As with many flows of practical interest in aeronautics, a fully resolved numerical simulation is impossible. As a result, numerical studies of the wake-vortex hazard usually do not include simulations of the near-wake. Instead, a simple counter-rotating vortex pair is typically used as model for the far-wake of an aircraft.

1.2.2 Axial velocity in trailing vortices

An aspect of the roll-up process described in section 1.2.1, is the formation of an axial velocity component during this process. An analysis of the axial flow in trailing line vortices was given by Batchelor (1964). In this work, the dynamical necessity of the occurrence of an axial flow in the trailing vortices was deduced for an inviscid roll-up process. In a coordinate system moving with the aircraft, an axial flow in the core region of the trailing vortex occurs which exceeds the free-stream velocity (flight velocity). In a coordinate system fixed to the ground, this means that the fluid in the core of the trailing vortices moves in the direction opposite to the direction of flight, see Moore and Saffman (1973) for more details.

In Batchelor (1964), a similarity solution was presented for this axial flow far downstream. The effect of viscosity was shown to be a reduction of this axial velocity. The effect of viscosity during the roll-up process was included in an analysis by Saffman (1992), showing that, depending on the wing shape, the axial velocity can either exceed the free-stream velocity or be smaller. In both cases, the difference of the axial velocity with respect to the free-stream velocity can be expected to be fairly small for three-dimensional lifting surfaces of high-aspect ratio. The experimental results of De Bruin et al. (1996) show a small excess velocity in the tip-vortex cores of six per cent at a distance corresponding to five wing spans behind the wing for a small angle of attack (around 5°). This angle of attack is typical for flight conditions of a conventional airliner.

1.3 Cooperative instabilities in vortex pairs

Counter-rotating vortex pairs are known to develop three-dimensional sinusoidal instabilities, as was shown in figure 1.1. In the 1970s, studies concerning the linear instability of a vortex pair were performed. Examples of these studies are those of Crow (1970) and Widnall et al. (1970). These stability analyses show that the occurring instabilities are caused by effects of the mutual velocity induction. As a result, these instabilities are commonly referred to as *cooperative instabilities*, with the self-induction of the vortices having a damping effect. Two branches of sinusoidal instabilities are predicted by linear stability analysis: long-wavelength instabilities, with a typical wavelength of the order of five to ten times the initial spacing between the vortices, and short-wavelength instabilities, with a much shorter wavelength of the order of the vortex core size. Long-wavelength instabilities are described in section 1.3.1 and short-wavelength instabilities in section 1.3.2. Both types of instabilities can occur also simultaneously, this situation is described in section 1.3.3.

1.3.1 Long-wavelength instability

The long-wavelength instability can frequently be observed in the atmosphere as a developing sinusoidal disturbance of the condensation trails behind a jet aircraft, as shown in figure 1.1. Linear stability analysis shows that the wavelength of the sinusoidal disturbance at which the maximum growth occurs is a function of the ratio of the vortex core radius and the spacing of the vortex pair in the initial unperturbed situation. This was shown in the first linear stability analysis of a counter-rotating wake vortex pair, which was presented by Crow (1970). Since this publication, the long-wavelength instability is commonly referred to as the Crow instability. The analysis of Crow is reviewed in more detail in section 2.1. The predicted wavelength of maximum amplification, the inclination with respect to the horizontal plane of

the plane in which the growth occurs and the initial exponential growth rate were found to agree with observations such as figure 1.1.

At later stages, the long-wavelength instability forms vortex-ring structures, which develop instabilities of smaller scales. This cascade of kinetic energy to ever smaller length scales makes the long-wavelength instability an important aspect of wake-vortex decay studies and this type of instability has received a lot of attention. Some of the work related to the long-wavelength instability is reviewed by Spalart (1998). An important aspect of wake-vortex decay is the interaction of the long-wavelength instability with ambient turbulence and with stratification of the atmosphere. The interaction of the Crow instability with an intense background turbulence field was studied numerically by a number of authors, see for example Risso et al. (1997).

Effects of stratification have been studied by various researchers, Robins and Delisi (1998) and Garten et al. (2001), for example. A wide range of Reynolds numbers and Froude numbers, the latter representing stratification, was studied by Garten et al. (2001). These authors observed either an acceleration or deceleration of the vortex reconnection process by ambient stratification, depending on the Froude number. Acceleration of the growth and subsequent vortex reconnection occurs when the baroclinically produced vorticity (as a result of the stratification) advects the vortices towards one another. Similarly, for different ambient stratification, baroclinically produced vorticity can advect the vortices away from one another, slowing down the evolution.

The more complicated situation of instability and growth for a double trailing-vortex pair was analyzed by Crouch (1997), using linearized eigenvalue formulations. As in the single trailing-vortex pair, the disturbances are assumed to be periodic along the axes of the vortices. Symmetric instabilities similar to the Crow instability with respect to wavelength and growth-rate were found. Additionally, symmetric and antisymmetric instability modes were found with maximum growth rate occurring at wavelength of around 1.5 times the initial distance between the circulation centroids on both sides of the double vortex pair. Although of shorter wavelength than the Crow instability in a single vortex pair, these instabilities have wavelengths which are long relative to the vortex-core size. Therefore, these modes are unrelated to the short-wavelength instability occurring in a single vortex pair and appear to be specific for the double pair.

1.3.2 Short-wavelength instability

The stability analysis by Crow (1970) for the counter-rotating vortex pair predicted a second branch of instabilities of much shorter wavelength than the long-wavelength instability. However, the expressions used for the induced velocities needed for the linearized eigenvalue problem are not valid for sinusoidal disturbances of these short wavelengths. Thus, this branch of predicted instabilities can be regarded as unphysical. A different stability analysis was presented by Widnall et al. (1970) for the vortex pair, based on expressions for the solution of the flow field within and near a curved vortex filament derived by the method of matched asymptotic expansions. This stability analysis predicts a similar short-wavelength branch of instabilities. In this case, these are expected to be physically meaningful. The dependence of the wavelength of the most amplified short-wavelength mode on the ratio of vortex core radius and initial vortex spacing was derived by Widnall et al. (1970). Furthermore, the effect of details of axial and circumferential velocity profiles on this wavelength was studied.

Later work on short-wavelength instabilities has usually been based on a stability analysis

for a single vortex filament located in an imposed strain field. Results from these studies can be used for vortex pairs, since the effect of the neighbor vortex on the vortex considered appears as an induced strain field. The stability analysis for a single vortex is usually based on a linearization of the inviscid Euler equations in cylindrical coordinates. Examples of these studies are those of Moore and Saffman (1975) and Tsai and Widnall (1976). In the absence of strain, these stability analyses show only stable infinitesimal disturbances rotating around the vortex filament. The stable disturbances are commonly known as *Kelvin modes*, see for example Saffman (1992). In a cylindrical coordinate system (r, θ, z) , these modes can be written as a perturbation on the basic flow as

$$[\hat{u}_r, \hat{u}_\theta, \hat{u}_z, \hat{p}] = [u(r), v(r), w(r), p(r)] e^{i(kz + m\theta + \sigma t)} \quad (1.12)$$

where r is the radial coordinate, k is the axial wavenumber and m is the azimuthal wavenumber. An eigenvalue problem can be derived from the linearized Euler equations for the temporal growth rate σ as the eigenvalues and corresponding eigenfunctions $u(r)$, $v(r)$, $w(r)$ and $p(r)$. An infinite number of modes exist, for specific combinations of σ , m , k . In the unstrained situation only real-valued eigenvalues σ result and therefore stable modes. The modes with azimuthal wavenumber $m = 0$ and $|m| = 1$ are of particular interest here, as will be shown later. For $m = 0$, the disturbance is axisymmetric and the axis of the vortex filament remains undisturbed and $u(0) = v(0) = 0$. For $|m| = 1$, the disturbance modes are *bending modes*, with a deformation of the vortex axis and a non-vanishing radial velocity perturbation for $r = 0$.

In case of an imposed strain, bands of unstable modes appear with a more complex radial structure than the long-wavelength instability. The occurrence of this short-wavelength instability can be explained as a resonance phenomenon of Kelvin modes with specific azimuthal wave numbers and the external strain field, see Tsai and Widnall (1976). The Kelvin modes of interest are those with a rather complicated spatial structure, as described by Widnall et al. (1974). The short-wavelength instability is more complicated than a sinusoidal perturbation of the vortex center without change in cross-sectional structure, i.e. for the short-wavelength instability the internal structure of the vortex core is deformed.

The connection with the short-wavelength instability makes Kelvin modes and the computation of their spatial structure of particular relevance to stability studies of vortex pairs.

A numerical study of the short-wavelength instability of a rectilinear vortex in a straining field of finite strength was presented by Robinson and Saffman (1984), showing that the weak-strain results, such as those of Moore and Saffman (1975) and Tsai and Widnall (1976), continue to be valid for finite strain.

A different branch of theoretical work related to the short-wavelength instability considers instabilities of flows containing elliptical streamlines, see for example Pierrehumbert (1986), Bayly (1986) and Waleffe (1990). These flows are shown to be unstable with respect to three-dimensional disturbances. The instability mechanism is related to the periodic straining experienced by plane-wave disturbances that are advected by the rotating base flow that can lead to resonance for matching frequencies of the wave and the straining field. Applying this theoretical work to strained vortices reveals identical instabilities as for example discussed by Moore and Saffman (1975) and Tsai and Widnall (1976). Therefore, the short-wavelength instability can be treated as an *elliptic instability*, see Leweke and Williamson (1998).

Theoretical studies of the short-wavelength instability including viscous effects were presented more recently. A linearization of the Navier-Stokes equations and the solution of a generalized (matrix) eigenvalue problem for a vortex pair consisting of two Lamb-Oseen vor-

tices (see section 1.1) was presented by Sipp et al. (1998), showing both long-wavelength and short-wavelength instabilities at wavelengths consistent with previous inviscid flow stability analyses.

The dynamics of the short-wavelength instability of a strained vortex at later stages in time was studied by Sipp (2000). This study revealed a weakly nonlinear saturation of the growth of this instability, with the saturation amplitude proportional to the rate of strain. This important finding could explain the fact that the short-wavelength instability is usually not observed in aircraft condensation trails, since for a typical aircraft cruise configuration, the spacing between the vortices is large compared to the vortex core size and the resulting strain field imposed on the tip-vortices is weak. In the more complicated situation of a high-lift configuration, trailing vortices occur at much closer spacings, see for example figure 1.3 of section 1.2. In this case, the relatively close spacing of the wing-tip vortices and flap-edge vortices can be expected to enforce a more significant short-wavelength mode than in cruise configuration. This phenomenon is not observed in visualization studies. However, this phenomenon forms the underlying mechanism for proposed methods for enhanced wake decay, see Rennich and Lele (1998) and section 1.4.

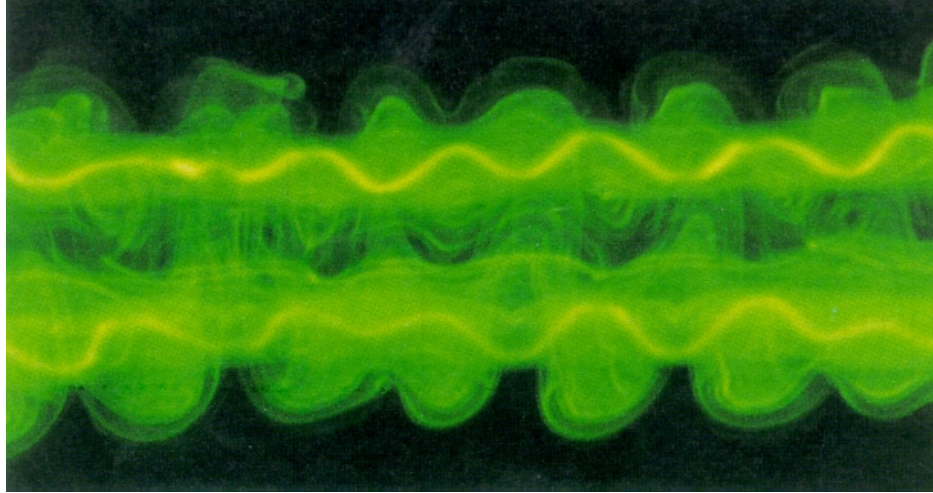
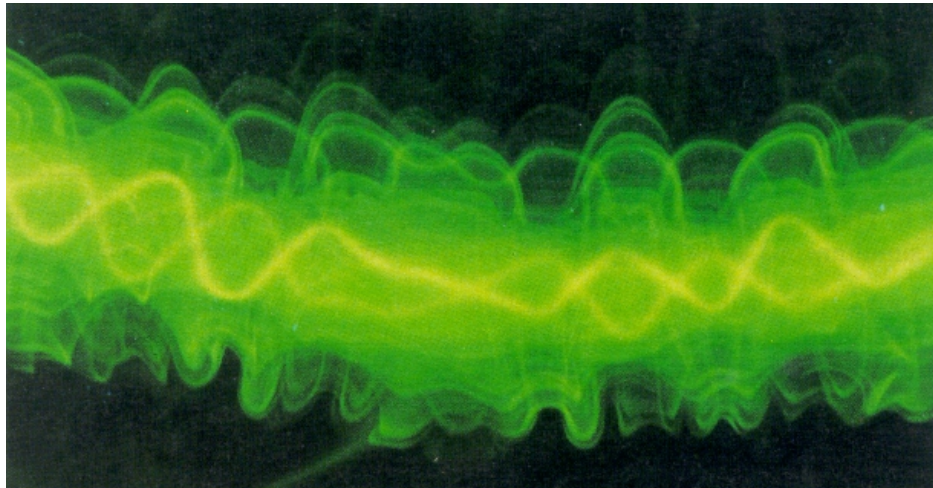
Numerical simulations of the evolution of the short-wavelength instability based on the time-dependent Navier-Stokes equations were reported only recently, see for example Orlandi et al. (1998) and Laporte and Corjon (2000).

1.3.3 Interaction of short-wavelength and long-wavelength instabilities

The three-dimensional instability of a counter-rotating vortex pair to short waves (of the order of the vortex core size) was studied experimentally by various researchers, see for example Thomas and Auerbach (1994) and Leweke and Williamson (1998).

In Leweke and Williamson (1998), an unforced closely-spaced counter-rotating vortex pair was studied, that was generated in a water tank by an instantaneous motion of two sharp-edged flaps. The resulting vortices were shown to have a velocity profile very close to that of a Lamb-Oseen vortex (axisymmetric two-dimensional vortex with a Gaussian vorticity distribution, see section 1.1). The typical vortex spacing was 2.5 cm and the Reynolds number based on circulation, $Re = \Gamma/\nu$, was in the range between 2400 and 2800. The unforced vortex pair developed both long-wavelength and short-wavelength instabilities, as can clearly be seen from figures 1.5 and 1.6, which reproduce some of the visualization results of Leweke and Williamson (1998). Figure 1.5 shows that the short-wavelength disturbance is in phase when viewed from the top. The side view reproduced in figure 1.6 shows the disturbance being out of phase. Furthermore, the centerlines were shown in Leweke and Williamson (1998) to be displaced in planes inclined approximately 45° with respect to the horizontal plane. This orientation coincides with the direction of maximum stretching in the strain field generated by the mutual velocity induction. The inclination of the planes in which the growth of short-wavelength disturbance occurs was observed to remain constant. The experimental results for the short-wavelength instability were shown to agree well with theoretical results, such as those of Tsai and Widnall (1976) and Waleffe (1990).

A significant coupling between the two types of instability can be observed, since the long-wavelength instability mode brings parts of the vortices closer together, other parts further apart, in a wavy periodic fashion. The short-wavelength instability is driven by the mutually induced strain in the vortex pair, which increases with decreasing separation. Thus, the growth of the short-wavelength was affected by the presence of the long-wavelength instabil-

FIGURE 1.5: *Water-tank experiment: top view (from Leweke and Williamson (1998))*FIGURE 1.6: *Water-tank experiment: side view (from Leweke and Williamson (1998))*

ity.

An important finding of the work by Leweke and Williamson (1998) is that the long-term evolution of a vortex pair when both types of instabilities are present, is quite different from the case with just the Crow instability. The authors found that, for each wavelength, two secondary vortex pairs are generated on the lower side of the primary pair. As described earlier, the case with the Crow instability alone develops vortex rings. These vortex rings are relatively large-scale structures which can persist for long periods of time. The interaction of the two types of instabilities was observed to enhance mixing and to distribute the kinetic energy in the initial large-scale structures to small-scale structures, with larger viscous dissipation, much more effectively.

From these observations, one can draw the conclusion that it would be favourable for a rapid

decay of an aircraft trailing-vortex pair to develop both types of instabilities simultaneously.

1.4 Decay of an aircraft vortex wake

The three-dimensional instabilities described in sections 1.3.1 and 1.3.2 are an important decay mechanism for a trailing-vortex pair. Other mechanisms are viscous decay of the vortices due to molecular viscosity and the interaction with ambient turbulence and stratification. In the earth atmosphere these last two contributions can be significant, but both are difficult to include in a wake decay model. Decay models predicting vortex-wake decay including these atmospheric effects have been developed, examples are presented in Sarpkaya (1998) and Sarpkaya (2000). These models can produce predictions that agree reasonably well with field data obtained from measurements around a number of U.S. airports. However, for some cases, large deviations between predictions and field data are observed, see Sarpkaya (2000). Even when these models give a correct decay for a given atmospheric condition, a problem that remains is an accurate characterization and prediction of these atmospheric conditions. In recent years, NASA has compiled a database of measurements from a range of measurements in the atmosphere, including field data of wake-vortex decay around various U.S. airports and measurements using a small aircraft probing the vortex wake of a large aircraft, see Vicroy et al. (1998). This database is to be used for validation of complex numerical simulations and decay models.

The hazard caused by a vortex-wake, with a developing Crow instability, to aircraft in cruise is reviewed by Rossow and James (2000). These authors state that the hazard in this cruise phase of flight persists for tens of minutes, longer than in the airport-approach phase, with a wake typically posing a hazard for several minutes.

Development of methods to enhance the decay of aircraft wake vortices has been reported by a number of researchers. A number of approaches has been studied:

- configuring the inboard vortices, in a high-lift configuration, such that these vortices remain in a region of high strain. Perturbations on these vortices will then grow very rapidly. These inboard vortices will excite a long-wavelength instability in the wing-tip vortex pair. This method was presented by Rennich and Lele (1998) and could accelerate the development of three-dimensional instabilities. Another study focusing on forcing of inboard vortices was presented by Cottet et al. (2000);
- perturbing the wing-tip vortices by internal and external density perturbations. This method was analyzed by Orlandi et al. (1998) as a means of initiating short-wavelength instabilities. The density perturbations were thought to be created by temperature variations produced by combustion of fuel in the wing-tip region. This method was envisaged for use during take-off and landings.

Extensive research remains necessary before either of these methods can be used in practice. A more practical method, with less potential benefit, seems to be the design optimization of new airliner for minimum vortex-wake generation. Since the wake-vortex hazard is particularly severe in the landing phase, this design optimization should emphasize high-lift configurations. The ratio of the vortex core radius and the spacing of vortices in a counter-rotating vortex pair forms the major parameter in the development of cooperative instabilities. Both

theory, see chapter 2, and numerical simulations, such as those of chapters 5 and 6, indicate that this ratio should be maximized for maximum wake decay. The spacing of vortices is directly related to the span of the wings of an aircraft. As a result of design constraints associated with structural efficiency (small span) and aerodynamic efficiency (large span) and the resulting compromise between the two, the span of wings is restricted to within a narrow range. The remaining degree of freedom is therefore the core radius of the trailing vortices. A design optimization can be envisaged that maximizes the core radii of the trailing vortices formed in the roll-up process.

1.5 Scaling of decay process

The present study of both the long-wavelength and short-wavelength instability considers a counter-rotating vortex pair as a model for the trailing vortex wake of an aircraft in cruise flight. The dynamics of three-dimensional instabilities in such a vortex pair are driven by the velocity field that the vortices induce on one another. This motivates a non-dimensionalization of time with a characteristic time-scale of $2\pi b^2/\Gamma$, with Γ the strength of the vortices of the vortex pair and b the spacing between the vortices. Thus, one non-dimensional time unit corresponds to the time in which the vortex pair moves one spacing downwards with velocity $\Gamma/2\pi b$. This method of non-dimensionalization of time enables a comparison of results for different vortex-pair spacings.

Consider the example of a Boeing 747-400 in cruise flight. The wing span of this aircraft is 64.4 m. For an elliptic wing loading, the separation distance of the trailing vortices can be shown to be $\pi/4$ times the wing span. In this case, $b = 50.58$ m. Assume that the aircraft is cruising at an altitude of 12,000 m and that the flight velocity is 0.85 the local speed of sound. According to the International Standard Atmosphere, the air density at this altitude is 0.3108 kg/m³ and the local speed of sound is 295.07 m/s. Therefore, the aircraft is flying at $0.85 \times 295.07 = 250.8$ m/s or 902.9 km/h.

The circulation of the trailing vortices can be computed from the equation

$$\Gamma = \frac{W}{\rho U b} \quad (1.13)$$

with W the weight of the aircraft, U the flight velocity. Estimating the mass of the aircraft at 300,000 kg, equation (1.13) gives:

$$\Gamma = \frac{300,000 \times 9.80665}{0.3108 \times 250.8 \times 50.58} = 746.2 \text{ m}^2/\text{s} \quad (1.14)$$

The vortex reconnection process in the evolution of the Crow instability was observed to occur between dimensionless time $T = 3$ and $T = 5$ in the various numerical simulations considered in chapter 5. At $T = 3$, the aircraft has traveled the following distance $D_{T=3}$ since $T = 0$:

$$D_{T=3} = U \cdot T \cdot \frac{2\pi b^2}{\Gamma} = 250.8 \cdot 3 \cdot \frac{2\pi \cdot 50.58^2}{746.2} = 16.208 \text{ km} \quad (1.15)$$

and similarly $D_{T=5} = 27.013$ km. Here, $T = 0$ can be thought of as an instance in time in which the roll-up phase of the wake-formation process, see section 1.2, is completed and the resulting trailing vortex pair gets slightly perturbed by atmospheric disturbances.

The Reynolds number of the flight condition can easily be computed from the circulation computed in equation (1.14). The dynamic viscosity of air at the altitude considered is given

as: $\mu = 1.4216 \cdot 10^{-5} \text{ kg/ms}$.

The Reynolds number based on circulation is therefore

$$Re_{\Gamma} = \frac{\Gamma}{\nu} = \frac{746.2}{1.4216 \cdot 10^{-5}/0.3108} = 1.631 \cdot 10^7 \quad (1.16)$$

This Reynolds number turns out to be unattainable in practical numerical simulations of vortex-pair instabilities, i.e. with a mesh density limited by the available computer facilities, the flow field becomes under-resolved at later stages of the evolution. Therefore, computational studies of vortex-pair instabilities typically use lower Reynolds numbers. The highest Reynolds number considered in the numerical simulations performed in the present study is two order of magnitude lower than that of relation (1.16). Here, vortex pairs at a range of Reynolds numbers from $O(10^3)$ to $O(10^5)$ are studied. A good understanding of the Reynolds number dependence of the flow phenomena that are studied in the present work is therefore of great relevance, since this understanding allows an extrapolation of at least some of the findings of the present computational study to Reynolds numbers typical of flight conditions.

1.6 Outline and objective of present study

Problems related to aircraft wake-vortex systems and the more general problem of three-dimensional instabilities which can occur in counter-rotating vortex pairs, have received a lot of attention in the past. However, a number of aspects require further study. The objective of the present study is to increase the understanding of a number of these remaining questions. Chapter 2 discusses the linear stability of vortex pairs. A review is presented of the stability analysis by Crow (1970), that introduced much of the understanding on three-dimensional instabilities in (aircraft) trailing vortex pairs, and of the later study by Widnall et al. (1970), that includes more details of the vortex core structure into the stability analysis. The main difference between the two analyses is in the formulation of the self-induced velocity of the vortex filaments. Also in chapter 2, a stability analysis equivalent to that of Crow (1970) is discussed for Rosenhead vortex filaments. Comparison of the three vortex filament based formulations shows the sensitivity of the predicted instabilities with respect to the used formulation for the self-induced velocity of the filaments. The results of the linear stability theory are used in the computational study of the Crow instability, both as basis for the initial conditions and as reference data in verifications of the obtained numerical results.

The remainder of chapter 2 focuses on the linear stability analysis of vortex pairs based on generalized (matrix) eigenvalue problems derived from linearization of either the Euler or the Navier-Stokes equations. The derivation of the resulting eigenvalue problem is discussed for Cartesian and cylindrical coordinate systems.

Based on the generalized eigenvalue problem in a cylindrical coordinate system, a computational method is derived for the spatial structure of Kelvin modes on a single vortex. Chapter 2 concludes with a proposed computational method for the growth rate of short-wavelength instability modes on a single vortex that uses the spatial structure of Kelvin modes of opposite azimuthal wave numbers.

The present research effort is numerical in nature and as such, consists for a significant part of the development of numerical tools capable of simulating incompressible flows governed

by the Navier-Stokes equations. In the course of the present study, two computational methods for three-dimensional flows were developed. The two methods are described in detail in chapter 3. The methods combine well-known techniques for the temporal integration of the governing equations with high-order accurate spatial discretization techniques, some of which were newly developed in the course of the present work. The spatial discretization methods are described in chapter 4, with a particular emphasis on the fourth-order accurate discretization method for Helmholtz/Poisson equations in three dimensions on a uniformly spaced rectangular computational domain, since it is a new development of the present study. Chapter 5 discusses a computational study of the long-wavelength instability, i.e. Crow instability. Due to practical limitations on computer resources, a model vortex pair is studied with a ratio of vortex core radius and vortex pair spacing that is larger than that of a trailing vortex wake of an aircraft. The relatively close spacing of the vortices reduces the required computational effort. Furthermore, the highest Reynolds numbers considered in the present study are about two orders of magnitude lower than the Reynolds number of a trailing vortex wake of a large airliner in cruise flight.

For the model vortex pair, the initial stage of the evolution of the Crow instability is discussed in section 5.4. This stage is dominated by the (nearly) exponential growth of sinusoidal perturbations of the vortices. The dynamics of the instability at this stage are well-studied and allow a verification of the developed numerical methods, by comparing the obtained results for this stage both with theoretical results from linear stability theory and with numerical results presented by various authors for similar test cases.

The later stage of the Crow instability is of greater practical relevance for the wake-vortex hazard. This stage of the evolution is characterized by the vortex-reconnection process, forming vortex rings, as shown in figure 1.1. A theoretical description of this phenomenon was presented by Kida and Takaoka (1994), studying the topology of vortex lines in the vortex pair at different instances in time. In section 5.5.2, the reconnection process is analyzed in detail using highly-accurate numerical results obtained in the present study. A comparison is made between the topology of the computed vortex lines and that of the theoretical analysis of Kida and Takaoka (1994), described in section 5.5.1. Section 5.6 presents a numerical study of this later stage of the Crow instability. With the limitations on computer resources the sensitivity to Reynolds number and spatial resolution parameters is analyzed.

Chapter 6 presents a computational study of the short-wavelength instability in a counter-rotating vortex pair. As described previously in this chapter, the dynamics of the short-wavelength instability have not been studied as extensively as those of the Crow instability. Some aspects of this instability, such as the non-linear saturation of the growth and the complicated flow features that occur at later stages of the development require more study. Increasing the understanding of these aspects of the short-wavelength instability forms one of the main objectives of the present study.

An important aspect of wake-vortex dynamics is the interaction of trailing vortices with the ground during take-off and landing. Chapter 7 discusses the rebound process of a vortex pair interacting with a solid surface. Numerical results from two-dimensional simulations are discussed that highlight the characteristic features of the rebound process.

Concluding remarks and directions for future work are given in chapter 8.

LINEAR STABILITY ANALYSIS



This chapter investigates the linear stability of a counter-rotating vortex pair. Infinitesimal perturbations of the vortices are studied with an assumed periodic dependence in the axial direction of the vortex pair. Figure 2.1 shows a sketch of such a perturbed vortex pair. The assumption of periodicity of the flow field in the axial direction is used throughout this chapter. The linear stability of these flows is analyzed using two types of methods:

- vortex-filament based methods. In this case, the vortex pair is assumed to consist of two vortex filaments of equal strength and opposite sign. Some characteristics of vortex filaments were described in section 1.1. The generated velocity field can be computed using Biot-Savart type integrals, with a singular self-induced velocity in case of a curved filament. A detailed study of this singularity is essential for a physically meaningful stability analysis and is therefore described in some length in this chapter;
- methods based on the linearized Euler or Navier-Stokes equations for small perturbations on a base flow consisting of either a single vortex or a counter-rotating vortex pair. With the assumed periodicity in the axial direction, an eigenvalue problem similar to the Orr-Sommerfeld equations, commonly used in linear stability analysis of boundary layers (see for example White (1974)), can be derived. Compared to the vortex-filament based methods, these methods have the advantage of allowing viscous effects to be included. Furthermore, methods based on the linearized Euler or Navier-Stokes equations are better suited for studying short-wavelength modes, since the velocity-induction integrals which appear in vortex-filament methods are typically valid only for a limited curvature of the filament. For very short instability modes, predictions by vortex-filament based methods can therefore be invalid. A major disadvantage of methods based on the linearized Euler or Navier-Stokes equations is the fact that quantitative data can only be obtained using numerical solution techniques, while vortex-filament based methods can be used to obtain analytical results for exponential growth rates, most unstable wavelengths, etc.

Section 2.1 presents a review of the stability analysis of Crow (1970). In the study of Crow (1970), the singularity of the self-induced velocity is removed by introducing the 'cut-off' line integral approach, where the integral is regularized using a cut-off parameter. This method discards the immediate vicinity of the point located at the vortex filament when evaluating the self-induced velocity. In Crow's study, the cut-off parameter is chosen such that known results for the self-induced rotation of a sinusoidal vortex filament and the propagation

velocity of a vortex ring, both with a constant vorticity distribution in the finite vortex core, are matched.

Section 2.1 presents a detailed analysis of this singular contribution, using a different derivation of the linearized eigenvalue problem than used by Crow (1970). When the singular contribution to the self-induced velocity is eliminated, the results of section 2.1 are identical to those of Crow (1970).

Section 2.2 presents a similar stability analysis based on vortex filaments. In this section, Rosenhead's method is used to regularize the velocity-induction integrals. Using this approach, the vortex filament can be thought of as having a finite core region, somewhat similar to a Lamb-Oseen vortex.

Section 2.3 reviews the stability analysis of Widnall et al. (1970), in which the singularity was eliminated using a description of the velocity field in the vortex core region based on the conservation equations for mass and vorticity formulated in a coordinate system moving with the perturbed vortex filament. The method of matched asymptotic expansions is used to match this solution to the velocity field outside the vortex core region. This approach allows the introduction of the details of the vortex core velocity distribution in the stability analysis. Comparison of the results of sections 2.1, 2.2 and 2.3 enables an assessment of the effect of using different methods of removing the singularity from the self-induced velocity expression.

The remaining sections of this chapter describe stability analyses using methods based on linearized Euler or Navier-Stokes equations for small perturbations. Section 2.4 presents a derivation of the generalized eigenvalue problem which results when the base flow is assumed to be periodic in the axial direction and the remaining two coordinate directions are taken as Cartesian. The Orr-Sommerfeld equations used in boundary layer studies typically use the assumption that the spatial variation in the direction normal to the solid wall is much larger than in the other direction and consequently, derivatives in the direction along the wall are neglected. This leads to a great simplification of the mathematical problem. However, for the flow field of interest here, a spatial dependence in two Cartesian coordinate directions remains, leading to a far more complicated eigenvalue problem. Section 2.4 summarizes results obtained by Sipp et al. (1998). These authors solved the resulting large matrix-eigenvalue problem. As with vortex-filament based methods, both long-wavelength and short-wavelength instability modes are predicted. However, the analysis by Sipp et al. (1998) showed short-wavelength instability modes at multiple branches.

Next, the transition to a cylindrical coordinate system is made, with section 2.5 describing the effect of an imposed strain field on an isolated vortex. In the unstrained situation, an infinite number of stable perturbations exist on a vortex column. These modes are commonly known as Kelvin modes, see for example Saffman (1992), and are described in some detail in section 2.6. Section 2.7 presents a derivation of the Orr-Sommerfeld equations formulated in cylindrical coordinates for a single vortex located in an imposed strain field. Based on this system of equations, section 2.7 describes how, in the absence of an imposed strain field, the resulting equations can be formulated in a suitable way for a computational method for Kelvin modes on a vortex.

Finally, a computational method is described that uses the spatial structure of specific Kelvin modes to predict the exponential growth rate of the short-wavelength instability mode at the axial wavelength of these Kelvin modes.

2.1 Review of stability analysis of Crow

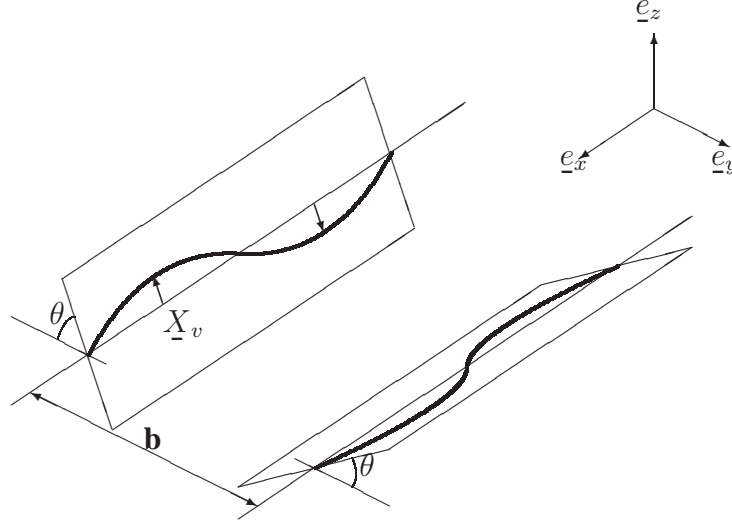


FIGURE 2.1: *Geometrical description of counter-rotating vortex pair with sinusoidal perturbation (symmetric configuration).*

The first linear stability analysis of a trailing vortex pair was presented by Crow (1970). Crow used a vortex filament based technique to derive a linearized eigenvalue problem for unstable sinusoidal perturbations of the vortices in the vortex pair shown in figure 2.1. This section presents a review of the original analysis presented in Crow (1970).

Figure 2.1 shows the configuration of the vortex pair, in which the left and right vortices have circulation $-\Gamma$ and Γ , respectively. The vortices are a distance b apart in the unperturbed situation. The unperturbed vortex pair would translate downward with a velocity $\Gamma/2\pi b$, so the coordinates of figure 2.1 must be envisaged as moving downward at that velocity as well. In an incompressible flow, vorticity and velocity are related through the kinematic relation (1.3) of section 1.1. The vorticity distribution is denoted by $\underline{\omega}(\underline{x})$. For a vortex filament which location at time t is given by $\underline{x} = \underline{x}_v(s)$, where s is a monotonically increasing parameter along the filament, the vorticity distribution was given by equation (1.4) as:

$$\underline{\omega} = \Omega(x', y'; s) \frac{d\underline{x}_v}{ds} / \left| \frac{d\underline{x}_v}{ds} \right| \quad (2.1)$$

with (x', y') local coordinates in the infinitesimal cross-section of the filament at $\underline{x}_v(s)$. Then with $dV(\underline{x}) = |d\underline{x}_v/ds| ds dS$, where dS denotes the cross-section of the filament C , the velocity induced in point \underline{x}_0 can be written as:

$$\underline{u}(\underline{x}_0) = -\frac{1}{4\pi} \int_C \frac{\underline{x}_0 - \underline{x}_v(s)}{|\underline{x}_0 - \underline{x}_v(s)|^3} \times \left\{ \frac{d\underline{x}_v}{ds} \int \int_S \Omega(x', y'; s) dS \right\} ds \quad (2.2)$$

The surface integral is the circulation $\Gamma(s)$ of the filament, so that

$$\underline{u}(\underline{x}_0) = -\frac{1}{4\pi} \int_C \Gamma(s) \frac{\underline{x}_0 - \underline{x}_v(s)}{|\underline{x}_0 - \underline{x}_v(s)|^3} \times \frac{d\underline{x}_v}{ds} ds \quad (2.3)$$

This expression is a singular integral for points \underline{x}_0 on the filament, with the induced velocity becoming unbounded. It is known as the Biot-Savart expression for the velocity induced by a vortex filament, and was previously discussed in section 1.1. Assuming the doubly-infinite vortex to be of constant strength Γ , at time t , located at

$$\underline{x}_v(s) = s\underline{e}_x + \underline{B} + \underline{X}_v(s, t) \quad (2.4)$$

with \underline{B} the cross-flow plane location of the unperturbed vortex and \underline{X}_v the cross-flow plane perturbation with respect to $s\underline{e}_x + \underline{B}$. Here, capital symbols denote cross-flow plane quantities. Assume $|\underline{X}_v(s, t)| \ll |\underline{B}|$ and a perturbation that is periodic in the x -coordinate direction, i.e.

$$\underline{X}_v(s, t) = \hat{\underline{X}}_v(t) e^{iks} \quad (2.5)$$

Expansion of equation (2.3) results in the following expression for the velocity induced at the point $x_0\underline{e}_x + \underline{X}_0$ not too close to the filament:

$$\begin{aligned} \underline{u}_v(x_0\underline{e}_x + \underline{X}_0) &= -\frac{\Gamma}{2\pi} \frac{(\underline{X}_0 - \underline{B}) \times \underline{e}_x}{|\underline{X}_0 - \underline{B}|^2} - \frac{\Gamma}{2\pi} \left[\frac{\underline{e}_x \times \hat{\underline{X}}_v}{|\underline{X}_0 - \underline{B}|^2} (i_1(\beta') + i_2(\beta')) + \right. \\ &\quad \left. \frac{(\underline{X}_0 - \underline{B}) \times \underline{e}_x (\underline{X}_0 - \underline{B}) \cdot \hat{\underline{X}}_v}{|\underline{X}_0 - \underline{B}|^4} i_3(\beta') \right] e^{ikx_0} \\ &\quad + \frac{\Gamma}{2\pi} \frac{(\underline{X}_0 - \underline{B}) \times \hat{\underline{X}}_v}{|\underline{X}_0 - \underline{B}|^3} \beta' i_2(\beta') e^{ikx_0} + O(\delta^2) \end{aligned} \quad (2.6)$$

where δ is the order of magnitude of the perturbation $\underline{X}_v(s, t)$.

In expression (2.6), the first three terms are contributions to the cross-flow plane velocity, the last one is in the x -coordinate direction. In expression (2.6), the following definitions are used

$$\beta' = k|\underline{X}_0 - \underline{B}| \quad (2.7)$$

$$i_1(\beta') = \int_0^\infty \frac{\beta' \xi \sin(\beta' \xi)}{(1 + \xi^2)^{3/2}} d\xi = \beta'^2 K_0(\beta') \quad (2.8)$$

$$i_2(\beta') = \int_0^\infty \frac{\cos(\beta' \xi)}{(1 + \xi^2)^{3/2}} d\xi = \beta' K_1(\beta') \quad (2.9)$$

$$i_3(\beta') = \int_0^\infty \frac{\cos(\beta' \xi)}{(1 + \xi^2)^{5/2}} d\xi = \frac{1}{3} i_1(\beta') + \frac{2}{3} i_2(\beta') \quad (2.10)$$

with K_n the modified Bessel function of order n .

In case the point \underline{x}_0 is close to the vortex filament, i.e. $\underline{x}_0 = s_0\underline{e}_x + \underline{B} + \underline{X}_v(s_0) + \underline{d}$, the integral is split-up in the parts $[-\infty, s_0 - \Delta]$, $[s_0 - \Delta, s_0 + \Delta]$ and $[s_0 + \Delta, \infty]$. For the non-singular part of the induced velocity, i.e. the integral excluding the integral around s_0 , an expansion very similar to the one used above, with $\underline{d} = 0$, leads to

$$\underline{u}_v^{ns}(\underline{x}_0 \rightarrow \underline{x}_v(s_0)) = -\frac{\Gamma k^2}{2\pi} (\underline{e}_x \times \hat{\underline{X}}_v) \omega(k\Delta) e^{iks_0} \quad (2.11)$$

with

$$\omega(k\Delta) = \frac{1}{2} \left\{ \frac{\cos(k\Delta) - 1}{k^2\Delta^2} + \frac{\sin(k\Delta)}{k\Delta} - C_i(k\Delta) \right\} \quad (2.12)$$

with $C_i(k\Delta)$ the Cosine integral, defined as

$$C_i(x) = - \int_x^\infty \frac{\cos(t)}{t} dt = \gamma + \ln(x) + \int_0^x \frac{\cos(t) - 1}{t} dt \quad (2.13)$$

where $\gamma \approx 0.5772$ is Euler's constant.

Figure 2.3 shows function $\omega(\delta)$. The figure uses a logarithmic axis for $\delta = k\Delta$, leading to a (nearly) linear dependence of ω on δ for very small δ . Figure 2.3 shows the logarithmic singularity of the self-induced velocity for points on the vortex filament.

Crow omitted the contribution due to the vortex filament between $s_0 - \Delta$ and $s_0 + \Delta$. Crow determined parameter Δ by matching results from his cut-off method for Rankine vortices (uniformly distributed vorticity in the vortex core and zero outside the core) with two classical results:

- the traveling displacement wave around a columnar vortex, with known angular frequency opposite to the circulatory flow for long wavelengths;
- the propagation of a slender vortex ring with known velocity

This results in $d \cong 0.3210 r_c$, where r_c represents the vortex core radius of the Rankine vortex.

The singular integral in the range $s_0 - \Delta$ to $s_0 + \Delta$, however, can be evaluated. This evaluation is given in Hoeijmakers (1989).

With $\underline{x}_v(s)$ the parametric description of the vortex filament and $\underline{x}_0 = \underline{x}_v(s_0) + \underline{d}$, where $\underline{d} \cdot \underline{x}'_v(s_0) = 0$, it can be shown that for $|\underline{d}| \rightarrow 0$, such that $|\underline{d}|/|\underline{x}'_v|\Delta \rightarrow 0$:

$$\begin{aligned} \underline{u}_v^s(\underline{x}_0 = \underline{x}_v(s_0) + \underline{d}) &= \lim_{|\underline{d}| \rightarrow 0} \left[- \frac{\Gamma}{2\pi} \frac{\underline{d} \times \underline{x}'_v(s_0)}{|\underline{d}|^2 |\underline{x}'_v(s_0)|} \right. \\ &\quad + \frac{\Gamma}{4\pi} \left\{ \frac{\underline{x}'_v(s_0) \times \underline{x}''_v(s_0)}{|\underline{x}'_v(s_0)|^3} \ln \left(\frac{2\Delta |\underline{x}'_v(s_0)|}{|\underline{d}|} \right) \right. \\ &\quad \left. \left. - \frac{(\underline{x}'_v(s_0) \times \underline{x}''_v(s_0)) \cdot \underline{d}}{|\underline{d}|^2 |\underline{x}'_v(s_0)|^3} \underline{d} \right\} \right] + O(|\underline{d}|) \end{aligned} \quad (2.14)$$

with the primes denoting differentiation with respect to s .

The first term of expression (2.14) is the $O(1/|\underline{d}|)$ singular contribution to the azimuthal velocity component usually ignored when working with discrete vortices in two-dimensional and three-dimensional situations. The second term in expression (2.14) represents the effect of curvature and consists of two parts:

- a logarithmically singular contribution pointing in the direction of the bi-normal $\underline{e}_b = (\underline{x}'_v \times \underline{x}''_v)/|\underline{x}'_v \times \underline{x}''_v|$;
- an $O(1)$ part in the direction of \underline{d} , i.e. radially from the vortex filament;

Except for the logarithmic term, the self-induced velocity depends on the direction along which the vortex filament is approached. It is therefore appropriate to take the average over

a circle, of radius R and centered at s_0 , in the plane perpendicular to the filament at $s = s_0$. This gives:

$$u_{v,a}^s = \frac{1}{\pi R^2} \int_0^{2\pi} \int_0^R u_v^s(x_v(s_0) + d) r dr d\theta = \frac{\Gamma \kappa}{4\pi} \ln \left(\frac{2\Delta |x_v'(s_0)|}{R} \right) \underline{e}_b \quad (2.15)$$

with \underline{e}_b denoting the bi-normal defined above and κ the curvature, $\kappa = |\underline{x}_v' \times \underline{x}_v''|/|\underline{x}_v'|^3$, with $R/|\underline{x}_v'(s_0)\Delta| < 1$.

In the present situation, $\underline{x}_v(s) = s\underline{e}_x + \hat{\underline{X}}_v(t)e^{iks}$ and the self-induced velocity becomes:

$$u_{v,a}^s(x_0 \rightarrow x_v(s_0)) = -\frac{\Gamma k^2}{4\pi} (\underline{e}_x \times \hat{\underline{X}}_v) e^{iks_0} \ln \left(\frac{2\Delta}{R} \right) + O(\delta^2) \quad (2.16)$$

with $R/\Delta < 1$. This indicates that this contribution increases the magnitude of the self-induced velocity compared to the value of the expression used in Crow (1970).

Now the system of governing equations for the motion of a vortex pair, consisting of two perturbed vortex filaments of equal, but opposite-signed strength Γ , with spacing b in the unperturbed situation. The situation is sketched in figure 2.1 and with the following characteristics:

$$\begin{aligned} \text{Filament 1: } \underline{x}_v(s) &= s\underline{e}_x + \underline{B}_1 + \hat{\underline{X}}_{v1}(t)e^{iks_0}; \quad \Gamma_1 = +\Gamma; \quad \underline{B}_1 = +\frac{b}{2}\underline{e}_y + h(t)\underline{e}_z \\ \text{Filament 2: } \underline{x}_v(s) &= s\underline{e}_x + \underline{B}_2 + \hat{\underline{X}}_{v2}(t)e^{iks_0}; \quad \Gamma_2 = -\Gamma; \quad \underline{B}_2 = -\frac{b}{2}\underline{e}_y + h(t)\underline{e}_z \end{aligned} \quad (2.17)$$

where $h(t)$ denotes the time-dependent z -coordinate, with $\frac{dh}{dt}$ representing the downward motion of the vortex pair.

The velocity induced at vortex filament 1 is given by:

$$\begin{aligned} u_v(s_0\underline{e}_x + \underline{B}_1 + \hat{\underline{X}}_{v1}(t)e^{iks_0}) &= -\frac{\Gamma\beta^2}{2\pi b^2} (-\underline{e}_y\hat{Z}_{v1} + \underline{e}_z\hat{Y}_{v1}) \left\{ \omega(k\Delta) + \ln \left(\frac{2\Delta}{R} \right) \right\} e^{iks_0} \\ &\quad -\frac{\Gamma}{2\pi b}\underline{e}_z + \frac{\Gamma}{2\pi b^2} [\underline{e}_y\hat{Z}_{v1} + \underline{e}_z\hat{Y}_{v1}] e^{iks_0} \\ &\quad +\frac{\Gamma}{2\pi b^2} \left[-\underline{e}_y\hat{Z}_{v2}\Psi(\beta) - \underline{e}_z\hat{Y}_{v2}\chi(\beta) \right] e^{iks_0} \\ &\quad -\frac{\Gamma}{2\pi b^2} \underline{e}_x\hat{Z}_{v2}\beta i_2(\beta) e^{iks_0} + O(\delta^2) \end{aligned} \quad (2.18)$$

with $\beta = kb$. The first term constitutes the cross-flow plane velocity components induced by filament 1 on itself, which is perpendicular to the plane of the perturbation. The other terms represent induction by filament 2. In the order given in equation (2.18), the velocity induction by filament 2 consists of:

- $O(1)$ cross-flow term representing the downward motion of the pair;
 - $O(\delta)$ cross-flow plane strain due to velocity field induced by vortex filament 2, directed at an angle $\pi/2 - \theta$ with respect to the horizontal plane;
 - $O(\delta)$ mutual cross-flow plane velocity field;
 - $O(\delta)$ axial velocity field
-

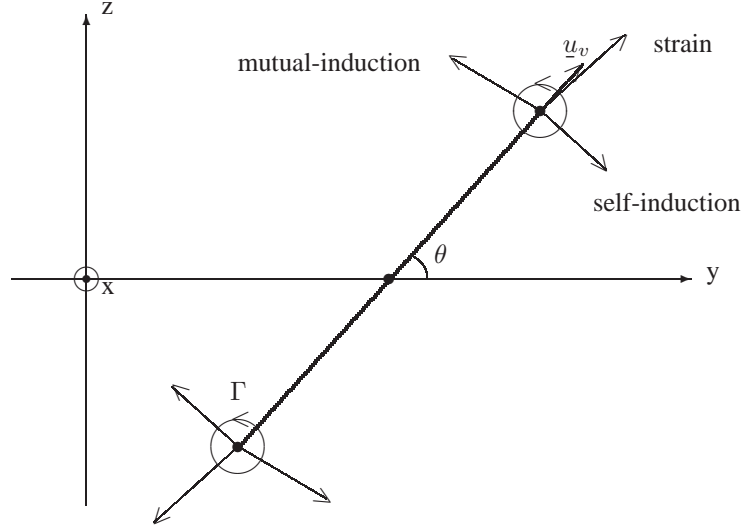


FIGURE 2.2: Components of velocity induction given in equation (2.18) for a coordinate system moving with the vortex pair for vortex filament 1. $\delta/\beta = 0.1$, $\theta = 48^\circ$, $\beta = 0.8$, $\omega(\delta) = 1.225$, $\Psi(\beta) = 1.05125$ and $\chi(\beta) = 0.6894$.

Figure 2.2 presents a sketch of the velocity components induced on vortex filament 1. The figure shows a projection onto the (y, z) -plane of the perturbed vortex filament 1 and the velocity components induced in the two positions along the filament at which the perturbation has a maximum. A coordinate system moving with the vortex pair is considered, therefore, the $O(1)$ down wash term of equation (2.18) is not shown. Within this moving frame of reference and for the specific choice of parameters, the sum of $O(\delta)$ induced velocity components is in the direction of the perturbation of the vortex filament. This situation occurs at every position on the vortex pair. This is the underlying mechanism for the exponential growth of the perturbation. Figure 2.2 shows the situation for $\delta/\beta = 0.1$, giving $\theta = 48^\circ$ and a scaled wave number $\beta = k \cdot b = 0.8$. The velocity vectors are drawn at lengths corresponding to the values of the components indicated in equation (2.18).

The motion of the vortex filament has to satisfy the kinematic relation:

$$\frac{\partial x_v}{\partial t} + u_v \frac{\partial x_v}{\partial s} = \underline{u}_v \quad (2.19)$$

In linearized form, equation (2.19) becomes

$$\frac{d\underline{B}_1}{dt} + \frac{d\hat{X}_{v1}}{dt} e^{iks_0} = (\underline{u}_v(x_v) \cdot \underline{e}_y) \underline{e}_y + (\underline{u}_v(x_v) \cdot \underline{e}_z) \underline{e}_z \quad (2.20)$$

For filament 2, expressions similar to (2.18) and (2.20) can be derived. Assume a time-

dependence of the radial perturbations as

$$\begin{aligned}
 Y_{v1}(s; t) &= \hat{Y}_{v1}(t)e^{iks} = \tilde{Y}_{v1}e^{at}e^{iks} \\
 Z_{v1}(s; t) &= \hat{Z}_{v1}(t)e^{iks} = \tilde{Z}_{v1}e^{at}e^{iks} \\
 Y_{v2}(s; t) &= \hat{Y}_{v2}(t)e^{iks} = \tilde{Y}_{v2}e^{at}e^{iks} \\
 Z_{v2}(s; t) &= \hat{Z}_{v2}(t)e^{iks} = \tilde{Z}_{v2}e^{at}e^{iks}
 \end{aligned} \tag{2.21}$$

With this assumed time-dependence, the following eigenvalue problem can be formulated for the dimensionless exponential growth rate $\alpha = a(2\pi b^2/\Gamma)$:

$$\begin{pmatrix} \alpha & -A & 0 & \Psi \\ -B & \alpha & \chi & 0 \\ 0 & -\Psi & \alpha & A \\ -\chi & 0 & B & \alpha \end{pmatrix} \begin{pmatrix} \tilde{Y}_{v1} \\ \tilde{Z}_{v1} \\ \tilde{Y}_{v2} \\ \tilde{Z}_{v2} \end{pmatrix} = 0 \tag{2.22}$$

with

$$A = 1 + \beta^2 \left\{ \omega(k\Delta) + \ln \left(\frac{2\Delta}{R} \right) \right\} \tag{2.23}$$

$$B = 1 - \beta^2 \left\{ \omega(k\Delta) + \ln \left(\frac{2\Delta}{R} \right) \right\} \tag{2.24}$$

$$\Psi = i_1(\beta) + i_2(\beta) = \beta^2 K_0(\beta) + \beta K_1(\beta) \tag{2.25}$$

$$\chi = -(i_1(\beta) + i_2(\beta) - 3i_3(\beta)) = i_2(\beta) = \beta K_1(\beta) \tag{2.26}$$

In expressions (2.23) and (2.24), the term involving $\ln \left(\frac{2\Delta}{R} \right)$ represents the effect of including the extra self-induction term derived in equation (2.16). Discarding this extra term gives the same linearized eigenvalue problem as obtained by Crow (1970). Functions $\chi(\beta)$ and $\Psi(\beta)$ represent the effect of mutual velocity induction. These functions are shown in figure 2.4. The eigenvalue problem (2.22) can be solved directly, but it is convenient to split it in a symmetric and an anti-symmetric part with the following definitions:

$$\begin{aligned}
 \tilde{Y}_{vS} &= \frac{1}{2} (\tilde{Y}_{v1} - \tilde{Y}_{v2}) \\
 \tilde{Z}_{vS} &= \frac{1}{2} (\tilde{Z}_{v1} + \tilde{Z}_{v2})
 \end{aligned} \tag{2.27}$$

$$\begin{aligned}
 \tilde{Y}_{vA} &= \frac{1}{2} (\tilde{Y}_{v1} + \tilde{Y}_{v2}) \\
 \tilde{Z}_{vA} &= \frac{1}{2} (\tilde{Z}_{v1} - \tilde{Z}_{v2})
 \end{aligned} \tag{2.28}$$

This gives two separate independent eigenvalue problems with eigenvalues

$$\begin{aligned}
 \alpha_S^2 &= (A - \Psi)(B + \chi) \\
 \alpha_A^2 &= (A + \Psi)(B - \chi)
 \end{aligned} \tag{2.29}$$

Using equations (2.29), the eigenvectors can be evaluated as

$$\begin{aligned}
 \tilde{Z}_{vS} &= \frac{\alpha_S}{A - \Psi} \tilde{Y}_{vS} = \pm \left(\frac{B + \chi}{A - \Psi} \right)^{1/2} \tilde{Y}_{vS} \\
 \tilde{Z}_{vA} &= \frac{\alpha_A}{A + \Psi} \tilde{Y}_{vA} = \pm \left(\frac{B - \chi}{A + \Psi} \right)^{1/2} \tilde{Y}_{vA}
 \end{aligned} \tag{2.30}$$

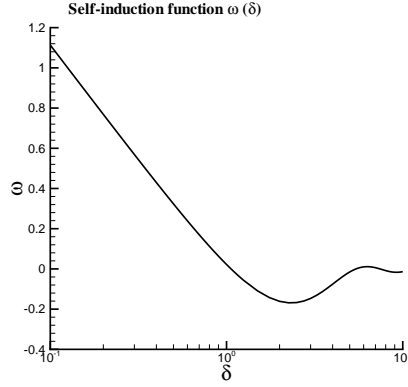


FIGURE 2.3: Self-induction function $\omega(\delta)$ from stability analysis of Crow (1970), where $\delta = k\Delta$.

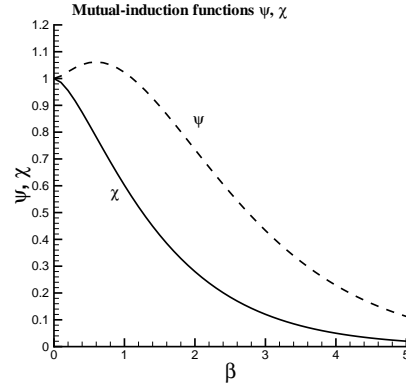


FIGURE 2.4: Mutual-induction functions $\chi(\beta)$ and $\Psi(\beta)$ from stability analysis of Crow (1970), where $\beta = k \cdot b$.

From equation (2.30) the inclination angle of the unstable modes with respect to the horizontal plane can be computed. For the inclination angle θ_S for the symmetric mode:

$$\tan(\theta_S) = \frac{\tilde{Z}_{vS}}{\tilde{Y}_{vS}} = \left(\frac{B + \chi}{A - \Psi} \right)^{1/2} \quad (2.31)$$

and similarly for the inclination angle θ_A for the anti-symmetric mode:

$$\tan(\theta_A) = \frac{\tilde{Z}_{vS}}{\tilde{Y}_{vS}} = \left(\frac{B - \chi}{A + \Psi} \right)^{1/2} \quad (2.32)$$

The stability diagram of the symmetric modes is shown in figure 2.5, showing regions of (in)stability in the $(\beta, \delta/\beta)$ -plane, which is equivalent to the $(k b, \Delta/b)$ -plane. Similarly, the stability diagram of anti-symmetric modes is shown in figure 2.6. The symmetric modes are stable in case α_S is purely imaginary and unstable otherwise. Similarly, a purely imaginary α_A denotes a stable anti-symmetric mode.

Figure 2.5 clearly shows the presence of symmetric long-wavelength instability modes in the lower left corner of the $(\beta, \delta/\beta)$ -plane. At these long wavelengths, figure 2.6 does not show anti-symmetric instability modes.

At much shorter wavelengths, i.e. larger β , both symmetric and anti-symmetric short-wavelength instability modes are predicted. Comparison of the growth rates of these modes in figures 2.5 and 2.6 shows that, in general, anti-symmetric short-wavelength modes are more unstable than symmetric short-wavelength modes.

For fixed values of $\delta/\beta = \Delta/b$, i.e. vertical cuts through the figures 2.5 and 2.6, the amplification rate and the corresponding inclination angle of the symmetric modes are shown in figures 2.7, 2.9 and 2.11, for $\delta/\beta = 0.1$ to $\delta/\beta = 0.3$. The figures 2.7, 2.9 and 2.11 indicate that the maximum growth rate of the long-wavelength instability occurs within a narrow band of β , especially for low values of δ/β . Another notable feature is the strong dependence of θ on β , i.e. instability modes at wavelengths slightly different from the wavelength of the most amplified mode have a markedly different inclination angle.

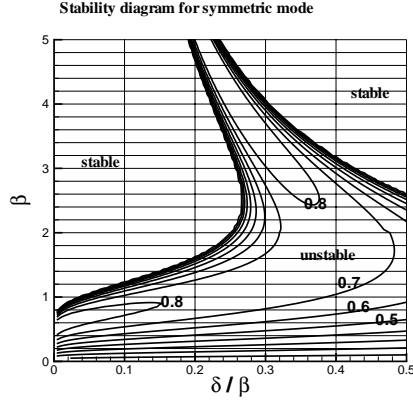


FIGURE 2.5: Stability diagram for symmetric modes: iso-contours of α_S

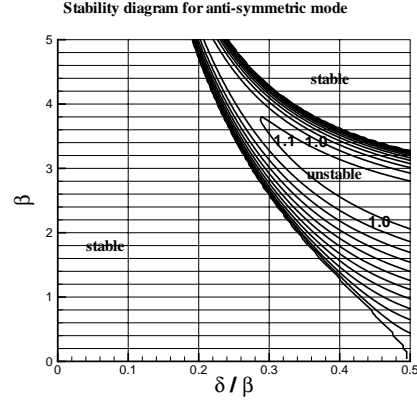


FIGURE 2.6: Stability diagram for anti-symmetric modes: iso-contours of α_A

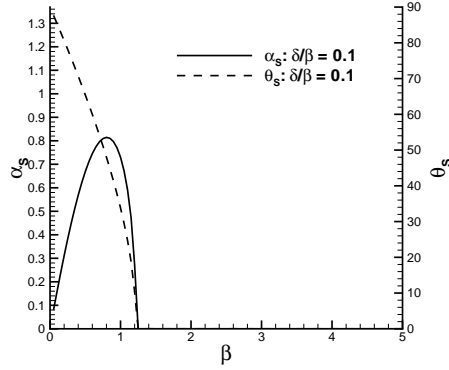


FIGURE 2.7: Exponential growth rate α and inclination angle versus $\beta = k \cdot b$: symmetric mode, $\delta/\beta = 0.1$ ($r_c/b = 0.312$)

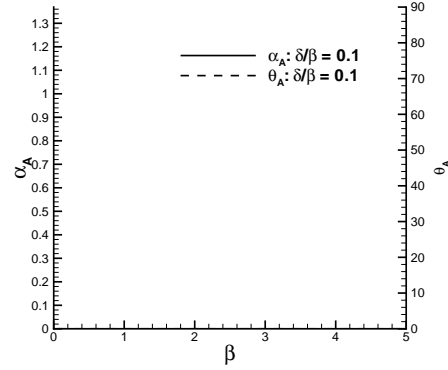


FIGURE 2.8: Exponential growth rate α and inclination angle versus $\beta = k \cdot b$: anti-symmetric mode, $\delta/\beta = 0.1$ ($r_c/b = 0.312$)

Similar results for the anti-symmetric modes are shown in figures 2.8, 2.10 and 2.12. Note that in figures 2.7 to 2.12, the inclination angle is set to zero for stable modes.

The maximum amplification rate α , the wavelength $\lambda/b = 2\pi/\beta$ of the most amplified instability mode and the inclination angle θ of this mode with respect to the horizontal plane are shown as a function of the ratio δ/β in figure 2.13 and 2.14 for symmetric modes. These figures show results for long-wavelength modes only, since symmetric short-wavelength modes are not particularly relevant. Figure 2.13 shows that for the symmetric long-wavelength instability modes, the exponential growth rate and the inclination angle have a weak dependence on the ratio δ/β . The latter is even nearly constant at approximately 48° , which is remarkable considering the strong dependence on δ/β of the inclination angle θ in the figures 2.7, 2.9

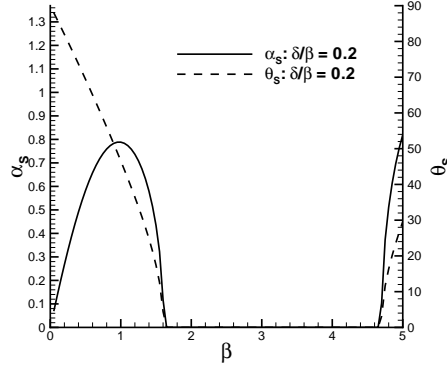


FIGURE 2.9: Exponential growth rate α and inclination angle versus $\beta = k \cdot b$: symmetric mode, $\delta/\beta = 0.2$ ($r_c/b = 0.623$)

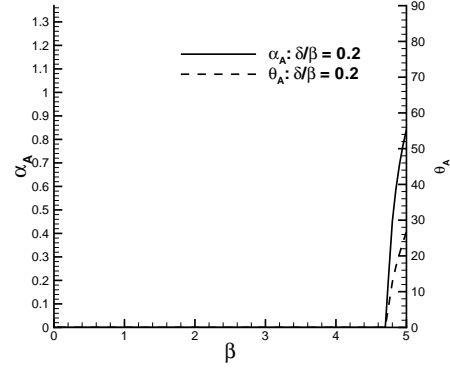


FIGURE 2.10: Exponential growth rate α and inclination angle versus $\beta = k \cdot b$: anti-symmetric mode, $\delta/\beta = 0.2$ ($r_c/b = 0.623$)

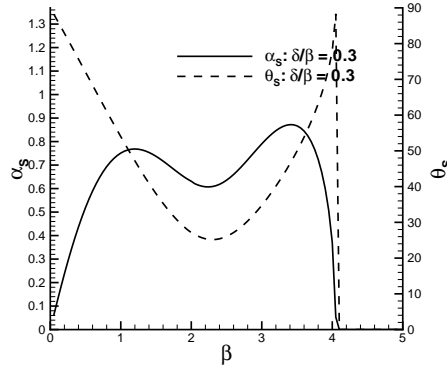


FIGURE 2.11: Exponential growth rate α and inclination angle versus $\beta = k \cdot b$: symmetric mode, $\delta/\beta = 0.3$ ($r_c/b = 0.935$)

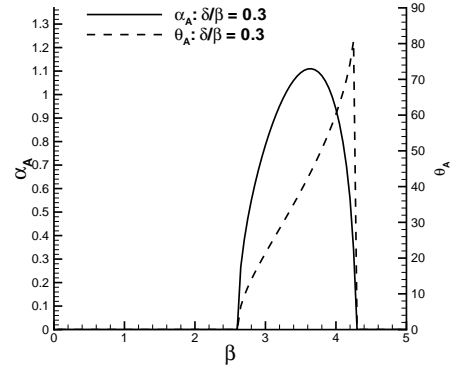


FIGURE 2.12: Exponential growth rate α and inclination angle versus $\beta = k \cdot b$: anti-symmetric mode, $\delta/\beta = 0.3$ ($r_c/b = 0.935$)

and 2.11. The dependence of the wavelength of the most amplified instability mode on this ratio can be seen to be significantly more pronounced.

Figures 2.15 and 2.16 show similar results for the anti-symmetric short-wavelength modes. It can be seen that the growth rate for this short-wavelength mode is somewhat larger than that of the symmetric long-wavelength modes. Again, the dependence of the growth rate and inclination angle on the ratio δ/β is weak, with the inclination angle nearly constant at around 48° .

Summarizing, the figures of this section show that:

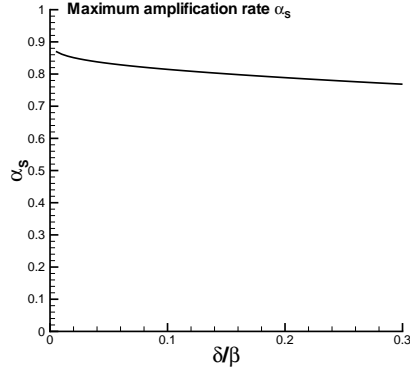


FIGURE 2.13: Maximum amplification rate α_S for symmetric modes versus δ/β .

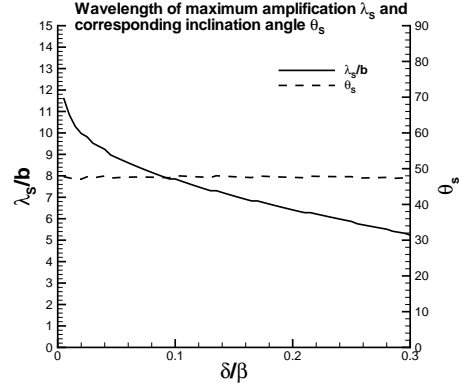


FIGURE 2.14: Wavelength of maximum amplification λ_S for symmetric modes and corresponding inclination angle θ_S .

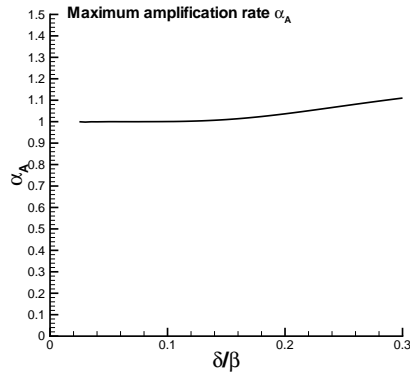


FIGURE 2.15: Maximum amplification rate α_A for anti-symmetric modes versus δ/β .

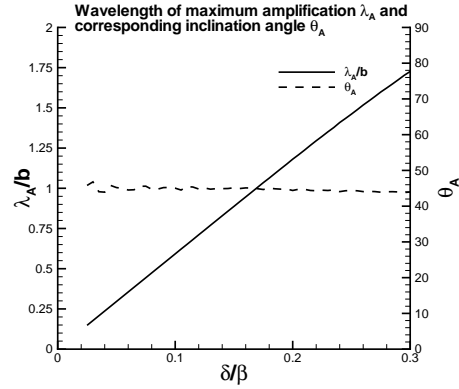


FIGURE 2.16: Wavelength of maximum amplification λ_A for anti-symmetric modes and corresponding inclination angle θ_A .

- for $\delta/\beta < 0.4$, three instability modes exist, each having a local maximum in growth rate along the β -axis. A symmetric instability mode occurs at a fairly large wavelength. Furthermore, instability modes of much shorter wavelengths are present for both symmetric and anti-symmetric configurations;
- for small δ/β , i.e. $\delta/\beta < 0.2$, the short-wavelength instability modes occur at $\beta > 5$ and are therefore not shown in the figures;
- the short-wavelength instabilities have a slightly larger growth rate than the long-wavelength instability;

- for decreasing spacing of the vortices, or increasing δ/β , the difference in wavelength of the long wavelength and short wavelength instabilities gets smaller;
- for $\delta/\beta < 0.3$, the inclination angle θ_S of the symmetric long-wavelength instability modes is around 48° . This angle has a very weak dependence on the ratio δ/β .

For a typical jet transport, with $\delta/\beta \approx 0.063$ according to Crow (1970), the following conclusions can be drawn from the stability analysis of Crow (1970):

- the most unstable long-wavelength mode occurs at $\beta = 0.73$. This corresponds to a wavelength of $8.6 b$. At this condition, the perturbations of the vortices are inclined at an angle of 48° with respect to the horizontal plane;
- the characteristic time scale $a^{-1} = 21 s$. Therefore, the initial growth-rate is such that the amplitude is doubled every $14.5 s$;
- the most unstable short-wavelength mode present at $\beta = 17$, which corresponds to a wavelength of around $0.37 b$.

2.2 Stability analysis for a pair of Rosenhead vortex filaments

In this section an equivalent stability analysis is presented for a counter-rotating vortex pair as in section 2.1. In section 2.1, the singularity of the velocity-induction integrals for points on either of the vortex filaments was eliminated by excluding the direct vicinity of the point considered from the integral. In Crow (1970), this approach was formulated in a way slightly different to that of section 2.1, but the resulting linearized eigenvalue problem is identical in case the singularity contribution is dropped from the integrals of section 2.1.

In this section, another approach is pursued. Here, the Biot-Savart integral, as given by equation (2.3) in section 2.1, is made uniformly valid throughout the domain by the following modification:

$$\underline{u}_v(\underline{x}_0) = -\frac{\Gamma}{4\pi} \int_C \frac{(\underline{x}_0 - \underline{x}_v(s))}{[|\underline{x}_0 - \underline{x}_v(s)|^2 + \hat{\mu}^2]^{3/2}} \times \frac{d\underline{x}_v}{ds} ds \quad (2.33)$$

with $\hat{\mu}$ a parameter, with dimension length, used to desingularize the integrand. The method used in equation (2.33) is named after Rosenhead. This expression is valid everywhere, also for $\underline{x}_0 \rightarrow \underline{x}_v(s)$.

The location of the filament is taken identical to that of section 2.1, i.e. equation (2.4):

$$\underline{x}_v(s) = s\underline{e}_x + \underline{B} + \underline{X}_v(s) \quad (2.34)$$

with \underline{B} the cross-flow plane location of the unperturbed vortex and \underline{X}_v the cross-flow plane perturbation with respect to $s\underline{e}_x + \underline{B}$. Again, capital symbols denote cross-flow plane quantities.

The velocity induced in a point not too close to a filament is derived in more detail here than in section 2.1, and starts with assuming small perturbations of the filament: $|\underline{X}_v(s)| \ll |\underline{B}|$. For the time being, the time-dependence of \underline{X}_v is not considered.

Using

$$\underline{x}_0 - \underline{x}_v(s) = (x_0 - s)\underline{e}_x + \underline{X}_0 - \underline{B} - \underline{X}_v(s) \quad (2.35)$$

and assuming $|\underline{X}_v(s)| \ll |\hat{\mu}|$ yields

$$\begin{aligned} |\underline{x}_0 - \underline{x}_v(s)|^2 + \hat{\mu}^2 &= |(x_0 - s)\underline{e}_x + \underline{X}_0 - \underline{B}|^2 + \hat{\mu}^2 - 2(\underline{X}_0 - \underline{B}) \cdot \underline{X}_v + O(\delta^2) \\ &= (|(x_0 - s)\underline{e}_x + \underline{X}_0 - \underline{B}|^2 + \hat{\mu}^2) \left\{ 1 - \frac{2(\underline{X}_0 - \underline{B}) \cdot \underline{X}_v}{(|(x_0 - s)\underline{e}_x + \underline{X}_0 - \underline{B}|^2 + \hat{\mu}^2)} + O(\delta^2) \right\} \end{aligned} \quad (2.36)$$

where δ is the order of the perturbation $\underline{X}_v(s)$.

With $\underline{r}_0 = (x_0 - s)\underline{e}_x + \underline{X}_0 - \underline{B}$ the induced velocity in a point \underline{x}_0 not too close to the filament can be written as:

$$\begin{aligned} \underline{u}_v(x_0\underline{e}_x + \underline{X}_0) &= -\frac{\Gamma}{4\pi} \int_{-\infty}^{\infty} \frac{(\underline{X}_0 - \underline{B}) \times \underline{e}_x}{(|\underline{r}_0|^2 + \hat{\mu}^2)^{3/2}} ds \\ &\quad - \frac{\Gamma}{4\pi} \left[\int_{-\infty}^{\infty} \frac{(x_0 - s)\underline{e}_x \times \underline{X}'_v(s)}{(|\underline{r}_0|^2 + \hat{\mu}^2)^{3/2}} ds - \int_{-\infty}^{\infty} \frac{\underline{X}_v \times \underline{e}_x}{(|\underline{r}_0|^2 + \hat{\mu}^2)^{3/2}} ds + \right. \\ &\quad \left. \int_{-\infty}^{\infty} \frac{3(\underline{X}_0 - \underline{B}) \cdot \underline{X}_v (\underline{X}_0 - \underline{B}) \times \underline{e}_x}{(|\underline{r}_0|^2 + \hat{\mu}^2)^{5/2}} ds \right] \\ &\quad + \frac{\Gamma}{4\pi} \int_{-\infty}^{\infty} \frac{(\underline{X}_0 - \underline{B}) \times \underline{X}'_v}{(|\underline{r}_0|^2 + \hat{\mu}^2)^{3/2}} ds + O(\delta^2) \end{aligned} \quad (2.37)$$

Treating term by term gives:

$$\begin{aligned} \underline{U}_v^{(0)}(x_0\underline{e}_x + \underline{X}_0) &= -\frac{\Gamma}{4\pi} \int_{-\infty}^{\infty} \frac{(\underline{X}_0 - \underline{B}) \times \underline{e}_x}{(|\underline{r}_0|^2 + \hat{\mu}^2)^{3/2}} ds \\ &= -\frac{\Gamma}{4\pi} (\underline{X}_0 - \underline{B}) \times \underline{e}_x \int_{-\infty}^{\infty} \frac{ds}{((x_0 - s)^2 + |\underline{X}_0 - \underline{B}|^2 + \hat{\mu}^2)^{3/2}} \\ &= -\frac{\Gamma}{2\pi} \frac{(\underline{X}_0 - \underline{B}) \times \underline{e}_x}{(|\underline{X}_0 - \underline{B}|^2 + \hat{\mu}^2)} \end{aligned} \quad (2.38)$$

which is the $O(1)$ cross-flow term, finite for any \underline{X}_0 , located in the cross-flow plane. As in section 2.1, assume a harmonic form for the perturbation $\underline{X}_v(s)$, i.e.

$$\begin{aligned} \underline{X}_v(s) &= \hat{\underline{X}}_v(t) e^{iks} \\ \underline{X}'_v(s) &= ik \hat{\underline{X}}_v(t) e^{iks} \end{aligned} \quad (2.39)$$

For the three $O(\delta)$ cross-flow plane contributions it follows:

$$\begin{aligned} \underline{U}_v^{(1,1)} &= -\frac{\Gamma}{4\pi} \int_{-\infty}^{\infty} \frac{(x_0 - s)\underline{e}_x \times \underline{X}'_v}{(|\underline{r}_0|^2 + \hat{\mu}^2)^{3/2}} ds \\ &= -\frac{\Gamma}{4\pi} (\underline{e}_x \times \hat{\underline{X}}'_v) ike^{ikx_0} \int_{-\infty}^{\infty} \frac{(x_0 - s)e^{-ik(x_0 - s)}}{((x_0 - s)^2 + |\underline{X}_0 - \underline{B}|^2 + \hat{\mu}^2)^{3/2}} ds \\ &= -\frac{\Gamma}{2\pi} \frac{(\underline{e}_x \times \hat{\underline{X}}'_v) e^{ikx_0}}{(|\underline{X}_0 - \underline{B}|^2 + \hat{\mu}^2)} \hat{i}_1(\beta') \end{aligned} \quad (2.40)$$

with

$$\hat{i}_1(\beta') = \int_0^\infty \frac{\beta' \xi \sin(\beta' \xi)}{(\xi^2 + 1)^{3/2}} d\xi \quad , \quad \beta'^2 = k^2 (|\underline{X}_0 - \underline{B}|^2 + \hat{\mu}^2) \quad (2.41)$$

and

$$\begin{aligned}
U_v^{(1,2)} &= \frac{\Gamma}{4\pi} \int_{-\infty}^{\infty} \frac{\underline{X}_v \times \underline{e}_x}{(|\underline{r}_0|^2 + \hat{\mu}^2)^{3/2}} ds \\
&= -\frac{\Gamma}{4\pi} (\underline{e}_x \times \hat{\underline{X}}_v) e^{ikx_0} \int_{-\infty}^{\infty} \frac{e^{-ik(x_0-s)} ds}{((x_0-s)^2 + |\underline{X}_0 - \underline{B}|^2 + \hat{\mu}^2)^{3/2}} \\
&= -\frac{\Gamma}{2\pi} \frac{\underline{e}_x \times \hat{\underline{X}}_v e^{ikx_0}}{(|\underline{X}_0 - \underline{B}|^2 + \hat{\mu}^2)} \hat{i}_2(\beta')
\end{aligned} \tag{2.42}$$

with

$$\hat{i}_2(\beta') = \int_0^\infty \frac{\cos(\beta' \xi)}{(\xi^2 + 1)^{3/2}} d\xi \tag{2.43}$$

and

$$\begin{aligned}
U_v^{(1,3)} &= -\frac{\Gamma}{4\pi} \int_{-\infty}^{\infty} \frac{3(\underline{X}_0 - \underline{B}) \cdot \underline{X}_v}{(|\underline{r}_0|^2 + \hat{\mu}^2)^{3/2}} (\underline{X}_0 - \underline{B}) \times \underline{e}_x ds \\
&= -\frac{\Gamma}{4\pi} e^{ikx_0} 3(\underline{X}_0 - \underline{B}) \cdot \hat{\underline{X}}_v (\underline{X}_0 - \underline{B}) \times \underline{e}_x \int_{-\infty}^{\infty} \frac{e^{-ik(x_0-s)} ds}{((x_0-s)^2 + |\underline{X}_0 - \underline{B}|^2 + \hat{\mu}^2)^{5/2}} \\
&= -\frac{\Gamma}{2\pi} \frac{3(\underline{X}_0 - \underline{B}) \cdot \hat{\underline{X}}_v (\underline{X}_0 - \underline{B}) \times \underline{e}_x}{(|\underline{X}_0 - \underline{B}|^2 + \hat{\mu}^2)^2} \hat{i}_3(\beta')
\end{aligned} \tag{2.44}$$

with

$$\hat{i}_3(\beta') = \int_0^\infty \frac{\cos(\beta' \xi)}{(\xi^2 + 1)^{5/2}} d\xi \tag{2.45}$$

The x -component, $O(\delta)$ term, is

$$\begin{aligned}
u^{(1)} \underline{e}_x &= \frac{\Gamma}{4\pi} \int_{-\infty}^{\infty} \frac{(\underline{X}_0 - \underline{B}) \times \underline{X}'_v}{(|\underline{r}_0|^2 + \hat{\mu}^2)^{3/2}} ds \\
&= \frac{\Gamma}{2\pi} \frac{(\underline{X}_0 - \underline{B}) \times \hat{\underline{X}}_v e^{ikx_0}}{(|\underline{X}_0 - \underline{B}|^2 + \hat{\mu}^2)^{3/2}} \beta' \hat{i}_2(\beta')
\end{aligned} \tag{2.46}$$

Therefore, summarizing, the following relation results which is the "Rosenhead equivalent" of equation (2.6) of section 2.1:

$$\begin{aligned}
u_v(x_0 \underline{e}_x + \underline{X}_0) &= -\frac{\Gamma}{2\pi} \frac{(\underline{X}_0 - \underline{B}) \times \underline{e}_x}{(|\underline{X}_0 - \underline{B}|^2 + \hat{\mu}^2)} \\
&\quad - \frac{\Gamma}{2\pi} \left[\frac{\underline{e}_x \times \hat{\underline{X}}_v}{(|\underline{X}_0 - \underline{B}|^2 + \hat{\mu}^2)} (\hat{i}_1 + \hat{i}_2) + \frac{3(\underline{X}_0 - \underline{B}) \times \underline{e}_x (\underline{X}_0 - \underline{B}) \cdot \hat{\underline{X}}_v}{(|\underline{X}_0 - \underline{B}|^2 + \hat{\mu}^2)^2} \hat{i}_3 \right] e^{ikx_0} \\
&\quad + \frac{\Gamma}{2\pi} \frac{(\underline{X}_0 - \underline{B}) \times \hat{\underline{X}}_v}{(|\underline{X}_0 - \underline{B}|^2 + \hat{\mu}^2)^{3/2}} \beta' \hat{i}_2 e^{ikx_0} + O(\delta^2)
\end{aligned} \tag{2.47}$$

This is the basic expression that is used in the remainder of the present stability analysis. It is also valid for the case $\underline{x}_0 = \underline{x}_v$, then

$$\beta'^2 = k^2 (\hat{\mu}^2 + |\underline{X}_v(s_0)|^2) = k^2 \hat{\mu}^2 (1 + O(\delta^2)) \tag{2.48}$$

Substitution of this relation in equation (2.47) gives:

$$\underline{u}_v(s_0 \underline{e}_x + \underline{X}_v(s_0)) = -\frac{\Gamma k^2}{2\pi} (\underline{e}_x \times \hat{\underline{X}}_v) e^{iks_0} \hat{\omega}(k\hat{\mu}) + O(\delta^2) \quad (2.49)$$

where the self-induction function $\hat{\omega}$ is defined as

$$\hat{\omega}(k\hat{\mu}) = \frac{\hat{i}_1(k\hat{\mu}) + \hat{i}_2(k\hat{\mu}) - 1}{k^2 \hat{\mu}^2} \quad (2.50)$$

As in section 2.1, the analysis proceeds with deriving the system of governing equations for the motion of a vortex pair, consisting of two perturbed vortex filaments of equal, but opposite-signed strength Γ , with spacing b in the unperturbed situation. A vortex pair is considered with the following properties, see equation (2.17):

$$\begin{aligned} \text{Filament 1: } \underline{x}_v(s) &= s\underline{e}_x + \underline{B}_1 + \hat{\underline{X}}_{v1}(t)e^{iks_0}; \quad \Gamma_1 = +\Gamma; \quad \underline{B}_1 = +\frac{b}{2}\underline{e}_y + h(t)\underline{e}_z \\ \text{Filament 2: } \underline{x}_v(s) &= s\underline{e}_x + \underline{B}_2 + \hat{\underline{X}}_{v2}(t)e^{iks_0}; \quad \Gamma_2 = -\Gamma; \quad \underline{B}_2 = -\frac{b}{2}\underline{e}_y + h(t)\underline{e}_z \end{aligned} \quad (2.51)$$

where $h(t)$ denotes the time-dependent z -coordinate, representing the downward motion of the vortex pair.

From equation (2.49), the velocity induced by vortex filament 1 at vortex filament 1, i.e. the self-induction, can be evaluated as:

$$\underline{u}_v^{(1 \rightarrow 1)} = -\frac{\Gamma_1 k^2}{2\pi} (-\underline{e}_y \hat{Z}_{v1} + \underline{e}_z \hat{Y}_{v1}) e^{iks_0} \hat{\omega}(k\hat{\mu}) + O(\delta^2) \quad (2.52)$$

The velocity induced by vortex filament 2 at vortex filament 1 can be evaluated using the following equation:

$$\begin{aligned} \underline{u}_v^{(2 \rightarrow 1)}(s_0 \underline{e}_x + \underline{X}_{v1}(s_0)) &= -\frac{\Gamma_2}{2\pi} \frac{(\underline{B}_1 - \underline{B}_2) \times \underline{e}_x}{(|\underline{B}_1 - \underline{B}_2|^2 + \hat{\mu}^2)} \\ &- \frac{\Gamma_2}{2\pi} \left[\frac{\underline{X}_{v1} \times \underline{e}_x}{(|\underline{B}_1 - \underline{B}_2|^2 + \hat{\mu}^2)} - \frac{2(\underline{B}_1 - \underline{B}_2) \cdot \underline{X}_{v1} (\underline{B}_1 - \underline{B}_2) \times \underline{e}_x}{(|\underline{B}_1 - \underline{B}_2|^2 + \hat{\mu}^2)^4} \right] e^{iks_0} \\ &- \frac{\Gamma_2}{2\pi} \left[\frac{\underline{e}_x \times \underline{X}_{v2} (\hat{i}_1 + \hat{i}_2)}{(|\underline{B}_1 - \underline{B}_2|^2 + \hat{\mu}^2)} + \frac{3(\underline{B}_1 - \underline{B}_2) \times \underline{e}_x (\underline{B}_1 - \underline{B}_2) \cdot \underline{X}_{v2} \hat{i}_3}{(|\underline{B}_1 - \underline{B}_2|^2 + \hat{\mu}^2)^2} \right] e^{iks_0} \\ &+ \frac{\Gamma_2}{2\pi} \frac{(\underline{B}_1 - \underline{B}_2) \times \underline{X}_{v2}}{(|\underline{B}_1 - \underline{B}_2|^2 + \hat{\mu}^2)^{3/2}} \beta' \hat{i}_2 e^{iks_0} + O(\delta^2) \end{aligned} \quad (2.53)$$

with the functions \hat{i}_1 , \hat{i}_2 and \hat{i}_3 defined by equations (2.41), (2.43) and (2.45). The first term is the $O(1)$ down wash induced by filament 2 at filament 1. The next two terms form the $O(\delta)$ cross-flow plane strain field induced by filament 2 at filament 1. The next two terms are the $O(\delta)$ cross-flow plane mutual induction terms. The last terms in expression (2.53) is the $O(\delta)$ induced axial velocity component.

In equation (2.53), parameter β' is defined as: $\beta' = k^2(|\underline{B}_1 - \underline{B}_2|^2 + \hat{\mu}^2) + h.o.t..$

Using the characteristics of the vortex pair (2.51), equation (2.53) can be written as:

$$\begin{aligned} \underline{u}_v^{(2 \rightarrow 1)}(s_0 \underline{e}_x + \underline{X}_{v1}(s_0)) &= +\frac{\Gamma_2}{2\pi b} \frac{\underline{e}_z}{1 + (\hat{\mu}/b)^2} \\ &- \frac{\Gamma_2}{2\pi b^2} \left[\frac{\underline{e}_y \hat{Z}_{v1}}{1 + (\hat{\mu}/b)^2} + \frac{\underline{e}_z \hat{Y}_{v1}}{[1 + (\hat{\mu}/b)^2]^2} (1 - (\hat{\mu}/b)^2) \right] e^{iks_0} \end{aligned}$$

$$\begin{aligned}
& -\frac{\Gamma_2}{2\pi b^2} \left[-\underline{e}_y \hat{Z}_{v2} \frac{\hat{i}_1 + \hat{i}_2}{1 + (\hat{\mu}/b)^2} + \underline{e}_z \hat{Y}_{v2} \left\{ \frac{\hat{i}_1 + \hat{i}_2}{1 + (\hat{\mu}/b)^2} - \frac{3\hat{i}_3}{[1 + (\hat{\mu}/b)^2]^2} \right\} \right] e^{iks_0} \\
& + \frac{\Gamma_2}{2\pi b^2} \left[\frac{\hat{Z}_{v2} \underline{e}_x}{[1 + (\hat{\mu}/b)^2]^{3/2}} \beta' \hat{i}_2 \right] e^{iks_0} + O(\delta^2)
\end{aligned} \tag{2.54}$$

In an equivalent way, the velocity induced by vortex filament 1 at vortex filament 2 can be evaluated as:

$$\begin{aligned}
& u_v^{(1 \rightarrow 2)}(s_0 \underline{e}_x + \underline{X}_{v2}(s_0)) = -\frac{\Gamma_1}{2\pi b} \frac{\underline{e}_z}{1 + (\hat{\mu}/b)^2} \\
& -\frac{\Gamma_1}{2\pi b^2} \left[\frac{\underline{e}_y \hat{Z}_{v2}}{1 + (\hat{\mu}/b)^2} + \frac{\underline{e}_z \hat{Y}_{v2}}{[1 + (\hat{\mu}/b)^2]^2} (1 - (\hat{\mu}/b)^2) \right] e^{iks_0} \\
& -\frac{\Gamma_1}{2\pi b^2} \left[-\underline{e}_y \hat{Z}_{v1} \frac{\hat{i}_1 + \hat{i}_2}{1 + (\hat{\mu}/b)^2} + \underline{e}_z \hat{Y}_{v1} \left\{ \frac{\hat{i}_1 + \hat{i}_2}{1 + (\hat{\mu}/b)^2} - \frac{3\hat{i}_3}{[1 + (\hat{\mu}/b)^2]^2} \right\} \right] e^{iks_0} \\
& -\frac{\Gamma_1}{2\pi b^2} \left[\frac{\hat{Z}_{v1} \underline{e}_x}{[1 + (\hat{\mu}/b)^2]^{3/2}} \beta' \hat{i}_2 \right] e^{iks_0} + O(\delta^2)
\end{aligned} \tag{2.55}$$

And finally for the velocity induced by vortex filament 2 at vortex filament 2:

$$u_v^{(2 \rightarrow 2)} = -\frac{\Gamma_2 k^2}{2\pi} (-\underline{e}_y \hat{Z}_{v2} + \underline{e}_z \hat{Y}_{v2}) e^{iks_0} \hat{\omega}(k\hat{\mu}) + O(\delta^2) \tag{2.56}$$

With the various contributions to the induced velocities, the stability of the vortex pair can be studied, starting from the kinematic condition given by equation (2.19) of section 2.1. Assuming a time-dependence of the perturbations as e^{at} , the following eigenvalue problem for a can be formulated:

$$\begin{aligned}
a\tilde{Y}_{v1} &= -\frac{\Gamma_1}{2\pi b^2} \left\{ -\tilde{Z}_{v1} k^2 b^2 \hat{\omega}(k\hat{\mu}) \right\} - \frac{\Gamma_2}{2\pi b^2} \left\{ \frac{\tilde{Z}_{v1}}{1 + (\hat{\mu}/b)^2} - \tilde{Z}_{v2} \frac{\hat{i}_1 + \hat{i}_2}{1 + (\hat{\mu}/b)^2} \right\} \\
a\tilde{Z}_{v1} &= -\frac{\Gamma_1}{2\pi b^2} \left\{ \tilde{Y}_{v1} k^2 b^2 \hat{\omega}(k\hat{\mu}) \right\} \\
& -\frac{\Gamma_2}{2\pi b^2} \left\{ \frac{\tilde{Y}_{v1} (1 - (\hat{\mu}/b)^2)}{[1 + (\hat{\mu}/b)^2]^2} + \tilde{Y}_{v2} \left[\frac{\hat{i}_1 + \hat{i}_2}{1 + (\hat{\mu}/b)^2} - \frac{3\hat{i}_3}{[1 + (\hat{\mu}/b)^2]^2} \right] \right\} \\
a\tilde{Y}_{v2} &= -\frac{\Gamma_2}{2\pi b^2} \left\{ -\tilde{Z}_{v2} k^2 b^2 \hat{\omega}(k\hat{\mu}) \right\} - \frac{\Gamma_1}{2\pi b^2} \left\{ \frac{\tilde{Z}_{v2}}{1 + (\hat{\mu}/b)^2} - \tilde{Z}_{v1} \frac{\hat{i}_1 + \hat{i}_2}{1 + (\hat{\mu}/b)^2} \right\} \\
a\tilde{Z}_{v2} &= -\frac{\Gamma_2}{2\pi b^2} \left\{ \tilde{Y}_{v2} k^2 b^2 \hat{\omega}(k\hat{\mu}) \right\} \\
& -\frac{\Gamma_1}{2\pi b^2} \left\{ \frac{\tilde{Y}_{v2} (1 - (\hat{\mu}/b)^2)}{[1 + (\hat{\mu}/b)^2]^2} + \tilde{Y}_{v1} \left[\frac{\hat{i}_1 + \hat{i}_2}{1 + (\hat{\mu}/b)^2} - \frac{3\hat{i}_3}{[1 + (\hat{\mu}/b)^2]^2} \right] \right\}
\end{aligned} \tag{2.57}$$

With Γ_1 and Γ_2 defined in equation (2.51) and defining $\alpha = a(2\pi b^2/\Gamma)$, eigenvalue problem (2.57) can be written as a matrix eigenvalue problem as:

$$\begin{pmatrix} \alpha & -A & 0 & \Psi \\ -B & \alpha & \chi & 0 \\ 0 & -\Psi & \alpha & A \\ -\chi & 0 & B & \alpha \end{pmatrix} \begin{pmatrix} \tilde{Y}_{v1} \\ \tilde{Z}_{v1} \\ \tilde{Y}_{v2} \\ \tilde{Z}_{v2} \end{pmatrix} = 0 \tag{2.58}$$

with

$$A = \frac{1}{1 + \hat{\mu}^2/b^2} + k^2 b^2 \hat{\omega}(k\hat{\mu}) \quad (2.59)$$

$$B = \frac{1 - \hat{\mu}^2/b^2}{(1 + \hat{\mu}^2/b^2)^2} - k^2 b^2 \hat{\omega}(k\hat{\mu}) \quad (2.60)$$

$$\Psi = \frac{\hat{i}_1 + \hat{i}_2}{1 + \hat{\mu}^2/b^2} \quad (2.61)$$

$$\chi = - \left(\frac{\hat{i}_1 + \hat{i}_2}{1 + \hat{\mu}^2/b^2} - \frac{3\hat{i}_3}{(1 + \hat{\mu}^2/b^2)^2} \right) \quad (2.62)$$

and the functions $\hat{i}_1(\beta')$, $\hat{i}_2(\beta')$ and $\hat{i}_3(\beta')$ given by equations (2.41), (2.43) and (2.45). The eigenvalue problem (2.58) has exactly the same form as that solved for Crow's problem, which solution was given by equations 2.27 to 2.32.

Now, the stability diagram of the symmetric modes for the Rosenhead vortices is shown

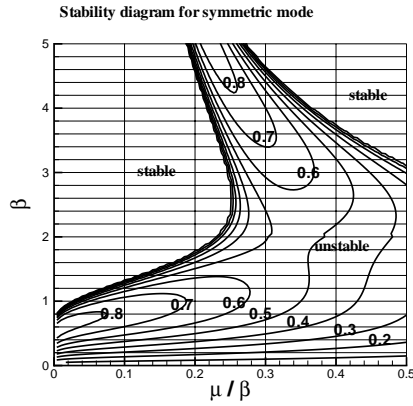


FIGURE 2.17: Stability diagram for symmetric modes: iso-contours of α_S

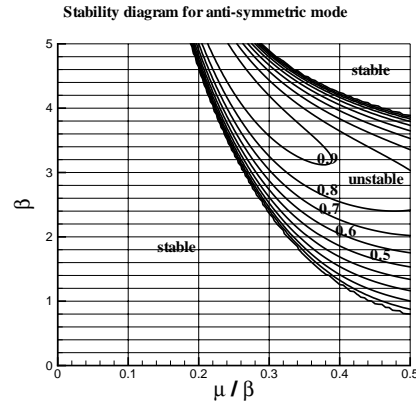


FIGURE 2.18: Stability diagram for anti-symmetric modes: iso-contours of α_A

in figure 2.17, showing regions of (in)stability in the $(\beta, \mu/\beta)$ -plane. Similarly, the stability diagram of anti-symmetric modes is shown in figure 2.18.

For the present "Rosenhead" vortex pair, the stability diagrams can be seen to be qualitatively very similar to those of the Crow's analysis, shown in figures 2.5 and 2.6 of section 2.1. Again, a symmetric long-wavelength instability is predicted with a maximum growth rate that is slightly smaller than that in the stability analysis of section 2.1. Similar to Crow's analysis, at much shorter wavelengths, both symmetric and anti-symmetric, short-wavelength instability modes are predicted.

For fixed values of $\mu/\beta = \hat{\mu}/b$, the amplification rate and the corresponding inclination angle of the symmetric modes are shown in figures 2.19, 2.21 and 2.23 for $\mu/\beta = 0.1$ to $\mu/\beta = 0.4$. Similar results for the anti-symmetric modes are shown in figures 2.20, 2.22 and 2.24. In figures 2.19 to 2.24, the inclination angle is set to zero for stable modes.

Comparing these figures with figures 2.7 to figure 2.12, it can be seen that the results for the

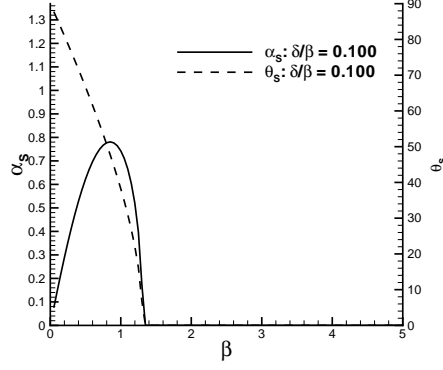


FIGURE 2.19: Exponential growth rate α and inclination angle versus $\beta = k \cdot b$: symmetric mode, $\mu/\beta = \hat{\mu}/b = 0.1$

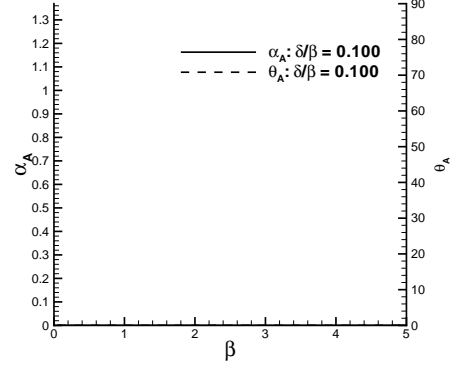


FIGURE 2.20: Exponential growth rate α and inclination angle versus $\beta = k \cdot b$: anti-symmetric mode, $\mu/\beta = \hat{\mu}/b = 0.1$

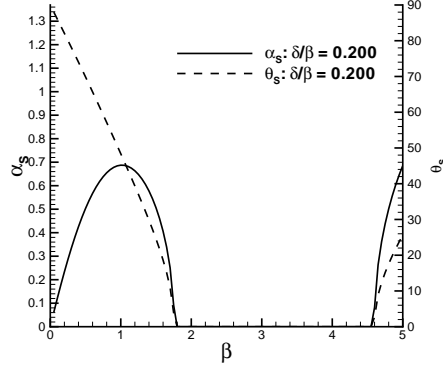


FIGURE 2.21: Exponential growth rate α and inclination angle versus $\beta = k \cdot b$: symmetric mode, $\mu/\beta = \hat{\mu}/b = 0.2$

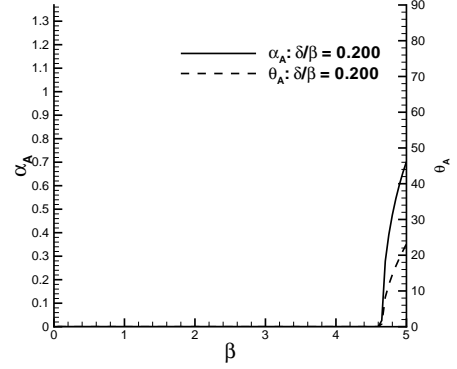


FIGURE 2.22: Exponential growth rate α and inclination angle versus $\beta = k \cdot b$: anti-symmetric mode, $\mu/\beta = \hat{\mu}/b = 0.2$

long-wavelength instability are fairly similar for both types of regularization considered, i.e. the cut-off method of Crow (1970) and the Rosenhead approach used in this section. The maximum amplification rate, the wavelength of the most amplified instability mode and the inclination angle of this mode with respect to the horizontal plane are shown as a function of the ratio μ/β in figure 2.25 and 2.26 for symmetric modes. Similar results for anti-symmetric short-wavelength modes are shown in figures 2.27 and 2.28. For both symmetric and anti-symmetric modes, the dependence of the inclination angle on the ratio μ/β is weak. The dependence of the growth rate on this ratio is larger than the dependence of the growth rate on the ratio δ/β in Crow's analysis.

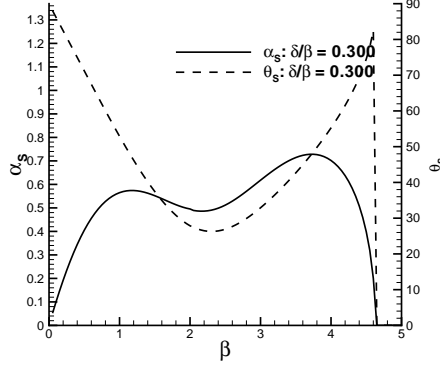


FIGURE 2.23: Exponential growth rate α and inclination angle versus $\beta = k \cdot b$: symmetric mode, $\mu/\beta = \hat{\mu}/b = 0.3$

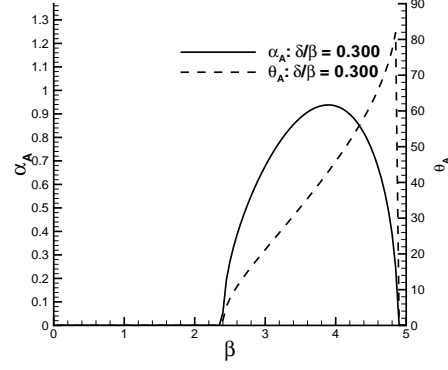


FIGURE 2.24: Exponential growth rate α and inclination angle versus $\beta = k \cdot b$: anti-symmetric mode, $\mu/\beta = \hat{\mu}/b = 0.3$

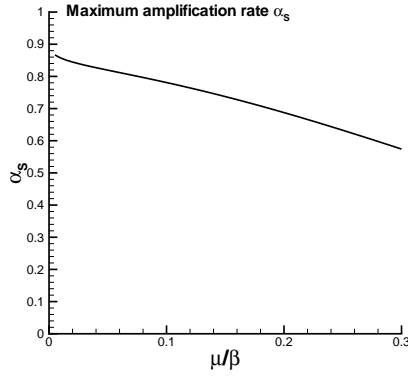


FIGURE 2.25: Maximum amplification rate α_S for symmetric modes versus μ/β .

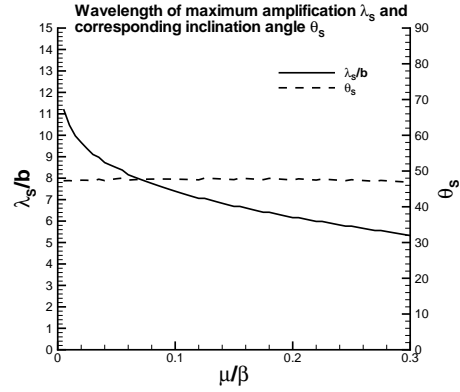


FIGURE 2.26: Wavelength of maximum amplification λ_S for symmetric modes and corresponding inclination angle θ_S .

In general, the growth rates predicted by the analysis based on the Rosenhead approach are somewhat smaller than those predicted by Crow (1970). The predicted inclination angles of the instability modes are similar for both methods, with an inclination angle of around 48° for the instability modes at vortex-pair spacings of interest in the present study, i.e. $\delta/\beta < 0.1$ and $\mu/\beta < 0.2$.

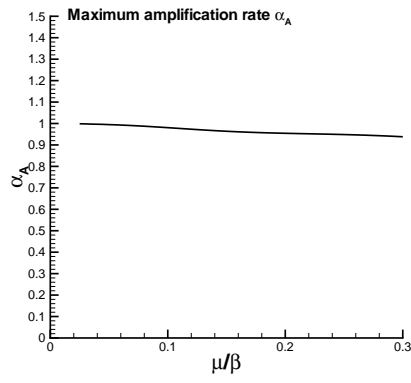


FIGURE 2.27: Maximum amplification rate α_A for anti-symmetric modes versus μ/β .

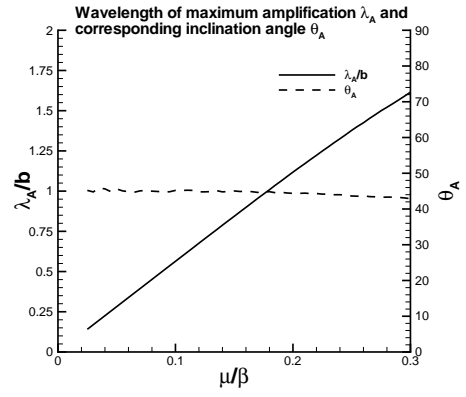


FIGURE 2.28: Wavelength of maximum amplification λ_A for anti-symmetric modes and corresponding inclination angle θ_A .

2.3 Stability analysis of Widnall

The linear stability of the trailing vortex pair from an aircraft was discussed in Widnall et al. (1970) using the method of matched asymptotic expansions, which gives a general solution for the flow field within and near a curved vortex filament with an arbitrary distribution of swirl and axial velocities. It was shown that details of the vorticity and axial velocity distributions affect the self-induced motion only through the kinetic energy of the swirl and the axial momentum flux.

In Crow's stability analysis, see Crow (1970) and section 2.1, the expression for the self-induced velocity is regularized using the 'cut-off' line integral technique, where the 'cut-off' parameter was chosen such that known results for the rotating sinusoidal vortex filament and vortex ring were matched for vortex cores with a constant vorticity distribution. Using this 'cut-off' approach, the effect of different swirl and axial velocity distributions is not apparent. To include these effects in the stability analysis, the method of matched asymptotic expansions was chosen by Widnall et al. (1970).

Deriving expressions for the self-induced motion and velocity distribution for a curved vortex filament with arbitrary deformation and deformation amplitude is not feasible. Therefore, in Widnall et al. (1970), the limiting case was considered in which the radius of curvature is large compared to the size of the vortex core. Then, the self-induced motion of the vortex filament can be obtained directly by analyzing the effects of curvature on the velocity and vorticity fields within and near the core.

Two asymptotic solutions, valid for a radius of curvature that is large compared to the vortex core, are used:

- an approximate solution valid in the vortex core and its immediate surroundings, the *inner solution*. This inner solution is expressed in terms of a coordinate system moving with the (unknown) self-induced motion. The local solution of the conservation equations for mass and vorticity plus the effects of distant elements of the vortex filament determine the self-induced motion. In this inner solution, the initial swirl and axial velocity profiles of the vortex core will be assumed to have radial symmetry. In the conservation equation for vorticity, the rotation of the moving coordinate system will introduce an apparent vorticity. However, in this stability analysis for the counter-rotating vortex-pair, rotation effects are ignored, since the self-induced rotation of the filaments is canceled by the induction of the other vortex filament in conditions of maximum instability. This cancellation of the self-induced rotation of the perturbations leads to the maximum exponential growth of the considered perturbations, since then the total included velocity along the filament will be aligned with the perturbation vector at the considered point on the filament. This situation was sketched in figure 2.2 of section 2.1. In the stability analysis by Widnall et al. (1970), viscous effects are neglected, as is the variation of properties of the vortex pair in the axial direction. In the resulting expressions for the velocity components, two constants appear, one that is proportional to twice the kinetic energy flux of the axial flow and another that represents the effect of the swirl distribution;
 - an *outer solution*, valid in all regions of the flow except the vortex core region. The velocity field is determined from a Biot-Savart integral, as used in section 2.1. The expressions for the velocity field contains a term representing the self-induced motion
-

of the sinusoidal vortex filament.

The two solution are matched in an intermediate region near the vortex core where both solution are assumed to be valid. This matching determines the previously unknown self-induced motion. Now, a general solution is obtained for the velocity field of a perturbed sinusoidal vortex filament of arbitrary vorticity and axial velocity distribution under the assumption that the radius of curvature of the filaments is large compared to the vortex cores.

The stability computation by Widnall et al. (1970) determines the the most amplified wave-

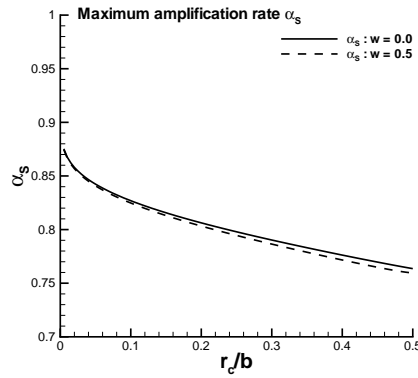


FIGURE 2.29: Maximum amplification rate α_S for symmetric modes versus r_c/b : with and without axial velocity.

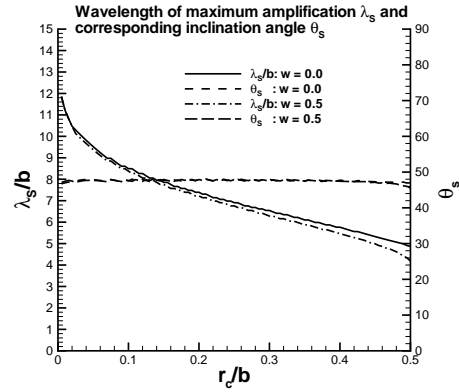


FIGURE 2.30: Wavelength of maximum amplification λ_S for symmetric modes and corresponding inclination angle θ_S : with and without axial velocity.

length for a given ratio r_c/b by searching for an axial wavelength for which the total induced velocity and the perturbation vector are exactly aligned, as sketched in figure 2.2.

Here, a linearized eigenvalue formulation similar to equation (2.22) is used. The difference with Crow's theory occurs through the different definition of the self-induction term, i.e. ω in equations (2.22), (2.23) and (2.23).

Using the method of Widnall et al. (1970), the self-induction term is written as:

$$\omega_{\text{Widnall}} = \frac{1}{2} \left[\ln \left(\frac{\lambda}{\pi b} \right) + \ln \left(\frac{b}{r_c} \right) + A - C - \gamma \right] \quad (2.63)$$

where r_c is the core radius of the vortex filament, b the spacing of the vortex pair, γ Euler's constant and λ the wavelength. In equation (2.63), the azimuthal velocity profile of the vortex determines the constant A , for a Rankine vortex this constant takes the value $1/4$. The effect of the axial velocity is included through the constant C , for a parabolic axial velocity profile this constant can be computed as $C = \bar{w}^2/3$, where \bar{w} represents the ratio of maximum axial velocity to maximum azimuthal velocity.

With definition (2.63), the stability computation can be performed in a similar way as in section 2.1. Here, only symmetric long-wavelength modes are considered. The maximum amplification rate for these modes is shown as a function of r_c/b in figure 2.29. Results are

shown for the situation without axial velocity ($\bar{w} = 0.0$) and with axial velocity ($\bar{w} = 0.5$). The result for vortex filaments without axial velocity is similar to the result of Crow's theory, when r_c/b and δ/β are chosen to represent an equivalent vortex filament. The presence of axial velocity in the filaments leads to a reduction of the amplification rate.

The wavelength at which the maximum amplification rate occurs and the corresponding inclination angle is shown as function of r_c/b in figure 2.30. Again, the results for filaments without axial velocity are similar to those of Crow's theory. The inclination angle of the most amplified perturbation can be seen to be nearly independent of the presence of an axial velocity component: for both $\bar{w} = 0.0$ and $\bar{w} = 0.5$, the inclination angle is nearly constant at around 47° . The wavelength of the most amplified mode shows a more pronounced dependence on axial velocity. The presence of axial velocity can be seen to reduce the wavelength of the most unstable mode for the long-wavelength instability. For the short-wavelength instability modes, not discussed here, the presence of an axial velocity component can be shown to lead to a larger wavelength of the most amplified mode.

The review of the theory of Widnall et al. (1970) presented in this section, shows that this theory is more general than that of Crow (1970), since different vortex types and effects of axial velocity can be included in the self-induction term by using appropriate values of the constants A and C .

2.4 Orr-Sommerfeld equations in Cartesian coordinates

The derivation of the eigenvalue system in a Cartesian coordinate system starts with the following perturbation on a two-dimensional basis flow field U, V, P

$$\begin{aligned} u(x, y, z) &= U(x, y) + \tilde{u}(x, y)e^{\sigma t}e^{ikz} \\ v(x, y, z) &= V(x, y) + \tilde{v}(x, y)e^{\sigma t}e^{ikz} \\ w(x, y, z) &= 0 + \tilde{w}(x, y)e^{\sigma t}e^{ikz} \\ \frac{p}{\rho}(x, y, z) &= P(x, y) + \tilde{p}(x, y)e^{\sigma t}e^{ikz} \end{aligned} \quad (2.64)$$

where k is the wave number in the third (periodic) spatial direction and σ is the exponential growth-rate of the perturbations $\tilde{u}, \tilde{v}, \tilde{w}, \tilde{p}$ imposed on the two-dimensional base flow U, V, P . With the base flow a solution to the full (non-linear) Navier-Stokes equations, the perturbations are governed up to first order in the perturbation amplitude by the linearized three-dimensional Navier-Stokes equations:

$$\frac{\partial \tilde{u}}{\partial x} + \frac{\partial \tilde{v}}{\partial y} + ik\tilde{w} = 0 \quad (2.65)$$

$$\sigma \tilde{u} + U \frac{\partial \tilde{u}}{\partial x} + \tilde{u} \frac{\partial U}{\partial x} + V \frac{\partial \tilde{u}}{\partial y} + \tilde{v} \frac{\partial U}{\partial y} = -\frac{\partial \tilde{p}}{\partial x} + \nu \left\{ \frac{\partial^2}{\partial x^2} + \frac{\partial^2}{\partial y^2} - k^2 \right\} \tilde{u} \quad (2.66)$$

$$\sigma \tilde{v} + U \frac{\partial \tilde{v}}{\partial x} + \tilde{u} \frac{\partial V}{\partial x} + V \frac{\partial \tilde{v}}{\partial y} + \tilde{v} \frac{\partial V}{\partial y} = -\frac{\partial \tilde{p}}{\partial y} + \nu \left\{ \frac{\partial^2}{\partial x^2} + \frac{\partial^2}{\partial y^2} - k^2 \right\} \tilde{v} \quad (2.67)$$

$$\sigma \tilde{w} + U \frac{\partial \tilde{w}}{\partial x} + V \frac{\partial \tilde{w}}{\partial y} = -ik\tilde{p} + \nu \left\{ \frac{\partial^2}{\partial x^2} + \frac{\partial^2}{\partial y^2} - k^2 \right\} \tilde{w} \quad (2.68)$$

Using equation (2.65), the perturbation in z -direction can be expressed in terms of the perturbations in the other two spatial directions

$$\tilde{w} = \frac{i}{k} \left[\frac{\partial \tilde{u}}{\partial x} + \frac{\partial \tilde{v}}{\partial y} \right] \quad (2.69)$$

Substituting this expression in equation (2.68) gives

$$\begin{aligned} \sigma \left\{ \frac{\partial \tilde{u}}{\partial x} + \frac{\partial \tilde{v}}{\partial y} \right\} + U \frac{\partial}{\partial x} \left\{ \frac{\partial \tilde{u}}{\partial x} + \frac{\partial \tilde{v}}{\partial y} \right\} + V \frac{\partial}{\partial y} \left\{ \frac{\partial \tilde{u}}{\partial x} + \frac{\partial \tilde{v}}{\partial y} \right\} = \\ -k^2 \tilde{p} + \nu \left\{ \frac{\partial^2}{\partial x^2} + \frac{\partial^2}{\partial y^2} - k^2 \right\} \left\{ \frac{\partial \tilde{u}}{\partial x} + \frac{\partial \tilde{v}}{\partial y} \right\} \end{aligned} \quad (2.70)$$

Thus, the pressure terms can be eliminated from the other two momentum equations (2.66) and (2.67), using the following equation

$$\begin{aligned} -k^2 \tilde{p} &= \sigma \left\{ \frac{\partial \tilde{u}}{\partial x} + \frac{\partial \tilde{v}}{\partial y} \right\} + U \frac{\partial}{\partial x} \left\{ \frac{\partial \tilde{u}}{\partial x} + \frac{\partial \tilde{v}}{\partial y} \right\} + V \frac{\partial}{\partial y} \left\{ \frac{\partial \tilde{u}}{\partial x} + \frac{\partial \tilde{v}}{\partial y} \right\} - \\ &\quad \nu \left\{ \frac{\partial^2}{\partial x^2} + \frac{\partial^2}{\partial y^2} - k^2 \right\} \left\{ \frac{\partial \tilde{u}}{\partial x} + \frac{\partial \tilde{v}}{\partial y} \right\} \\ &= \left[\sigma \frac{\partial}{\partial x} + U \frac{\partial^2}{\partial x^2} + V \frac{\partial^2}{\partial x \partial y} - \nu \left\{ \frac{\partial^2}{\partial x^2} + \frac{\partial^2}{\partial y^2} - k^2 \right\} \frac{\partial}{\partial x} \right] \tilde{u} + \\ &\quad \left[\sigma \frac{\partial}{\partial y} + U \frac{\partial^2}{\partial x \partial y} + V \frac{\partial^2}{\partial y^2} - \nu \left\{ \frac{\partial^2}{\partial x^2} + \frac{\partial^2}{\partial y^2} - k^2 \right\} \frac{\partial}{\partial y} \right] \tilde{v} \end{aligned} \quad (2.71)$$

Taking the derivative of equation (2.71) in x -direction, leads to the following expression

$$\begin{aligned}
 -k^2 \frac{\partial \tilde{p}}{\partial x} = & \left[\sigma \frac{\partial^2}{\partial x^2} + \frac{\partial U}{\partial x} \frac{\partial^2}{\partial x^2} + U \frac{\partial^3}{\partial x^3} + \frac{\partial V}{\partial x} \frac{\partial^2}{\partial x \partial y} + V \frac{\partial^3}{\partial x^2 \partial y} \right. \\
 & \left. - \nu \left\{ \frac{\partial^2}{\partial x^2} + \frac{\partial^2}{\partial y^2} - k^2 \right\} \frac{\partial^2}{\partial x^2} \right] \tilde{u} + \\
 & \left[\sigma \frac{\partial^2}{\partial x \partial y} + \frac{\partial U}{\partial x} \frac{\partial^2}{\partial x \partial y} + U \frac{\partial^3}{\partial x^2 \partial y} + \frac{\partial V}{\partial x} \frac{\partial^2}{\partial y^2} + V \frac{\partial^3}{\partial x \partial y^2} \right. \\
 & \left. - \nu \left\{ \frac{\partial^2}{\partial x^2} + \frac{\partial^2}{\partial y^2} - k^2 \right\} \frac{\partial^2}{\partial x \partial y} \right] \tilde{v}
 \end{aligned} \tag{2.72}$$

Similarly for the derivative in y -direction

$$\begin{aligned}
 -k^2 \frac{\partial \tilde{p}}{\partial y} = & \left[\sigma \frac{\partial^2}{\partial x \partial y} + \frac{\partial U}{\partial y} \frac{\partial^2}{\partial x^2} + U \frac{\partial^3}{\partial x^2 \partial y} + \frac{\partial V}{\partial y} \frac{\partial^2}{\partial x \partial y} + V \frac{\partial^3}{\partial x \partial y^2} \right. \\
 & \left. - \nu \left\{ \frac{\partial^2}{\partial x^2} + \frac{\partial^2}{\partial y^2} - k^2 \right\} \frac{\partial^2}{\partial x \partial y} \right] \tilde{u} + \\
 & \left[\sigma \frac{\partial^2}{\partial y^2} + \frac{\partial U}{\partial y} \frac{\partial^2}{\partial x \partial y} + U \frac{\partial^3}{\partial x \partial y^2} + \frac{\partial V}{\partial y} \frac{\partial^2}{\partial y^2} + V \frac{\partial^3}{\partial y^3} \right. \\
 & \left. - \nu \left\{ \frac{\partial^2}{\partial x^2} + \frac{\partial^2}{\partial y^2} - k^2 \right\} \frac{\partial^2}{\partial y^2} \right] \tilde{v}
 \end{aligned} \tag{2.73}$$

Equations (2.72) and (2.73) can be used to eliminate the pressure terms from the linearized momentum equations (2.66) and (2.66):

$$\begin{aligned}
 & \left[(\sigma - \nu \Delta) \left(\frac{\partial^2}{\partial x^2} - k^2 \right) \right] \tilde{u} + \left[(\sigma - \nu \Delta) \frac{\partial^2}{\partial x \partial y} \right] \tilde{v} + \\
 & \left[\left\{ \frac{\partial U}{\partial x} + U \frac{\partial}{\partial x} + V \frac{\partial}{\partial y} \right\} \left(\frac{\partial^2}{\partial x^2} - k^2 \right) + \frac{\partial V}{\partial x} \frac{\partial^2}{\partial x \partial y} \right] \tilde{u} + \\
 & \left[\left\{ \frac{\partial U}{\partial x} + U \frac{\partial}{\partial x} + V \frac{\partial}{\partial y} \right\} \frac{\partial^2}{\partial x \partial y} + \frac{\partial V}{\partial x} \left(\frac{\partial^2}{\partial y^2} - k^2 \right) - k^2 \left(\frac{\partial U}{\partial y} - \frac{\partial V}{\partial x} \right) \right] \tilde{v} = 0 \tag{2.74}
 \end{aligned}$$

and

$$\begin{aligned}
 & \left[(\sigma - \nu \Delta) \frac{\partial^2}{\partial x \partial y} \right] \tilde{u} + \left[(\sigma - \nu \Delta) \left(\frac{\partial^2}{\partial y^2} - k^2 \right) \right] \tilde{v} + \\
 & \left[\left\{ \frac{\partial V}{\partial y} + U \frac{\partial}{\partial x} + V \frac{\partial}{\partial y} \right\} \frac{\partial^2}{\partial x \partial y} + \frac{\partial U}{\partial y} \left(\frac{\partial^2}{\partial x^2} - k^2 \right) - k^2 \left(\frac{\partial V}{\partial x} - \frac{\partial U}{\partial y} \right) \right] \tilde{u} + \\
 & \left[\left\{ \frac{\partial V}{\partial y} + U \frac{\partial}{\partial x} + V \frac{\partial}{\partial y} \right\} \left(\frac{\partial^2}{\partial y^2} - k^2 \right) + \frac{\partial U}{\partial y} \frac{\partial^2}{\partial x \partial y} \right] \tilde{v} = 0 \tag{2.75}
 \end{aligned}$$

with $\Delta = \frac{\partial^2}{\partial x^2} + \frac{\partial^2}{\partial y^2} - k^2$.

The system of equations (2.74) and (2.75) can be written as a generalized eigenvalue problem in matrix notation

$$\left[(\sigma - \nu \Delta) \begin{pmatrix} A_{11} & A_{12} \\ A_{21} & A_{22} \end{pmatrix} + \begin{pmatrix} B_{11} & B_{12} \\ B_{21} & B_{22} \end{pmatrix} \right] \begin{pmatrix} \tilde{u} \\ \tilde{v} \end{pmatrix} = 0 \tag{2.76}$$

with

$$A_{11} = \frac{\partial^2}{\partial x^2} - k^2; \quad A_{12} = A_{21} = \frac{\partial^2}{\partial x \partial y}; \quad A_{22} = \frac{\partial^2}{\partial y^2} - k^2 \quad (2.77)$$

and

$$\begin{aligned} B_{11} &= \left\{ \frac{\partial U}{\partial x} + U \frac{\partial}{\partial x} + V \frac{\partial}{\partial y} \right\} \left(\frac{\partial^2}{\partial x^2} - k^2 \right) + \frac{\partial V}{\partial x} \frac{\partial^2}{\partial x \partial y} \\ B_{12} &= \left\{ \frac{\partial U}{\partial x} + U \frac{\partial}{\partial x} + V \frac{\partial}{\partial y} \right\} \frac{\partial^2}{\partial x \partial y} + \frac{\partial V}{\partial x} \left(\frac{\partial^2}{\partial y^2} - k^2 \right) + k^2 \zeta \\ B_{21} &= \left\{ \frac{\partial V}{\partial y} + U \frac{\partial}{\partial x} + V \frac{\partial}{\partial y} \right\} \frac{\partial^2}{\partial x \partial y} + \frac{\partial U}{\partial y} \left(\frac{\partial^2}{\partial x^2} - k^2 \right) - k^2 \zeta \\ B_{22} &= \left\{ \frac{\partial V}{\partial y} + U \frac{\partial}{\partial x} + V \frac{\partial}{\partial y} \right\} \left(\frac{\partial^2}{\partial y^2} - k^2 \right) + \frac{\partial U}{\partial y} \frac{\partial^2}{\partial x \partial y} \end{aligned} \quad (2.78)$$

where $\zeta = \frac{\partial V}{\partial x} - \frac{\partial U}{\partial y}$, the vorticity of the unperturbed two-dimensional flow field. System (2.76) with elements (2.77) and (2.78) can be reduced to the following generalized eigenvalue problem

$$\left[(\sigma - \nu \Delta) \begin{pmatrix} \hat{A}_{11} & \hat{A}_{12} \\ 0 & \hat{A}_{22} \end{pmatrix} + \begin{pmatrix} \hat{B}_{11} & \hat{B}_{12} \\ \hat{B}_{21} & \hat{B}_{22} \end{pmatrix} \right] \begin{pmatrix} \tilde{u} \\ \tilde{v} \end{pmatrix} = 0 \quad (2.79)$$

with

$$\hat{A}_{11} = \frac{\partial^2}{\partial x^2} - k^2; \quad \hat{A}_{12} = \frac{\partial^2}{\partial x \partial y}; \quad \hat{A}_{22} = \frac{\partial^2}{\partial x^2} + \frac{\partial^2}{\partial y^2} - k^2 \quad (2.80)$$

and

$$\begin{aligned} \hat{B}_{11} &= B_{11} \\ \hat{B}_{12} &= B_{12} \\ \hat{B}_{21} &= \frac{1}{k^2} \left[\frac{\partial^2}{\partial x \partial y} B_{11} - \left(\frac{\partial^2}{\partial x^2} - k^2 \right) B_{21} \right] \\ \hat{B}_{22} &= \frac{1}{k^2} \left[\frac{\partial^2}{\partial x \partial y} B_{12} - \left(\frac{\partial^2}{\partial x^2} - k^2 \right) B_{22} \right] \end{aligned} \quad (2.81)$$

Expanding the coefficients in equation (2.81) gives

$$\begin{aligned} \hat{B}_{11} &= \left\{ \frac{\partial U}{\partial x} + U \frac{\partial}{\partial x} + V \frac{\partial}{\partial y} \right\} \left(\frac{\partial^2}{\partial x^2} - k^2 \right) + \frac{\partial V}{\partial x} \frac{\partial^2}{\partial x \partial y} \\ \hat{B}_{12} &= \left\{ \frac{\partial U}{\partial x} + U \frac{\partial}{\partial x} + V \frac{\partial}{\partial y} \right\} \frac{\partial^2}{\partial x \partial y} + \frac{\partial V}{\partial x} \left(\frac{\partial^2}{\partial y^2} - k^2 \right) + k^2 \zeta \\ \hat{B}_{21} &= -\frac{\partial V}{\partial x} \left\{ -\frac{\partial^2}{\partial x^2} + \frac{\partial^2}{\partial y^2} + k^2 \right\} - 2 \frac{\partial U}{\partial x} \frac{\partial^2}{\partial x \partial y} + 2 \zeta_x \frac{\partial}{\partial x} + \zeta_{xx} \\ \hat{B}_{22} &= \left\{ \frac{\partial V}{\partial y} + U \frac{\partial}{\partial x} + V \frac{\partial}{\partial y} \right\} \left\{ \frac{\partial^2}{\partial x^2} + \frac{\partial^2}{\partial y^2} - k^2 \right\} \\ &\quad + 2 \frac{\partial U}{\partial x} \frac{\partial^2}{\partial x^2} + 2 \frac{\partial V}{\partial x} \frac{\partial^2}{\partial x \partial y} + \zeta_x \frac{\partial}{\partial y} + \zeta_y \frac{\partial}{\partial x} + \zeta_{xy} \end{aligned} \quad (2.82)$$

2.4.1 Formulation in terms of a stream function

The generalized eigenvalue problem (2.79) with coefficients (2.80) and (2.82) was formulated in Sipp et al. (1998) with the two-dimensional base flow described in terms of a stream function $\psi(x, y)$, with the two-dimensional velocity field $U(x, y) = \psi_y(x, y)$ and $V(x, y) = -\psi_x(x, y)$. Using this stream function, the velocity field satisfies the solenoidality constraint automatically. With this stream function $\psi(x, y)$, the coefficients (2.82) can be rewritten as:

$$\begin{aligned}
 \hat{B}_{11} &= \left\{ \psi_y \frac{\partial}{\partial x} - \psi_x \frac{\partial}{\partial y} + \psi_{xy} \right\} \left(\frac{\partial^2}{\partial x^2} - k^2 \right) - \psi_{xx} \frac{\partial^2}{\partial x \partial y} \\
 \hat{B}_{12} &= \left\{ \psi_y \frac{\partial}{\partial x} - \psi_x \frac{\partial}{\partial y} + \psi_{xy} \right\} \frac{\partial^2}{\partial x \partial y} - \psi_{xx} \left(\frac{\partial^2}{\partial y^2} - k^2 \right) + k^2 \zeta \\
 \hat{B}_{21} &= \psi_{xx} \left(-\frac{\partial^2}{\partial x^2} + \frac{\partial^2}{\partial y^2} + k^2 \right) - 2\psi_{xy} \frac{\partial^2}{\partial x \partial y} + 2\zeta_x \frac{\partial}{\partial x} + \zeta_{xx} \\
 \hat{B}_{22} &= \left\{ \psi_y \frac{\partial}{\partial x} - \psi_x \frac{\partial}{\partial y} - \psi_{xy} \right\} \Delta + \\
 &\quad 2\psi_{xy} \frac{\partial^2}{\partial x^2} - 2\psi_{xx} \frac{\partial^2}{\partial x \partial y} + \zeta_x \frac{\partial}{\partial y} + \zeta_y \frac{\partial}{\partial x} + \zeta_{xy}
 \end{aligned} \tag{2.83}$$

Again with ζ the vorticity of the two-dimensional base flow, $\zeta = -(\psi_{xx} + \psi_{yy})$. The generalized eigenvalue problem (2.79) with coefficients (2.80) and (2.83) is identical to the system presented by Sipp et al. (1998), except for the minus sign in the term $\psi_{xx}(\frac{\partial^2}{\partial y^2} - k^2)$ in \hat{B}_{12} . Apparently, this is a typographical error in Sipp et al. (1998).

2.4.2 Normal mode analysis due to Sipp et al. (1998)

A linear stability analysis of a vortex pair was presented by Sipp et al. (1998). The base flow field used is a superposition of two Lamb-Oseen vortices of radius r_c and separation distance b . The aspect ratio r_c/b characterizes this flow field. Both the long-wavelength Crow instability and short-wavelength Widnall instability were studied. In this study, generalized eigenvalue problem (2.79) with coefficients (2.80) and (2.83) was discretized using a spectral Chebyshev collocation method in both remaining spatial directions. The resulting non-symmetric dense matrix eigenvalue problem was solved using standard linear algebra routines on a supercomputer. This analysis was performed for $r_c/b = 0.2$ and for $\nu = 0$, i.e. inviscid flow. Eigenvalues and corresponding eigenvectors were computed for this aspect ratio for a wide range of wave numbers k in the periodic direction, showing various instability regimes. The results for the generalized eigenvalue problem can be summarized as follows:

- for small wave numbers k ($k \cdot r_c \ll 1$), an instability band occurs for symmetric perturbations. This is the well-known Crow instability. Anti-symmetric perturbations in this wave-number range are found to be stable;
 - from $k \cdot r_c > 2$, a number of distinct instability bands is present. The short-wavelength instabilities occur for both symmetric and anti-symmetric perturbations;
 - for decreasing aspect ratio r_c/b , the anti-symmetric short-wavelength modes have a larger growth rate than the symmetric modes.
-

2.5 Isolated vortex in a plain strain field

In this section, the deformation of an isolated vortex located in a plain strain field is considered. In a counter-rotating vortex pair, the vortices impose a strain field on another. The strain occurs in the plane normal to the axial direction of the vortex, which is chosen to coincide with the z -coordinate direction. The flow field is assumed to be constant in this axial direction and to have a vanishing axial velocity component, i.e. $u_z = 0$.

In the center of a vortex, the strength ϵ of the strain induced by the other vortex can be approximated as: $\epsilon = \frac{1}{2}(\frac{\partial v}{\partial x} + \frac{\partial u}{\partial y}) \approx \Gamma/2\pi b^2$, with Γ the circulation of the vortices, b the spacing and u and v the velocity components in the cross-flow plane.

The deformation of the vortex is studied by deriving and solving an equation governing the radial perturbation of the basic flow field. This equation is derived from the Euler equations for an incompressible flow, which for a cylindrical coordinate system (r, θ, z) can be written as:

$$\frac{\partial u_r}{\partial r} + \frac{u_r}{r} + \frac{1}{r} \frac{\partial u_\theta}{\partial \theta} + \frac{\partial u_z}{\partial z} = 0 \quad (2.84)$$

$$\frac{\partial u_r}{\partial t} + u_r \frac{\partial u_r}{\partial r} + \frac{u_\theta}{r} \frac{\partial u_r}{\partial \theta} + u_z \frac{\partial u_r}{\partial z} - \frac{u_\theta^2}{r} = -\frac{\partial p}{\partial r} \quad (2.85)$$

$$\frac{\partial u_\theta}{\partial t} + u_r \frac{\partial u_\theta}{\partial r} + \frac{u_\theta}{r} \frac{\partial u_\theta}{\partial \theta} + u_z \frac{\partial u_\theta}{\partial z} + \frac{u_r u_\theta}{r} = -\frac{\partial p}{\partial \theta} \quad (2.86)$$

$$\frac{\partial u_z}{\partial t} + u_r \frac{\partial u_z}{\partial r} + \frac{u_\theta}{r} \frac{\partial u_z}{\partial \theta} + u_z \frac{\partial u_z}{\partial z} = -\frac{\partial p}{\partial z} \quad (2.87)$$

with p denoting the pressure divided by the constant density. The axial direction of the vortex corresponds to the z -coordinate direction. The vortex is assumed to have an azimuthal velocity distribution $u_\theta(r) = r\Omega(r)$, where $\Omega(r)$ denotes the angular rotation. For a Lamb-Oseen vortex, introduced in section 1.1, this function is given by

$$\Omega(r) = \frac{1 - \exp(-r^2)}{r^2} \quad (2.88)$$

Following the work of Moore and Saffman (1975), the perturbed velocity field can be written as an expansion in terms of ϵ

$$\begin{bmatrix} u_r \\ u_\theta \\ u_z \end{bmatrix} = \begin{bmatrix} 0 \\ r\Omega(r) \\ 0 \end{bmatrix} + \epsilon \begin{bmatrix} \frac{f}{r} \sin 2\theta \\ \frac{1}{2} \frac{df}{dr} \cos 2\theta \\ 0 \end{bmatrix} \quad (2.89)$$

where the function $f(r)$ represents the effect of the strain field. This function $f(r)$ is determined by the requirement of obtaining a steady two-dimensional flow in planes normal to the axial direction. The formulation used in the expansion (2.89) is chosen such that for functions f continuous in r , the flow is solenoidal up to order ϵ , as can be shown by introducing the expansion in the continuity equation (2.84):

$$\frac{\partial}{\partial r} \left\{ \epsilon \frac{f}{r} \sin 2\theta \right\} + \frac{1}{r} \frac{\partial}{\partial \theta} \left\{ r\Omega + \epsilon \frac{1}{2} \frac{df}{dr} \cos 2\theta \right\} + \epsilon \frac{f}{r^2} \sin 2\theta = 0 \quad (2.90)$$

The governing equation for the strain function $f(r)$ can be derived from eliminating the pressure from the momentum equations (2.85) and (2.86). Since steady flow in the (r, θ) -planes is considered, the z -dependence and temporal derivatives can be omitted from these

equations, resulting in:

$$u_r \frac{\partial u_r}{\partial r} + \frac{u_\theta}{r} \frac{\partial u_r}{\partial \theta} - \frac{u_\theta^2}{r} = -\frac{\partial p}{\partial r} \quad (2.91)$$

$$u_r \frac{\partial u_\theta}{\partial r} + \frac{u_\theta}{r} \frac{\partial u_\theta}{\partial \theta} + \frac{u_r u_\theta}{r} = -\frac{\partial p}{\partial \theta} \quad (2.92)$$

Eliminating the pressure leads to the following equation:

$$\left[\frac{\partial u_r}{\partial \theta} \frac{\partial u_r}{\partial r} + u_r \frac{\partial^2 u_r}{\partial r \partial \theta} + \frac{1}{r} \frac{\partial u_\theta}{\partial \theta} \frac{\partial u_r}{\partial \theta} + \frac{u_\theta}{r} \frac{\partial^2 u_r}{\partial \theta^2} - \frac{2u_\theta}{r} \frac{\partial u_\theta}{\partial \theta} \right] - \quad (2.93)$$

$$\left[u_r \frac{\partial u_\theta}{\partial r} + r \left\{ \frac{\partial u_r}{\partial r} \frac{\partial u_\theta}{\partial r} + u_r \frac{\partial^2 u_\theta}{\partial r^2} \right\} + \frac{\partial u_\theta}{\partial r} \frac{\partial u_\theta}{\partial \theta} + u_\theta \frac{\partial^2 u_\theta}{\partial r \partial \theta} + u_r \frac{\partial u_\theta}{\partial r} + u_\theta \frac{\partial u_r}{\partial r} \right] = 0$$

Using expansion (2.89), equation (2.94) can be written in powers of ϵ . Assembling terms involving first-order terms of ϵ , the governing equation for $f(r)$ can be derived:

$$\left[\epsilon \sin 2\theta \left\{ -4\Omega \frac{f}{r} + 2\Omega \frac{df}{dr} \right\} + O(\epsilon^2) \right] -$$

$$\left[\epsilon \sin 2\theta \left\{ \frac{f}{r} \left(\Omega + r \frac{d\Omega}{dr} \right) + \left(\frac{df}{dr} - \frac{f}{r} \right) \left(\Omega + r \frac{d\Omega}{dr} \right) + f \left(2 \frac{d\Omega}{dr} + r \frac{d^2 \Omega}{dr^2} \right) \right. \right. -$$

$$\left. \left. \left(\Omega + r \frac{df}{dr} \right) \frac{df}{dr} - \Omega r \frac{d^2 f}{dr^2} + \frac{f}{r} \left(\Omega + r \frac{d\Omega}{dr} \right) + \Omega \left(\frac{df}{dr} - \frac{f}{r} \right) \right\} + O(\epsilon^2) \right] = 0 \quad (2.94)$$

Some arranging of the terms in equation (2.94) leads to the governing equation for the function $f(r)$:

$$\frac{d^2 f}{dr^2} + \frac{1}{r} \frac{df}{dr} - \left(\frac{3 \frac{d\Omega}{dr} + r \frac{d^2 \Omega}{dr^2}}{\Omega r} + \frac{4}{r^2} \right) f = 0 \quad (2.95)$$

Equation (2.95) has the following boundary conditions: $f(r)/r^2 \rightarrow 1$ as $r \rightarrow \infty$. Furthermore, f is bounded for $r \rightarrow 0$. As a result of the boundary conditions, it is more

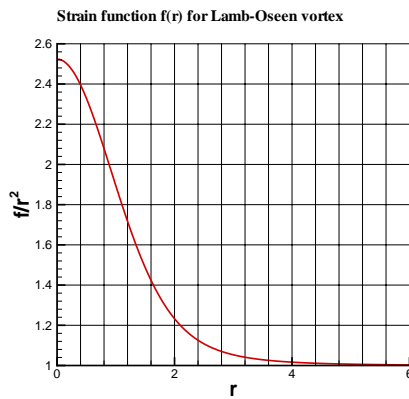


FIGURE 2.31: Function $f(r)$ for Lamb-Oseen vortex

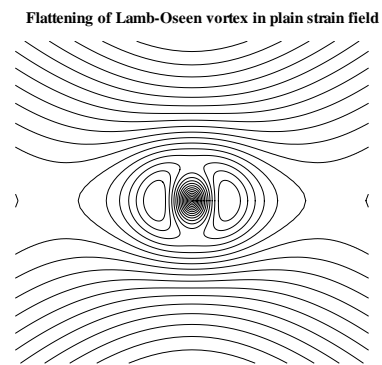


FIGURE 2.32: Lamb-Oseen vortex in strain field: u_θ contours, $\epsilon = 0.05$

convenient to solve for $\tilde{f} = f/r^2$ instead of f . Expressing f , $\frac{df}{dr}$ and $\frac{d^2f}{dr^2}$ in terms of \tilde{f} gives:

$$\begin{aligned} f &= \tilde{f}r^2 \\ \frac{df}{dr} &= r^2 \left(\frac{d\tilde{f}}{dr} + \frac{2}{r} \tilde{f} \right) \\ \frac{d^2f}{dr^2} &= r^2 \left(\frac{d^2\tilde{f}}{dr^2} + \frac{4}{r} \frac{d\tilde{f}}{dr} + \frac{2}{r^2} \tilde{f} \right) \end{aligned} \quad (2.96)$$

With these relations, equation (2.95) becomes:

$$\frac{d^2\tilde{f}}{dr^2} + \frac{5}{r} \frac{d\tilde{f}}{dr} - \left(\frac{3\frac{d\Omega}{dr} + r\frac{d^2\Omega}{dr^2}}{\Omega r} \right) \tilde{f} = 0 \quad (2.97)$$

For $\Omega(r)$ of a Lamb-Oseen vortex:

$$\begin{aligned} \frac{d\Omega}{dr} &= \frac{2 \left[(r^2 + 1) \exp(-r^2) - 1 \right]}{r^3} \\ \frac{d^2\Omega}{dr^2} &= \frac{6 - (4r^4 + 6r^2 + 6) \exp(-r^2)}{r^4} \end{aligned} \quad (2.98)$$

And with these expressions it can easily be derived that

$$\frac{3\frac{d\Omega}{dr} + r\frac{d^2\Omega}{dr^2}}{\Omega r} = \frac{-4r^2 \exp(-r^2)}{1 - \exp(-r^2)} \quad (2.99)$$

Thus, equation (2.97) becomes

$$\frac{d^2\tilde{f}}{dr^2} + \frac{5}{r} \frac{d\tilde{f}}{dr} + 4 \frac{r^2 \exp(-r^2)}{1 - \exp(-r^2)} \tilde{f} = 0 \quad (2.100)$$

with the following boundary conditions: $\tilde{f} \rightarrow 1$ for $r \rightarrow \infty$, $\frac{d\tilde{f}}{dr} = 0$ for $r = 0$.

Figure 2.31 shows the numerical solution of equation (2.100). The solution is obtained using three-point central-difference expressions for both first and second derivatives. The figure shows that the strain in the center of the Lamb-Oseen vortex is about 2.5 times stronger than in the far-field of the vortex. With this known function $f(r)$, velocity field expansion (2.89) can be used to compute the perturbed velocity field. Figure 2.32 shows the flattening of a Lamb-Oseen vortex for $\epsilon = 0.05$. Shown are iso-contours of the perturbed azimuthal velocity field u_θ .

2.6 Computation of Kelvin waves

In this section, infinitesimal helical disturbances are considered on a straight vortex column. As described in section 1.3.2, these neutrally stable modes are commonly known as *Kelvin modes*. These modes play an important role in the formation of short-wavelength instability modes, i.e. the occurrence of the short-wavelength instability can be explained as a resonance phenomenon of Kelvin modes with specific azimuthal wave numbers and the external strain field, see Tsai and Widnall (1976). As indicated in section 1.3.2 of the introduction to the present study, the majority of the studies of the short-wavelength instability in a counter-rotating vortex pair is based on a stability analysis for a single vortex filament located in an imposed strain field. Results from these studies can be used for vortex pairs, since the effect of the neighbor vortex on the vortex considered appears as an induced strain field. The effect of an imposed strain field on a vortex was studied in section 2.5. The stability analysis for a single vortex is usually based on a linearization of the inviscid Euler equations in cylindrical coordinates. Examples of these studies are those of Moore and Saffman (1975) and Tsai and Widnall (1976). In the absence of strain, these stability analyses only show stable infinitesimal disturbances rotating around the vortex filament. An infinite number of these stable disturbances exist. As indicated by equation (1.12) of section 1.3.2, the disturbances can be written as

$$[\hat{u}_r, \hat{u}_\theta, \hat{u}_z, \hat{p}] = [u(r), v(r), w(r), p(r)] e^{i(kz+m\theta+\sigma t)} \quad (2.101)$$

where r is the radial coordinate, k is the axial wavenumber and m is the azimuthal wavenumber. In equation (2.101), σ represents the exponential growth rate and $u(r)$, $v(r)$, $w(r)$ and $p(r)$ are the components of the eigenfunctions. If σ is real, the vortex column is stable. Instability occurs for complex σ . The eigenvalues σ and corresponding eigenfunctions can be obtained in various ways. For specific simple velocity distributions of the vortex, analytical results can be obtained. In Saffman (1992), results are presented for the specific case of the uniform vortex with uniform axial flow:

$$\begin{aligned} u_\theta &= \begin{cases} \Omega r & \text{for } r < a \\ \Omega \frac{a^2}{r} & \text{for } r \geq a \end{cases} \\ u_z &= \begin{cases} \text{constant} & \text{for } r < a \\ 0 & \text{for } r \geq a \end{cases} \end{aligned} \quad (2.102)$$

A dispersion relation can be derived relating parameters σ , m , k , Ω and w for infinitely many of these infinitesimal helical modes. In general, one has to resort to numerical methods for the computation of Kelvin modes.

For the short-wavelength instability, the Kelvin modes with azimuthal wavenumber $|m| = 1$ are of particular interest. For these azimuthal wave numbers, the disturbance modes are *bending modes*, with a deformation of the vortex axis and a non-vanishing velocity perturbation at $r = 0$. For the simple vortex of equation (2.102), the case $|m| = 1$ and the limit of short axial wavelengths can be studied analytically. In this case, the following symmetry relation can be shown to exist:

$$\sigma(k, 1) = \sigma(-k, 1) = -\sigma^*(-k, -1) \quad (2.103)$$

with superscript $*$ denoting the complex conjugate. An important feature of the modes with $|m| = 1$ is the existence of axial wavelengths for which $\sigma = 0$. In the absence of an axial velocity component, the first three roots are $k \cdot a = 2.5$, 4.4 and 6.2.

As a result of the symmetry relation (2.103), disturbances of the vortex core boundary can be written as a superposition of modes with axial wave numbers of opposite signs:

$$r = a + \delta e^{i(kz+\theta+\sigma t)} + \delta e^{i(-kz+\theta+\sigma t)} + c.c.$$

$$= a + 4\delta \cos(kz) \cos(\theta + \sigma t) \quad (2.104)$$

which is a stationary disturbance. In equation (2.104), $c.c$ denotes the complex conjugate of the previous complex expression. Here, the simple case of a uniform vortex with velocity profile (2.102) and $w = 0$ was considered.

The eigenfunctions for $|m| = 1$ modes have an internal structure, and are the ones of interest in the formation of short-wavelength instabilities, see Widnall et al. (1974).

For more complicated velocity profiles, for example those given by expressions (1.7) and (1.9), the computation of the Kelvin modes with $\sigma = 0$ requires a numerical procedure.

In the present study, two computational methods for Kelvin modes on a vortex column with a Lamb-Oseen velocity profile are considered:

- a method based on the Orr-Sommerfeld equation formulated in a cylindrical coordinate system. The derivation of the generalized eigenvalue problem is similar to that for the Cartesian coordinate system, discussed in section 2.4. For the Kelvin-mode computation, the complexity of the set of equations is greatly reduced. This method is described in detail in section 2.7;
- a method based on a normal mode analysis of the Euler equations in cylindrical coordinates with a base flow consisting of a single unstrained vortex. This method is based on the work presented in Sipp (2000) and is described in detail in chapter 6. The method forms the basis of the computational method for specifying the initial conditions for the Navier-Stokes simulations of the short-wavelength instability performed in the present study. The method used in chapter 6 lacks the obvious relation to the Orr-Sommerfeld equations, but has a simpler structure.

2.7 Orr-Sommerfeld equations in cylinder coordinates

The generalized eigenvalue system governing the linear dynamics of perturbations on a single Lamb-Oseen vortex located in a plain strain field is derived in this section. The effect of strain on the flow field in planes perpendicular to the vortex axis was discussed in section 2.5. In this section, the base flow is written as:

$$\begin{aligned} u_r &= U(r, \theta) = \epsilon \frac{f}{r} \sin(2\theta) \\ u_\theta &= V(r, \theta) = r\Omega(r) + \epsilon \frac{1}{2} \frac{df}{dr} \cos(2\theta) \\ u_z &= W(r, \theta) = 0 \end{aligned} \quad (2.105)$$

where ϵ denotes the rate of strain and $f(r)$ the strain function, governed by equation (2.95) and shown in figure 2.31 for a Lamb-Oseen vortex. The three-dimensional Navier-Stokes equations in cylinder coordinates for an incompressible flow are (as given in White (1974)):

$$\begin{aligned} \frac{\partial u_r}{\partial t} + u_r \frac{\partial u_r}{\partial r} + \frac{u_\theta}{r} \frac{\partial u_r}{\partial \theta} + u_z \frac{\partial u_r}{\partial z} - \frac{u_\theta^2}{r} = \\ - \frac{\partial p}{\partial r} + \nu \left\{ \Delta_r u_r - \frac{u_r}{r^2} - \frac{2}{r^2} \frac{\partial u_\theta}{\partial \theta} \right\} \end{aligned} \quad (2.106)$$

$$\begin{aligned} \frac{\partial u_\theta}{\partial t} + u_r \frac{\partial u_\theta}{\partial r} + \frac{u_\theta}{r} \frac{\partial u_\theta}{\partial \theta} + u_z \frac{\partial u_\theta}{\partial z} + \frac{u_r u_\theta}{r} = \\ - \frac{1}{r} \frac{\partial p}{\partial \theta} + \nu \left\{ \Delta_r u_\theta - \frac{u_\theta}{r^2} + \frac{2}{r^2} \frac{\partial u_r}{\partial \theta} \right\} \end{aligned} \quad (2.107)$$

$$\frac{\partial u_z}{\partial t} + u_r \frac{\partial u_z}{\partial r} + \frac{u_\theta}{r} \frac{\partial u_z}{\partial \theta} + u_z \frac{\partial u_z}{\partial z} = -\frac{\partial p}{\partial z} + \nu \Delta_r u_z \quad (2.108)$$

$$\frac{1}{r} \frac{\partial r u_r}{\partial r} + \frac{1}{r} \frac{\partial u_\theta}{\partial \theta} + \frac{\partial u_z}{\partial z} = 0 \quad (2.109)$$

with Δ_r denoting the Laplace operator in a cylindrical coordinate system:

$$\Delta_r = \frac{\partial^2}{\partial r^2} + \frac{1}{r} \frac{\partial}{\partial r} + \frac{1}{r^2} \frac{\partial^2}{\partial \theta^2} + \frac{\partial^2}{\partial z^2} \quad (2.110)$$

Equations (2.106), (2.107) and (2.108) are the momentum equations in the three coordinate directions and (2.109) is the continuity equation.

The next step in the derivation of the eigenvalue problem is the introduction of small three-dimensional perturbations on the two-dimensional flow field given by relations (2.105). These perturbations are assumed to be periodic in the z -coordinate direction and have an exponential time-dependence. This gives:

$$\begin{aligned} u_r(r, \theta, z) &= U(r, \theta) + \hat{u}_r(r, \theta) e^{\sigma t} e^{ikz} \\ u_\theta(r, \theta, z) &= V(r, \theta) + \hat{u}_\theta(r, \theta) e^{\sigma t} e^{ikz} \\ u_z(r, \theta, z) &= 0 + \hat{u}_z(r, \theta) e^{\sigma t} e^{ikz} \\ p/\rho(r, \theta, z) &= P(r, \theta) + \hat{p}(r, \theta) e^{\sigma t} e^{ikz} \end{aligned} \quad (2.111)$$

where $P(r, \theta)$ is the pressure of two-dimensional flow field given by the velocity components (2.105). In equation (2.111), k is the wave number in the periodic z -coordinate direction and σ is the exponential growth-rate of the perturbations.

Introducing expansion (2.111) into the momentum equations (2.106), (2.107) and (2.108) and assuming that viscous effects can be neglected leads to

$$\sigma \hat{u}_r + U \frac{\partial \hat{u}_r}{\partial r} + \hat{u}_r \frac{\partial U}{\partial r} + \frac{V}{r} \frac{\partial \hat{u}_r}{\partial \theta} + \frac{\hat{u}_r}{r} \frac{\partial U}{\partial \theta} - 2 \frac{V \hat{u}_\theta}{r} = -\frac{\partial \hat{p}}{\partial r} \quad (2.112)$$

$$\sigma \hat{u}_\theta + U \frac{\partial \hat{u}_\theta}{\partial r} + \hat{u}_r \frac{\partial V}{\partial r} + \frac{V}{r} \frac{\partial \hat{u}_\theta}{\partial \theta} + \frac{\hat{u}_r}{r} \frac{\partial V}{\partial \theta} + \frac{U \hat{u}_\theta}{r} + \frac{V \hat{u}_r}{r} = -\frac{1}{r} \frac{\partial \hat{p}}{\partial \theta} \quad (2.113)$$

$$\sigma \hat{u}_z + U \frac{\partial \hat{u}_z}{\partial r} + \frac{V}{r} \frac{\partial \hat{u}_z}{\partial \theta} = -ik \hat{p} \quad (2.114)$$

$$\frac{\partial \hat{u}_r}{\partial r} + \frac{\hat{u}_r}{r} + \frac{1}{r} \frac{\partial \hat{u}_\theta}{\partial \theta} + ik \hat{u}_z = 0 \quad (2.115)$$

Using the continuity equation (2.115), it can be seen that \hat{u}_z can be written in terms of the velocity components \hat{u}_r and \hat{u}_θ as:

$$\hat{u}_z = \frac{i}{k} \left\{ \frac{\partial \hat{u}_r}{\partial r} + \frac{\hat{u}_r}{r} + \frac{1}{r} \frac{\partial \hat{u}_\theta}{\partial \theta} \right\} \quad (2.116)$$

Substitution of expression (2.116) in the momentum equation (2.114) gives

$$\begin{aligned} -k^2 \hat{p} &= \sigma \left\{ \frac{\partial \hat{u}_r}{\partial r} + \frac{\hat{u}_r}{r} + \frac{1}{r} \frac{\partial \hat{u}_\theta}{\partial \theta} \right\} + U \frac{\partial}{\partial r} \left\{ \frac{\partial \hat{u}_r}{\partial r} + \frac{\hat{u}_r}{r} + \frac{1}{r} \frac{\partial \hat{u}_\theta}{\partial \theta} \right\} + \\ &\quad \frac{V}{r} \frac{\partial}{\partial \theta} \left\{ \frac{\partial \hat{u}_r}{\partial r} + \frac{\hat{u}_r}{r} + \frac{1}{r} \frac{\partial \hat{u}_\theta}{\partial \theta} \right\} \end{aligned} \quad (2.117)$$

which can be rewritten as

$$\begin{aligned} -k^2 \hat{p} = & \left[\sigma \left(\frac{\partial}{\partial r} + \frac{1}{r} \right) + U \frac{\partial}{\partial r} \left(\frac{\partial}{\partial r} + \frac{1}{r} \right) + \frac{V}{r} \frac{\partial^2}{\partial r \partial \theta} + \frac{V}{r^2} \frac{\partial}{\partial \theta} \right] \hat{u}_r + \\ & \left[\frac{\sigma}{r} \frac{\partial}{\partial \theta} + U \frac{\partial}{\partial r} \left(\frac{1}{r} \frac{\partial}{\partial \theta} \right) + \frac{V}{r^2} \frac{\partial^2}{\partial \theta^2} \right] \hat{u}_\theta \end{aligned} \quad (2.118)$$

With expression (2.118), the pressure terms in the momentum equations (2.112) and (2.113) can be written as:

$$\begin{aligned} -k^2 \frac{\partial \hat{p}}{\partial r} = & \left[\sigma \frac{\partial}{\partial r} \left(\frac{\partial}{\partial r} + \frac{1}{r} \right) + \frac{\partial U}{\partial r} \frac{\partial}{\partial r} \left(\frac{\partial}{\partial r} + \frac{1}{r} \right) + U \frac{\partial}{\partial r} \left(\frac{\partial}{\partial r} \left(\frac{\partial}{\partial r} + \frac{1}{r} \right) \right) + \right. \\ & \left. \frac{1}{r} \frac{\partial V}{\partial r} \frac{\partial^2}{\partial r \partial \theta} + \frac{V}{r} \frac{\partial^3}{\partial r^2 \partial \theta} + \left(\frac{1}{r^2} \frac{\partial V}{\partial r} - 2 \frac{V}{r^3} \right) \frac{\partial}{\partial \theta} \right] \hat{u}_r + \\ & \left[\sigma \frac{\partial}{\partial r} \left(\frac{1}{r} \frac{\partial}{\partial \theta} \right) + \frac{\partial U}{\partial r} \frac{\partial}{\partial r} \left(\frac{1}{r} \frac{\partial}{\partial \theta} \right) + U \frac{\partial}{\partial r} \left(\frac{\partial}{\partial r} \left(\frac{1}{r} \frac{\partial}{\partial \theta} \right) \right) + \right. \\ & \left. \left(\frac{1}{r^2} \frac{\partial V}{\partial r} - 2 \frac{V}{r^3} \right) \frac{\partial^2}{\partial \theta^2} + \frac{V}{r^2} \frac{\partial^3}{\partial r \partial \theta^2} \right] \hat{u}_\theta \end{aligned} \quad (2.119)$$

and

$$\begin{aligned} -k^2 \frac{\partial \hat{p}}{\partial \theta} = & \left[\sigma \frac{\partial}{\partial \theta} \left(\frac{\partial}{\partial r} + \frac{1}{r} \right) + \frac{\partial U}{\partial \theta} \frac{\partial}{\partial r} \left(\frac{\partial}{\partial r} + \frac{1}{r} \right) + U \frac{\partial}{\partial \theta} \left(\frac{\partial}{\partial r} \left(\frac{\partial}{\partial r} + \frac{1}{r} \right) \right) + \right. \\ & \left. \frac{1}{r} \frac{\partial V}{\partial \theta} \frac{\partial^2}{\partial r \partial \theta} + \frac{V}{r} \frac{\partial^3}{\partial r \partial \theta^2} + \frac{1}{r^2} \frac{\partial V}{\partial \theta} \frac{\partial}{\partial \theta} + \frac{V}{r^2} \frac{\partial^2}{\partial \theta^2} \right] \hat{u}_r + \\ & \left[\frac{\sigma}{r} \frac{\partial^2}{\partial \theta^2} + \frac{\partial U}{\partial \theta} \frac{\partial}{\partial r} \left(\frac{1}{r} \frac{\partial}{\partial \theta} \right) + U \frac{\partial}{\partial \theta} \left(\frac{\partial}{\partial r} \left(\frac{1}{r} \frac{\partial}{\partial \theta} \right) \right) + \frac{1}{r^2} \frac{\partial V}{\partial \theta} \frac{\partial^2}{\partial \theta^2} + \frac{V}{r^2} \frac{\partial^3}{\partial \theta^3} \right] \hat{u}_\theta \end{aligned} \quad (2.120)$$

Using these expressions in the momentum equations (2.112) and (2.113), the following generalized eigenvalue system can be obtained

$$\left[\sigma \begin{pmatrix} A_{11} & A_{12} \\ A_{21} & A_{22} \end{pmatrix} + \begin{pmatrix} B_{11} & B_{12} \\ B_{21} & B_{22} \end{pmatrix} \right] \begin{pmatrix} \hat{u}_r \\ \hat{u}_\theta \end{pmatrix} = 0 \quad (2.121)$$

where

$$A_{11} = \frac{\partial}{\partial r} \left(\frac{\partial}{\partial r} + \frac{1}{r} \right) - k^2 \quad (2.122)$$

$$A_{12} = \frac{\partial}{\partial r} \left(\frac{1}{r} \frac{\partial}{\partial \theta} \right) \quad (2.123)$$

$$A_{21} = \frac{1}{r} \frac{\partial}{\partial \theta} \left(\frac{\partial}{\partial r} + \frac{1}{r} \right) \quad (2.124)$$

$$A_{22} = \frac{1}{r^2} \frac{\partial^2}{\partial \theta^2} - k^2 \quad (2.125)$$

and

$$B_{11} = \frac{\partial U}{\partial r} \frac{\partial}{\partial r} \left(\frac{\partial}{\partial r} + \frac{1}{r} \right) + U \frac{\partial}{\partial r} \left(\frac{\partial}{\partial r} \left(\frac{\partial}{\partial r} + \frac{1}{r} \right) \right) + \frac{1}{r} \frac{\partial V}{\partial r} \frac{\partial^2}{\partial r \partial \theta} + \frac{V}{r} \frac{\partial^3}{\partial r^2 \partial \theta} + \left(\frac{1}{r^2} \frac{\partial V}{\partial r} - 2 \frac{V}{r^3} \right) \frac{\partial}{\partial \theta} - k^2 \left(U \frac{\partial}{\partial r} + \frac{\partial U}{\partial r} + \frac{V}{r} \frac{\partial}{\partial \theta} \right) \quad (2.126)$$

$$B_{12} = \frac{\partial U}{\partial r} \frac{\partial}{\partial r} \left(\frac{1}{r} \frac{\partial}{\partial \theta} \right) + U \frac{\partial}{\partial r} \left(\frac{\partial}{\partial r} \left(\frac{1}{r} \frac{\partial}{\partial \theta} \right) \right) + \left(\frac{1}{r^2} \frac{\partial V}{\partial r} - 2 \frac{V}{r^3} \right) \frac{\partial^2}{\partial \theta^2} + \frac{V}{r^2} \frac{\partial^3}{\partial r \partial \theta^2} - k^2 \left(\frac{1}{r} \frac{\partial U}{\partial \theta} - 2 \frac{V}{r} \right) \quad (2.127)$$

$$B_{21} = \frac{1}{r} \frac{\partial U}{\partial \theta} \frac{\partial}{\partial r} \left(\frac{\partial}{\partial r} + \frac{1}{r} \right) + \frac{U}{r} \frac{\partial}{\partial \theta} \left(\frac{\partial}{\partial r} \left(\frac{\partial}{\partial r} + \frac{1}{r} \right) \right) + \frac{1}{r^2} \frac{\partial V}{\partial \theta} \frac{\partial^2}{\partial r \partial \theta} + \frac{V}{r^2} \frac{\partial^3}{\partial r \partial \theta^2} + \frac{1}{r^3} \frac{\partial V}{\partial \theta} \frac{\partial}{\partial \theta} + \frac{V}{r^3} \frac{\partial^2}{\partial \theta^2} - k^2 \left(\frac{\partial V}{\partial r} + \frac{V}{r} \right) \quad (2.128)$$

$$B_{22} = \frac{1}{r} \frac{\partial U}{\partial \theta} \frac{\partial}{\partial r} \left(\frac{1}{r} \frac{\partial}{\partial \theta} \right) + \frac{U}{r} \frac{\partial}{\partial \theta} \left(\frac{\partial}{\partial r} \left(\frac{1}{r} \frac{\partial}{\partial \theta} \right) \right) + \frac{1}{r^3} \frac{\partial V}{\partial \theta} \frac{\partial^2}{\partial \theta^2} + \frac{V}{r^3} \frac{\partial^3}{\partial \theta^3} - k^2 \left(U \frac{\partial}{\partial r} + \frac{V}{r} \frac{\partial}{\partial \theta} + \frac{1}{r} \frac{\partial V}{\partial \theta} + \frac{U}{r} \right) \quad (2.129)$$

The velocity components U and V of the two-dimensional base flow were defined in equations (2.105) as an expansion in terms of the strain ϵ up to first order. From relations (2.105), it can be derived that

$$\frac{\partial U}{\partial r} = \epsilon \left(\frac{1}{r} \frac{df}{dr} - \frac{f}{r^2} \right) \sin(2\theta) \quad (2.130)$$

$$\frac{\partial U}{\partial \theta} = 2\epsilon \frac{f}{r} \cos(2\theta) \quad (2.131)$$

$$\frac{\partial V}{\partial r} = \Omega + r \frac{d\Omega}{dr} + \frac{\epsilon}{2} \frac{d^2 f}{dr^2} \cos(2\theta) \quad (2.132)$$

$$\frac{\partial V}{\partial \theta} = -\epsilon \frac{df}{dr} \sin(2\theta) \quad (2.133)$$

The coefficients B_{11} to B_{22} can therefore be written as a combination of the contribution for the unstrained situation and a contribution representing the effect of the strain on the base flow. Generalized eigenvalue problem (2.121) can be rewritten as:

$$\left[\sigma \begin{pmatrix} A_{11} & A_{12} \\ A_{21} & A_{22} \end{pmatrix} + \begin{pmatrix} B_{11}^{(0)} & B_{12}^{(0)} \\ B_{21}^{(0)} & B_{22}^{(0)} \end{pmatrix} + \epsilon \begin{pmatrix} B_{11}^{(\epsilon)} & B_{12}^{(\epsilon)} \\ B_{21}^{(\epsilon)} & B_{22}^{(\epsilon)} \end{pmatrix} \right] \begin{pmatrix} \hat{u}_r \\ \hat{u}_\theta \end{pmatrix} = 0 \quad (2.134)$$

With coefficients A_{11} , A_{12} , A_{21} and A_{22} identical to those of formulation (2.121). The coefficients for the unstrained situation are given by:

$$B_{11}^{(0)} = \Omega \frac{\partial^3}{\partial r^2 \partial \theta} + \left(\frac{d\Omega}{dr} + \frac{\Omega}{r} \right) \frac{\partial^2}{\partial r \partial \theta} + \left(\frac{1}{r} \frac{d\Omega}{dr} - \frac{\Omega}{r^2} - \Omega k^2 \right) \frac{\partial}{\partial \theta} \quad (2.135)$$

$$B_{12}^{(0)} = \left(\frac{1}{r} \frac{d\Omega}{dr} - \frac{\Omega}{r^2} \right) \frac{\partial^2}{\partial \theta^2} + \frac{\Omega}{r} \frac{\partial^3}{\partial r \partial \theta^2} + 2\Omega k^2 \quad (2.136)$$

$$B_{21}^{(0)} = \frac{\Omega}{r} \frac{\partial^3}{\partial r \partial \theta^2} + \frac{\Omega}{r^2} \frac{\partial^2}{\partial \theta^2} - k^2 \left(2\Omega + r \frac{d\Omega}{dr} \right) \quad (2.137)$$

$$B_{22}^{(0)} = \frac{\Omega}{r^2} \frac{\partial^3}{\partial \theta^3} - k^2 \Omega \frac{\partial}{\partial \theta} \quad (2.138)$$

The matrix elements representing the effect of strain are given by:

$$\begin{aligned}
 B_{11}^{(\epsilon)} = & \sin(2\theta) \left[\left(\frac{1}{r} \frac{df}{dr} - \frac{f}{r^2} \right) \frac{\partial}{\partial r} \left(\frac{\partial}{\partial r} + \frac{1}{r} \right) + \frac{f}{r} \frac{\partial}{\partial r} \left(\frac{\partial}{\partial r} \left(\frac{\partial}{\partial r} + \frac{1}{r} \right) \right) - \right. \\
 & \left. k^2 \left(\frac{f}{r} \frac{\partial}{\partial r} + \frac{1}{r} \frac{df}{dr} - \frac{f}{r^2} \right) \right] + \\
 & \cos(2\theta) \left[\frac{1}{2r} \frac{d^2 f}{dr^2} \frac{\partial^2}{\partial r \partial \theta} + \frac{1}{2r} \frac{df}{dr} \frac{\partial^3}{\partial r^2 \partial \theta} + \left(\frac{1}{2r^2} \frac{d^2 f}{dr^2} - \frac{1}{r^3} \frac{df}{dr} \right) \frac{\partial}{\partial \theta} - \right. \\
 & \left. k^2 \frac{1}{2r} \frac{df}{dr} \frac{\partial}{\partial \theta} \right] \quad (2.139)
 \end{aligned}$$

$$\begin{aligned}
 B_{12}^{(\epsilon)} = & \sin(2\theta) \left[\left(\frac{1}{r} \frac{df}{dr} - \frac{f}{r^2} \right) \frac{\partial}{\partial r} \left(\frac{1}{r} \frac{\partial}{\partial \theta} \right) + \frac{f}{r} \frac{\partial}{\partial r} \left(\frac{\partial}{\partial r} \left(\frac{1}{r} \frac{\partial}{\partial \theta} \right) \right) \right] + \\
 & \cos(2\theta) \left[\left(\frac{1}{2r^2} \frac{d^2 f}{dr^2} - \frac{1}{r^3} \frac{df}{dr} \right) \frac{\partial^2}{\partial \theta^2} + \frac{1}{2r^2} \frac{df}{dr} \frac{\partial^3}{\partial r \partial \theta^2} - 2k^2 \left(\frac{f}{r^2} - \frac{1}{r} \frac{df}{dr} \right) \right] \quad (2.140)
 \end{aligned}$$

$$\begin{aligned}
 B_{21}^{(\epsilon)} = & \sin(2\theta) \left[\frac{f}{r^2} \frac{\partial}{\partial \theta} \left(\frac{\partial}{\partial r} \left(\frac{\partial}{\partial r} + \frac{1}{r} \right) \right) - \frac{1}{r^2} \frac{df}{dr} \frac{\partial^2}{\partial r \partial \theta} - \frac{1}{r^3} \frac{df}{dr} \frac{\partial}{\partial \theta} \right] + \\
 & \cos(2\theta) \left[2 \frac{f}{r^2} \frac{\partial}{\partial r} \left(\frac{\partial}{\partial r} + \frac{1}{r} \right) + \frac{1}{2r^3} \frac{df}{dr} \frac{\partial^2}{\partial \theta^2} - k^2 \left(\frac{1}{2} \frac{d^2 f}{dr^2} + \frac{1}{2r} \frac{df}{dr} \right) \right] \quad (2.141)
 \end{aligned}$$

$$\begin{aligned}
 B_{22}^{(\epsilon)} = & \sin(2\theta) \left[\frac{f}{r^2} \frac{\partial}{\partial \theta} \left(\frac{\partial}{\partial r} \left(\frac{1}{r} \frac{\partial}{\partial \theta} \right) \right) - \frac{1}{r^3} \frac{df}{dr} \frac{\partial^2}{\partial \theta^2} - k^2 \left(\frac{f}{r} \frac{\partial}{\partial r} - \frac{1}{r} \frac{df}{dr} + \frac{f}{r^2} \right) \right] + \\
 & \cos(2\theta) \left[2 \frac{f}{r^2} \frac{\partial}{\partial r} \left(\frac{1}{r} \frac{\partial}{\partial \theta} \right) + \frac{1}{2r^3} \frac{df}{dr} \frac{\partial^3}{\partial \theta^3} - k^2 \frac{1}{2r} \frac{df}{dr} \frac{\partial}{\partial \theta} \right] \quad (2.142)
 \end{aligned}$$

Generalized eigenvalue system (2.134) can be used as the basis of a computational method for Kelvin modes. In such a method, neutrally stable helical modes on an unstrained vortex are sought for, leading to a great reduction of complexity of the eigenvalue system. The Kelvin modes are computed from a normal mode analysis of the remaining equations. This computational method based on the Orr-Sommerfeld equations in cylinder coordinates is discussed in section 2.7.1. In section 2.7.2, a computational method is derived for the determination of the growth rate of short-wavelength instability modes, which are assumed to originate from the resonance of two Kelvin modes with the imposed strain field. This method uses previously computed Kelvin modes for specific azimuthal and axial wave numbers as input data. These Kelvin modes can be computed using either the method described in section 2.7.1 or the method of chapter 6.

2.7.1 Kelvin modes computation from Orr-Sommerfeld equation

The generalized eigenvalue problem (2.134) can be used as basis for a computational method for Kelvin modes. With a vanishing growth-rate σ and an azimuthal dependence of the linear perturbations as in equation (2.101), equation (2.134) reduces to

$$\begin{pmatrix} B_{11} & B_{12} \\ B_{21} & B_{22} \end{pmatrix} \begin{pmatrix} \tilde{u}_r \\ \tilde{u}_\theta \end{pmatrix} = 0 \quad (2.143)$$

with the coefficients B_{11}, \dots, B_{22} given by

$$\begin{aligned} B_{11} &= im \left[\Omega \left(\frac{\partial^2}{\partial r^2} + \frac{1}{r} \frac{\partial}{\partial r} - \frac{1}{r^2} - k^2 \right) + \frac{d\Omega}{dr} \left(\frac{\partial}{\partial r} + \frac{1}{r} \right) \right] \\ B_{12} &= -m^2 \left[\frac{\Omega}{r} \frac{\partial}{\partial r} + \left(\frac{1}{r} \frac{d\Omega}{dr} - \frac{\Omega}{r^2} \right) \right] + 2\Omega k^2 \\ B_{21} &= -m^2 \left[\frac{\Omega}{r} \frac{\partial}{\partial r} + \frac{\Omega}{r^2} \right] - k^2 \left(2\Omega + r \frac{d\Omega}{dr} \right) \\ B_{22} &= -im \left(\frac{m^2}{r^2} + k^2 \right) \Omega \end{aligned} \quad (2.144)$$

From system (2.143) with coefficients (2.144) and equations (2.116) and (2.118), it can be seen that the flow field perturbations for azimuthal wavenumbers $m = -1$ and $m = +1$ have the following form

$$\begin{bmatrix} \tilde{u}_r \\ \tilde{u}_\theta \\ \tilde{u}_z \\ \tilde{p} \end{bmatrix}_{m=-1} = \begin{bmatrix} iu_{\pm 1} \\ v_{\pm 1} \\ w_{\pm 1} \\ p_{\pm 1} \end{bmatrix} \quad \text{and} \quad \begin{bmatrix} \tilde{u}_r \\ \tilde{u}_\theta \\ \tilde{u}_z \\ \tilde{p} \end{bmatrix}_{m=+1} = \begin{bmatrix} -iu_{\pm 1} \\ v_{\pm 1} \\ -w_{\pm 1} \\ p_{\pm 1} \end{bmatrix} \quad (2.145)$$

with $u_{\pm 1}, v_{\pm 1}, w_{\pm 1}$ and $p_{\pm 1}$ real functions of r .

For $m = -1$, the system of equations for $u_{\pm 1}, v_{\pm 1}$ becomes

$$\begin{bmatrix} \Omega \left(\frac{\partial^2}{\partial r^2} + \frac{1}{r} \frac{\partial}{\partial r} - \frac{1}{r^2} - k^2 \right) + \frac{d\Omega}{dr} \left(\frac{\partial}{\partial r} + \frac{1}{r} \right) & -\Omega \left(\frac{1}{r} \frac{\partial}{\partial r} - \frac{1}{r^2} \right) - \frac{1}{r} \frac{d\Omega}{dr} + 2\Omega k^2 \\ -\Omega \left(\frac{1}{r} \frac{\partial}{\partial r} + \frac{1}{r^2} \right) - k^2 \left(2\Omega + r \frac{d\Omega}{dr} \right) & \left(\frac{1}{r^2} + k^2 \right) \Omega \end{bmatrix} \begin{bmatrix} u_{\pm 1} \\ v_{\pm 1} \end{bmatrix} = 0 \quad (2.146)$$

The pressure perturbation $p_{\pm 1}$ in equation (2.145) is governed by a second order differential equation that is derived in section 6.1.2. A detailed analysis of the behaviour of this equation in the vicinity of the vortex axis $r = 0$ shows that

$$\begin{aligned} \frac{\partial p_{\pm 1}}{\partial r}(0) &= 1 \\ u_{\pm 1}(0) &= -m \end{aligned} \quad (2.147)$$

for $|m| = 1$, see equation (6.25) of section 6.1.2. Furthermore, the perturbations are assumed to vanish for $r \rightarrow \infty$. Kelvin modes can be computed from system of equations (2.146) by searching for axial wavenumbers k for which non-trivial solutions exist. Homogeneous system of equations (2.146) has non-trivial solutions for wavenumbers k which lead to a singular discretization matrix. This computational method is not pursued here. Instead, an equivalent method is used that is described in detail in section 6.1, based on a discretization of the linearized Euler equations in cylinder coordinates using a Chebyshev collocation method.

2.7.2 Computation of growth rate of short-wavelength instability

From the generalized eigenvalue problem (2.134), the most unstable short-wavelength instability modes can be found by discretization and subsequent solution of the eigenvalue problem for a wide range of axial wave numbers k . This would be a computationally expensive procedure since the discretized problem will involve large non-sparse matrices. The computation of a matrix-eigenvalue problem for a non-symmetric matrix can be performed using the QZ method, see for example Golub and van Loan (1996). A common problem that occurs in the computation of large matrix-eigenvalue problems, is the occurrence of spurious modes. Spurious modes are the result of round-off errors and are difficult to separate from correctly computed eigen vectors.

Therefore, a computational method for the growth rate of the short-wavelength instability which does not involve the solution of a large matrix-eigenvalue is of practical relevance and is studied here. The basis of the method is the assumption that short-wavelength instability modes are a manifestation of the interaction of two stationary Kelvin modes with azimuthal wave number $|m| = 1$ with the imposed strain field. With this assumption, the growth rate can be computed from

$$\left[\sigma/\epsilon \begin{pmatrix} A_{11} & A_{12} \\ A_{21} & A_{22} \end{pmatrix} + \begin{pmatrix} B_{11}^{(\epsilon)} & B_{12}^{(\epsilon)} \\ B_{21}^{(\epsilon)} & B_{22}^{(\epsilon)} \end{pmatrix} \right] \begin{pmatrix} \hat{u}_r \\ \hat{u}_\theta \end{pmatrix} = 0 \quad (2.148)$$

with the coefficients A_{11}, \dots, A_{22} given by equations (2.122) to (2.125) and the coefficients $B_{11}^{(\epsilon)}, \dots, B_{22}^{(\epsilon)}$ by equations (2.139) to (2.142).

In case $[\hat{u}_r, \hat{u}_\theta]$ is a normal mode computed using either the method discussed in the previous section or the method of chapter 6, the growth rate of the short-wavelength instability can be directly computed from equation (2.148). A notable feature of equation (2.148) is that the growth rate scales linearly with the imposed strain rate ϵ . Another interesting property is the absence of $\Omega(r)$ from both the coefficients A_{11}, \dots, A_{22} and $B_{11}^{(\epsilon)}, \dots, B_{22}^{(\epsilon)}$. The details of the velocity profile of the vortex enter the problem by the dependence of strain function $f(r)$ on the type of vortex considered. For the Lamb-Oseen vortex, function $f(r)$ was computed in section 2.5.

DESCRIPTION OF NUMERICAL METHODS

3 Chapter

This chapter describes the numerical methods used in the present study for the time-accurate three-dimensional incompressible flow simulations based on the Navier-Stokes equations. The flows considered here, dominated by the presence of an interacting vortex pair, are characterized by maximum velocity magnitudes small enough to justify the incompressibility assumption. The temporal evolution of three-dimensional instabilities in the vortical flows is of particular interest here. Therefore, a time-accurate temporal integration method needs to be used. The Navier-Stokes equations for the incompressible flow of a Newtonian medium are discussed in section 3.1 as well as a number of possible temporal integration methods. The time-advancement technique used in the present numerical methods, is described in detail in section 3.2.

For the three-dimensional time-accurate flow simulations, two different methods have been developed. The two methods use compact finite-difference methods for the spatial discretization. Compact finite-difference methods are finite-difference discretization methods with a higher-order accuracy than more conventional finite-difference methods for a given stencil width. The discretization methods used in the two Navier-Stokes simulation tools are described in detail in chapter 4. Both Navier-Stokes methods use the time-advancement technique described in section 3.2, which results in a system of Helmholtz equations for updated velocity components and a Poisson equation for a pressure-like variable. The two methods are different in the way these Helmholtz and Poisson equations are discretized and solved:

- The first method is a parallel method based on a novel three-dimensional compact finite-difference discretization method for the 3D Helmholtz and Poisson equations. The stencil used for the discretization of the Laplace operator is derived in section 4.5 and the resulting fourth-order accurate solution method in section 4.7. In this solution method, sparse linear systems of equations are solved using iterative solution techniques described in section 3.7.

The method has been developed to enable parallel simulations on multi-processor machines. The parallelization of this method is based on a decomposition of the computational domain in sub-domains in one coordinate direction. A brief introduction of parallelization techniques is presented in section 3.4.

This Navier-Stokes method is described in detail in section 3.5 of this chapter and is referred to as the *parallel method* in the present study;

- The second method solves the Navier-Stokes equations in three dimensions exploiting the assumed periodicity of the flow field in one spatial direction. In this study, this
-

periodic direction coincides with the axial direction of the vortex pair.

The periodicity allows for an expansion of the flow field in terms of a Fourier series expansion. This Fourier expansion is used in the solution method for the Helmholtz and Poisson equations, leading to decoupled Helmholtz equations in two-dimensional space for each of the wave numbers in the periodic direction. For the solution of these 2D Helmholtz equations, a fast direct solver is used that is described in section 4.6. It follows the method presented in Sun and Zhuang (1997). This solver is based on a two-dimensional compact stencil of fourth-order accuracy, derived in section 4.4.

This Navier-Stokes method is described in detail in section 3.6 of this chapter and is referred to as the *hybrid method* or *hybrid Fourier collocation / compact finite-difference method* in the present study.

The Navier-Stokes equations for incompressible three-dimensional flow and various temporal integration techniques for these equations are described in section 3.1. The temporal integration method used in the present study is then described in more detail in section 3.2. Section 3.3 describes spatial filter operations that are implemented in the two Navier-Stokes methods. These low-pass filters enhance the numerical stability of the methods by damping under-resolved modes from the simulated flow field. Then, an introduction in parallelization techniques for numerical methods is presented in section 3.4. This section reviews the various parallel programming techniques and motivates the choice of the programming model that is used in the parallel Navier-Stokes method. This parallel Navier-Stokes method is described in detail in section 3.5. Next, the hybrid Fourier collocation / compact finite-difference Navier-Stokes method is described in detail in section 3.6. Finally, iterative solution techniques for linear systems of equations are discussed in section 3.7. This section describes the Conjugate Gradient type of solution methods, that are used in the parallel Navier-Stokes method.

3.1 Temporal integration of Navier-Stokes equations for incompressible flows

The Navier-Stokes equations for the incompressible flow of a Newtonian medium in Cartesian coordinates are given by

$$\frac{\partial u}{\partial t} + u \frac{\partial u}{\partial x} + v \frac{\partial u}{\partial y} + w \frac{\partial u}{\partial z} = -\frac{1}{\rho} \frac{\partial p}{\partial x} + \nu \Delta u \quad (3.1)$$

$$\frac{\partial v}{\partial t} + u \frac{\partial v}{\partial x} + v \frac{\partial v}{\partial y} + w \frac{\partial v}{\partial z} = -\frac{1}{\rho} \frac{\partial p}{\partial y} + \nu \Delta v \quad (3.2)$$

$$\frac{\partial w}{\partial t} + u \frac{\partial w}{\partial x} + v \frac{\partial w}{\partial y} + w \frac{\partial w}{\partial z} = -\frac{1}{\rho} \frac{\partial p}{\partial z} + \nu \Delta w \quad (3.3)$$

$$\frac{\partial u}{\partial x} + \frac{\partial v}{\partial y} + \frac{\partial w}{\partial z} = 0 \quad (3.4)$$

where (u, v, w) denote the components of the velocity in the three coordinate directions, p is the pressure, ρ the (constant) density and ν the (constant) kinematic viscosity of the medium. Relation (3.4) is the divergence-free constraint on the velocity field, as a result of the incompressibility of the flow. In the remainder of this chapter p will denote the pressure divided by the constant density of the medium.

The complicating factor in finding solutions to the time-dependent incompressible Navier-Stokes equations is the need to satisfy the divergence-free constraint on the velocity field. A number of methods have been developed for the temporal integration of the Navier-Stokes for an incompressible flow to deal with this constraint:

- Projection methods, originally introduced by Chorin (1967). These methods utilize an auxiliary velocity field that is projected onto the divergence-free space through the solution of a Poisson equation for a quantity directly related to the pressure. Well-known variants are fractional time-stepping methods, or time-splitting methods, see for example Kim and Moin (1985);
- In two-dimensional flow simulations a method used by many researchers is the formulation in terms of the stream function ψ and the vorticity ω_z of the velocity field, defined by relation (1.1) of section 1.1. In the two-dimensional situation, the only non-vanishing component of vorticity is the component perpendicular to the 2D plane, i.e. ω_z . Using a formulation in terms of vorticity, the momentum conservation equations for the two spatial directions combine to a single scalar equation for ω_z and a Poisson equation for ψ :

$$\begin{aligned} \frac{\partial \omega_z}{\partial t} + \psi_y \frac{\partial \omega_z}{\partial x} - \psi_x \frac{\partial \omega_z}{\partial y} &= \nu \Delta \omega_z \\ \Delta \psi &= -\omega_z \end{aligned} \quad (3.5)$$

Similar to the projection methods, a Poisson equation needs to be solved at every time-step. In three-dimensional simulations, this formulation leads to a system of conservation equations for the three components of vorticity and the Poisson equation for ψ . Therefore, the advantages of this method over methods using primitive variables vanishes and another method is usually chosen;

- The Marker-and-Cell (MAC) method of Harlow and Welch (1965). This method was devised for both confined flows and flows with a free surface. The method uses pressure and velocity as primary variables, defined on a staggered mesh. Typically, a second-order accurate spatial discretization method is used in such a way that constraint (3.4) is satisfied implicitly. The pressure is computed from a Poisson equation;
- The artificial compressibility method proposed by Chorin, see Chorin (1967). This approach differs from the other methods in a number of ways. This method does not result in a Poisson equation. Instead, the flow is governed by a set of hyperbolic equations that is very similar to the set of hyperbolic equations that govern time-dependent compressible flows. The equations are obtained by introducing an artificial (finite) speed of wave propagation and an additional pseudo time-like coordinate. For simulations of steady flows this method performs satisfactory (Chorin (1967)). Time-accurate simulations require convergence of the set of hyperbolic equations at each 'physical' time step by marching in pseudo time to a 'steady' state solution. For these time-accurate simulations, the effect of artificial compressibility needs to be minimized, leading to a stiff system of equations, see Chorin (1967) and Kim and Moin (1985).

In the present study, focusing on time-dependent flows, the fractional time-stepping method due to Kim and Moin (1985) is used. This temporal integration method was studied in detail

and compared to other temporal integration methods in Canuto et al. (1987). The method is well-suited for Direct Numerical Simulations (DNS) and Large Eddy Simulations (LES) of incompressible flows. Second-order accuracy in time is obtained in simulations using this time-advancement method. The method of Kim and Moin (1985) is described in detail in section 3.2 and forms the basis for the two computational methods that have been developed.

3.2 Fractional time-stepping method

The Navier-Stokes equations for the incompressible flow of a Newtonian medium in Cartesian coordinates are integrated in time using the fractional time-stepping method due to Kim and Moin (1985). This method is second-order accurate in time. The solution of the Navier-Stokes equations is advanced from time level n to $n + 1$ in three steps:

- In the first step, the second-order explicit Adams-Bashfort method is applied to the nonlinear convection terms and the second-order implicit Crank-Nicholson scheme to the viscous terms. Implicit treatment of the viscous terms eliminates the numerical viscous stability restriction, which is particularly severe for low-Reynolds number flows, as discussed by Kim and Moin (1985).
Omitting the pressure term from the momentum equations, for each coordinate direction i , an intermediate velocity field with component v_i can be obtained from:

$$v_i - u_i^n = -\delta t \left(\frac{3}{2} H_i^n - \frac{1}{2} H_i^{n-1} \right) + \frac{\nu \delta t}{2} (\Delta v_i + \Delta u_i^n) \quad (3.6)$$

where δt denotes the time-step, ν the (constant) kinematic viscosity and H_i^n the nonlinear convection terms at time-level n .

Equation (3.6) can be rewritten as a Helmholtz equation

$$\left(1 - \frac{\nu \delta t}{2} \Delta \right) v_i = -\delta t \left(\frac{3}{2} H_i^n - \frac{1}{2} H_i^{n-1} \right) + \left(1 + \frac{\nu \delta t}{2} \Delta \right) u_i^n \quad (3.7)$$

In a three-dimensional situation, equation (3.7) corresponds to a system of three independent Helmholtz equations. Since, equation (3.6) was obtained from the momentum equations by omitting the pressure term, the intermediate velocity field with components v_i will not be divergence-free;

- The next step in the temporal integration is the computation of a pressure-like variable from the intermediate velocity field. Quantity ϕ , defined as $p = \phi + (\nu \delta t / 2) \Delta \phi$ (here, p is the pressure divided by the constant density), can be computed from the Poisson equation

$$\Delta \phi = \frac{1}{\delta t} \frac{\partial v_i}{\partial x_i} \quad (3.8)$$

where the divergence of the intermediate velocity field forms the forcing term;

- From the computed pressure-like variable ϕ , a solenoidal velocity field at the new time-level $n + 1$ is computed as

$$u_i^{n+1} = v_i - \delta t \frac{\partial \phi}{\partial x_i} \quad (3.9)$$

Equations (3.7), (3.8) and (3.9) form the basis of the two Navier-Stokes simulation methods, described in detail in sections 3.5 and 3.6.

3.3 Compact-difference low-pass filter

The compact finite-difference discretization methods used in both Navier-Stokes methods are based on symmetric stencils, usually referred to as central-differences in the context of more conventional finite-difference methods. It is well-known from literature that application of central-difference discretization techniques in numerical methods for flow simulations can lead to the formation of short wave-length oscillations in the computational domain. These oscillations are a result of growing under-resolved modes. In the present computational methods, this problem is tackled using a low-pass filter operation, applied to the flow field solution after a number of time-steps.

Another method to control the formation of these oscillations, is the introduction of an artificial viscosity term into the system of discretized equations. This artificial viscosity term usually depends on even-derivatives of the flow field and adds significant dissipation in regions of the flow field with steep gradients. This method is typically used in second-order accurate finite-volume discretizations of either the Euler or Navier-Stokes equations for a compressible flow. For higher-order accurate methods, this method can be used with a higher-order equivalent of the artificial viscosity term. However, in high-order accurate discretization methods, this approach is not widely used. Here, the filtering approach is preferred, since it allows for a more direct control of the artificial dissipation. The filter operation implemented in both Navier-Stokes methods is based on a low-pass filter defined for a one-dimensional domain. In the actual implementation, an extension to multiple spatial directions is made, as described in section 3.5 for the parallel method and section 3.6 for the hybrid method.

Here, subsection 3.3.1 describes the principles of these low-pass compact-difference filters, that were previously presented by Lele (1992). The formulation of this filter operation in the vicinity of different types of domain boundaries is discussed in subsections 3.3.2 and 3.3.3.

3.3.1 Filtering data on a one-dimensional domain

Consider a quantity f defined on a one-dimensional computational domain with uniformly spaced mesh points $x_j = j \cdot h$ with $j = 0, \dots, M$, shown in figure 3.1. On this domain, quantity f has a discrete value f_j in the mesh points x_j . Figure 3.1 shows the shortest resolvable mode on this mesh, both as cosine wave and as discrete *sawtooth* wave. This shortest resolvable mode is similarly known as *odd-even decoupling* mode. Damping this mode from the signal is one of the objectives of applying the low-pass filter.

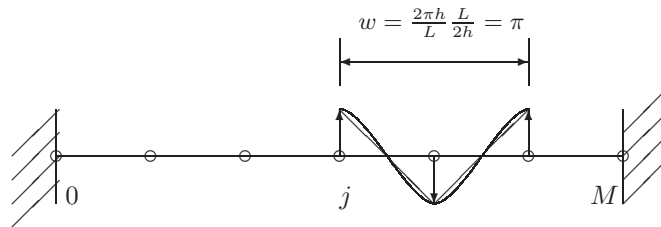


FIGURE 3.1: *Shortest resolvable wave on uniformly spaced one-dimensional domain*

Assuming periodic boundary conditions, function f can be decomposed in Fourier compo-

nents

$$f_j = \sum_{k=-\frac{M}{2}}^{\frac{M}{2}} \hat{f}_k \exp\left(\frac{2\pi i k x_j}{L}\right) \quad (3.10)$$

where L is the length of the computational domain with $M + 1$ mesh points and M is even. The function values f_j are real-valued, thus for $1 \leq k \leq \frac{M}{2}$: $\hat{f}_k = \hat{f}_{-k}^*$ and $\hat{f}_0 = \hat{f}_0^*$, where superscript $*$ denotes the complex conjugate, see Lele (1992). A scaled wave number w can be introduced, defined as

$$w = \frac{2\pi k h}{L} = \frac{2\pi k}{M} \quad (3.11)$$

which has the value π for the shortest resolvable wave with wavelength $2h$. Quantity f on the one-dimensional mesh can be filtered using an expression of the form:

$$\alpha \tilde{f}_{j-1} + \tilde{f}_j + \alpha \tilde{f}_{j+1} = \sum_{i=0}^{N/2} a_i \frac{[f_{j+i} + f_{j-i}]}{2} + O(h^N) \quad (3.12)$$

where \tilde{f}_j is the filtered value of quantity f at node x_j . Application of equation (3.12) to a function on a one-dimensional domain corresponds to applying a low-pass filter to the function, see Lele (1992). The dissipative behaviour is controlled by parameter α : the low-pass filter is more dissipative for lower values of α .

Coefficients a_i in equation (3.12) are determined by developing both left-hand and right-hand side of the equation in Taylor series expansions and equating coefficients of corresponding orders. To achieve a truncation error of $O(h^N)$, the coefficients $a_0, \dots, a_{N/2}$ need to be determined. The $N/2$ equation resulting from Taylor series matching are

$$\begin{aligned} a_0 + a_1 + a_2 + \dots + a_{\frac{N}{2}} &= 1 + 2\alpha \\ a_1 + 2^2 a_2 + \dots + \left(\frac{N}{2}\right)^2 a_{\frac{N}{2}} &= 2\alpha \\ a_1 + 2^4 a_2 + \dots + \left(\frac{N}{2}\right)^4 a_{\frac{N}{2}} &= 2\alpha \\ \vdots & \\ a_1 + 2^{N-2} a_2 + \dots + \left(\frac{N}{2}\right)^{N-2} a_{\frac{N}{2}} &= 2\alpha \end{aligned} \quad (3.13)$$

The additional equation required to determine $N/2 + 1$ coefficients a_i is derived from the constraint that the shortest resolvable mode is eliminated by application of equation (3.12). For this derivation, it is convenient to introduce the *Fourier transfer function* $T(w)$. Function $T(w)$ is the ratio of amplitudes of waves with scaled wave number w before and after filtering. For filter operation (3.12), $T(w)$ is given by

$$T(w) = \frac{a_0 + \sum_{i=1}^{N/2} a_i \cos(i w)}{1 + 2\alpha \cos(w)} \quad (3.14)$$

Equation (3.14) indicates the bounds on α : $-0.5 < \alpha < 0.5$ for a regular $T(w)$. With these bounds on α , the additional equation for a_i is derived from $T(\pi) = 0$, or

$$a_0 + \sum_{i=1}^{N/2} (-1)^i a_i = 0 \quad (3.15)$$

For 6th, 8th and 10th order accuracy the coefficients a_i are given in table 3.1. With these coefficients known, the truncation error of equation (3.12) can be analyzed. For the 6th-order accurate scheme, this truncation error is given by

$$T.E. = \frac{h^6}{32}(1 - 2\alpha)f_j^{(6)} + \frac{h^8}{128}(1 - 2\alpha)f_j^{(8)} + H.O.T \quad (3.16)$$

where $f_j^{(6)}$ and $f_j^{(8)}$ denote the 6th and 8th-derivate of quantity f in mesh point x_j , respectively. In equation (3.16), $H.O.T$ refers to the higher-order terms, which can be shown to contain even derivatives only.

Similar to the error analysis for a discretization of a linear advection equation, see for example Hirsch (1988), terms in the truncation error with even derivatives correspond to the *dissipative* behaviour and terms involving odd derivatives represent the *dispersion* error. In the context of a linear advection equation, dissipation decreases the amplitude of an advected wave, while dispersion modifies the wave propagation speed. Typically, both the change in amplitude and wave propagation speed depend on the wave length of the advected wave.

Symmetric schemes of type (3.12) are therefore dissipative and non-dispersive. Since all terms in the right-hand side of equation (3.16) can be shown to contain the factor $(1 - 2\alpha)$, the truncation error vanishes for $\alpha = 0.5$. However, from the coefficients shown in table (3.1) it can be seen that in this case, equation (3.12) reduces to an identity which leaves function f unaltered.

The dissipative and dispersive behaviour of filter schemes can similarly be analyzed using the Fourier transfer function $T(w)$. In this case, the real part of $T(w)$ corresponds to the dissipative behaviour and the imaginary part to the dispersive behaviour.

Figures 3.2 and 3.3 show the Fourier transfer function (real part only, imaginary part is equal to zero) for filter (3.12) for $\alpha = 0.0$ and $\alpha = 0.25$, respectively. The deviation of the curve from the value 1 indicates damping (dissipation) of the wave at that wave number. Figures 3.2 and 3.3 show that for a given wave number, damping increases with decreasing α and that the damping is restricted to higher wave numbers for higher α . Wave number $w = 0$ corresponds to the average of function f along the one-dimensional domain. Since $T(0) = 1$, it can be seen that this average is unchanged when applying the low-pass filter.

TABLE 3.1: Values of a_i for various orders of formal accuracy.

order	6	8	10
a_0	$\frac{11+10\alpha}{16}$	$\frac{93+70\alpha}{128}$	$\frac{193+126\alpha}{256}$
a_1	$\frac{15+34\alpha}{32}$	$\frac{7+18\alpha}{16}$	$\frac{105+302\alpha}{256}$
a_2	$\frac{-3+6\alpha}{16}$	$\frac{-7+14\alpha}{32}$	$\frac{-15+30\alpha}{64}$
a_3	$\frac{1-2\alpha}{32}$	$\frac{1-2\alpha}{16}$	$\frac{45-90\alpha}{512}$
a_4		$\frac{-1+2\alpha}{128}$	$\frac{-5+10\alpha}{256}$
a_5			$\frac{1-2\alpha}{512}$

Filter operation (3.12) with stencil width $N + 1$ for N th-order accuracy, can be applied to the nodes of the one-dimensional domain for which the stencil on the right-hand side fits within the domain. In the vicinity of the domain edges, a different treatment is necessary, depending

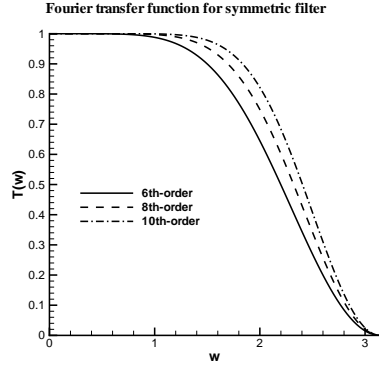


FIGURE 3.2: *Fourier transfer function for filter (3.12): $\alpha = 0.0$*

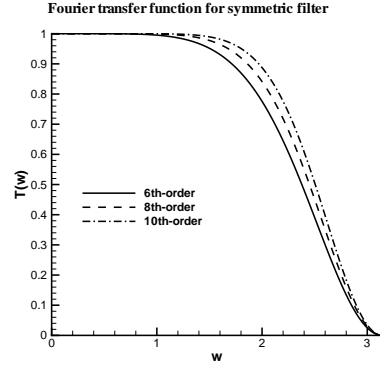


FIGURE 3.3: *Fourier transfer function for filter (3.12): $\alpha = 0.25$*

on the boundary conditions that are prescribed at the edges. The following distinction can be made

- The first situation is that depicted in figure 3.1 and the top sketch of figure 3.4, where the domain edges correspond to the end points of the computational domain and the data represented on the mesh is not periodic. This is the most common situation and will be referred to as *general non-periodic* domain boundary. For this case, the formulation of the filter operations is discussed in section 3.3.2.
- The second situation is shown in the lower two sketches of figure 3.4. On the left, filter expressions can be used that use function values left of mesh node $j = 0$. Two possible conditions are shown:
 - periodic boundary conditions, shown in the lower sketch of figure 3.4
 - sub-domain interface boundary conditions, which occur when the computational domain is decomposed in multiple sub-domains, connected at sub-domain interfaces. This is shown in the middle sketch of figure 3.4

In the present study, the expressions for both types of boundary conditions are referred to as *sub-domain interface* boundary conditions. In both cases, operation (3.12) can be used for mesh points in the vicinity of the left domain edge, except for the edge mesh point itself. For this case, the formulation of the filter operations is discussed in section 3.3.3.

3.3.2 General non-periodic domain boundary

For this type of boundaries, two different approaches can be thought of:

- lowering the order of the filter operation (3.12) and in this way decreasing the stencil width near the domain edges. Thus, symmetric stencils of decreasing stencil width are used towards the domain edge. The first mesh node from the domain edge uses a

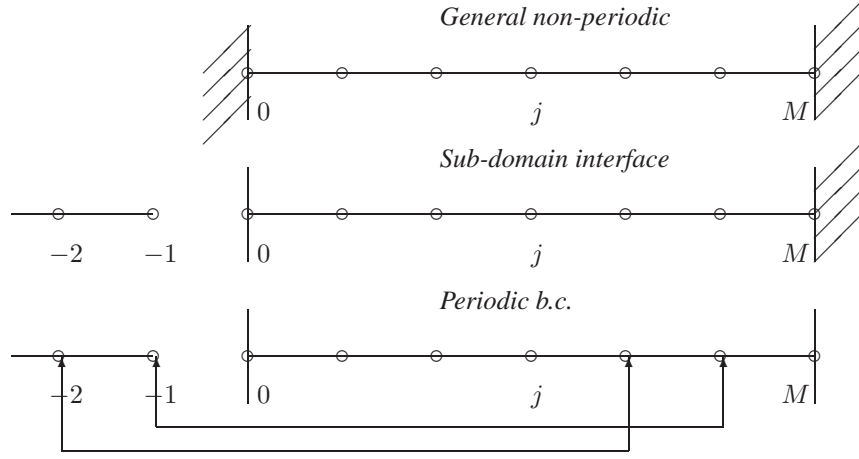


FIGURE 3.4: Summary of different boundary conditions on a one-dimensional domain

second-order accurate expression, the second node uses a fourth-order accurate expression and so on until the order of accuracy of the scheme (3.12), used in the interior of the computational domain is reached. In this approach, the mesh node on the domain edges is not included in the filter operation.

- using filter operations with a non-symmetric stencil on the right-hand side in the vicinity of the domain edges. In this approach, the order of accuracy of the scheme (3.12) used in the interior of the computational domain can be maintained, with stencils that become increasingly non-symmetric towards the domain edge. The mesh node on the domain edge is included in the filter operation.

The latter approach requires the introduction of a new class of filter operations. Here, the situation that occurs on the left domain edge is discussed. The expressions for the right domain edge can be derived in a similar way.

The quantity f in the node on the left domain edge can be filtered using an expression of the form:

$$\tilde{f}_0 + \alpha \tilde{f}_1 = \sum_{k=0}^N a_k f_k + O(h^N) \quad (3.17)$$

As in the computation of the coefficients for equation (3.12), Taylor series expansions of both left-hand and right-hand side need to be matched up to $O(h^N)$ and the shortest resolvable mode eliminated completely to get the required $N + 1$ equations for the coefficients a_0, \dots, a_N .

The first mesh point away from the left boundary of the domain ($j = 1$) uses

$$\alpha \tilde{f}_0 + \tilde{f}_1 + \alpha \tilde{f}_2 = a_0 f_1 + a_1 \frac{[f_0 + f_2]}{2} + \sum_{i=2}^N a_i f_{1+i} \quad (3.18)$$

and the second mesh node from the left boundary ($j = 2$)

$$\alpha \tilde{f}_1 + \tilde{f}_2 + \alpha \tilde{f}_3 = a_0 f_2 + a_1 \frac{[f_1 + f_3]}{2} + a_2 \frac{[f_0 + f_4]}{2} + \sum_{i=3}^N a_i f_{2+i} \quad (3.19)$$

Similar operations are used for subsequent mesh points until equation (3.12) can be used. The coefficients for filter operations (3.17), (3.18), (3.19) and subsequent operations are given in table 3.2 for 10th-order accuracy. Figure 3.5 shows the real part of the Fourier transfer

TABLE 3.2: *Left boundary: a_i for 10th-order accuracy.*

node	0	1	2	3	4
a_0	$\frac{1023+\alpha}{1024}$	$\frac{1+1022\alpha}{1024}$	$\frac{-1+2\alpha}{1024}$	$\frac{1-2\alpha}{1024}$	$\frac{-1+2\alpha}{1024}$
a_1	$\frac{5+507\alpha}{512}$	$\frac{507+10\alpha}{512}$	$\frac{5+502\alpha}{512}$	$\frac{-5+10\alpha}{512}$	$\frac{5-10\alpha}{512}$
a_2	$\frac{-45+45\alpha}{1024}$	$\frac{45+934\alpha}{1024}$	$\frac{979+90\alpha}{1024}$	$\frac{45+934\alpha}{1024}$	$\frac{-45+90\alpha}{1024}$
a_3	$\frac{15-15\alpha}{128}$	$\frac{-15+30\alpha}{128}$	$\frac{15+98\alpha}{128}$	$\frac{113-30\alpha}{128}$	$\frac{15+98\alpha}{128}$
a_4	$\frac{-105+105\alpha}{512}$	$\frac{105-210\alpha}{512}$	$\frac{-105+210\alpha}{512}$	$\frac{105+302\alpha}{512}$	$\frac{407+210\alpha}{512}$
a_5	$\frac{63-63\alpha}{256}$	$\frac{-63+126\alpha}{256}$	$\frac{63-126\alpha}{256}$	$\frac{-63+126\alpha}{256}$	$\frac{63+130\alpha}{256}$
a_6	$\frac{-105+105\alpha}{512}$	$\frac{105-210\alpha}{512}$	$\frac{-105+210\alpha}{512}$	$\frac{105-210\alpha}{512}$	$\frac{-105+210\alpha}{512}$
a_7	$\frac{15-15\alpha}{128}$	$\frac{-15+30\alpha}{128}$	$\frac{15-30\alpha}{128}$	$\frac{-15+30\alpha}{128}$	$\frac{15-30\alpha}{128}$
a_8	$\frac{-45+45\alpha}{1024}$	$\frac{45-90\alpha}{1024}$	$\frac{-45+90\alpha}{1024}$	$\frac{45-90\alpha}{1024}$	$\frac{-45+90\alpha}{1024}$
a_9	$\frac{5-5\alpha}{512}$	$\frac{-5+10\alpha}{512}$	$\frac{5-10\alpha}{512}$	$\frac{-5+10\alpha}{512}$	$\frac{5-10\alpha}{512}$
a_{10}	$\frac{-1+\alpha}{1024}$	$\frac{1-2\alpha}{1024}$	$\frac{-1+2\alpha}{1024}$	$\frac{1-2\alpha}{1024}$	$\frac{-1+2\alpha}{1024}$

function for filter schemes (3.17), (3.18) and (3.19) for $\alpha = 0.25$. The imaginary part of the Fourier transfer function for these filters is shown in figure 3.6.

Since filter expressions (3.17), (3.18) and (3.19) are non-symmetric, these schemes are both dissipative and dispersive. The imaginary part of the Fourier transfer function is larger in amplitude closer to the domain edge, where the schemes are more non-symmetric than further from the domain edge. From figure 3.6, it can be seen that the dispersive behaviour is significant only for the higher wave numbers.

In contrast to the Fourier transfer function for the symmetric equations (3.12), the real part exceeds the value 1 for certain high wave numbers, as shown in figure 3.5, indicating that these modes are attenuated by application of the non-symmetric schemes.

3.3.3 Sub-domain interface boundary condition

Figure 3.1 shows the different boundary conditions on a one-dimensional domain. The lower two sketches show the situations for periodic boundary conditions and for sub-domain boundary conditions, respectively. As stated in the introduction of section 3.3, both conditions are referred to as *sub-domain interface* boundary conditions. In filter operations for mesh nodes in the vicinity of $j = 0$, function values at $j < 0$ can be used. This data corresponds to data from the adjacent sub-domain in case of sub-domain interface boundary conditions. For periodic boundary conditions this data corresponds to function values in the vicinity of the other edge of the computational domain. With these boundary conditions and suitable data exchange, filter operation (3.12) can be used for all nodes with $j \neq 0$. For $j = 0$, an operation is used of the form

$$\tilde{f}_0 + \alpha \tilde{f}_1 = \sum_{i=0}^N a_i f_{-N/2+i} + O(h^N) \quad (3.20)$$

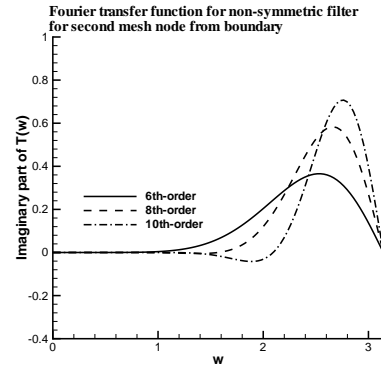
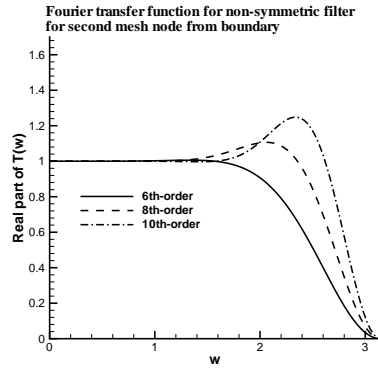
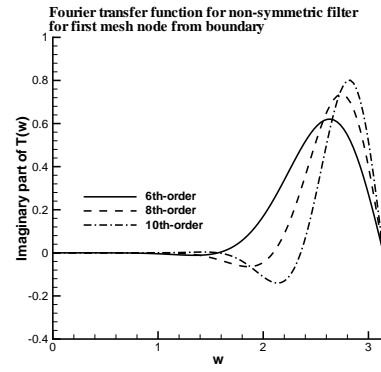
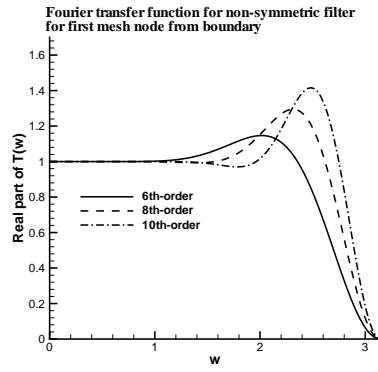
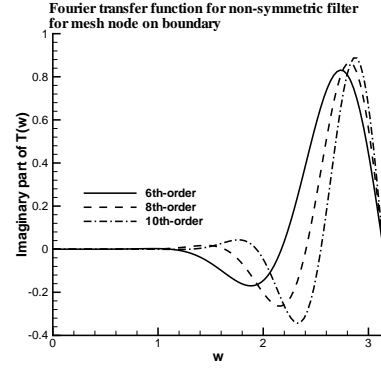
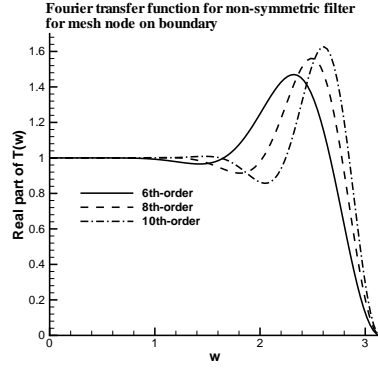


FIGURE 3.5: Real part of Fourier transfer function for filters (3.17), (3.18) and (3.19), $\alpha = 0.25$.

FIGURE 3.6: Imaginary part of Fourier transfer function for filters (3.17), (3.18) and (3.19), $\alpha = 0.25$.

For various order of accuracy, the coefficients a_i from the right-hand side of (3.20) are given in table 3.3. It can be seen that the coefficients in the stencil of operation (3.20) have a distribution that is much closer to symmetry than for operation (3.17). For non-symmetric stencils,

the Fourier transfer function has both a real (dissipative) and an imaginary (dispersive) part. For filter expression (3.20) and $\alpha = 0.25$, the real part of the Fourier transfer function is shown in figure 3.7 and the imaginary part in figure 3.8.

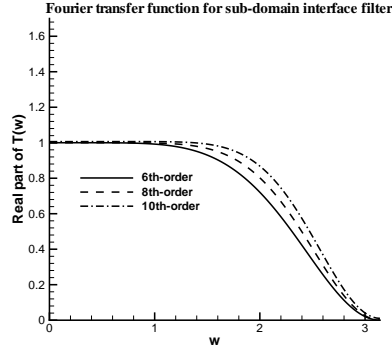


FIGURE 3.7: Real part of Fourier transfer function for filter expression (3.20), $\alpha = 0.25$.

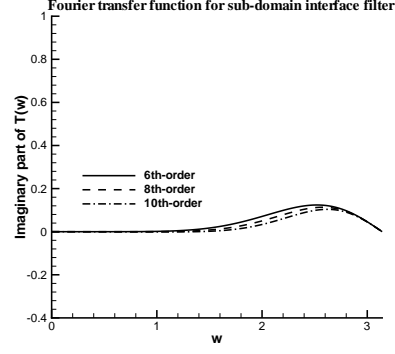


FIGURE 3.8: Imaginary part Fourier transfer function for filter expression (3.20), $\alpha = 0.25$.

Comparing figure 3.7 and the top picture of figure 3.5 shows that due to the smaller asymmetry of expression (3.20) relative to equation (3.17), the real part of the Fourier transfer function is much closer to that of the symmetric filter. Similarly, figure 3.8 and the top picture of figure 3.6 show that the imaginary part, and as a result the dispersion error, is much smaller for expression (3.20). Therefore, on sub-domain interfaces, application of equation (3.20) is preferred over equation (3.17).

TABLE 3.3: Values of a_i for interface treatment, left block boundary

Order	4	6	8	10
a_0	$\frac{-1+\alpha}{16}$	$\frac{1-\alpha}{64}$	$\frac{-1+\alpha}{256}$	$\frac{1-\alpha}{1024}$
a_1	$\frac{1-\alpha}{4}$	$\frac{-3+3\alpha}{32}$	$\frac{1-\alpha}{32}$	$\frac{-5+5\alpha}{512}$
a_2	$\frac{5+3\alpha}{8}$	$\frac{15-15\alpha}{64}$	$\frac{-7+7\alpha}{64}$	$\frac{45-45\alpha}{1024}$
a_3	$\frac{1+3\alpha}{4}$	$\frac{11+5\alpha}{16}$	$\frac{7-7\alpha}{32}$	$\frac{-15+15\alpha}{128}$
a_4	$\frac{-1+\alpha}{16}$	$\frac{15+49\alpha}{64}$	$\frac{93+35\alpha}{128}$	$\frac{105-105\alpha}{512}$
a_5		$\frac{-3+3\alpha}{32}$	$\frac{7+25\alpha}{32}$	$\frac{193+63\alpha}{256}$
a_6		$\frac{1-\alpha}{64}$	$\frac{-7+7\alpha}{64}$	$\frac{105+407\alpha}{512}$
a_7			$\frac{1-\alpha}{32}$	$\frac{-15+15\alpha}{128}$
a_8			$\frac{-1+\alpha}{256}$	$\frac{45-45\alpha}{1024}$
a_9				$\frac{-5+5\alpha}{512}$
a_{10}				$\frac{1-\alpha}{1024}$

3.4 Parallelization techniques

A number of programming models exist that can be used to parallelize a numerical method. These models need to provide communication and synchronization between parallel tasks. Classifications of the different models have been presented by various researchers. Here, the classifications of Grune et al. (2000) is followed:

- *Shared variables.* In this model, a collection of processes communicates through shared variables. To enable this, at least part of the address spaces of the processes overlap. Variables stored in these overlapping address spaces are the shared variables. A major issue in this model is the synchronization of the access to the variables. Different methods have been developed to guarantee the synchronized memory access;
- *Tuple space.* A tuple space is a shared address space in a parallel program that is located on top of the various parallel processes, each with their own local memory. This extra shared memory block can be accessed by all the processes. The tuple space is an associative data field, i.e. storing data pairs of values: one value is the *key* to the pair and the other is the actual stored variable. These stored variables can be retrieved by a search operation on the keys of the data pairs. This kind of data structure is quite different from those traditionally used in numerical methods for fluid dynamics. A numerical method based on such an associative data structure can certainly be devised, however, without matching the computational efficiency of the more traditional implementations. Again, synchronization of the access to the variables is an important issue for which several solutions exist;
- *Message passing.* In this model, each of the processes can access only its own local data. The exchange of data between the processes is performed using either one of the two following methods:
 - *point-to-point communication.* Here, synchronized sets of *send* and *receive* statements send data from one process to another.
 - *collective communication.* An example is the *broadcast* operation, which distributes data from one process to all other processes in a single statement.

The *send* and *receive* functions can be implemented either as *blocking* or *non-blocking*. A *blocking* version means that the program waits until the corresponding *send* and *receive* statements have been completed successfully. In the *non-blocking* implementation, the program continues irrespective of a successful completion of both the *send* and *receive* statements.

In a *synchronous* communication implementation, the parallel program works with blocking *sends* and blocking *receives* and in an *asynchronous* communication implementation, with non-blocking *sends* and blocking *receives*.

In the last decade, standardized libraries have been developed providing functions for a broad range of message passing tasks. The first of these libraries was PVM (Parallel Virtual Machine), see Geist et al. (1993). The de-facto standard library is MPI (Message Passing Interface), see Message Passing Forum (1994);

- *Parallel object-oriented programming.* The idea behind object-oriented programming is 'encapsulation' of data and functions that can operate on this data in 'objects'.

This programming paradigm has gained a lot of popularity in the last decades, especially since the introduction of the C++ programming language, see Stroustrup (1986). Object-orientation is supposed to lead to better structured programs. In parallel object-oriented programming, several objects are allowed to execute at the same time on different processors. Inside each object, a process is executed. Communication is performed through operations that form the interface between different objects. In a real implementation, this communication is very similar to that of the *message passing* model. In recent years, extensions of the C++ programming language have been made to create a 'parallel' version of the language. So far, these efforts have not resulted in a standardized language and these 'parallel' C++ versions are not widely used for numerical simulations. A notable advantage of such a 'parallel' language over a library, that is linked with a program at compile-time, is that the implementation can be strictly type-checked, leading to a less error-prone code development;

- *Data parallelism*. In this model, all processes execute the same program. However, the operations are performed on different parts of a data set. The most common application of this model is the parallel execution of 'loops' in a computer program. The distribution of a loop over the different processors can be either determined by the programmer or by the compiler. The latter case is usually referred to as *automatic parallelization*. Development of these compilers has received a lot of attention, but remains a very complicated problem (Grune et al. (2000)). For computer programs with a transparent structure of the loops and data dependencies, reasonable results can be obtained with these automatic parallelizing compilers.

Better results can be obtained when the programmer introduces extra information to the compiler through specific statements in the computer program. In recent years, an industry standard for these statements was formulated (OpenMP OpenMP (1998)). As a result, this parallel programming technique has gained much in popularity;

Apart from the parallel programming model chosen for the parallelization of the numerical method, the type of computer hardware, on which the parallel program is to be executed, is an important issue. The following distinction can be made for computers with multiple processors:

- *Distributed memory* computers. In this case, each of the processors has its own local memory. A distributed memory computer can be either a single machine with multiple processors or built as a cluster of smaller machines connected in a network;
- *Shared memory* computers. Here, all processors are connected to one block of memory, which forms a single address space. Each of the processors can access all data in this address space.

In theory each of the parallel programming models mentioned earlier can be made to work on both types of computers. However, the *shared variables*, *tuple space* and *data parallelism* models are far more suitable for implementation on shared-memory computers than on distributed-memory computers, since these models use an address space that is accessible from all processors. An implementation on a distributed memory machine requires complicated and expensive communication operations of the operating system.

The *message passing* model is the most flexible of the models, since it can be efficiently implemented on both types of machines. However, on shared-memory machines, the simplicity

of the single address space is not exploited.

The *parallel object-oriented programming* model can be as flexible as the *message passing* model in case the communication between the different objects is implemented as explicit send/receive operations and not based on a partly shared address space.

In numerical methods applied to fluid dynamics problems, parallelism is usually obtained using either the *message passing* model or *data parallelism*. Typically, computational methods for fluid dynamics simulations spend most of the CPU time on floating-point operations. Since these operations are performed most efficiently with methods implemented in the more traditional programming languages, such as FORTRAN and C, and to a lesser extent C++, the majority of the numerical methods is written in these languages. The ability to use the *message passing* and *data parallelism* models in combination with these programming languages is the main reason for the widespread use of these two models in computational fluid dynamics.

The majority of the parallel programs in use for fluid dynamics simulations is based on the *message passing* paradigm, for a number of reasons:

- Most fluid dynamics problems allow the computational domain to be decomposed into a number of sub-domains. This decomposition enables a large degree of independence between the computations performed on the various sub-domains. The required exchange of data between these sub-domains and the synchronization of the processes can be efficiently performed using a small set of *message passing* functions. This type of parallelization is typically referred to as *coarse-grain parallelization*;
- With an adequate domain-decomposition technique and a good balancing of the computational load on the processors, the speed-up obtained with this model is, in most realistic situations, better than with other models;
- The number of tasks that cannot to be performed in parallel for the *coarse-grain parallelization* is typically smaller than in the *data parallel* approach. In the *data parallel* approach, time-consuming loops are performed in parallel (commonly referred to as *fine-grain parallelization*), but the parts of the program that are executed sequentially lead to a less-favorable load balancing and speed-up compared to the ones obtained using the *message passing* model;
- The *message passing* model is typically implemented as a library of functions that can be easily linked with a computer program written in most of the common programming languages. A number of standardized libraries exist (MPI, PVM and others), leading to parallel programs that can be easily ported to different computers.

Given these advantages, the parallelization of the parallel Navier-Stokes method developed in the present study is based on domain decomposition techniques and the *message passing* paradigm. The implementation is based mainly on *synchronous point-to-point* communication statements.

3.5 Parallel compact finite-difference method

In the parallel simulation method, the Navier-Stokes equations governing incompressible flow of a Newtonian fluid are integrated in time using the fractional time-stepping method due to Kim and Moin (1985). This method is second-order accurate in time. The required steps were previously described in section 3.2. The present method uses a three-dimensional rectangular domain with a constant mesh spacing in all three spatial directions. Furthermore, the implementation of the method assumes that this mesh spacing is identical for the three directions, so that there is only a single parameter representing the mesh density.

Based on these assumptions, the Helmholtz equation (3.7) in three dimensions is discretized using the fourth-order accurate Helmholtz solution method described in section 4.7. The non-linear convection terms H_i on the right-hand side of equation (3.7) are discretized using a sixth-order accurate compact finite-difference scheme for first-derivatives in all three spatial directions. The used schemes were presented by Lele (1992) and are described in section 4.1. The Laplace operator appearing on the right-hand side of equation (3.7), as a result of the implicit integration of the viscous terms, is similarly discretized using one-dimensional compact finite-difference expressions, of sixth-order accuracy, in the three spatial directions. The one-dimensional schemes used here, are described in section 4.2.

The solution of these Helmholtz equations, one for each of the three velocity components, gives an intermediate velocity field. The next step consists of computing the divergence of this intermediate velocity field, again using the sixth-order accurate compact finite-difference method of section 4.1.

The computed divergence forms the forcing term for the pressure Poisson equation (3.8), which is discretized using the same method as used for the three Helmholtz equations for the intermediate velocity field. Finally, a time-step is completed using equation (3.9).

An essential feature of the present method, is the decomposition of the computational domain in multiple sub-domains. This domain decomposition complicates the temporal integration method described above. The complications caused by the domain decomposition are the following:

- The domain decomposition introduces a number of new sub-domain boundaries, forming interfaces between adjacent sub-domains. To minimize the effect of these artificial sub-domain boundaries, a specific formulation for the various finite-difference stencils and compact-difference filter stencils is used. In both cases, data from the adjacent sub-domain is included in the stencil. For the spatial filter, this newly-developed formulation for the sub-domain boundaries is presented in subsection 3.3.3. For the first-derivative and the second-derivative approximation, these formulations are described in section 4.1 and section 4.2, respectively. The required data transfer for these sub-domain interface schemes is described in subsection 3.5.2;
- the flow field data in the multiple sub-domains needs to be coupled. Here, this coupling is achieved by using an overlap of the sub-domains in combination with an exchange of the computed flow field data in the overlapping parts of the sub-domains. This data exchange is described in section 3.5.2.

In the present study, this decomposition is performed in one spatial direction, chosen to coincide with the axial direction of the vortex pair. The details of this decomposition are described

in section 3.5.2, which describes the parallelization of the present Navier-Stokes method, using definitions introduced previously in section 3.4. The use of a domain-decomposition method is one of the factors that resulted in the choice for a *collocated mesh formulation*. Section 3.5.1 describes the advantages of this approach in more detail.

3.5.1 Collocated mesh formulation

In contrast to many implementations of methods for the incompressible Navier-Stokes equations employing a *staggered mesh*, a *collocated mesh* is used in the present numerical methods. A staggered mesh defines the data points for velocity components and pressure at different positions, typically, the pressure node is located in the cell center and the velocity components are staggered half a mesh width from that position. In the collocated-mesh approach, the more conventional method of defining all the unknowns at one and the same data point is used.

The staggered-mesh approach has a number of important advantages over the collocated-mesh approach, see for example Kim and Moin (1985): no ad hoc boundary conditions for the pressure are required and with a second-order accurate central-difference discretization of the spatial derivatives and in the absence of time-differencing errors, global conservation of momentum, kinetic energy and circulation of the flow field is achieved. However, in both of the Navier-Stokes methods described in this chapter, spatial derivatives are discretized using high-order accurate schemes, rendering the staggered-mesh approach less attractive. One of the complications that results from using a staggered-mesh in conjunction with a high-order spatial discretization, is the complexity of the required interpolation operations. This requirement is a result of the different locations of the nodes in which the velocity components and pressure are defined. The complexity is caused by the requirement to perform the interpolation with at least the same order of accuracy as that of the spatial discretization. Furthermore, the global conservation shown for second-order accurate central-difference discretization of the spatial derivatives does not hold for higher-order accurate schemes. As a consequence of these considerations, the collocated-mesh approach is preferred in the two Navier-Stokes methods used in this study.

3.5.2 Parallelization of the method

The parallelization of the present Navier-Stokes method is based on a decomposition of the computational domain in combination with message passing, that couples the data in the sub-domains and performs the required communication. The motivation for this choice is given in section 3.4.

Domain decomposition

Figure 3.9 shows an example of a computational domain decomposed in one spatial direction. On the three sub-domain interfaces, an overlap is present of three layers of mesh nodes. The sub-domains have identical dimensions and mesh nodes with indices (i, j, k) , $i \in [0, N_I]$, $j \in [0, N_J]$, $k \in [0, N_K]$. Assuming that the i -coordinate direction is the direction of the decomposition, the faces $(0, j, k)$, $(1, j, k)$ and $(2, j, k)$ of the sub-domain on the right of an interface and the faces $(N_I - 2, j, k)$, $(N_I - 1, j, k)$ and (N_I, j, k) of the sub-domain on the left of the interface are shared.

In the vicinity of the sub-domain interfaces, data from the adjacent sub-domain needs to be

used in the stencils of the various finite-difference expressions used in the spatial discretization of the governing equations. For this purpose, data from each of the blocks is copied to an *interface-array*, and this array is sent to the neighboring sub-domain. Figure 3.10 shows the interface between sub-domains 0 and 1 of figure 3.9 in more detail. The sketch shows the transfer of data to interface-arrays with two layers of mesh nodes: data from the faces $(N_I - 4, j, k)$ and $(N_I - 3, j, k)$ of the sub-domain on the left of the interface is copied to the interface-array used by the sub-domain on the right-hand side of the interface. The large solid circles in figure 3.10 indicate mesh nodes on the sub-domain interface in both sub-domains. For these mesh nodes, stencils for first and second-derivatives are presented in sections 4.1 and 4.2, respectively. With the two layers of mesh points, a 6th-order accurate expression can be used for both derivatives. After each time-step data within the overlapping parts of the computational domain has changed. An exchange of all flow field data takes place that involves copying data of face $(2, j, k)$ of sub-domain 1 to face (N_I, j, k) of sub-domain 0, copying data of face $(N_I - 2, j, k)$ of sub-domain 0 to face $(0, j, k)$ of sub-domain 1 and averaging data of faces $(N_I - 1, j, k)$ and $(1, j, k)$ of sub-domains 0 and 1, respectively. A similar exchange is performed after computation of the intermediate velocity field. The Helmholtz equations (3.7) for the intermediate velocity field have Dirichlet boundary conditions prescribed on the sub-domain interface. The components of the intermediate velocity field are exchanged to enable a correct computation of the forcing terms of the Poisson equation (3.8) for the modified pressure, which is solved with Neumann boundary conditions prescribed on the sub-domain interface.

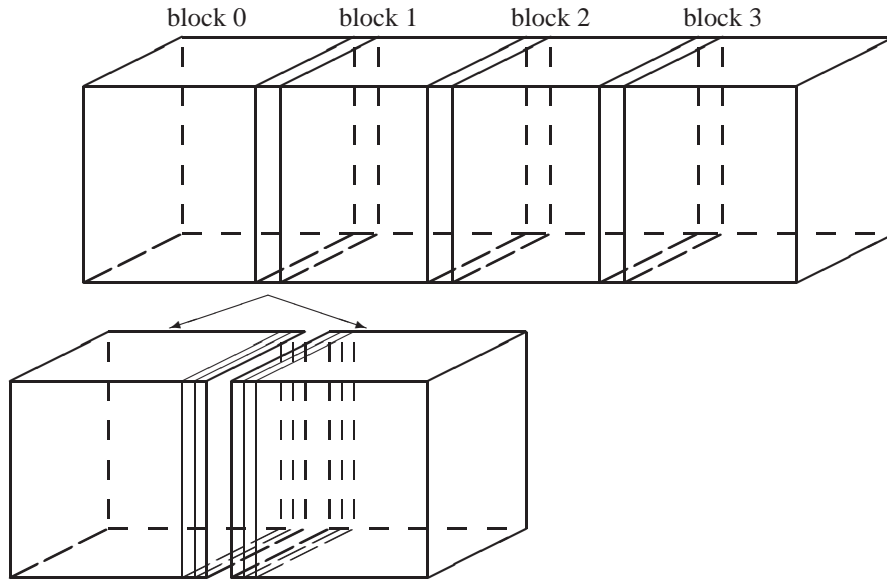


FIGURE 3.9: Domain decomposition in one spatial direction

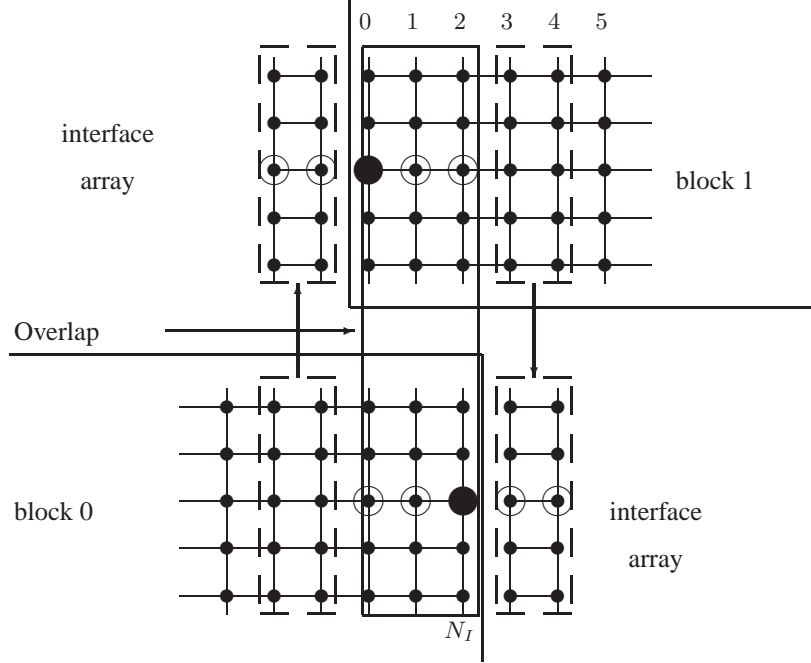


FIGURE 3.10: Schematic view of sub-domain overlap and data transfer

Message passing strategy

The domain decomposition described earlier forms the basis of the parallelization of the simulation method. With the computational domain decomposed in sub-domains, a message passing strategy needs to be formulated that provides the required communication and synchronization statements in a parallel simulation. In this study, the SPMD (Single Program Multiple Data) paradigm is used for the parallelization. As the name indicates, a single set of instruction (identical for all processes) is executed on a different data set for each of the processes. To achieve a different program execution for each of the processes, functions from the MPI message passing library, see Message Passing Forum (1994), are called to return the number of processes and the process rank to each of the processes. This process rank is used throughout the program to take different branches within the program, performing appropriate program statements.

The first of these different branches involves the input from file by process with rank 0 of run-time parameters: number of time steps to be taken, time step, reference values for velocity, density, etc. This process will now send this data to all other processes in a *broadcast* operation.

The next step involves the input of information that prescribes which sub-domains are assigned to each process. This information determines the computational load of the processes and is called *load balancing*. Again, process with rank 0 reads this data from file and a broadcast operation distributes this data. These broadcast operations form the only *collective* communication statements in the program.

The next step consists of reading mesh data, boundary condition information and the initial

solution for each of the sub-domains allocated to each of the processors.

To proceed, a *message passing strategy* needs to be determined. The boundary conditions imposed on the computational domain and the decomposition of this computational domain in sub-domains determine the *topology* of the simulation. This topology assigns an index to each of the sub-domains and contains information about the connection between the sub-domains.

Based on this *topology* and the number of processes used in the simulation, the message passing strategy can be determined using the following steps:

- Definition of a data type containing: interface index, indices of both sub-domain on the left and right side of interface, indices of processes to which these sub-domains are assigned;
- A linked-list is initiated for the storage of the topology. The nodes of the list will represent each of the sub-domain interfaces, with data stored as elements of the newly-defined data type;
- A search operation is performed to determine the number and the location of sub-domain interfaces. This search operation uses the boundary condition and load balance information. For each interface that is found, a new node will be added to the linked-list, containing the information about the connected sub-domains;
- Additionally, each of the interfaces is checked: the boundary condition information should be consistent with that prescribed for the load balancing and the meshes of the sub-domains should overlap in the way shown in figures 3.9 and 3.10.

With the *topology* information stored in this *interface* based method, enough information is available in the parallel program to perform the required communication and synchronization tasks. After the determination of the topology, the program will proceed with the actual temporal integration of the governing equations. A number of data-exchange operations are used to couple the solution of the various sub-domains.

These data exchange operations are performed by the concurrent traversing of the linked-list containing the *topology* on all processors. For each list element, representing a sub-domain interface, the corresponding processes will perform the required send/receive operations. When both sub-domains are assigned to the same process, the data exchange is implemented as a simple memory-copy operation.

The parallel execution procedure described above is sketched in figure 3.11 for a parallel simulation using 4 processes. Each of these processes is depicted as one of the large boxes in the figure. Process indices are $0, \dots, 3$, from left to right.

The horizontal arrows indicate communication statements between the processes. From figure 3.11 it can be seen that after reading the input and distribution of the input parameters, the processes perform similar operation concurrently on different data. In this way, an excellent load balancing can be achieved.

The mesh data, boundary condition information, initial conditions and output are stored in separate files for each of the sub-domains. Each of the processes performs the input/output for the assigned sub-domains. These input/output operations can therefore be performed in parallel. In figure 3.11, the flow field is advanced in time from time level $n = 0$ to time level $n = n_t$, with a number of communication/synchronization operations during each of these

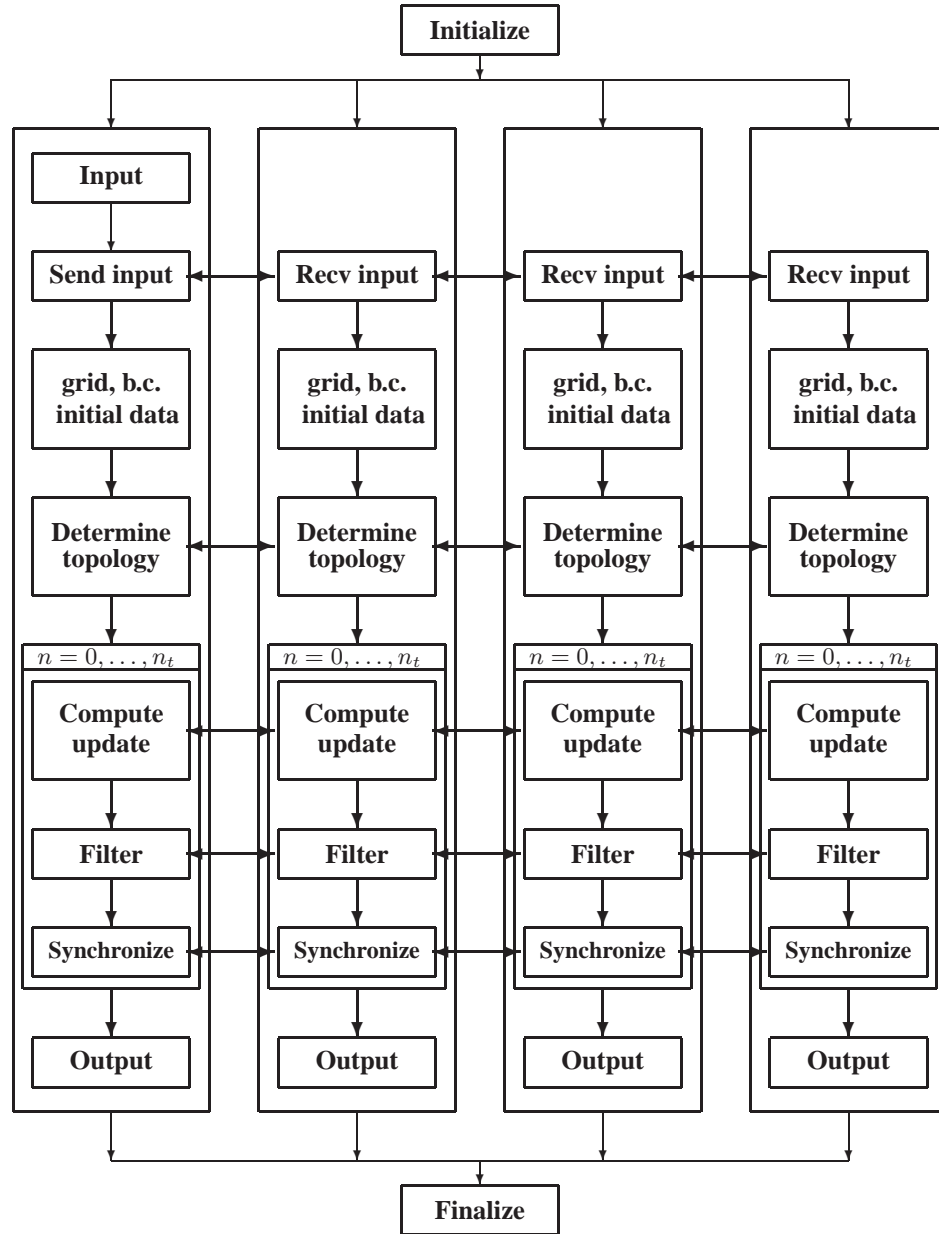


FIGURE 3.11: Flow chart of parallel 3D Navier-Stokes solver running on 4 processors

time-steps.

The message passing strategy described here has proven to be both flexible and robust for the test cases performed.

Implementation details

In the present implementation, the following functions from the (MPI) library are used:

- **MPI_Init**: initialization of the parallel procedure
- **MPI_Finalize**: finalizing the parallel procedure
- **MPI_Comm_size**: returns the number of processes in the parallel procedure
- **MPI_Comm_rank**: returns the rank of process that calls the function
- **MPI_Barrier**: synchronization of the various processes in the procedure: all processes wait for the last to reach this statement
- **MPI_Send** and **MPI_Recv**: point-to-point communication of data from one process to another. *Blocking* versions are used.
- **MPI_Bcast**: broadcasting of input and load balance information to all processes.
- **MPI_Address**, **MPI_Type_struct** and **MPI_Type_commit**: definition of user-defined data type to be used by MPI

Newly defined data types are used in the broadcast, send and receive statements. The capability to define new data types enables the transfer of different data items (possibly of different type), contained in a single element of the new data type, in a single function call. This can lead to both a reduction in communication overhead (less connections need to be established) and program complexity, since in the data communication, the size of the messages is simply the size of a single element of the new data type, instead of a locally unknown number of elements of one of the primitive data types.

Newly defined data types need to be redefined for MPI. In this MPI definition, the sizes and relative locations of the elements that form the data type are computed and stored in an element of type **MPI_Datatype**. For this definition, the functions **MPI_Address**, **MPI_Type_struct** and **MPI_Type_commit** are used.

3.5.3 Implementation of spatial filter

The present method employs a high-order accurate low-pass filter to damp under-resolved modes of the three-dimensional flow field. Spatial filtering in more than one spatial dimension can be performed in two ways:

- successive application of one-dimensional expressions, of the form (3.12), in the multiple coordinate directions. In each of these coordinate directions, tridiagonal systems of equations result for all mesh lines in that spatial direction;
- application of a multi-dimensional filter operation derived from a tensor product of the one-dimensional expressions. In this case, a single large system of equations needs to be solved to filter a quantity in the computational domain.

The first approach involves a smaller computational cost than the second approach. This first approach was pursued in Visbal and Gaitonde (1998), describing a three-dimensional

Navier-Stokes solver based on compact finite-difference discretization methods in a curvilinear coordinate system. However, the result of the filtering depends on the order in which the successive filtering operations are performed.

In the present work, a formulation of the filter in multiple spatial directions is used, based on the symmetric filter operation (3.12) of section 3.3. Here, 10th-order accuracy is used for the spatial filtering. The Fourier analysis of filter schemes for different orders of accuracy was discussed in section 3.3, showing that as the order of accuracy increases, the damping is more concentrated in the short-wavelength part of the wave number spectrum. Since the spatial discretization of the governing equations employs 4th-order and 6th-order accurate schemes, a filter scheme of at least 8th-order accuracy should be used. A limitation on the used order of accuracy is the required computational of the evaluation of the filter expression. For the present simulation method, 10th-order accuracy of the filter has proved to be a good compromise between accuracy and computational work.

The formulation in multiple spatial directions is derived by performing a tensor product of three one-dimensional spatial filtering operations. This approach gives for the three-dimensional equivalent of operation (3.12):

$$\begin{aligned}
& \tilde{f}_{i,j,k} + \alpha_i (\tilde{f}_{i-1,j,k} + \tilde{f}_{i+1,j,k}) + \alpha_j (\tilde{f}_{i,j-1,k} + \tilde{f}_{i,j+1,k}) + \alpha_k (\tilde{f}_{i,j,k-1} + \tilde{f}_{i,j,k+1}) + \\
& \alpha_i \cdot \alpha_j (\tilde{f}_{i-1,j-1,k} + \tilde{f}_{i+1,j-1,k} + \tilde{f}_{i-1,j+1,k} + \tilde{f}_{i+1,j+1,k}) + \\
& \alpha_i \cdot \alpha_k (\tilde{f}_{i-1,j,k-1} + \tilde{f}_{i+1,j,k-1} + \tilde{f}_{i-1,j,k+1} + \tilde{f}_{i+1,j,k+1}) + \\
& \alpha_j \cdot \alpha_k (\tilde{f}_{i,j-1,k-1} + \tilde{f}_{i,j+1,k-1} + \tilde{f}_{i,j-1,k+1} + \tilde{f}_{i,j+1,k+1}) + \\
& \alpha_i \cdot \alpha_j \cdot \alpha_k (\tilde{f}_{i-1,j-1,k-1} + \tilde{f}_{i+1,j-1,k-1} + \tilde{f}_{i-1,j+1,k-1} + \tilde{f}_{i+1,j+1,k-1} + \\
& \tilde{f}_{i-1,j-1,k+1} + \tilde{f}_{i+1,j-1,k+1} + \tilde{f}_{i-1,j+1,k+1} + \tilde{f}_{i+1,j+1,k+1}) \quad (3.21) \\
& = \sum_{l,m,n=0}^N a_{l,m,n} f_{i-N/2+l,j-N/2+m,k-N/2+n} + O(h^N)
\end{aligned}$$

where α_i , α_j and α_k are the filter coefficients in the three corresponding spatial directions, h the (constant) uniform mesh spacing and N the order of the truncation error. The right-hand side of operation (3.21) represents a weighted summation of function values in central point (i, j, k) and the $(N+1)^3 - 1$ nearest neighbors. The left-hand side of operation (3.21) contains filtered quantities in 27 mesh points: central point (i, j, k) and the 26 nearest neighbors. Application of operation (3.21) results in a sparse-matrix system of equations, with a maximum of 27 non-zero elements per row.

Scheme (3.21) can be applied to those mesh points far enough from the domain boundary to allow the right-hand side stencil to be evaluated. As stated in section 3.3, near domain boundaries, a different formulation of the filter operation is required: either using a lower order of accuracy of the stencils in the vicinity of the domain boundary or applying non-symmetric stencils of the same order of accuracy as used for the mesh points in the central part of the computational domain.

In the present parallel Navier-Stokes solver, this last approach is followed. In the vicinity of the boundaries of the computational domain, the non-symmetric schemes of section 3.3.2 are used. Near the sub-domain interfaces, that result from the decomposition of the computational domain, the non-symmetric schemes introduced in section 3.3.3 are used, again of 10th-order accuracy. The required data transfer is described in section 3.5.2. The resulting symmetric linear systems of equations are solved using the pre-conditioned Conjugate Gradient method, described in section 3.7.

For the test case studied in the present work, the computational cost of applying equation (3.21) to the flow field variables u , v , w and p , is typically less than one third of the solution of the pressure Poisson equation. The spatial filtering is typically applied every fifth time-step. Therefore, the computational time required to perform the spatial filtering is acceptable.

3.6 Hybrid method

As stated in the introduction of this chapter, the hybrid Fourier collocation/compact finite-difference method has been designed to use the periodicity of the flow field in one spatial direction. In the present study, the method is used for the temporal integration of flow fields consisting of two counter-rotating vortices, with perturbations that are periodic in the axial direction. For this type of flows, the following expansion in the periodic direction is well-suited:

$$\begin{aligned} u(x, y, z) &= \sum_{k=1}^{N+1} \hat{u}(k; y, z) \sin(k\pi x) & v(x, y, z) &= \sum_{k=0}^N \hat{v}(k; y, z) \cos(k\pi x); \\ w(x, y, z) &= \sum_{k=0}^N \hat{w}(k; y, z) \cos(k\pi x) & p(x, y, z) &= \sum_{k=0}^N \hat{p}(k; y, z) \cos(k\pi x); \end{aligned} \quad (3.22)$$

The Fourier coefficients \hat{u} , \hat{v} , \hat{w} and \hat{p} are real-valued. The first five modes for the cosine series are plotted in figure 3.12. For the sine series, used for the component of velocity in the axial direction, the first five modes are plotted in figure 3.13.

The transformations (3.22) from real-space to Fourier space or vice versa can be efficiently performed using Fast Sine Transformation (FST) and Fast Cosine Transformation (FCT) methods. The FST and FCT methods are special forms of the well-known Fast Fourier Transform (FFT) method. These methods are described in, for example, Brigham (1974). In case N in equation (3.22) is an integer power of 2, the FST and FCT methods can perform the transformation in $O(N \log_2 N)$ operations. A straightforward formulation using a matrix-vector multiplication would involve $O(N^2)$ operations. The underlying mechanism for this increased efficiency is a recursive relation known as the *Danielson-Lanczos Lemma*, see for example Brigham (1974). Methods based on this recursive relation are known since the middle of the 1960s.

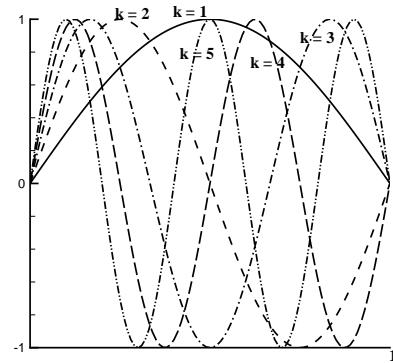
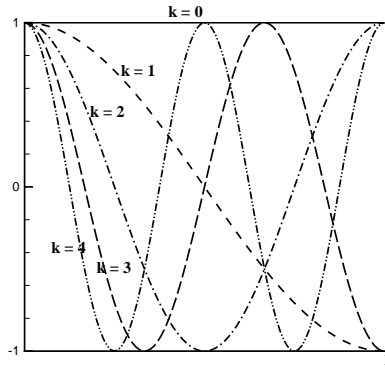


FIGURE 3.12: First 5 basis functions for FCT FIGURE 3.13: First 5 basis functions for FST

In the hybrid Navier-Stokes method, expansion (3.22) is employed in the solution of the three Helmholtz equations (3.7), one for each of the three components of the intermediate velocity

field, and the pressure Poisson equation (3.8). With the introduction of the Fourier expansion (3.22), the temporal integration proceeds in the following way:

- The three components of the intermediate velocity field, v_i , for, $i = 1, 2, 3$, are computed from the Fourier transformed momentum conservation equations (3.7). Using expansion (3.22), these transformed momentum equations can be written as:

$$\left(\frac{\partial^2}{\partial y^2} + \frac{\partial^2}{\partial z^2} - \left\{ \frac{2}{\nu \delta t} + k^2 \pi^2 \right\} \right) \hat{v}_i(k; y, z) = \hat{r}_i(k; y, z) \quad (3.23)$$

for wave numbers $k = 0, \dots, N$. In equation (3.23), $\hat{v}_i(k; y, z)$ and $\hat{r}_i(k; y, z)$ represent Fourier coefficients of the transformed intermediate velocity component $v_i(x, y, z)$ and of the forcing term $r_i(x, y, z)$, defined as:

$$r_i(x, y, z) = \left(\Delta + \frac{2}{\nu \delta t} \right) u_i^n(x, y, z) + \frac{2}{\nu} \left(\frac{3}{2} H_i^n - \frac{1}{2} H_i^{n-1} \right) \quad (3.24)$$

on the right-hand side of equations (3.7). For the component of the intermediate velocity in the periodic direction, a sine series expansion is used for both $\hat{v}_i(k; y, z)$ and $\hat{r}_i(k; y, z)$. The two velocity components in the non-periodic directions use cosine series expansions.

The forcing term $r_i(x, y, z)$ is evaluated in real-space using sixth-order accurate compact finite-difference methods for both first and second derivatives, similar to the method used in the parallel method described in section 3.5. Then, either the FCT or FST method is used to compute the coefficients $\hat{r}_i(k; y, z)$, with $k = 0, \dots, N$.

Then, the coefficients $\hat{v}_i(k; y, z)$ are computed from the Helmholtz equations (3.23) for $k = 0, \dots, N$. The intermediate velocity field in real-space is then computed using the FCT and FST methods;

- The next step computes the divergence of the intermediate velocity field in physical space using a similar technique as used in the parallel method, described in section 3.5, i.e. sixth-order accurate compact finite-difference methods are used for the computation of the derivatives.

With this known divergence, the forcing term for the pressure Poisson equation (3.8) can be computed in physical space. The FCT method is then used to compute the cosine series expansion of this forcing term.

Using the Fourier expansion (3.22), pressure Poisson equation (3.8) can be written as:

$$\left(\frac{\partial^2}{\partial y^2} + \frac{\partial^2}{\partial z^2} - k^2 \pi^2 \right) \hat{\phi}(k; y, z) = \hat{r}_p(k; y, z) \quad (3.25)$$

for wave numbers $k = 0, \dots, N$. In equation (3.25) $\hat{r}_p(k; y, z)$ denotes the coefficients of the cosine series expansion of the forcing term. Similarly, $\hat{\phi}(k; y, z)$ represents the coefficients of the cosine series expansion of the modified pressure $\phi(x, y, z)$. The FCT method is then used to compute $\phi(x, y, z)$ and finally the new pressure in real-space is computed using $p = \phi - (\nu \delta t / 2) \Delta \phi$;

- The final step projects the intermediate velocity field with components v_i onto a solenoidal space using equation (3.9). This step can be performed in physical space. Here, the first-derivatives on the right-hand side of equation (3.9) are computed using compact finite-difference expressions of sixth-order accuracy given in section 4.1.

The spatial discretization of Helmholtz equations (3.23) and (3.25), in the two non-periodic directions y and z , are solved using the fourth-order accurate direct solution method described in section 4.6. This method is based on a 9-point compact finite-difference stencil for the Laplace operator, described in section 4.4.

3.6.1 Implementation of spatial filter

The present hybrid Fourier collocation / compact finite-difference method applies a high-order accurate low-pass filter to the three-dimensional flow field in the following way:

- the first step involves a transformation of the flow field data from real-space to Fourier space using the appropriate transformation method for the different variables. The velocity components in the y and z spatial directions and the pressure employ the Fast Cosine Transform method, while the velocity component in the x -direction is transformed using the Fast Sine Transform method. The Fourier transformation replaces $u(x, y, z)$ by $\hat{u}(k; y, z)$, and similarly for v , w and p . Thus, for each wave number k in the axial direction, a two-dimensional data set, representing Fourier coefficients, occurs;
- the second step involves the spatial filtering of the transformed data in the two non-periodic spatial directions. This filtering operation is derived in a similar way as the three-dimensional formulation (3.21). Again, the one-dimensional filter operation (3.12) forms the basis of the filter. The resulting expression is:

$$\begin{aligned} & \tilde{f}_{i,j} + \alpha_i (\tilde{f}_{i-1,j} + \tilde{f}_{i+1,j}) + \alpha_j (\tilde{f}_{i,j-1} + \tilde{f}_{i,j+1}) + \\ & \quad \alpha_i \cdot \alpha_j (\tilde{f}_{i-1,j-1} + \tilde{f}_{i+1,j-1} + \tilde{f}_{i-1,j+1} + \tilde{f}_{i+1,j+1}) \\ &= \sum_{l,m=0}^N a_{l,m} \tilde{f}_{i-N/2+l,j-N/2+m} + O(h^N) \end{aligned} \quad (3.26)$$

with α_i and α_j the filter coefficients in the corresponding spatial directions, h the (constant) uniform mesh spacing and N the order of the truncation error. Again, 10th-order accuracy is used for the spatial filtering;

- in the third step, the flow field is filtered in the periodic direction. The Fourier series expansion used in the periodic direction allows a nearly trivial filtering operation in this periodic direction, i.e. the Fourier coefficients for the various wave numbers just need to be multiplied with the Fourier transfer function of the filter operation. For the symmetric compact-difference filter (3.12), this transfer function is given by equation (3.14) in terms of a scaled wave number w ;
- in the last step, the flow field data is transformed from Fourier space back to real-space.

The left-hand side of operation (3.26) contains filtered quantities in 9 mesh points: central point (i, j) and the 8 nearest neighbors. For N th-order accuracy, the right-hand side of operation (3.26) is a two-dimensional stencil containing function values in $(N + 1)^2$ mesh points centered around the central point (i, j) .

The formulation of the filter for mesh points in the vicinity of the domain boundaries differs from that used in the parallel method described in section 3.5. The implementation of the spatial filter in the hybrid method uses symmetric stencils with a lower order of accuracy in

the vicinity of domain boundaries.

For each axial wave number, application of the filter operation in the two non-periodic spatial directions, leads to a symmetric linear system of equations. This system is sparse and can be solved using a fast direct solution method, similar to that of the Helmholtz equations in two dimensions described in section 4.6.

3.7 Iterative solution methods for linear systems of equations

The parallel method for solving the Navier-Stokes equations for incompressible flow that has been developed in the present study, employs a novel three-dimensional compact finite-difference stencil as the basis for the solution method for both 3D Helmholtz and Poisson equations that result from the temporal integration described in section 3.2. As was mentioned in the introduction of this chapter, this method is an *iterative* solution method.

This section describes the methods used for the iterative solution of the sparse linear system of equations. Different methods are used for symmetric and non-symmetric linear systems. The method used for symmetric linear systems is described in section 3.7.2, the one for non-symmetric systems in section 3.7.3.

3.7.1 Direct and iterative methods for linear systems

The linear system of equations

$$A\underline{x} = \underline{b} \quad (3.27)$$

can be solved using either *direct* methods or *iterative* methods, see for example Golub and van Loan (1996). Direct methods involve the factorization of the coefficient matrix A , which is impractical if A is a large sparse matrix, because the resulting factorization typically leads to a dense matrix. The coefficient matrices of interest here are all large sparse matrices, since these matrices result from the application of finite-difference expressions.

In contrast, iterative methods generate a sequence of approximate solutions $\underline{x}^{(k)}$ (with k the iteration number):

$$\underline{x}^{(k+1)} = \underline{x}^{(k)} + P^{-1}(\underline{b} - A\underline{x}^{(k)}) \quad (3.28)$$

where the vector $\underline{b} - A\underline{x}^{(k)}$ is called the *residual* at iteration k , and is denoted by $\underline{r}^{(k)}$. In equation (3.28), P is the iteration matrix. The recurrence equation (3.28) can only be efficient when the inverse of P , P^{-1} , is easily computable and sparse. The methods considered here, involve coefficient matrix A only in the context of matrix-vector multiplications. The essential requirement for an efficient linear-system solver is that the approximate solution $\underline{x}^{(k)}$ converges quickly to the required accuracy and that the matrix-vector multiplications can be carried out efficiently.

Different families of iterative methods can be distinguished:

- *standard* iterative methods. Well-known examples are: Jacobi, Gauss-Seidel, SOR (Successive Over-Relaxation), etc. The methods use different iteration matrices P . These methods are simple methods to use, but suffer from a number of drawbacks:
 - typically, a large number of iterations is required for convergence. The convergence behaviour depends on the condition number of the matrix;

- the more efficient methods, such as SOR, require a number of suitably chosen parameters for a good convergence. Typically, the parameters depend on the eigenvalue spectrum of the coefficient matrix A . For many practical situations, the computation of the eigenvalue spectrum requires an impractical amount of work;
- *Krylov sub-space* methods. These methods operate in *Krylov* space, which can be introduced for the case where coefficient matrix A is a sparse positive definite symmetric matrix and considering the first few iterations of the recurrence (3.28):

$$\begin{aligned}
 \underline{x}^{(1)} &= \underline{x}^{(0)} + P^{-1}\underline{r}^{(0)} \\
 \underline{x}^{(2)} &= \underline{x}^{(1)} + P^{-1}(\underline{b} - A\underline{x}^{(1)} - AP^{-1}\underline{r}^{(0)}) \\
 &= \underline{x}^{(0)} + 2P^{-1}\underline{r}^{(0)} - P^{-1}AP^{-1}\underline{r}^{(0)} \\
 \underline{x}^{(3)} &= \dots
 \end{aligned} \tag{3.29}$$

From recurrence (3.29), it can be seen that the update of $\underline{x}^{(k)}$ relative to $\underline{x}^{(0)}$ is the linear space spanned by the base vectors:

$$P^{-1}\underline{r}^{(0)}, P^{-1}A(P^{-1}\underline{r}^{(0)}), \dots, (P^{-1}A)^{k-1}(P^{-1}\underline{r}^{(0)}) \tag{3.30}$$

or written differently as

$$\begin{aligned}
 \underline{x}_k &\in \underline{x}_0 + \text{span}\left\{P^{-1}\underline{r}_0, P^{-1}A(P^{-1}\underline{r}^{(0)}), \dots, (P^{-1}A)^{k-1}(P^{-1}\underline{r}^{(0)})\right\} \\
 &\in \underline{x}_0 + K^k(P^{-1}A; P^{-1}\underline{r}^{(0)})
 \end{aligned} \tag{3.31}$$

This space spanned by the k vectors is called the *Krylov space* of dimension k belonging to A and $\underline{r}^{(0)}$.

Important members of this class of iterative methods are:

- the *Conjugate Gradient* method. This method is applicable when A is a symmetric positive definite matrix. This method is closely related to the *steepest-descent* approach (Golub and van Loan (1996)), and was first formulated as method to compute the exact solution of the N by N system $A\underline{x} = \underline{b}$ in N steps, see Hestenes and Stiefel (1952). Due to the nature of the method, using exact arithmetic, it can be shown to lead to the exact solution. the method was formulated as an efficient method to compute the approximate solution iteratively, see Reid (1971). This method is described in section 3.7.2;
 - the *Bi-Conjugate Gradient* method. This method is an extension of the Conjugate Gradient method for non-symmetric coefficient matrices. This method is described in section 3.7.3;
 - the *Generalized Minimal Residual*(GMRES) method, introduced by Saad and Schulz (1986). This method is an efficient method applicable to both symmetric and non-symmetric matrices, however, with a more complicated implementation and a larger memory requirement than the previous two methods;
 - the *Quasi-Minimum Residual*(QMR) method, see Freund and Nachtigal (1991). As with the GMRES method, both symmetric and non-symmetric linear systems of equations can be tackled.
-

The choice of most suitable technique is a complicated matter and depends on a number of factors, including the properties of the coefficient matrices at hand. Here, the Conjugate Gradient method is chosen for symmetric matrices and the Bi-Conjugate Gradient method for non-symmetric systems of equations. The relative simplicity of both methods has been an important factor in their choice. Both methods are used in conjunction with pre-conditioning techniques described in section 3.7.4.

3.7.2 The Conjugate Gradient method

The *Conjugate Gradient* method uses the identity matrix as iteration matrix: $P = I$, the resulting Krylov space is then: $K^{(k)}(A; \underline{r}^{(0)})$.

The method is based on a minimization, in some sense, of the distance of the k -th approximate solution $\underline{\hat{x}}^{(k)}$ to the exact solution $\underline{\hat{x}}$. Since $\underline{\hat{x}}$ is unknown, this minimization procedure is ill-posed. Instead, the distance is minimized in the norm: $\|\cdot\|_A$, defined as

$$\|\underline{v}\|_A = (\underline{v}, A\underline{v})^{\frac{1}{2}} \quad (3.32)$$

The Conjugate Gradient method thus solves the minimization problem

$$\min_{\underline{y} \in K^{(k)}(A; \underline{r}^{(0)})} \|\underline{y} - \underline{\hat{x}}\|_A \quad (3.33)$$

This minimization problem is solved in the following way. A search direction \underline{p}_k is generated, which in the first iteration is equal to the initial residual $\underline{r}^{(0)} = \underline{b} - A\underline{x}^{(0)}$. In figure 3.14 the situation is sketched at iteration $k+1$. The search direction $\underline{p}^{(k)}$ is shown starting from the previous approximate solution $\underline{x}^{(k)}$. The new approximate solution $\underline{x}^{(k+1)}$ will be on the vector $\underline{p}^{(k)}$ such that the distance to $\underline{x}^{(k)}$ is minimized. This is found by constructing $\underline{x}^{(k+1)} - \underline{x}^{(k)}$ perpendicular to $\underline{p}^{(k)}$. This is equivalent to minimizing $f(\underline{x}^{(k)} + \alpha_k \underline{p}^{(k)})$ along $\underline{p}^{(k)}$, where f is given by:

$$f = \frac{1}{2} \underline{x} \cdot A\underline{x} - \underline{x} \cdot \underline{b} \quad (3.34)$$

A projection of this function f onto the plane spanned by the mutually perpendicular vectors $\underline{p}^{(k+1)}$ and $\underline{r}^{(k)}$ is shown in figure 3.15, where ellipses denote iso-contours of f .

The residual $\underline{r}^{(k)}$ is the gradient of the function f and is thus perpendicular to the tangent $f = \text{constant}$ at $\underline{x}^{(k)}$, because $\underline{x}^{(k)}$ is a minimal point. Now, the next search direction $\underline{p}^{(k+1)}$ must pass through the center of the ellipse, which gives the lowest residual in this plane. Thus, this iterative process can be summarized as choosing the sequence of improved estimates

$$\underline{x}^{(k+1)} = \underline{x}^{(k)} + \alpha_k \underline{p}^{(k)} \quad (3.35)$$

while carrying out the recurrence

$$\begin{aligned} \alpha_k &= \frac{\underline{r}^{(k)} \cdot \underline{r}^{(k)}}{\underline{p}^{(k)} \cdot A\underline{p}^{(k)}} \\ \underline{r}^{(k+1)} &= \underline{r}^{(k)} - \alpha_k A\underline{p}^{(k)} \\ \beta_k &= \frac{\underline{r}^{(k+1)} \cdot \underline{r}^{(k+1)}}{\underline{r}^{(k)} \cdot \underline{r}^{(k)}} \\ \underline{p}^{(k+1)} &= \underline{r}^{(k+1)} - \beta_k \underline{p}^{(k)} \end{aligned} \quad (3.36)$$

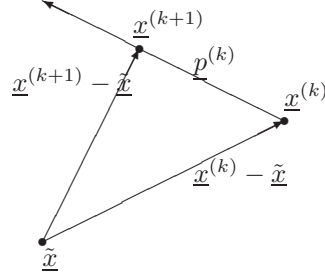


FIGURE 3.14: *Geometric interpretation of the Conjugate Gradient method: construction of search direction $\underline{p}^{(k)}$ that minimizes the distance from $\underline{x}^{(k+1)}$ to $\tilde{\underline{x}}$.*

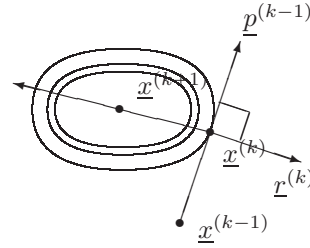


FIGURE 3.15: *Geometric interpretation of the Conjugate Gradient method: shown is a projection of f onto the plane spanned by orthogonal vectors $\underline{p}^{(k-1)}$ and $\underline{x}^{(k)}$.*

Using exact arithmetic, this procedure leads to the exact solution $\tilde{\underline{x}}$ in N steps. This principle was used by Hestenes and Stiefel (1952). However, N is an unrealistically large number of iterations for practical systems. Therefore, the process is stopped when a certain prescribed convergence criterion is reached. This approximate solution variant was first described by Reid (1971).

3.7.3 The Bi-Conjugate Gradient method

The Conjugate Gradient method is only applicable to symmetric positive definite matrices. For non-symmetric coefficient matrices A , the Bi-Conjugate Gradient method was introduced. For this method, there is no relation to the minimization problem of section 3.7.2. Apart from the set of vectors $\underline{r}^{(k)}$ and $\underline{p}^{(k)}$, an additional set $\overline{\underline{r}}^{(k)}$ and $\overline{\underline{p}}^{(k)}$ is introduced. Again a sequence of improved estimates is performed

$$\underline{x}_{k+1} = \underline{x}_k + \alpha_k \underline{p}_k \quad (3.37)$$

while now satisfying the recurrence

$$\begin{aligned} \alpha_k &= \frac{\overline{\underline{r}}^{(k)} \cdot \underline{r}^{(k)}}{\overline{\underline{p}}^{(k)} \cdot A \underline{p}^{(k)}} \\ \underline{r}^{(k+1)} &= \underline{r}^{(k)} - \alpha_k A \underline{p}^{(k)} \\ \overline{\underline{r}}^{(k+1)} &= \overline{\underline{r}}^{(k)} - \alpha_k A^T \overline{\underline{p}}^{(k)} \\ \beta_k &= \frac{\overline{\underline{r}}^{(k+1)} \cdot \underline{r}^{(k+1)}}{\overline{\underline{r}}^{(k)} \cdot \underline{r}^{(k)}} \\ \underline{p}^{(k+1)} &= \underline{r}^{(k+1)} - \beta_k \underline{p}^{(k)} \\ \overline{\underline{p}}^{(k+1)} &= \overline{\underline{r}}^{(k+1)} - \beta_k \overline{\underline{p}}^{(k)} \end{aligned} \quad (3.38)$$

3.7.4 Preconditioning

In the previous sections it was assumed that $P = I$. Taking $P \neq I$, instead of equation (3.27) the following linear system is solved

$$P^{-1} A \underline{x} = P^{-1} \underline{b} \quad (3.39)$$

This can lead to an improvement of the convergence rate by manipulating the spectral condition number of the linear system. A requirement for P is that $P^{-1}A$ is still a sparse system and in case of the Conjugate Gradient method this product needs to be symmetric. In the present work, the Gauss-Jacobi preconditioner is used, with $P = D$, D the diagonal part of A . This leads to an acceptable performance of the solver.

3.7.5 Implementation of matrix-vector multiplications

In both the Conjugate Gradient and the Bi-Conjugate Gradient methods, the majority of the computational work involves the computation of the various matrix-vector multiplications. Therefore, the implementation of the matrix-vector multiplications in these linear-system solvers was carefully studied. Two types of implementations have been compared:

- *row-indexed sparse storage* implementation This method involves two arrays: an array containing the non-zero elements of the coefficient matrix A and an array containing the indices of these non-zero elements. Both have a dimension equal to the number of non-zero elements of A . The method works for an arbitrary structure and variation of the non-zero elements of coefficient matrix A . This implementation followed the method described in Press et al. (1994). A matrix-vector multiplication involves a single loop over all non-zero elements, where the index array returns the index for the data array as a function of the loop index;
- *matrix-free* implementation This method performs a matrix-vector multiplication exploiting the known structure of the coefficient matrix A . In the present study, application of the compact-finite difference solver to three-dimensional Helmholtz/Poisson equations in a uniformly spaced rectangular domain, leads to a sparse matrix system of linear equations with a maximum of 27 non-zero elements per row. The uniformity of the mesh leads to coefficients that have identical values on each of the rows of the coefficient matrix. The location of these non-zero elements is uniquely determined by the chosen numbering of the unknowns.
With this structure known, the matrix-vector multiplications can be performed using a well-designed system of loops, that ensures an efficient memory access pattern. Since, the non-zero elements of the coefficient matrix are identical on all rows, only a single set of these elements is stored.

The first method was implemented first since it is easily implemented and very general. The second method is used in all later versions of the Navier-Stokes solver since the memory requirement is much lower: a factor of 4 difference compared to the *row-indexed sparse storage* implementation was observed in three-dimensional parallel simulations. Additionally, the *matrix-free* implementation was seen to be about 2 times faster per iteration, as a result of the less-efficient indirect addressing of coefficients in the sparse storage implementation.

SPATIAL DISCRETIZATION METHODS

4 Chapter

This chapter describes a family of finite-difference discretization methods commonly known as *compact finite-difference* or *compact-difference* methods. The designation *compact* originates from the property that for a given order of accuracy, these methods typically require a narrower stencil than conventional finite-difference formulations.

For a given stencil width, the increase in accuracy is obtained by introducing additional information in the local approximation of a derivative. The discretization methods considered here, use a formulation in which the approximation of a derivative in the point considered is taken in combination with the values of the derivative in the two neighboring points along a one-dimensional domain. For example, for an approximation of the first-derivative one can take

$$\alpha \left(\frac{\partial f}{\partial x} \right)_{i-1} + \left(\frac{\partial f}{\partial x} \right)_i + \alpha \left(\frac{\partial f}{\partial x} \right)_{i+1} = \sum_{k=1}^{m/2-1} c_k \frac{f_{i+k} - f_{i-k}}{2kh} + O(h^m) \quad (4.1)$$

where f is a quantity on a uniformly spaced one-dimensional domain $x_i = i \cdot h$, $i = 0, \dots, N$ with (constant) mesh spacing h . The coefficients α and c_i are obtained by matching coefficients of Taylor series expansions of both left-hand and right-hand side of equation (4.1) up to order m . The extra coefficient α introduced in the left-hand side of equation (4.1) compared to a conventional finite-difference approximation, can be used to either increase the order of the truncation error for a given stencil width on the right-hand side of equation (4.1) or to improve the resolving properties of expression (4.1) for short-wavelength modes represented on the one-dimensional domain. The resolving properties for short-wavelength modes for a compact-difference formulation such as equation (4.1) are in general significantly better than those of a conventional finite-difference approximation for a given stencil width. This better resolution is commonly referred to as *spectral-like* resolution, since a high resolution of short-wavelength modes is a characteristic feature of *spectral methods*, which use basis functions which are defined in the entire computational domain. In general, these basis functions are orthogonal polynomials, with the choice of polynomial determined by the boundary conditions prescribed on the considered problem. Spectral methods are described in detail in Canuto et al. (1987) and are widely used for high-resolution simulations of the Navier-Stokes equations for incompressible flows. However, spectral methods are restricted in the type of boundary conditions that can be imposed on the computational domain. This restriction does not occur for compact finite-difference methods. The combination of higher accuracy than traditional finite-difference methods and the greater flexibility in the prescription of boundary conditions compared to spectral methods, formed the motivation for the choice of the meth-

ods described in this chapter.

Equations similar to (4.1) can be formulated for higher derivatives as well, with the right-hand side a combination of classical central-difference approximations for that derivative for various orders of accuracy.

Using equations of the form (4.1), the derivative in all points of a one-dimensional domain can be obtained by solution of a tri-diagonal system of equations. This requires $O(2N)$ operations. Instead of the tri-diagonal system in equation (4.1), the derivative can also be computed from a penta-diagonal system of equations. Expressions of the type (4.1) are described in detail in Lele (1992) and are also referred to as *generalized Padé schemes*. These schemes are suited for the evaluation of a derivative in terms of known function values in the computational domain. Expressions for first and second-derivatives are described in sections 4.1 and 4.2, respectively.

Section 4.3 describes the complexities that occur when the compact-difference approach is used to discretize differential operators in multiple spatial directions.

In this chapter, the spatial discretization of either ordinary differential equations (ODEs) or partial differential equations (PDEs) with compact finite-difference methods is studied, i.e. the computation of unknown function values from a boundary value problem, is more complicated and not widely-used in computational methods for fluid mechanics.

Sections 4.4 and 4.5 describe compact finite-difference discretizations of the Laplace operator in two and three dimensions, respectively.

The resulting stencils form the basis of fourth-order accurate solution methods for both Poisson and Helmholtz type of equations, that occur in temporal integration methods for the Navier-Stokes equations for an incompressible flow. Section 4.6 describes a fast direct solver for the Poisson and Helmholtz type of equations in a two-dimensional domain. The solution technique for the Poisson and Helmholtz type of equations in a three-dimensional domain is described in section 4.7 and is tested for on a model problem in section 4.8, showing the resolving properties of this newly derived method.

4.1 Spatial discretization of first-derivative

In the present study two Navier-Stokes methods have been developed: a parallel compact-finite difference method, described in detail in section 3.5 and a hybrid compact-finite difference / Fourier collocation method, described in section 3.6. Both methods use the temporal integration method described in section 3.2. In the time-integration method of section 3.2, first-derivatives appear in the right-hand side of the Helmholtz equations (3.7) in the form of the non-linear convection terms H_i , in the right-hand side of the pressure Poisson equation (3.8) and in the velocity projection step (3.9).

These derivatives can be approximated with expressions of the form (4.1) with an appropriate formulation near the domain boundaries, as described by Lele (1992).

In the parallel numerical method, the computational domain is decomposed in a number of sub-domains. This results in a number of sub-domain interfaces. A sketch of these sub-domain interfaces and the overlap of the two sub-domains was presented in figures 3.9 and 3.10. Similar to the discussion of the spatial low-pass filter operations in section 3.3, a distinction can be made between

- *general non-periodic* domain boundary condition. For this boundary condition, the formulation presented by Lele (1992) for mesh points in the vicinity of domain edges can be used;
- *sub-domain interface* boundary condition. For this boundary condition, new expressions are derived that use data from the adjacent sub-domain. The data transfer from one sub-domain to another is shown in figure 3.10.

Similar to figure 3.4 of section 3.3, describing the stencils used in the spatial filtering, figure 4.1 shows a one-dimensional computational domain with uniform mesh spacing for the two different boundary types on the left boundary edge.

In both cases, the function values of quantity f in the mesh points $i = 0, \dots, N$ are denoted by f_i , the constant mesh spacing by h . The first-derivatives at a mesh node i , f'_i , in the interior

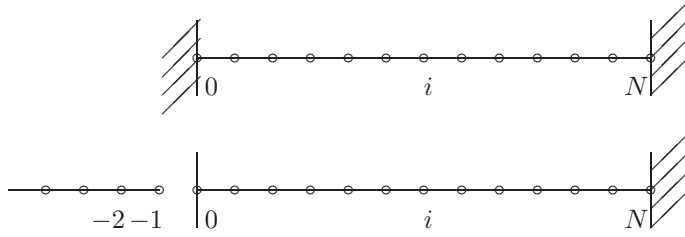


FIGURE 4.1: Uniformly spaced one-dimensional domain

part of the computational domain can be approximated using an expression of the form

$$\alpha f'_{i-1} + f'_i + \alpha f'_{i+1} = a \frac{f_{i+1} - f_{i-1}}{2h} + b \frac{f_{i+2} - f_{i-2}}{4h} \quad (4.2)$$

This implicit expression was given in Lele (1992). The coefficients a , b and α are determined using Taylor series expansions and equating coefficients of corresponding orders. For a sixth-order accurate scheme:

$$\alpha = \frac{1}{3}, \quad a = \frac{14}{9}, \quad b = \frac{1}{9} \quad (4.3)$$

Application of equation (4.2) to one either of the domains shown in figure 4.1 with an appropriate treatment of the domain edges leads to a tri-diagonal system of equations for the first-derivative.

The two boundary conditions shown in figure 4.1 require a different formulation of the approximation near $i = 0$: the *general non-periodic* domain boundary condition shown in the upper-half of figure 4.1 is discussed in section 4.1.1, the *sub-domain interface* boundary condition is discussed in section 4.1.2.

4.1.1 General non-periodic domain boundary

The first-derivative at the left domain edge $i = 0$ is computed using the equation

$$f'_0 + 2f'_1 = \frac{1}{h} \left(-\frac{5}{2}f_0 + 2f_1 + \frac{1}{2}f_2 \right) + O(h^3) \quad (4.4)$$

The first-derivative at the first mesh point from the boundary, $i = 1$, is approximated using the fourth-order accurate expression

$$\frac{1}{4}f'_0 + f'_1 + \frac{1}{4}f'_2 = \frac{3}{4} \frac{f_2 - f_0}{h} + O(h^4) \quad (4.5)$$

At the other edge of the computational domain, i.e. around $i = N$, equations similar to (4.4) and (4.5) to be used.

For mesh points $i \in [2, \dots, N - 2]$, equation (4.2) with coefficients (4.3) can be used.

In Lele (1992), the discretization of a model problem involving first-derivatives based on equation (4.2) in the interior part of the computational domain and equations (4.4) and (4.5) for the boundaries was analyzed, showing the discretization method to be accurate and stable.

4.1.2 Sub-domain interface boundary condition

With this boundary condition and a data transfer described in section 3.5.2, equation (4.2) can be used for all mesh nodes $i \neq 0$. For the first-derivative in mesh node $i = 0$, a fourth-order accurate expression can be used of the form

$$f'_0 + \alpha f'_1 = \frac{1}{h} (af_{-2} + bf_{-1} + cf_0 + df_1 + ef_2) \quad (4.6)$$

with coefficients

$$a = \frac{1 - \alpha}{12}, \quad b = \frac{-4 + 3\alpha}{6}, \quad c = -\frac{3}{2}\alpha, \quad d = \frac{4 + 5\alpha}{6}, \quad e = \frac{-1 + 3\alpha}{12} \quad (4.7)$$

In equation (4.6), f_i with negative indices correspond to function values from the adjacent sub-domain.

4.2 Spatial discretization of second-derivative

In the time-integration method of section 3.2, second-derivatives appear in the right-hand side of the Helmholtz equations (3.7) as the Laplacian of the velocity component at the previous time level. This term originates from the Crank-Nicholson method for the implicit integration of the viscous terms of the Navier-Stokes equations.

The discretization of second-derivatives on a one-dimensional domain is very similar to that of the first-derivatives. Again, a distinction will be made between general non-periodic boundary conditions and sub-domain interface boundary conditions. Both situations were shown in figure 4.1.

For points $i \in [2, \dots, N - 2]$, the second-derivative f''_i can be approximated to sixth-order accuracy using the following expression presented in Lele (1992)

$$\frac{2}{11}f''_{i-1} + f''_i + \frac{2}{11}f''_{i+1} = \frac{3}{11} \frac{f_{i+2} - 2f_i + f_{i-2}}{4h^2} + \frac{12}{11} \frac{f_{i+1} - 2f_i + f_{i-1}}{h^2} \quad (4.8)$$

Similar to the computation of the first-derivatives, application of equation (4.8) with an appropriate treatment of the boundary edges gives rise to a tri-diagonal system of equations. Section 4.2.1 discusses the treatment of general non-periodic boundary conditions and section 4.2.2 the sub-domain interface boundary conditions.

4.2.1 General non-periodic domain boundary

The second-derivative at the left boundary edge $i = 0$ is obtained from

$$f''_0 + 11f''_1 = \frac{1}{h^2} (13f_0 - 27f_1 + 15f_2 - f_3) + O(h^3) \quad (4.9)$$

As in the computation of the first derivatives, the derivative in point $i = 1$ is approximated using a fourth-order accurate expression. In this case

$$\frac{1}{10}f_0'' + f_1'' + \frac{1}{10}f_2'' = \frac{6}{5h^2}(f_2 - 2f_1 + f_0) + O(h^4) \quad (4.10)$$

For general non-periodic boundary conditions prescribed on $i = N$, equations similar to (4.9) and (4.10) can be derived.

4.2.2 Sub-domain interface boundary condition

The second-derivative in point $i = 0$ at a sub-domain interface is computed using a fourth-order accurate expression of the form

$$f_0'' + \alpha f_1'' = \frac{1}{h^2}(af_{-2} + bf_{-1} + cf_0 + df_1 + ef_2 + ff_3) \quad (4.11)$$

with coefficients

$$\begin{aligned} a &= -\frac{1}{12}, & b &= \frac{16 - \alpha}{12}, & c &= \frac{16\alpha - 30}{12}, \\ d &= \frac{16 - 30\alpha}{12}, & e &= \frac{16\alpha - 1}{12}, & f &= -\frac{1}{12}\alpha \end{aligned} \quad (4.12)$$

Again, function values with a negative index are taken from the adjacent sub-domain, as sketched in figure 4.1. The coefficient α in equation (4.11) is a parameter that can be used to either increase the accuracy of equation (4.11) to fifth-order or to tune the characteristics in Fourier space. With suitable data exchange, equation (4.8) can be used for mesh node $i = 1$.

4.3 Spatial discretization of Laplace operator

This section describes the difficulties that arise when the discretization of the Laplace operator in two dimensions is based on the one-dimensional expression for the second-derivative from the previous section. It will show the requirement for a derivation in terms of Taylor series expansions in multiple spatial directions.

A fourth-order accurate discretization based on compact finite-difference schemes will be derived on a uniformly spaced mesh with identical mesh widths in both spatial directions. In the two-dimensional situation, an expression is sought that relates the Laplace operator at a mesh point (i, j) and its 4 immediate neighbors (points $(i - 1, j)$, $(i + 1, j)$, $(i, j - 1)$ and $(i, j + 1)$) to the function values in point (i, j) and its 8 neighbors (points $(i - 1, j)$, $(i + 1, j)$, $(i, j - 1)$, $(i, j + 1)$, $(i - 1, j - 1)$, $(i - 1, j + 1)$, $(i + 1, j - 1)$, $(i + 1, j + 1)$).

As an illustration of the complications that result when applying one-dimensional derivative expressions for spatial derivative operators in multiple dimensions, consider the fourth-order accurate expression for the second-derivative

$$\frac{1}{12}f_{i-1}'' + \frac{5}{6}f_i'' + \frac{1}{12}f_{i+1}'' = \frac{f_{i-1} - 2f_i + f_{i+1}}{h^2} + O(h^4) \quad (4.13)$$

Applying this scheme to the Laplace operator in two dimensions

$$\Delta = \frac{\partial^2}{\partial x^2} + \frac{\partial^2}{\partial y^2} \quad (4.14)$$

results in the following equation for all mesh points (i, j) in a two-dimensional computational domain

$$\begin{aligned} & \frac{1}{12} \left[\left(\frac{\partial^2 f}{\partial x^2} \right)_{i-1,j} + \left(\frac{\partial^2 f}{\partial x^2} \right)_{i+1,j} + \left(\frac{\partial^2 f}{\partial y^2} \right)_{i,j-1} + \left(\frac{\partial^2 f}{\partial y^2} \right)_{i,j+1} \right] + \frac{5}{6} \Delta f_{i,j} \\ &= \frac{f_{i-1,j} + f_{i+1,j} + f_{i,j-1} + f_{i,j+1} - 4f_{i,j}}{h^2} \end{aligned} \quad (4.15)$$

Equation (4.15) cannot be used as a discretization method for the Laplace operator, since the Laplace operator (4.14) appears just for mesh points (i, j) , not for the neighbors $(i \pm 1, j)$ and $(i, j \pm 1)$. To correct this, consider the expression that results from summation of the following finite-difference expressions

$$\begin{aligned} & \frac{1}{12} \left(\frac{\partial^2 f}{\partial x^2} \right)_{i-1,j-1} + \frac{5}{6} \left(\frac{\partial^2 f}{\partial x^2} \right)_{i,j-1} + \frac{1}{12} \left(\frac{\partial^2 f}{\partial x^2} \right)_{i+1,j-1} = \\ & \quad \frac{f_{i-1,j-1} - 2f_{i,j-1} + f_{i+1,j-1}}{h^2} + O(h^4) \\ & \frac{1}{12} \left(\frac{\partial^2 f}{\partial x^2} \right)_{i-1,j+1} + \frac{5}{6} \left(\frac{\partial^2 f}{\partial x^2} \right)_{i,j+1} + \frac{1}{12} \left(\frac{\partial^2 f}{\partial x^2} \right)_{i+1,j+1} = \\ & \quad \frac{f_{i-1,j+1} - 2f_{i,j+1} + f_{i+1,j+1}}{h^2} + O(h^4) \\ & \frac{1}{12} \left(\frac{\partial^2 f}{\partial y^2} \right)_{i-1,j-1} + \frac{5}{6} \left(\frac{\partial^2 f}{\partial y^2} \right)_{i-1,j} + \frac{1}{12} \left(\frac{\partial^2 f}{\partial y^2} \right)_{i-1,j+1} = \\ & \quad \frac{f_{i-1,j-1} - 2f_{i-1,j} + f_{i-1,j+1}}{h^2} + O(h^4) \\ & \frac{1}{12} \left(\frac{\partial^2 f}{\partial y^2} \right)_{i+1,j-1} + \frac{5}{6} \left(\frac{\partial^2 f}{\partial y^2} \right)_{i+1,j} + \frac{1}{12} \left(\frac{\partial^2 f}{\partial y^2} \right)_{i+1,j+1} = \\ & \quad \frac{f_{i+1,j-1} - 2f_{i+1,j} + f_{i+1,j+1}}{h^2} + O(h^4) \end{aligned} \quad (4.16)$$

Summation gives the expression

$$\begin{aligned} & \frac{1}{12} [\Delta f_{i-1,j-1} + \Delta f_{i+1,j-1} + \Delta f_{i-1,j+1} + \Delta f_{i+1,j+1}] + \\ & \frac{5}{6} \left[\left(\frac{\partial^2 f}{\partial x^2} \right)_{i,j-1} + \left(\frac{\partial^2 f}{\partial x^2} \right)_{i,j+1} + \left(\frac{\partial^2 f}{\partial y^2} \right)_{i-1,j} + \left(\frac{\partial^2 f}{\partial y^2} \right)_{i+1,j} \right] = \\ & \quad \frac{2}{h^2} [f_{i-1,j-1} + f_{i+1,j-1} + f_{i-1,j+1} + f_{i+1,j+1}] - \\ & \quad \frac{2}{h^2} [f_{i,j-1} + f_{i,j+1} + f_{i-1,j} + f_{i+1,j}] \end{aligned} \quad (4.17)$$

Combining equations (4.15) and (4.17), the following expression involving Laplace operators in the neighboring points can be obtained

$$\begin{aligned} & \frac{1}{120} [\Delta f_{i-1,j-1} + \Delta f_{i+1,j-1} + \Delta f_{i-1,j+1} + \Delta f_{i+1,j+1}] + \\ & \frac{1}{12} [\Delta f_{i-1,j} + \Delta f_{i+1,j} + \Delta f_{i,j-1} + \Delta f_{i,j+1}] + \frac{5}{6} \Delta f_{i,j} = \\ & \frac{1}{h^2} \left[\frac{1}{5} \{f_{i-1,j-1} + f_{i+1,j-1} + f_{i-1,j+1} + f_{i+1,j+1}\} - \right. \end{aligned}$$

$$-4f_{i,j} + \frac{4}{5} \{f_{i-1,j} + f_{i+1,j} + f_{i,j-1} + f_{i,j+1}\} \quad (4.18)$$

In equation (4.18), isolated second derivatives in either one of the spatial directions do not appear. Laplace operators in mesh point (i, j) and all its 8 neighbors are present, not just the 4 immediate neighbors. Rescaling and rewriting equation (4.18) in matrix notation leads to

$$\begin{pmatrix} \frac{1}{100} & \frac{1}{10} & \frac{1}{100} \\ \frac{1}{10} & 1 & \frac{1}{10} \\ \frac{1}{100} & \frac{1}{10} & \frac{1}{100} \end{pmatrix} \Delta f_{i,j} = \frac{1}{h^2} \begin{pmatrix} \frac{6}{25} & \frac{24}{25} & \frac{6}{25} \\ \frac{24}{25} & -\frac{24}{5} & \frac{24}{25} \\ \frac{6}{25} & \frac{24}{25} & \frac{6}{25} \end{pmatrix} f_{i,j} + O(h^4) \quad (4.19)$$

Here, the two-dimensional situation is analyzed. For the Laplace operator in three dimensions a similar analysis can be carried out.

Summarizing, this section shows:

- Straightforward application of one-dimensional compact finite-difference expressions does not lead to a useful expression involving the Laplace operators in a mesh point and that at its nearest neighbors. Instead, the nearest neighbors enter the equation as second-derivatives in just one of the spatial directions;
- Modifying the obtained equation to include Laplace operators in the nearest neighbors leads to equation (4.19), involving Laplace operators in a mesh point and that in all its neighbors;
- To derive compact finite-difference discretizations of Laplace operators in two and three dimensions, a derivation involving a two-dimensional or three-dimensional initial assumption of the form of the expression and a subsequent Taylor series matching is required.

4.4 Spatial discretization of 2D Laplace operator

The fourth-order accurate compact finite-difference stencil for the Laplace operator in two dimensions, which relates the Laplace operator in a point (i, j) and its 4 immediate neighbours $(i-1, j)$, $(i+1, j)$, $(i, j-1)$ and $(i, j+1)$, is assumed to have the following form:

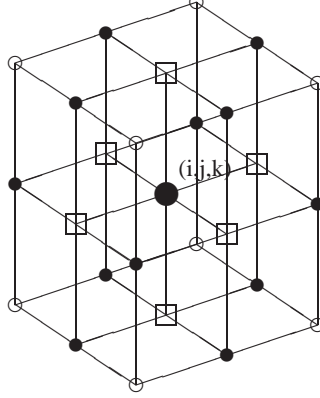
$$\begin{aligned} \Delta f_{i,j} + \alpha (\Delta f_{i-1,j} + \Delta f_{i+1,j} + \Delta f_{i,j-1} + \Delta f_{i,j+1}) = \\ a_1 \frac{f_{i-1,j} + f_{i+1,j} + f_{i,j-1} + f_{i,j+1} - 4f_{i,j}}{h^2} + \\ a_2 \frac{f_{i-1,j-1} + f_{i+1,j-1} + f_{i-1,j+1} + f_{i+1,j+1} - 4f_{i,j}}{2h^2} \end{aligned} \quad (4.20)$$

The two terms on the right-hand side of equation (4.20) are chosen such that Taylor series expansions up to fourth-order accuracy contain terms involving

$$\left(\frac{\partial^2 f}{\partial x^2} + \frac{\partial^2 f}{\partial y^2} \right)_{i,j}, \quad \left(\frac{\partial^4 f}{\partial x^4} + \frac{\partial^4 f}{\partial y^4} \right)_{i,j} \quad \text{and} \quad \left(\frac{\partial^4 f}{\partial x^2 \partial y^2} \right)_{i,j} \quad (4.21)$$

Matching corresponding coefficients gives the three equations for the unknowns α , a_1 and a_2 :

$$\begin{aligned} 1 + 4\alpha &= a_1 + a_2 \\ 12\alpha &= a_1 + a_2 \\ 4\alpha &= a_2 \end{aligned} \quad (4.22)$$

FIGURE 4.2: Stencil of compact-difference Laplace operator around node (i, j, k) .

Therefore, for a fourth-order accurate expression the coefficients are

$$\alpha = \frac{1}{8}, \quad a_1 = 1, \quad a_2 = \frac{1}{2} \quad (4.23)$$

Finally, the fourth-order accurate expression for the 2-D Laplace operator can be written in matrix notation as:

$$\begin{pmatrix} \frac{1}{8} & \frac{1}{8} & \frac{1}{8} \\ \frac{1}{8} & 1 & \frac{1}{8} \\ \frac{1}{8} & \frac{1}{8} & \frac{1}{8} \end{pmatrix} \Delta f_{i,j} = \frac{1}{h^2} \begin{pmatrix} \frac{1}{4} & 1 & \frac{1}{4} \\ 1 & -5 & 1 \\ \frac{1}{4} & 1 & \frac{1}{4} \end{pmatrix} f_{i,j} + O(h^4) \quad (4.24)$$

This equation was presented in Sun and Zhuang (1997), where a fast direct solver for Helmholtz equations with Neumann boundary conditions was derived.

4.5 Spatial discretization of 3D Laplace operator

The fourth-order accurate compact finite-difference stencil for the Laplace operator in three dimensions, which relates the Laplace operator in a point (i, j, k) and its 6 immediate neighbors $(i-1, j, k)$, $(i+1, j, k)$, $(i, j-1, k)$, $(i, j+1, k)$, $(i, j, k-1)$ and $(i, j, k+1)$, the points indicated as \square in figure 4.2, is assumed to have the following form:

$$\begin{aligned} \Delta f_{i,j,k} + \alpha (\Delta f_{i-1,j,k} + \Delta f_{i+1,j,k} + \Delta f_{i,j-1,k} + \Delta f_{i,j+1,k} + \Delta f_{i,j,k-1} + \Delta f_{i,j,k+1}) = \\ a_1 (f_{i-1,j,k} + f_{i+1,j,k} + f_{i,j-1,k} + f_{i,j+1,k} + f_{i,j,k-1} + f_{i,j,k+1} - 6f_{i,j,k})/h^2 + \\ \frac{a_2}{4} (f_{i-1,j-1,k} + f_{i-1,j+1,k} + f_{i+1,j-1,k} + f_{i+1,j+1,k} + \\ f_{i-1,j,k-1} + f_{i-1,j,k+1} + f_{i+1,j,k-1} + f_{i+1,j,k+1} + \\ f_{i,j-1,k-1} + f_{i,j-1,k+1} + f_{i,j+1,k-1} + f_{i,j+1,k+1} - 12f_{i,j,k})/h^2 + \\ \frac{a_3}{4} (f_{i-1,j-1,k-1} + f_{i-1,j+1,k-1} + f_{i+1,j-1,k-1} + f_{i+1,j+1,k-1} + \\ f_{i-1,j-1,k+1} + f_{i-1,j+1,k+1} + f_{i+1,j-1,k+1} + f_{i+1,j+1,k+1} - 8f_{i,j,k})/h^2 + O(h^4) \end{aligned} \quad (4.25)$$

Similar to the two-dimensional stencil of section 4.4, the parameters α , a_1 , a_2 and a_3 can be determined by matching Taylor series expansions.

The left-hand side of equation (4.25) can be expanded as

$$\begin{aligned}
& \Delta f_{i,j,k} + \alpha (\Delta f_{i-1,j,k} + \Delta f_{i+1,j,k} + \Delta f_{i,j-1,k} + \Delta f_{i,j+1,k} + \Delta f_{i,j,k-1} + \Delta f_{i,j,k+1}) \\
&= (1 + 6\alpha) \Delta f_{i,j,k} + \\
& \alpha h^2 \left[\frac{\partial^4 f}{\partial x^4} + \frac{\partial^4 f}{\partial y^4} + \frac{\partial^4 f}{\partial z^4} + 2 \left(\frac{\partial^4 f}{\partial x^2 \partial y^2} + \frac{\partial^4 f}{\partial x^2 \partial z^2} + \frac{\partial^4 f}{\partial y^2 \partial z^2} \right) \right]_{i,j,k} + O(h^4)
\end{aligned} \tag{4.26}$$

To obtain a fourth-order accurate stencil, the following Taylor series expansions are used for the right-hand side of equation (4.25):

- the term associated with a_1 , involving the 6 nodes indicated as \square in figure 4.2:

$$\begin{aligned}
& f_{i-1,j,k} + f_{i+1,j,k} + f_{i,j-1,k} + f_{i,j+1,k} + f_{i,j,k-1} + f_{i,j,k+1} - 6f_{i,j,k} \\
&= h^2 \Delta f_{i,j,k} + \\
& \frac{h^4}{12} \left[\frac{\partial^4 f}{\partial x^4} + \frac{\partial^4 f}{\partial y^4} + \frac{\partial^4 f}{\partial z^4} \right]_{i,j,k} + O(h^6)
\end{aligned} \tag{4.27}$$

- the term associated with a_2 , involving the 12 nodes depicted as \bullet in figure 4.2:

$$\begin{aligned}
& f_{i-1,j-1,k} + f_{i-1,j+1,k} + f_{i+1,j-1,k} + f_{i+1,j+1,k} + \\
& f_{i-1,j,k-1} + f_{i-1,j,k+1} + f_{i+1,j,k-1} + f_{i+1,j,k+1} + \\
& f_{i,j-1,k-1} + f_{i,j-1,k+1} + f_{i,j+1,k-1} + f_{i,j+1,k+1} - 12f_{i,j,k} \\
&= 4h^2 \Delta f_{i,j,k} + \\
& \frac{h^4}{3} \left[\frac{\partial^4 f}{\partial x^4} + \frac{\partial^4 f}{\partial y^4} + \frac{\partial^4 f}{\partial z^4} + 3 \left\{ \frac{\partial^4 f}{\partial x^2 \partial y^2} + \frac{\partial^4 f}{\partial x^2 \partial z^2} + \frac{\partial^4 f}{\partial y^2 \partial z^2} \right\} \right]_{i,j,k} + O(h^6)
\end{aligned} \tag{4.28}$$

- the term associated with a_3 , involving the 8 nodes depicted as \circ in figure 4.2:

$$\begin{aligned}
& f_{i-1,j-1,k-1} + f_{i-1,j+1,k-1} + f_{i+1,j-1,k-1} + f_{i+1,j+1,k-1} + \\
& f_{i-1,j-1,k+1} + f_{i-1,j+1,k+1} + f_{i+1,j-1,k+1} + f_{i+1,j+1,k+1} - 8f_{i,j,k} \\
&= 4h^2 \Delta f_{i,j,k} + \\
& h^4 \left[\frac{1}{3} \left\{ \frac{\partial^4 f}{\partial x^4} + \frac{\partial^4 f}{\partial y^4} + \frac{\partial^4 f}{\partial z^4} \right\} + 2 \left\{ \frac{\partial^4 f}{\partial x^2 \partial y^2} + \frac{\partial^4 f}{\partial x^2 \partial z^2} + \frac{\partial^4 f}{\partial y^2 \partial z^2} \right\} \right]_{i,j,k} + O(h^6)
\end{aligned} \tag{4.29}$$

For fourth-order accuracy, the Taylor series coefficients corresponding to terms involving the various even derivatives:

$$\Delta f_{i,j,k}, \quad \left(\frac{\partial^4 f}{\partial x^4} + \frac{\partial^4 f}{\partial y^4} + \frac{\partial^4 f}{\partial z^4} \right), \quad \left(\frac{\partial^4 f}{\partial x^2 \partial y^2} + \frac{\partial^4 f}{\partial x^2 \partial z^2} + \frac{\partial^4 f}{\partial y^2 \partial z^2} \right) \tag{4.30}$$

need to be matched. The following equations for the unknown coefficients result:

$$\begin{aligned}
a_1 + a_2 + a_3 &= (1 + 6\alpha) \\
a_1 + a_2 + a_3 &= 12\alpha \\
a_2 + 2a_3 &= 8\alpha
\end{aligned} \tag{4.31}$$

Solving system of equations (4.31) gives:

$$\alpha = \frac{1}{6}, \quad a_1 = \frac{2}{3} + \beta, \quad a_2 = \frac{4}{3} - 2\beta, \quad a_3 = \beta \tag{4.32}$$

with β a parameter, that can be chosen to eliminate the nodes of one of the three groups in the stencil and/or tune the behavior of the scheme in Fourier space. The choice $\beta = \frac{2}{3}$ would result in the cancellation of 12 nodes from the stencil, $\beta = 0$ would eliminate the 8 vertices of the stencil.

4.6 Fast 2D Poisson/Helmholtz solver

In this section, the spatial discretization of the two-dimensional Helmholtz equation

$$\frac{\partial^2 f}{\partial x^2} + \frac{\partial^2 f}{\partial y^2} - \lambda f(x, y) = r(x, y) \quad (4.33)$$

in a rectangular computational domain $\Omega = [0, L_x] \times [0, L_y]$ is studied. The domain contains the uniform mesh with nodes (i, j) , $i = 0, \dots, N_I$, $j = 0, \dots, N_J$. The mesh spacing $h = L_x/N_I = L_y/N_J$. A fourth-order accurate discretization for equation (4.33) in this domain based on compact finite-difference equation (4.24) will be derived, similar to that of Sun and Zhuang (1997).

To find a discretization for the Helmholtz equation (4.33), the left-hand side of equation (4.24) needs to be rewritten in terms of quantities in mesh point (i, j) by means of a Taylor series expansion. This gives

$$\frac{1}{h^2} \begin{pmatrix} \frac{1}{4} & 1 & \frac{1}{4} \\ 1 & -5 & 1 \\ \frac{1}{4} & 1 & \frac{1}{4} \end{pmatrix} f_{i,j} = \frac{3}{2} \Delta f_{i,j} + \frac{h^2}{8} \Delta^2 f_{i,j} + O(h^4) \quad (4.34)$$

Using equation (4.33), the terms involving Δf and $\Delta^2 f$ can be rewritten as

$$\begin{aligned} \Delta f_{i,j} &= r_{i,j} + \lambda f_{i,j} \\ \Delta^2 f_{i,j} &= \Delta r_{i,j} + \lambda r_{i,j} + \lambda^2 f_{i,j} \end{aligned} \quad (4.35)$$

Introducing relations (4.35) in equation (4.34) and moving all $f_{i,j}$ terms on the right-hand side to the left-hand side gives

$$\frac{1}{h^2} \begin{pmatrix} \frac{1}{4} & 1 & \frac{1}{4} \\ 1 & -d & 1 \\ \frac{1}{4} & 1 & \frac{1}{4} \end{pmatrix} f_{i,j} = \frac{3}{2} r_{i,j} + \frac{h^2}{8} (\lambda r_{i,j} + \Delta r_{i,j}) + O(h^4) \quad (4.36)$$

where the diagonal term d is given by

$$d = 5 + \frac{\lambda h^2 + 12}{8} \lambda h^2 \quad (4.37)$$

With an approximation of Δr of second-order accuracy or more, equation (4.36) is a fourth-order accurate discretization of the Helmholtz equation (4.33).

Applying equation (4.36) to the Helmholtz equation (4.33) on the domain Ω results in the following system of equations

$$\mathbf{A} \underline{f} = \frac{3}{2} h^2 \underline{r} + \frac{h^4}{8} (\lambda \underline{r} + \Delta \underline{r}) - \underline{u}_d - 2h \underline{u}_n + O(h^6) \quad (4.38)$$

where \underline{f} is a vector containing the unknown function values $f_{i,j}$, \underline{r} is the vector representing the forcing term of equation (4.33) in the mesh points with unknown function values.

Similarly, $\Delta \underline{r}$ is the vector containing the Laplacian of the forcing term in the mesh points. Vectors \underline{u}_d and \underline{u}_n are introduced to represent the prescribed Dirichlet and Neumann boundary conditions, respectively.

In equation (4.38), \mathbf{A} represents the sparse discretization matrix. In the various vectors of equation (4.38), a lexicographic numbering of the elements is used. With Dirichlet boundary conditions prescribed on all boundaries of domain Ω , the vectors have a length $(N_I - 1) \times (N_J - 1)$. In case Neumann boundary conditions are prescribed on a domain boundary, the function values at this boundary are unknowns that need to be included in the vectors.

4.6.1 Formulation of boundary conditions

Applying equation (4.36) to a problem with Dirichlet boundary conditions prescribed on all boundaries results in a linear system of equations of dimension $(N_I - 1) \times (N_J - 1)$. Using lexicographic numbering of the unknowns, vector \underline{f} is given by

$$\underline{f} = [\{f_{1,1}, \dots, f_{N_I-1,1}\}; \dots; \{f_{1,N_J-1}, \dots, f_{N_I-1,N_J-1}\}] \quad (4.39)$$

Then, $(N_I - 1) \times (N_J - 1)$ by $(N_I - 1) \times (N_J - 1)$ matrix \mathbf{A} in equation (4.38) has the following structure

$$\mathbf{A} = \begin{pmatrix} \mathbf{A}_1 & \mathbf{A}_2 & 0 & \dots & 0 & 0 & 0 \\ \mathbf{A}_2 & \mathbf{A}_1 & \mathbf{A}_2 & \dots & 0 & 0 & 0 \\ \vdots & \vdots & \vdots & & \vdots & \vdots & \vdots \\ 0 & 0 & 0 & \dots & \mathbf{A}_2 & \mathbf{A}_1 & \mathbf{A}_2 \\ 0 & 0 & 0 & \dots & 0 & \mathbf{A}_2 & \mathbf{A}_1 \end{pmatrix} \quad (4.40)$$

Where \mathbf{A}_1 and \mathbf{A}_2 are $(N_J - 1)$ by $(N_J - 1)$ matrices:

$$\mathbf{A}_1 = \begin{pmatrix} -d & 1 & 0 & \dots & 0 & 0 & 0 \\ 1 & -d & 1 & \dots & 0 & 0 & 0 \\ \vdots & \vdots & \vdots & & \vdots & \vdots & \vdots \\ 0 & 0 & 0 & \dots & 1 & -d & 1 \\ 0 & 0 & 0 & \dots & 0 & 1 & -d \end{pmatrix} \quad (4.41)$$

and

$$\mathbf{A}_2 = \begin{pmatrix} 1 & \frac{1}{4} & 0 & \dots & 0 & 0 & 0 \\ \frac{1}{4} & 1 & \frac{1}{4} & \dots & 0 & 0 & 0 \\ \vdots & \vdots & \vdots & & \vdots & \vdots & \vdots \\ 0 & 0 & 0 & \dots & \frac{1}{4} & 1 & \frac{1}{4} \\ 0 & 0 & 0 & \dots & 0 & \frac{1}{4} & 1 \end{pmatrix} \quad (4.42)$$

For Dirichlet boundary conditions, the 4 vertices of the computational domain give rise to the following elements of \underline{u}_d :

$$\begin{aligned} \underline{u}_d(1, 1) &= f_{0,1} + f_{1,0} && + \frac{1}{4} [f_{0,0} + f_{0,2} + f_{2,0}] \\ \underline{u}_d(N_I - 1, 1) &= f_{N_I,1} + f_{N_I-1,0} && + \frac{1}{4} [f_{N_I,0} + f_{N_I,2} + f_{N_I-2,0}] \\ \underline{u}_d(1, N_J - 1) &= f_{0,N_J-1} + f_{1,N_J} && + \frac{1}{4} [f_{0,N_J} + f_{0,N_J-2} + f_{2,N_J}] \\ \underline{u}_d(N_I - 1, N_J - 1) &= f_{N_I,N_J-1} + f_{N_I-1,N_J} && + \frac{1}{4} [f_{N_I,N_J} + f_{N_I,N_J-2} + f_{N_I-2,N_J}] \end{aligned} \quad (4.43)$$

where the indices indicate a position in the vector corresponding to the particular numbering of the unknowns. And similarly due to the 4 edges:

$$\begin{aligned}
\bar{u}_d(i, 1) &= f_{i,0} + \frac{1}{4} [f_{i-1,0} + f_{i+1,0}] & ; i = 2, \dots, N_I - 2 \\
\bar{u}_d(i, N_J - 1) &= f_{i,N_J} + \frac{1}{4} [f_{i-1,N_J} + f_{i+1,N_J}] & ; i = 2, \dots, N_I - 2 \\
\bar{u}_d(1, j) &= f_{0,j} + \frac{1}{4} [f_{0,j-1} + f_{0,j+1}] & ; j = 2, \dots, N_J - 2 \\
\bar{u}_d(N_I - 1, j) &= f_{N_I,j} + \frac{1}{4} [f_{N_I,j-1} + f_{N_I,j+1}] & ; j = 2, \dots, N_J - 2
\end{aligned} \tag{4.44}$$

The situation for Neumann boundary conditions is more complicated. Here, the case with a Neumann boundary condition on the $j = 0$ edge is considered as an example. Then, the function values along $j = 0$ are unknowns and the discretized system of equations has the form:

$$\mathbf{A} = \begin{pmatrix} \mathbf{A}_1 & 2\mathbf{A}_2 & 0 & \dots & 0 & 0 & 0 \\ \mathbf{A}_2 & \mathbf{A}_1 & \mathbf{A}_2 & \dots & 0 & 0 & 0 \\ \vdots & \vdots & \vdots & & \vdots & \vdots & \vdots \\ 0 & 0 & 0 & \dots & \mathbf{A}_2 & \mathbf{A}_1 & \mathbf{A}_2 \\ 0 & 0 & 0 & \dots & 0 & \mathbf{A}_2 & \mathbf{A}_1 \end{pmatrix} \tag{4.45}$$

Now, \mathbf{A} is a $N_J \times (N_I - 1)$ by $N_J \times (N_I - 1)$ matrix, where the $(N_I - 1)$ by $(N_I - 1)$ sub-matrices are identical to (4.41) and (4.42).

The contributions of the edge $j = 0$ to \bar{u}_n can be derived by applying equation (4.38) to nodes along this edge and eliminating mesh points in the stencil with $j = -1$ using the finite-difference expression

$$f_{i,1} - f_{i,-1} = 2h \left(\frac{\partial f}{\partial y} \right)_{i,0} + \frac{h^3}{3} \left(\frac{\partial^3 f}{\partial y^3} \right)_{i,0} + O(h^5) \tag{4.46}$$

The third-derivative in equation (4.46) can be rewritten as

$$\left(\frac{\partial^3 f}{\partial y^3} \right)_{i,0} = \frac{\partial}{\partial y} \left[\Delta f_{i,0} - \left(\frac{\partial^2 f}{\partial x^2} \right)_{i,0} \right] = \frac{\partial}{\partial y} \left[r_{i,0} + \lambda f_{i,0} - \left(\frac{\partial^2 f}{\partial x^2} \right)_{i,0} \right] \tag{4.47}$$

For the $j = 0$ edge the following system results

$$\begin{aligned}
\mathbf{A} f_{i,0} &= \frac{3}{2} h^2 r_{i,0} + \frac{h^4}{8} (\lambda r_{i,0} + \Delta r_{i,0}) + \\
& 2h \left[\frac{1}{4} \left(\frac{\partial f}{\partial y} \right)_{i-1,0} + \left(\frac{\partial f}{\partial y} \right)_{i,0} + \frac{1}{4} \left(\frac{\partial f}{\partial y} \right)_{i+1,0} \right] + \\
& \frac{h^3}{3} \left[\frac{1}{4} \left(\frac{\partial^3 f}{\partial y^3} \right)_{i-1,0} + \left(\frac{\partial^3 f}{\partial y^3} \right)_{i,0} + \frac{1}{4} \left(\frac{\partial^3 f}{\partial y^3} \right)_{i+1,0} \right] + O(h^5) \\
&= \frac{3}{2} h^2 r_{i,0} + \frac{h^4}{8} (\lambda r_{i,0} + \Delta r_{i,0}) + 2h \left[\frac{3}{2} \left(\frac{\partial f}{\partial y} \right)_{i,0} + \frac{h^2}{4} \left(\frac{\partial^3 f}{\partial x^2 \partial y} \right)_{i,0} \right] + \\
& \frac{h^3}{3} \left[\frac{\partial}{\partial y} \left\{ \frac{r_{i-1,0}}{4} + r_{i,0} + \frac{r_{i+1,0}}{4} \right\} + \right. \\
& \quad \left. \lambda \frac{\partial}{\partial y} \left\{ \frac{f_{i-1,0}}{4} + f_{i,0} + \frac{f_{i+1,0}}{4} \right\} - \right.
\end{aligned}$$

$$\frac{\partial^2}{\partial x^2} \left\{ \frac{1}{4} \left(\frac{\partial f}{\partial y} \right)_{i-1,0} + \left(\frac{\partial f}{\partial y} \right)_{i,0} + \frac{1}{4} \left(\frac{\partial f}{\partial y} \right)_{i+1,0} \right\} + O(h^5) \quad (4.48)$$

Expanding the last term of equation (4.48) around $(i, 0)$, the contribution to vector \underline{u}_n can be written as

$$\begin{aligned} \underline{u}_n(i, 0) = & -\frac{3}{2} \left(\frac{\partial f}{\partial y} \right)_{i,0} - \lambda \frac{h^2}{24} \left[\left(\frac{\partial f}{\partial y} \right)_{i-1,0} + 4 \left(\frac{\partial f}{\partial y} \right)_{i,0} + \left(\frac{\partial f}{\partial y} \right)_{i+1,0} \right] \\ & - \frac{h^2}{24} \left[\left(\frac{\partial r}{\partial y} \right)_{i-1,0} + 4 \left(\frac{\partial r}{\partial y} \right)_{i,0} + \left(\frac{\partial r}{\partial y} \right)_{i+1,0} \right] \end{aligned} \quad (4.49)$$

For the vertices $(1, 0)$ and $(N_I - 1, 0)$, an additional contribution results for \underline{u}_d .

4.6.2 Fast direct solution procedure

In this section, the solution of equation (4.33) subject to Dirichlet boundary conditions on this domain is studied.

The matrix \mathbf{A} in equation (4.40) can be tridiagonalized using either a Fast Sine Transform or a Fast Cosine Transform. Here, the Fast Sine Transform (FST) will be used.

$$\mathbf{A} = \mathbf{S} \mathbf{\Lambda} \mathbf{S}^{-1} \quad (4.50)$$

where \mathbf{S} is an $(N_I - 1) \times (N_J - 1)$ by $(N_I - 1) \times (N_J - 1)$ block-diagonal matrix with diagonal matrices \mathbf{S}_1 :

$$\mathbf{S}_1 = \begin{pmatrix} \sin\left(\frac{\pi}{N_I}\right) & \sin\left(\frac{2\pi}{N_I}\right) & \dots & \sin\left(\frac{(N_I-1)\pi}{N_I}\right) \\ \sin\left(\frac{2\pi}{N_I}\right) & \sin\left(\frac{4\pi}{N_I}\right) & \dots & \sin\left(\frac{2(N_I-1)\pi}{N_I}\right) \\ \vdots & \vdots & & \vdots \\ \sin\left(\frac{(N_I-1)\pi}{N_I}\right) & \sin\left(\frac{2(N_I-1)\pi}{N_I}\right) & \dots & \sin\left(\frac{(N_I-1)^2\pi}{N_I}\right) \end{pmatrix} \quad (4.51)$$

The matrix $\mathbf{\Lambda}$ has a block structure similar to \mathbf{A} , but with diagonal sub-matrices:

$$\mathbf{\Lambda} = \begin{pmatrix} \mathbf{\Lambda}_1 & \mathbf{\Lambda}_2 & 0 & \dots & 0 & 0 & 0 \\ \mathbf{\Lambda}_2 & \mathbf{\Lambda}_1 & \mathbf{\Lambda}_2 & \dots & 0 & 0 & 0 \\ \vdots & \vdots & \vdots & & \vdots & \vdots & \vdots \\ 0 & 0 & 0 & \dots & \mathbf{\Lambda}_2 & \mathbf{\Lambda}_1 & \mathbf{\Lambda}_2 \\ 0 & 0 & 0 & \dots & 0 & \mathbf{\Lambda}_2 & \mathbf{\Lambda}_1 \end{pmatrix} \quad (4.52)$$

Where $\mathbf{\Lambda}_1$ and $\mathbf{\Lambda}_2$ are $(N_I - 1)$ by $(N_I - 1)$ matrices:

$$\mathbf{\Lambda}_1 = \begin{pmatrix} \lambda_1^{(1)} & 0 & \dots & 0 \\ 0 & \lambda_1^{(2)} & \dots & 0 \\ \vdots & \vdots & & \vdots \\ 0 & 0 & \dots & \lambda_1^{(N_I-1)} \end{pmatrix} ; \quad \mathbf{\Lambda}_2 = \begin{pmatrix} \lambda_2^{(1)} & 0 & \dots & 0 \\ 0 & \lambda_2^{(2)} & \dots & 0 \\ \vdots & \vdots & & \vdots \\ 0 & 0 & \dots & \lambda_2^{(N_I-1)} \end{pmatrix} \quad (4.53)$$

The diagonal entries in matrices $\mathbf{\Lambda}_1$ and $\mathbf{\Lambda}_2$ in equation (4.53) can be computed from:

$$\mathbf{S}^{-1} \mathbf{A} = \mathbf{\Lambda} \mathbf{S}^{-1} \quad (4.54)$$

where \mathbf{S}^{-1} can be computed from

$$\mathbf{S}^{-1} = \frac{2}{N_I} \mathbf{S} \quad (4.55)$$

With the known matrix $\mathbf{\Lambda}$, the linear system of equations can be transformed into

$$\begin{aligned} \mathbf{A}\underline{f} &= \underline{b} \\ \downarrow \\ \mathbf{\Lambda}\underline{y} &= \mathbf{S}^{-1}\underline{b} \\ \downarrow \\ \underline{f} &= \mathbf{S}\underline{y} \end{aligned} \quad (4.56)$$

Due to the diagonal structure of the sub-matrices of $\mathbf{\Lambda}$, the vector \underline{y} in equation (4.56) can be computed from $(N_I - 1)$ independent tridiagonal systems of equations of size $(N_J - 1)$. In equation (4.56), the multiplications involving \mathbf{S}^{-1} and \mathbf{S} are not evaluated as matrix-vector multiplications. Fast Sine Transform routines are employed for this purpose.

4.7 Iterative 3D Poisson/Helmholtz solver

In this section, a fourth-order accurate spatial discretization for the Helmholtz equation

$$\left(\frac{\partial^2}{\partial x^2} + \frac{\partial^2}{\partial y^2} - \lambda \right) f(x, y, z) = r(x, y, z) \quad (4.57)$$

in a three-dimensional rectangular computational domain $\Omega = [0, L_x] \times [0, L_y] \times [0, L_z]$, with uniform mesh spacing h in all coordinate direction, is studied.

The number of mesh points in the three coordinate directions is N_I , N_J and N_K , respectively. Compact finite-difference expression (4.25) with coefficients (4.32) is used as basis

$$\begin{aligned} \Delta f_{i,j,k} + \frac{1}{6} \left\{ \Delta f_{i-1,j,k} + \Delta f_{i+1,j,k} + \Delta f_{i,j-1,k} + \Delta f_{i,j+1,k} + \Delta f_{i,j,k-1} + \Delta f_{i,j,k+1} \right\} = \\ \frac{1}{h^2} \left(\frac{2}{3} + \beta \right) (f_{i-1,j,k} + f_{i+1,j,k} + f_{i,j-1,k} + f_{i,j+1,k} + f_{i,j,k-1} + f_{i,j,k+1} - 6f_{i,j,k}) + \\ \frac{1}{4h^2} \left(\frac{4}{3} - 2\beta \right) (f_{i-1,j-1,k} + f_{i+1,j-1,k} + f_{i-1,j+1,k} + f_{i+1,j+1,k} + \\ f_{i-1,j,k-1} + f_{i+1,j,k-1} + f_{i-1,j,k+1} + f_{i+1,j,k+1} + \\ f_{i,j-1,k-1} + f_{i,j+1,k-1} + f_{i,j-1,k+1} + f_{i,j+1,k+1} - 12f_{i,j,k}) + \\ \frac{\beta}{4h^2} (f_{i-1,j-1,k-1} + f_{i+1,j-1,k-1} + f_{i-1,j+1,k-1} + f_{i+1,j+1,k-1} + \\ f_{i-1,j-1,k+1} + f_{i+1,j-1,k+1} + f_{i-1,j+1,k+1} + f_{i+1,j+1,k+1} - 8f_{i,j,k}) + O(h^4) \end{aligned} \quad (4.58)$$

Equation (4.58) can be used to solve the Helmholtz equation (4.57) by first developing the left-hand side of (4.58) into Taylor series expansions up to fourth-order accuracy, this gives:

$$\begin{aligned} \Delta f_{i,j,k} + \frac{1}{6} (\Delta f_{i-1,j,k} + \Delta f_{i+1,j,k} + \Delta f_{i,j-1,k} + \Delta f_{i,j+1,k} + \Delta f_{i,j,k-1} + \Delta f_{i,j,k+1}) \\ = 2\Delta f_{i,j,k} + \frac{h^2}{6} \Delta^2 f_{i,j,k} + O(h^4) \end{aligned} \quad (4.59)$$

Using equation (4.57), equation (4.59) can be written as

$$\begin{aligned} & \Delta f_{i,j,k} + \frac{1}{6} (\Delta f_{i-1,j,k} + \Delta f_{i+1,j,k} + \Delta f_{i,j-1,k} + \Delta f_{i,j+1,k} + \Delta f_{i,j,k-1} + \Delta f_{i,j,k+1}) \\ = & 2r_{i,j,k} + \frac{h^2}{6} (\lambda r_{i,j,k} + \Delta r_{i,j,k}) + \frac{1}{6} (12 + \lambda h^2) \lambda f_{i,j,k} + O(h^4) \end{aligned} \quad (4.60)$$

The function values on the right-hand side of equation (4.60) need to be moved to the left-hand side of equation (4.58), resulting in the following expression on a 27-point stencil

$$\begin{aligned} & \frac{1}{h^2} \left[-d f_{i,j,k} + \left(\frac{2}{3} + \beta \right) (f_{i-1,j,k} + f_{i+1,j,k} + f_{i,j-1,k} + f_{i,j+1,k} + f_{i,j,k-1} + f_{i,j,k+1}) + \right. \\ & \left(\frac{1}{3} - \frac{\beta}{2} \right) (f_{i-1,j-1,k} + f_{i+1,j-1,k} + f_{i-1,j+1,k} + f_{i+1,j+1,k} + \\ & f_{i-1,j,k-1} + f_{i+1,j,k-1} + f_{i-1,j,k+1} + f_{i+1,j,k+1} + \\ & f_{i,j-1,k-1} + f_{i,j+1,k-1} + f_{i,j-1,k+1} + f_{i,j+1,k+1}) + \\ & \frac{\beta}{4} (f_{i-1,j-1,k-1} + f_{i+1,j-1,k-1} + f_{i-1,j+1,k-1} + f_{i+1,j+1,k-1} + \\ & f_{i-1,j-1,k+1} + f_{i+1,j-1,k+1} + f_{i-1,j+1,k+1} + f_{i+1,j+1,k+1}) \left. \right] \\ = & 2r_{i,j,k} + \frac{h^2}{6} (\lambda r_{i,j,k} + \Delta r_{i,j,k}) + O(h^4) \end{aligned} \quad (4.61)$$

where diagonal element $d = (8 + 2\beta) + \frac{12 + \lambda h^2}{6} \lambda$. The evaluation of Δr in equation (4.61) thus needs to be of second-order accuracy only to guarantee fourth-order accuracy.

Applying equation (4.61) to the Helmholtz equation (4.57) on the domain Ω results in the following system of equations

$$\mathbf{A} \underline{f} = 2h^2 \underline{r} + \frac{h^4}{6} (\lambda \underline{r} + \Delta \underline{r}) - \underline{u}_d - 2h \underline{u}_n + O(h^6) \quad (4.62)$$

where similar to the two-dimensional situation, \underline{f} is a vector containing the unknown function values $f_{i,j,k}$, \underline{r} is the vector representing the forcing term of equation (4.57) in the mesh points with unknown function values and $\Delta \underline{r}$ is the vector containing the Laplacian of the forcing term in the mesh points. Dirichlet and Neumann boundary conditions are represented by the vectors \underline{u}_d and \underline{u}_n , respectively.

A lexicographic numbering of the vector elements is used, leading to vectors of length $(N_I - 1) \times (N_J - 1) \times (N_K - 1)$ when Dirichlet boundary conditions are prescribed on all boundaries of domain Ω . In this case, vector \underline{u}_n in equation (4.62) vanishes.

4.7.1 Formulation of boundary conditions

In case Dirichlet boundary conditions are prescribed, elements of \underline{u}_d are obtained by moving known function values from the left-hand side of equation (4.62) to the right-hand side. In this case, a lexicographic numbering of the unknown function values $f_{i,j,k}$ similar to (4.39) is used.

The contributions due to Neumann boundary conditions are represented as elements of the vector \underline{u}_n in equation (4.62). As in the two-dimensional case, the discussion of the implementation is restricted to one boundary. Here, the implementation of Neumann boundary conditions prescribed on the face $(0, j, k)$ is taken as representative for all domain boundaries.

An expression similar to (4.46) is used to eliminate nodes with $i = -1$:

$$f_{1,j,k} - f_{-1,j,k} = 2h \left(\frac{\partial f}{\partial x} \right)_{0,j,k} + \frac{h^3}{3} \left(\frac{\partial^3 f}{\partial x^3} \right)_{0,j,k} + O(h^5) \quad (4.63)$$

The third-derivative in equation (4.63) can be rewritten as

$$\begin{aligned} \left(\frac{\partial^3 f}{\partial x^3} \right)_{0,j,k} &= \frac{\partial}{\partial x} \left[\Delta f_{0,j,k} - \left(\frac{\partial^2 f}{\partial y^2} \right)_{0,j,k} - \left(\frac{\partial^2 f}{\partial z^2} \right)_{0,j,k} \right] \\ &= \frac{\partial}{\partial x} \left[r_{0,j,k} + \lambda f_{0,j,k} - \left(\frac{\partial^2 f}{\partial y^2} \right)_{0,j,k} - \left(\frac{\partial^2 f}{\partial z^2} \right)_{0,j,k} \right] \end{aligned} \quad (4.64)$$

For the face $i = 0$, equation (4.61) results in:

$$\begin{aligned} &-d f_{i,j,k} + \left(\frac{2}{3} + \beta \right) (2f_{1,j,k} + f_{0,j-1,k} + f_{0,j+1,k} + f_{0,j,k-1} + f_{0,j,k+1}) + \\ &\left(\frac{1}{3} - \frac{\beta}{2} \right) (2f_{1,j-1,k} + 2f_{1,j+1,k} + 2f_{1,j,k-1} + 2f_{1,j,k+1} + \\ &\quad f_{0,j-1,k-1} + f_{0,j+1,k-1} + f_{0,j-1,k+1} + f_{0,j+1,k+1}) + \\ &\quad \frac{\beta}{2} (f_{1,j-1,k-1} + f_{1,j+1,k-1} + f_{1,j-1,k+1} + f_{1,j+1,k+1}) \\ = &2h^2 r_{0,j,k} + \frac{h^4}{6} (\lambda r_{0,j,k} + \Delta r_{0,j,k}) + \\ &2h \left[\left(\frac{2}{3} + \beta \right) \left(\frac{\partial f}{\partial x} \right)_{0,j,k} + \right. \\ &\quad \left(\frac{1}{3} - \frac{\beta}{2} \right) \left\{ \left(\frac{\partial f}{\partial x} \right)_{0,j-1,k} + \left(\frac{\partial f}{\partial x} \right)_{0,j+1,k} + \right. \\ &\quad \left. \left(\frac{\partial f}{\partial x} \right)_{0,j,k-1} + \left(\frac{\partial f}{\partial x} \right)_{0,j,k+1} \right\} + \\ &\quad \frac{\beta}{4} \left\{ \left(\frac{\partial f}{\partial x} \right)_{0,j-1,k-1} + \left(\frac{\partial f}{\partial x} \right)_{0,j+1,k-1} + \right. \\ &\quad \left. \left(\frac{\partial f}{\partial x} \right)_{0,j-1,k+1} + \left(\frac{\partial f}{\partial x} \right)_{0,j+1,k+1} \right\} \left. \right] + \\ &\frac{h^3}{3} \left[\left(\frac{2}{3} + \beta \right) \left(\frac{\partial^3 f}{\partial x^3} \right)_{0,j,k} + \right. \\ &\quad \left(\frac{1}{3} - \frac{\beta}{2} \right) \left\{ \left(\frac{\partial^3 f}{\partial x^3} \right)_{0,j-1,k} + \left(\frac{\partial^3 f}{\partial x^3} \right)_{0,j+1,k} + \right. \\ &\quad \left. \left(\frac{\partial^3 f}{\partial x^3} \right)_{0,j,k-1} + \left(\frac{\partial^3 f}{\partial x^3} \right)_{0,j,k+1} \right\} + \\ &\quad \frac{\beta}{4} \left\{ \left(\frac{\partial^3 f}{\partial x^3} \right)_{0,j-1,k-1} + \left(\frac{\partial^3 f}{\partial x^3} \right)_{0,j+1,k-1} + \right. \\ &\quad \left. \left(\frac{\partial^3 f}{\partial x^3} \right)_{0,j-1,k+1} + \left(\frac{\partial^3 f}{\partial x^3} \right)_{0,j+1,k+1} \right\} \left. \right] + O(h^5) \end{aligned} \quad (4.65)$$

with $d = (8 + 2\beta) + \frac{12+\lambda h^2}{6}\lambda h^2$.

The additional term involving first derivatives of f can be rewritten as

$$2 \left(\frac{\partial f}{\partial x} \right)_{0,j,k} + \frac{h^2}{3} \left\{ \left(\frac{\partial^3 f}{\partial x \partial y^2} \right)_{0,j,k} + \left(\frac{\partial^3 f}{\partial x \partial z^2} \right)_{0,j,k} \right\} + O(h^4) \quad (4.66)$$

Using equation (4.64), the terms involving third-derivatives can be rewritten as

$$\begin{aligned} & \frac{\partial}{\partial x} \left[\left(\frac{2}{3} + \beta \right) r_{0,j,k} + \left(\frac{1}{3} - \frac{\beta}{2} \right) \left\{ r_{0,j-1,k} + r_{0,j+1,k} + r_{0,j,k-1} + r_{0,j,k+1} \right\} + \right. \\ & \quad \left. \frac{\beta}{4} \left\{ r_{0,j-1,k-1} + r_{0,j+1,k-1} + r_{0,j-1,k+1} + r_{0,j+1,k+1} \right\} \right] + \\ & \lambda \frac{\partial}{\partial x} \left[\left(\frac{2}{3} + \beta \right) f_{0,j,k} + \left(\frac{1}{3} - \frac{\beta}{2} \right) \left\{ f_{0,j-1,k} + f_{0,j+1,k} + f_{0,j,k-1} + f_{0,j,k+1} \right\} + \right. \\ & \quad \left. \frac{\beta}{4} \left\{ f_{0,j-1,k-1} + f_{0,j+1,k-1} + f_{0,j-1,k+1} + f_{0,j+1,k+1} \right\} \right] - \\ & \left(\frac{\partial^2}{\partial y^2} + \frac{\partial^2}{\partial z^2} \right) \left[\left(\frac{2}{3} + \beta \right) f_{0,j,k} + \left(\frac{1}{3} - \frac{\beta}{2} \right) \left\{ f_{0,j-1,k} + f_{0,j+1,k} + f_{0,j,k-1} + f_{0,j,k+1} \right\} + \right. \\ & \quad \left. \frac{\beta}{4} \left\{ f_{0,j-1,k-1} + f_{0,j+1,k-1} + f_{0,j-1,k+1} + f_{0,j+1,k+1} \right\} \right] \end{aligned} \quad (4.67)$$

The term $\left(\frac{\partial^2}{\partial y^2} + \frac{\partial^2}{\partial z^2} \right) \left[\right]$ in equation (4.67) can be reduced to

$$2 \left\{ \left(\frac{\partial^3 f}{\partial x \partial y^2} \right)_{0,j,k} + \left(\frac{\partial^3 f}{\partial x \partial z^2} \right)_{0,j,k} \right\} + O(h^2) \quad (4.68)$$

canceling the similar term in equation (4.66).

With equations (4.66) and (4.67), equation (4.65) can be written as

$$\begin{aligned} & -d f_{i,j,k} + \left(\frac{2}{3} + \beta \right) (2f_{1,j,k} + f_{0,j-1,k} + f_{0,j+1,k} + f_{0,j,k-1} + f_{0,j,k+1}) + \\ & \left(\frac{1}{3} - \frac{\beta}{2} \right) (2f_{1,j-1,k} + 2f_{1,j+1,k} + 2f_{1,j,k-1} + 2f_{1,j,k+1} + \\ & \quad f_{0,j-1,k-1} + f_{0,j+1,k-1} + f_{0,j-1,k+1} + f_{0,j+1,k+1}) + \\ & \quad \frac{\beta}{2} (f_{1,j-1,k-1} + f_{1,j+1,k-1} + f_{1,j-1,k+1} + f_{1,j+1,k+1}) \\ & = 2h^2 r_{0,j,k} + \frac{h^4}{6} (\lambda r_{0,j,k} + \Delta r_{0,j,k}) + 2h \underline{u}_n(0, j, k) + O(h^5) \end{aligned} \quad (4.69)$$

where

$$\begin{aligned} \underline{u}_n(0, j, k) &= 2 \left(\frac{\partial f}{\partial x} \right)_{0,j,k} + \\ & \quad \frac{h^2}{6} \left[\left(\frac{2}{3} + \beta \right) \left(\frac{\partial r}{\partial x} \right)_{0,j,k} + \right. \end{aligned}$$

$$\begin{aligned}
& \left(\frac{1}{3} - \frac{\beta}{2}\right) \left\{ \left(\frac{\partial r}{\partial x}\right)_{0,j-1,k} + \left(\frac{\partial r}{\partial x}\right)_{0,j+1,k} + \right. \\
& \quad \left. \left(\frac{\partial r}{\partial x}\right)_{0,j,k-1} + \left(\frac{\partial r}{\partial x}\right)_{0,j,k+1} \right\} + \\
& \frac{\beta}{4} \left\{ \left(\frac{\partial r}{\partial x}\right)_{0,j-1,k-1} + \left(\frac{\partial r}{\partial x}\right)_{0,j+1,k-1} + \right. \\
& \quad \left. \left(\frac{\partial r}{\partial x}\right)_{0,j-1,k+1} + \left(\frac{\partial r}{\partial x}\right)_{0,j+1,k+1} \right\} + \\
& \lambda \frac{h^2}{6} \left[\left(\frac{2}{3} + \beta\right) \left(\frac{\partial f}{\partial x}\right)_{0,j,k} + \right. \\
& \quad \left(\frac{1}{3} - \frac{\beta}{2}\right) \left\{ \left(\frac{\partial f}{\partial x}\right)_{0,j-1,k} + \left(\frac{\partial f}{\partial x}\right)_{0,j+1,k} + \right. \\
& \quad \left. \left(\frac{\partial f}{\partial x}\right)_{0,j,k-1} + \left(\frac{\partial f}{\partial x}\right)_{0,j,k+1} \right\} + \\
& \quad \frac{\beta}{4} \left\{ \left(\frac{\partial f}{\partial x}\right)_{0,j-1,k-1} + \left(\frac{\partial f}{\partial x}\right)_{0,j+1,k-1} + \right. \\
& \quad \left. \left(\frac{\partial f}{\partial x}\right)_{0,j-1,k+1} + \left(\frac{\partial f}{\partial x}\right)_{0,j+1,k+1} \right\} \Big] \tag{4.70}
\end{aligned}$$

As in the two-dimensional case, the contributions due to the Neumann boundary conditions can be written as elements of vector \underline{u}_n .

4.7.2 Iterative solution procedure

The linear systems of equations that result from application of the present compact finite-difference discretization method for the Poisson/Helmholtz equations are not suitable for a direct solution method. Instead, the systems are solved using an efficient iterative method. Here, the pre-conditioned Conjugate Gradient method, described in section 3.7, is used. The matrix-vector multiplications required in this Krylov method are implemented as well-designed systems of loops. In this case storage of matrix elements is not required.

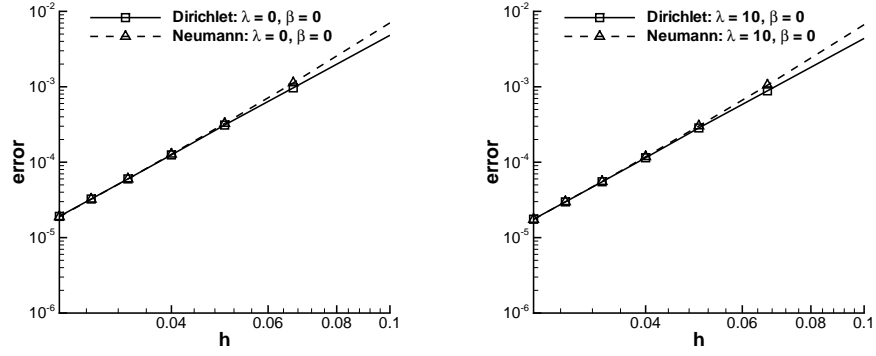
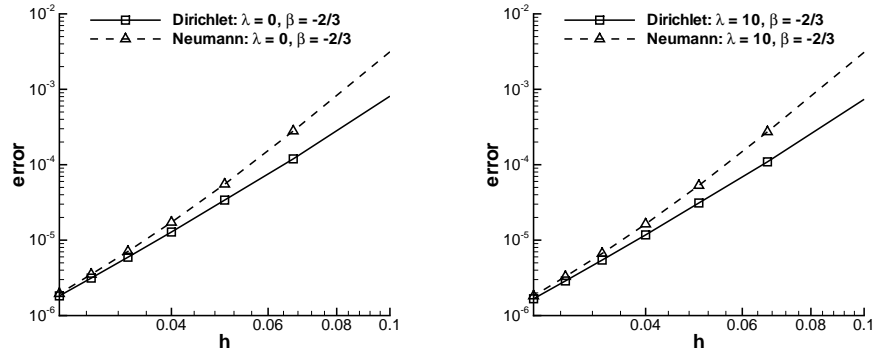
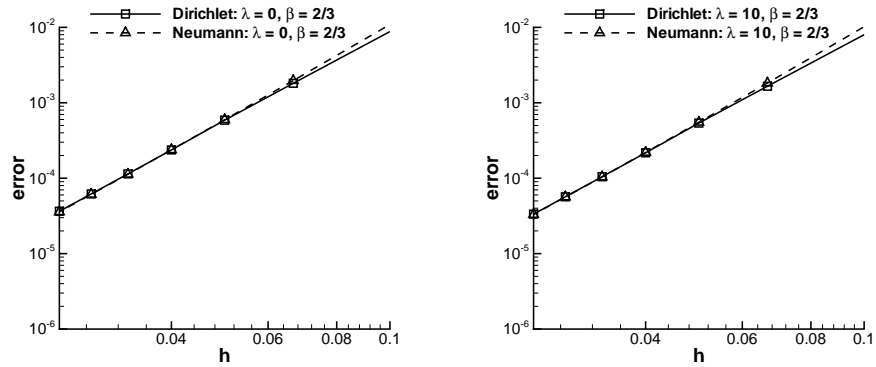
4.8 Application to 3D model problem

The accuracy of the three-dimensional Helmholtz solver, described in section 4.7, is analyzed by performing a mesh-refinement study for a problem with a known exact solution. The problem to be solved is the Helmholtz equation (4.57) in a three-dimensional rectangular computational domain $\Omega = [0, L_x] \times [0, L_y] \times [0, L_z]$, with uniform mesh spacing h in the three coordinate directions and $L_x = L_y = L_z = 1$. Thus, the mesh points are $(x, y, z)_{i,j,k} = h \cdot (i, j, k)$, with indices $i \in [0, \dots, N_I]$, $j \in [0, \dots, N_J]$ and $k \in [0, \dots, N_K]$. Here, $N_I = N_J = N_K$. The forcing term $r(x, y, z)$ on the right-hand side of equation (4.57) is given by

$$\begin{aligned}
r(x, y, z) &= -12\pi^2 \cos(2\pi x) \sin(2\pi y) \sin(2\pi z) \\
&\quad - \lambda \left[1 + x + \cos(2\pi x) \sin(2\pi y) \sin(2\pi z) \right] \tag{4.71}
\end{aligned}$$

with the exact solution of equation (4.57):

$$f(x, y, z) = 1 + x + \cos(2\pi x) \sin(2\pi y) \sin(2\pi z) \tag{4.72}$$

FIGURE 4.3: Maximum error for $\lambda = 0$ and $\lambda = 10$: $\beta = 0$ FIGURE 4.4: Maximum error for $\lambda = 0$ and $\lambda = 10$: $\beta = -\frac{2}{3}$ FIGURE 4.5: Maximum error for $\lambda = 0$ and $\lambda = 10$: $\beta = \frac{2}{3}$

Two sets of boundary conditions are considered:

TABLE 4.1: Results for model problem with exact solution (4.72) ($\beta = 0$).

Dirichlet: $\lambda = 0$				Neumann: $\lambda = 0$			
h	max. error	L_2 norm	iter	max. error	L_2 norm	iter	
$\frac{1}{10}$	$4.81351 \cdot 10^{-3}$	$6.28649 \cdot 10^{-5}$	15	$7.03758 \cdot 10^{-3}$	$8.83731 \cdot 10^{-5}$	6	
$\frac{1}{15}$	$9.67446 \cdot 10^{-4}$	$5.79165 \cdot 10^{-6}$	21	$1.12494 \cdot 10^{-3}$	$7.27796 \cdot 10^{-6}$	8	
$\frac{1}{20}$	$3.10890 \cdot 10^{-4}$	$1.10908 \cdot 10^{-6}$	26	$3.25727 \cdot 10^{-4}$	$1.36645 \cdot 10^{-6}$	11	
$\frac{1}{25}$	$1.24971 \cdot 10^{-4}$	$3.24600 \cdot 10^{-7}$	30	$1.27614 \cdot 10^{-4}$	$3.84024 \cdot 10^{-7}$	14	
$\frac{1}{30}$	$6.00456 \cdot 10^{-5}$	$1.11789 \cdot 10^{-7}$	34	$5.99446 \cdot 10^{-5}$	$1.37586 \cdot 10^{-7}$	17	
$\frac{1}{35}$	$3.24980 \cdot 10^{-5}$	$4.70629 \cdot 10^{-8}$	35	$3.23088 \cdot 10^{-5}$	$5.80508 \cdot 10^{-8}$	20	
$\frac{1}{40}$	$1.91310 \cdot 10^{-5}$	$2.22963 \cdot 10^{-8}$	38	$1.88639 \cdot 10^{-5}$	$2.75621 \cdot 10^{-8}$	24	

Dirichlet: $\lambda = 10$				Neumann: $\lambda = 10$			
h	max. error	L_2 norm	iter	max. error	L_2 norm	iter	
$\frac{1}{10}$	$4.37620 \cdot 10^{-3}$	$5.74069 \cdot 10^{-5}$	14	$6.65803 \cdot 10^{-3}$	$8.24150 \cdot 10^{-5}$	6	
$\frac{1}{15}$	$8.83647 \cdot 10^{-4}$	$5.31933 \cdot 10^{-6}$	21	$1.04945 \cdot 10^{-3}$	$6.72974 \cdot 10^{-6}$	8	
$\frac{1}{20}$	$2.84521 \cdot 10^{-4}$	$1.02030 \cdot 10^{-6}$	25	$3.01967 \cdot 10^{-4}$	$1.26084 \cdot 10^{-6}$	11	
$\frac{1}{25}$	$1.14448 \cdot 10^{-4}$	$2.87648 \cdot 10^{-7}$	29	$1.17992 \cdot 10^{-4}$	$3.54132 \cdot 10^{-7}$	14	
$\frac{1}{30}$	$5.50169 \cdot 10^{-5}$	$1.02951 \cdot 10^{-7}$	32	$5.53570 \cdot 10^{-5}$	$1.26854 \cdot 10^{-7}$	17	
$\frac{1}{35}$	$2.97817 \cdot 10^{-5}$	$4.33514 \cdot 10^{-8}$	35	$2.98176 \cdot 10^{-5}$	$5.35202 \cdot 10^{-8}$	20	
$\frac{1}{40}$	$1.75359 \cdot 10^{-5}$	$2.05409 \cdot 10^{-8}$	37	$1.74036 \cdot 10^{-5}$	$2.54109 \cdot 10^{-8}$	24	

- Dirichlet boundary conditions on all 6 faces of the computational domain. In this case, the coefficient matrix is symmetric and the approximate solution is obtained using the pre-conditioned Conjugate Gradient method;
- Neumann boundary conditions on the faces $i = 0$ and $i = N_I$ and Dirichlet boundary conditions on the 4 other faces. Therefore:

$$\begin{aligned}
\left(\frac{\partial f}{\partial x}\right)_{0,j,k} &= \left(\frac{\partial f}{\partial x}\right)_{N_I,j,k} = 1 \\
\left(\frac{\partial r}{\partial x}\right)_{0,j,k} &= \left(\frac{\partial r}{\partial x}\right)_{N_I,j,k} = -\lambda
\end{aligned} \tag{4.73}$$

Thus, function $f(x, y, z)$ has a non-zero slope on the faces $i = 0$ and $i = N_I$. For $\lambda \neq 0$, the derivative of the forcing term $r(x, y, z)$ is non-zero as well. Therefore, the formulation for the Neumann boundary conditions described in section 4.7 can be properly tested with this model problem.

The coefficient matrix is non-symmetric for this case and the pre-conditioned Bi-Conjugate Gradient method is used to obtain the approximate solution.

For both the Conjugate Gradient and Bi-Conjugate Gradient method, a simple Jacobi preconditioner is used. Results are compared for both types of boundary conditions, for:

- meshes with different mesh widths: h is varied from 0.1 to 0.025;
- $\lambda = 0$ and $\lambda = 10$;
- different values of the coefficient β : $\beta = 0$, $\beta = -\frac{2}{3}$ and $\beta = \frac{2}{3}$ are considered, eliminating the 8 mesh points depicted as \circ , the 6 mesh points indicated as \square and the 12 points depicted as \bullet in the finite-difference stencil shown in figure 4.2, respectively.

The results are summarized in table 4.1 for $\beta = 0$, in table 4.2 for $\beta = -\frac{2}{3}$ and in table 4.3 for $\beta = \frac{2}{3}$. The tables show the maximum deviation from the exact solution (4.72), the L_2 norm of the error and the number of iterations required for convergence of the (Bi)-Conjugate Gradient solver to a tolerance of 10^{-12} for a mesh width that is decreased from $h = 0.1$ to $h = 0.025$. Figure 4.3 shows the dependence of the maximum error with mesh width for

TABLE 4.2: Results for model problem with exact solution (4.72) ($\beta = -\frac{2}{3}$).

Dirichlet: $\lambda = 0$				Neumann: $\lambda = 0$			
h	max. error	L_2 norm	iter	max. error	L_2 norm	iter	
$\frac{1}{10}$	$8.09828 \cdot 10^{-4}$	$1.08460 \cdot 10^{-5}$	14	$3.14025 \cdot 10^{-3}$	$3.19297 \cdot 10^{-5}$	6	
$\frac{1}{15}$	$1.19493 \cdot 10^{-4}$	$7.37307 \cdot 10^{-7}$	21	$2.79455 \cdot 10^{-4}$	$1.38688 \cdot 10^{-6}$	8	
$\frac{1}{20}$	$3.39588 \cdot 10^{-5}$	$1.22886 \cdot 10^{-7}$	26	$5.51676 \cdot 10^{-5}$	$1.86440 \cdot 10^{-7}$	11	
$\frac{1}{25}$	$1.28136 \cdot 10^{-5}$	$3.22772 \cdot 10^{-8}$	34	$1.72242 \cdot 10^{-5}$	$4.44708 \cdot 10^{-8}$	13	
$\frac{1}{30}$	$5.93874 \cdot 10^{-6}$	$1.11038 \cdot 10^{-8}$	45	$7.08112 \cdot 10^{-6}$	$1.46250 \cdot 10^{-8}$	17	
$\frac{1}{35}$	$3.13958 \cdot 10^{-6}$	$4.56447 \cdot 10^{-8}$	48	$3.51712 \cdot 10^{-6}$	$5.87807 \cdot 10^{-9}$	22	
$\frac{1}{40}$	$1.82233 \cdot 10^{-6}$	$2.12921 \cdot 10^{-9}$	59	$1.95263 \cdot 10^{-6}$	$2.70937 \cdot 10^{-9}$	30	

Dirichlet: $\lambda = 10$				Neumann: $\lambda = 10$			
h	max. error	L_2 norm	iter	max. error	L_2 norm	iter	
$\frac{1}{10}$	$7.36139 \cdot 10^{-4}$	$9.96129 \cdot 10^{-6}$	14	$3.09625 \cdot 10^{-3}$	$3.11138 \cdot 10^{-5}$	6	
$\frac{1}{15}$	$1.09139 \cdot 10^{-4}$	$6.79839 \cdot 10^{-7}$	20	$2.72758 \cdot 10^{-4}$	$1.32704 \cdot 10^{-6}$	8	
$\frac{1}{20}$	$3.10893 \cdot 10^{-5}$	$1.13304 \cdot 10^{-7}$	25	$5.29991 \cdot 10^{-5}$	$1.75530 \cdot 10^{-7}$	11	
$\frac{1}{25}$	$1.17384 \cdot 10^{-5}$	$2.97547 \cdot 10^{-8}$	34	$1.63333 \cdot 10^{-5}$	$4.14872 \cdot 10^{-8}$	13	
$\frac{1}{30}$	$5.44275 \cdot 10^{-6}$	$1.02348 \cdot 10^{-8}$	42	$6.65485 \cdot 10^{-6}$	$1.35789 \cdot 10^{-8}$	17	
$\frac{1}{35}$	$2.87737 \cdot 10^{-6}$	$4.20699 \cdot 10^{-9}$	48	$3.28571 \cdot 10^{-6}$	$5.44366 \cdot 10^{-9}$	23	
$\frac{1}{40}$	$1.67047 \cdot 10^{-6}$	$1.96240 \cdot 10^{-9}$	57	$1.81723 \cdot 10^{-6}$	$2.50547 \cdot 10^{-9}$	29	

$\lambda = 0$ and $\lambda = 10$, for coefficient $\beta = 0$. Figures 4.4 and 4.5 show similar results for coefficient $\beta = -\frac{2}{3}$ and $\beta = \frac{2}{3}$, respectively.

In figures 4.3, 4.4 and 4.5 the maximum deviation from the exact solution has a linear dependence in a double logarithmic axis system for the finer meshes. From the slope of these curves, it can be seen that the maximum error behaves asymptotically as $O(h^4)$. The numerical error is slightly larger when Neumann boundary conditions are prescribed on part of

TABLE 4.3: Results for model problem with exact solution (4.72) ($\beta = \frac{2}{3}$).

Dirichlet: $\lambda = 0$				Neumann: $\lambda = 0$		
h	max. error	L_2 norm	iter	max. error	L_2 norm	iter
$\frac{1}{10}$	$8.78799 \cdot 10^{-3}$	$1.14734 \cdot 10^{-4}$	15	$1.09014 \cdot 10^{-2}$	$1.46626 \cdot 10^{-4}$	6
$\frac{1}{15}$	$1.81418 \cdot 10^{-3}$	$1.08422 \cdot 10^{-5}$	23	$1.96898 \cdot 10^{-3}$	$1.32219 \cdot 10^{-5}$	10
$\frac{1}{20}$	$5.87690 \cdot 10^{-4}$	$2.09498 \cdot 10^{-6}$	29	$5.96140 \cdot 10^{-4}$	$2.54925 \cdot 10^{-6}$	15
$\frac{1}{25}$	$2.37108 \cdot 10^{-4}$	$5.92601 \cdot 10^{-7}$	35	$2.37980 \cdot 10^{-4}$	$7.23811 \cdot 10^{-7}$	18
$\frac{1}{30}$	$1.14148 \cdot 10^{-4}$	$2.12467 \cdot 10^{-7}$	40	$1.12803 \cdot 10^{-4}$	$2.60575 \cdot 10^{-7}$	23
$\frac{1}{35}$	$6.18550 \cdot 10^{-5}$	$8.95594 \cdot 10^{-8}$	42	$6.10989 \cdot 10^{-5}$	$1.10228 \cdot 10^{-7}$	27
$\frac{1}{40}$	$3.64398 \cdot 10^{-5}$	$4.24628 \cdot 10^{-8}$	45	$3.57746 \cdot 10^{-5}$	$5.24155 \cdot 10^{-8}$	32

Dirichlet: $\lambda = 10$				Neumann: $\lambda = 10$		
h	max. error	L_2 norm	iter	max. error	L_2 norm	iter
$\frac{1}{10}$	$7.99145 \cdot 10^{-3}$	$1.04796 \cdot 10^{-4}$	11	$1.01919 \cdot 10^{-2}$	$1.35613 \cdot 10^{-4}$	6
$\frac{1}{15}$	$1.65711 \cdot 10^{-3}$	$9.95676 \cdot 10^{-6}$	22	$1.82493 \cdot 10^{-3}$	$1.21898 \cdot 10^{-5}$	11
$\frac{1}{20}$	$5.37844 \cdot 10^{-4}$	$1.92709 \cdot 10^{-6}$	29	$5.50810 \cdot 10^{-4}$	$2.34925 \cdot 10^{-6}$	14
$\frac{1}{25}$	$2.17140 \cdot 10^{-4}$	$5.45511 \cdot 10^{-7}$	34	$2.19629 \cdot 10^{-4}$	$6.67045 \cdot 10^{-7}$	19
$\frac{1}{30}$	$1.04587 \cdot 10^{-4}$	$1.95660 \cdot 10^{-7}$	39	$1.04054 \cdot 10^{-4}$	$2.40163 \cdot 10^{-7}$	23
$\frac{1}{35}$	$5.66849 \cdot 10^{-5}$	$8.24943 \cdot 10^{-8}$	42	$5.63480 \cdot 10^{-5}$	$1.01602 \cdot 10^{-7}$	27
$\frac{1}{40}$	$3.34009 \cdot 10^{-5}$	$3.91189 \cdot 10^{-8}$	45	$3.29895 \cdot 10^{-5}$	$4.83173 \cdot 10^{-8}$	31

the domain boundary than for Dirichlet boundary conditions on all 6 faces of the computational domain. The effect of increasing λ is to enhance convergence of the iterative solution method, as a result of the more favourable condition number when a larger diagonal element is present in the coefficient matrix. Furthermore, the numerical error is somewhat smaller for a larger value of parameter λ .

The asymptotic 4th-order behaviour is not affected by changes in parameter β . However, both the magnitude of the maximum error from the exact solution and the convergence behaviour of the (Bi)-Conjugate Gradient method change with changing β . The numerical errors for $\beta = \frac{2}{3}$ (which eliminates 12 mesh points from the finite-difference stencil) can be seen to be larger than for $\beta = 0$ and $\beta = -\frac{2}{3}$, for both Dirichlet and Dirichlet/Neumann boundary conditions prescribed on the boundary of the computational domain. The convergence behaviour of the (Bi)-Conjugate Gradient method is in general most favourable for $\beta = 0$.

Summarizing, it can be concluded that the discretization method developed for the Poisson/Helmholtz equations is in fact a 4th-order accurate method for the two combinations of prescribed boundary conditions considered here, i.e. Dirichlet on all 6 faces and a combination of Dirichlet and Dirichlet/Neumann boundary conditions prescribed on the computational domain. Parameter β affects both the magnitude of the numerical error and the convergence behaviour of the iterative linear-system solver.

RESULTS FOR CROW INSTABILITY



This chapter presents a numerical study of the long-wavelength instability in a counter-rotating vortex pair, commonly known as Crow instability. In chapter 1, the Crow instability was introduced as one of two branches of cooperative instabilities predicted by linear stability theory for a counter-rotating vortex pair, see section 1.3. Figure 1.1 shows a manifestation of this long-wavelength instability in an aircraft wake vortex pair. The figure shows the condensation trails in the wake of an aircraft. The trails result from the condensation of water vapour present in the engine exhaust gases. A part of the condensation products is subsequently entrained in the trailing vortices. This phenomenon enables an observation of some of the features of the Crow instability. The most notable features that can be seen from the sequence of plots of figure 1.1 are the occurrence of growing sinusoidal perturbations and the subsequent formation of ring-like structures.

The linear stability of the counter-rotating vortex pair was investigated in chapter 2, predicting an exponential growth of the initial infinitesimal symmetric sinusoidal perturbations of the vortex pair.

In the present study, the initial phase of the evolution of the instability, characterized by the exponential growth of the sinusoidal perturbations, is referred to as the *linear* stage of the development. For large perturbation amplitudes, not governed by the linear stability theory, more complicated flow features occur. Examples are the vortex reconnection and vortex-ring formation shown in figure 1.1. This phase of the evolution is referred to as the *nonlinear* stage of the development. Based on numerical results, the characteristic features of the nonlinear stage of the long-wavelength instability are discussed in section 5.5, showing more details of the vortical flow field at these later stages of the development than a visualization by condensation trails typically observed in the atmosphere reveals.

In the present study, the temporal evolution of a single mode of the long-wavelength instability is studied, i.e. the size of the computational domain in the axial direction is chosen equal to one wavelength of the most amplified mode predicted by the linear stability theory. Similar numerical studies have been performed in the past by various researchers. A number of these previous studies are reviewed in section 5.1, which describes the objective of the present numerical study and the relation with the reviewed previous work.

Section 5.2 lists the numerical simulations that are discussed in this chapter.

The determination of the initial condition used in the numerical simulations is described in detail in section 5.3. Based on this method for the initialization of the flow field, a number

of numerical results are described in this chapter. These results have been obtained using the two Navier-Stokes methods for three-dimensional flow described in chapter 3.

The parallel method, described in section 3.5, is mainly used for the numerical simulation of the linear stages of the development of the instability. Numerical results for this stage of the development of the Crow instability are discussed in section 5.4. The numerical results are compared with the results predicted by linear stability theory for the wavelength considered. For small sinusoidal perturbations on each of the vortices, the initial growth should match the exponential growth rate of the linear stability theory.

Numerical results for the nonlinear stage of the development of the Crow instability are discussed in section 5.6. Because of the higher computational efficiency of the hybrid Navier-Stokes method, described in section 3.6, the hybrid method is used for the numerical simulation of the nonlinear stage of the instability.

The discussion of the numerical results for the long-wavelength instability focuses on the physical aspects of the instability as well as on numerical aspects of high-resolution simulations of this instability.

5.1 Review of previous work

The numerical results presented and discussed in this chapter investigate the long-wavelength instability in a counter-rotating vortex pair. Cooperative instabilities in vortex pairs have been studied extensively in the past, experimentally, theoretically and numerically. Some work on the long-wavelength instability was reviewed in section 1.3.1. Theoretical work on the long-wavelength instability is usually based on linear stability theory with the vortices forming the vortex pair represented as vortex filaments, see sections 2.1 and 2.3. The experimental work most relevant to this study is that of Leweke and Williamson (1998). These researchers presented visualizations of cooperative instabilities in a vortex pair with a spacing and a Reynolds number similar to the ones employed in the numerical simulations performed in the present study.

The numerical work presented in the past, mainly focuses on the dynamics of vortex pairs at Reynolds numbers, based on circulation, that are orders of magnitude lower than that for the trailing vortex wake of an aircraft in cruise flight. A fully resolved simulation of the trailing vortex wake, at a Reynolds number characteristic of the cruise flight condition, is not feasible with the currently available computer resources. In case predictions of trailing-vortex evolution, that are relevant for flight conditions, are required, an extrapolation to higher Reynolds numbers needs to be performed.

As stated in section 1.3.1, the interaction of the Crow instability with either ambient turbulence or stratification has been studied extensively by various researchers. Effects of ambient turbulence on the evolution of the Crow instability are studied in, for example, Risso et al. (1997), Proctor (1996), Holzäpfel (1999) and Corjon et al. (1999). Typically, numerical simulations of vortex pairs immersed in a turbulent atmosphere require the computational domain to include more than one wavelength of the most amplified instability mode in the axial direction. The ambient turbulence interacts with the long-wavelength instability to form structures at length-scales different from the wavelength of the most amplified instabil-

ity mode. Limiting the computational domain to one wavelength of the most amplified mode obtained from linear stability theory would therefore impose an unphysical constraint on the evolution of the flow field.

A consequence of using such a large computational domain is that the small-scale structures in the flow field are relatively coarsely resolved, since the total number of grid points is limited by the restrictions on computation time. As a result, these studies typically use a Large Eddy Simulation model to achieve meaningful results. The numerical methods used in the present study do not include a Large Eddy sub-grid scale model or any other turbulence model, and are therefore limited to low-Reynolds number flows.

The effect of stratification was studied in, for example, Garten et al. (2001), Robins and Delisi (1998) and Daracq et al. (1999). The effects of stratification on the evolution of the long-wavelength instability, for the vortex-pair spacings and Reynolds numbers typical for numerical studies, are fairly well understood.

In the present work, effects of stratification are not included either. Instead, the focus is on the evolution of the long-wavelength instability in an unstratified medium. Effects of ambient turbulence are similarly excluded. The present chapter discusses the details of the flow field during the evolution of the Crow instability over long time-intervals using high-resolution simulations. Furthermore, the computational aspects of these simulations are subject of study.

The work by Garten et al. (2001) includes a number of high-resolution results for the

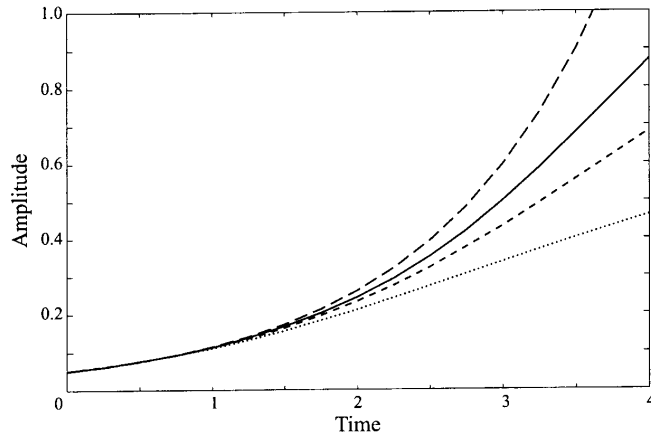


FIGURE 5.1: *Results from Garten et al. (2001): evolution of instability amplitude for a pair of Lamb-Oseen vortices ($r_c/b = 0.098$), for $Re = 628$ (dotted), 942 (short-dashed) and 1260 (solid). Theoretical prediction by Crow (1970) indicated with long-dashed line. Amplitude is plotted in terms of b .*

unstratified situation. These authors studied a pair of Lamb-Oseen vortices with a spacing such that $r_c/b = 0.098$. For this aspect ratio, linear stability theory predicts a wavelength of the most amplified instability mode $\lambda = 8.6 b$ and an inclination of the perturbations with

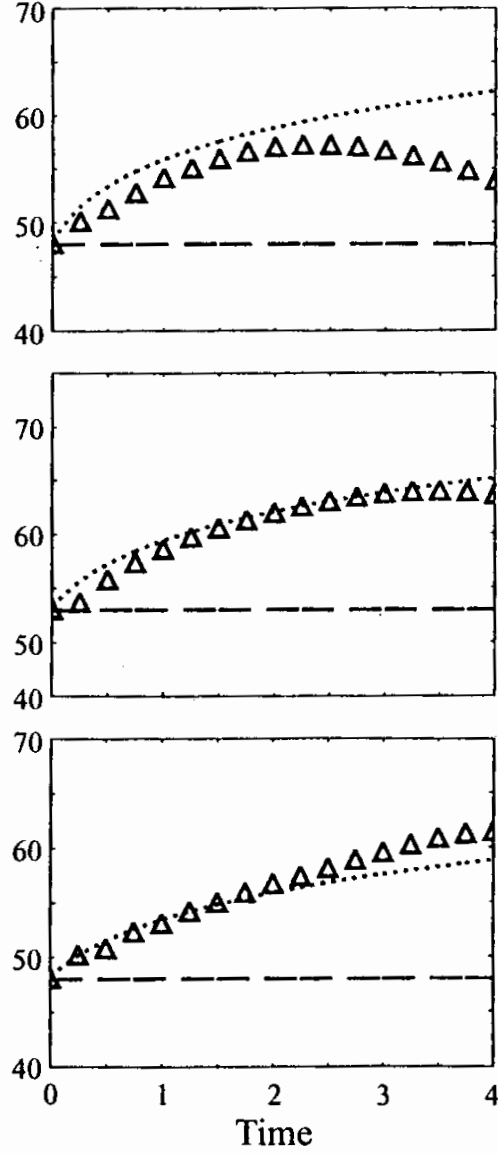


FIGURE 5.2: Results from Garten *et al.* (2001): inclination angle ($^\circ$) versus non-dimensional time. Shown are results for three Reynolds numbers: 628 (top), 942 (middle) and 1260 (bottom)

respect to the horizontal of 48° . Both the linear regime and the vortex-reconnection phase were studied in detail. Some of their results for the unstratified situation are summarized in figures 5.1 and 5.2. Figure 5.1 shows the evolution of the instability amplitude versus non-dimensional time for Reynolds numbers $Re_\Gamma = 628, 942$ and 1260 compared to the inviscid

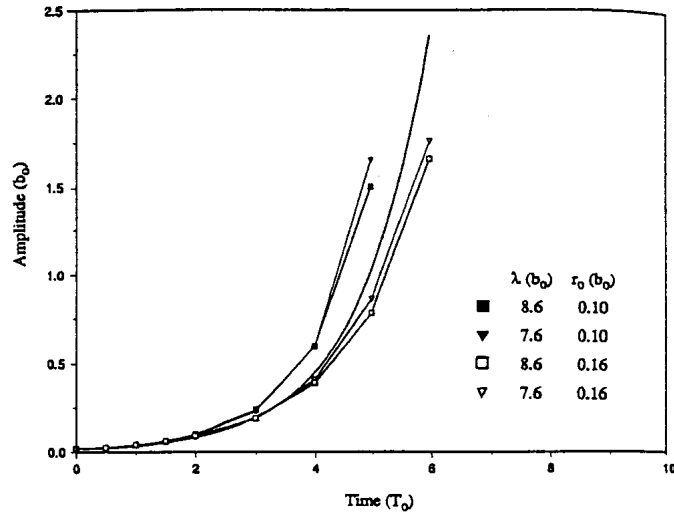


FIGURE 5.3: Results from Robins and Delisi (1997): growth-rate of perturbation, $Re = 2930$.

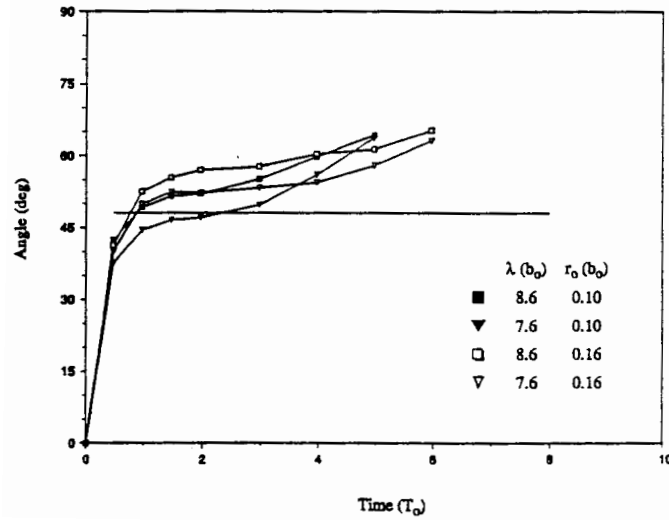


FIGURE 5.4: Results from Robins and Delisi (1997): increase of inclination angle, $Re = 2930$, compared to theoretical prediction shown as solid horizontal line. (initial perturbation in horizontal plane)

theoretical prediction by Crow (1970). It can be observed that as the Reynolds number increases the agreement with the prediction by Crow (1970) improves as a result of the smaller rate of viscous decay of the vortices.

Time is non-dimensionalized using the same method as used in the present study. Simi-

larly, figure 5.2 shows the evolution of the inclination angle of the perturbations for the three Reynolds numbers. In this figure, triangles indicate the computed inclination angle. A rapid increase of the inclination angle can be observed relative to the inclination angle of about 45° for the linear stability theory. Depending on Reynolds number, the inclination angle at the time of commencement of vortex reconnection is around 60 to 65° . This increase in inclination angle can be (partly) attributed to the increase in vortex core radius, resulting from viscous diffusion. The figure compares the computed inclination angle with a theoretical prediction without including the effect of the vortex-core increase (long-dashed lines) and with inclusion of this viscous effect (dotted lines). It can be observed that inclusion of the effect of the increase in vortex core radius gives the correct trend in that it increases the inclination angle.

The work by Garten et al. (2001), introduces a characteristic time-scale of vortex reconnection based on the circulation of each of the vortex tubes at the position of furthest separation and that of closest approach of the vortices. In their work, the circulation of the vortex tube with positive vorticity at the position of furthest separation is denoted by Γ_f and the circulation at the position of closest approach of the vortices by Γ_c . Γ_c reduces during the vortex-reconnection process as a result of viscous diffusion canceling vorticity of opposite signs of the two vortex tubes. The characteristic time-scale of vortex reconnection t_R is the negative inverse of $\frac{d\Gamma_c}{dt}$ at the instant in time when $\Gamma_c = \Gamma_f/2$. The results presented in Garten et al. (2001) show that $t_R \sim 1/Re$ for the unstratified situation. Furthermore, it was shown that a larger Re delays the onset of the vortex reconnection and increases the rate at which the reconnection proceeds once it does commence.

The results presented by Garten et al. (2001) were obtained using a spectral Navier-Stokes method using Fourier collocation techniques in the three spatial directions. Simulations were presented for Reynolds numbers in the range of 628 to 1260 using spatial resolutions varying from $128 \times 128 \times 256$ Fourier modes to $256 \times 256 \times 512$ Fourier modes, with the z -coordinate coinciding with the vertical direction. For the vortex core radius chosen by Garten et al. (2001), i.e. $r_c/b = 0.098$, the number of grid points per core radius varies from 2.3 to 4.5 for the different meshes. This shows that for the kind of spatial resolutions used here, high-order accurate spatial discretization techniques are needed, since for the number of grid points per core radius used here, a second-order accurate method would have far too much numerical dissipation.

For the finest mesh and $Re = 1260$, these authors note that the spatial resolution was such that decreasing the spatial resolution by a factor of 4 in each spatial direction and applying a spatial filter (the upper half of the wave number was zeroed every 30 time steps), resulted in a change of the numerical results of only a few per cent for the amplitude of the instability and position of the vortex tubes. Thus, for the spatial discretization technique used by Garten et al. (2001), 2.3 to 4.5 grid points per core radius gives an adequate spatial resolution. The results are therefore well-suited for comparison with the results presented in this chapter.

Another numerical study describing numerical results for the evolution of the Crow instability in the unstratified situation, is the study by Robins and Delisi (1997). These authors studied a vortex pair consisting of Lamb-Oseen vortices at aspect ratio $r_c/b = 0.16$ and a pair of vortices with uniform cores at aspect ratio $r_c/b = 0.10$. Prescribed wavelengths of $7.6 b$ and $8.6 b$ were considered. The results were computed for a Reynolds number $Re = 2930$. These

authors use a numerical method for the Navier-Stokes equations based on a discretization technique that combines a Fourier-collocation method for two spatial directions (the axial direction and the horizontal cross-flow direction) and a compact finite-difference method for the vertical direction (a sixth-order accurate scheme presented by Lele (1992)). Furthermore, their method employs a spatial filtering technique that is very similar to the one used in both numerical methods developed and used in the present study. The results presented in Robins and Delisi (1997) were obtained using 181 mesh points in the vertical direction and 129 in the horizontal cross-flow direction, resulting in a spatial resolution with 2.4 and 3.8 mesh points per vortex core radius, for the uniform-core vortices and the Lamb-Oseen vortices, respectively. For the high-order accurate spatial discretization methods used by Robins and Delisi (1997), this appears to give a sufficient resolution.

Some of the results of Robins and Delisi (1997) are summarized in figures 5.3 and 5.4, showing the evolution of the perturbation amplitude and the inclination angle. These figures show the dependence on aspect ratio r_c/b of the vortex pair and prescribed instability wavelength. Qualitatively, the results of Robins and Delisi (1997) are consistent with those of Garten et al. (2001), showing a roughly exponential growth up to fairly large amplitudes and an increase of the inclination angle of the perturbations up to around 60° to 65° .

5.2 Numerical results

The numerical results discussed in this chapter have been obtained using the parallel Navier-Stokes method described in section 3.5, or the hybrid Navier-Stokes method, described in section 3.6. For the present test case with a periodic spatial coordinate direction, the hybrid Fourier collocation/compact-difference Navier-Stokes method is computationally more efficient, since it explicitly uses this periodic dependence. Therefore, the hybrid method is used in simulations of the nonlinear stage of the instability, which require the temporal integration of the flow over long periods of time.

A number of the parameters characterizing the present test case are defined in figure 5.5. This figure shows a sketch of a rectangular computational domain containing a counter-rotating vortex pair with an initial sinusoidal perturbation. The spacing of the vortex pair without perturbation is denoted by b . The axial direction of the vortex pair is chosen to coincide with the x -coordinate direction.

Table 5.1 presents the parameters of the simulations that have been obtained using the parallel method. Similarly, the results obtained using the hybrid method, based on a Fourier expansion in the periodic direction, are summarized in table 5.2. In both table 5.1 and table 5.2, the first two columns present the Reynolds number based on circulation, i.e. $Re_\Gamma = \Gamma/\nu$, and the core size ratio r_c/b of the vortex pair. From the linear stability analyses presented in chapter 2, it follows that for a given vorticity distribution of the vortices, ratio r_c/b determines the wavelength λ relative to the spacing b of the most amplified instability mode. Here, the vortices forming the vortex pair are Lamb-Oseen vortices. For this vortex pair, the theory of Widnall et al. (1970) is used to determine this wavelength and the corresponding inclination angle of the perturbations with respect to the horizontal plane.

The initialization of the flow field is described in more detail in section 5.3. For a given vortex type, the quantities Γ/ν and r_c/b are the only degrees of freedom characterizing the flow

TABLE 5.1: *Parameters of parallel simulations*

Γ/ν	r_c/b	$\Gamma[\frac{m^2}{s}]$	λ/b	$\theta[^\circ]$	mesh	α_f	$L_x[m]$	$L_y = L_z[m]$	# proc.
$6.7 \cdot 10^3$	0.20	10.0	8.0	45°	81^3	0.10	$8.0 b$	$8.0 b$	4
$6.7 \cdot 10^3$	0.20	10.0	8.0	45°	81^3	0.25	$8.0 b$	$8.0 b$	4
$6.7 \cdot 10^5$	0.20	10.0	8.0	45°	81^3	0.05	$8.0 b$	$8.0 b$	4
$6.7 \cdot 10^5$	0.20	10.0	8.0	45°	81^3	0.10	$8.0 b$	$8.0 b$	4
$6.7 \cdot 10^5$	0.20	10.0	8.0	45°	81^3	0.25	$8.0 b$	$8.0 b$	4
$6.7 \cdot 10^5$	0.20	10.0	8.0	45°	121^3	0.10	$8.0 b$	$8.0 b$	4
$6.7 \cdot 10^5$	0.20	10.0	8.0	45°	121^3	0.25	$8.0 b$	$8.0 b$	4

TABLE 5.2: *Parameters of hybrid Fourier/finite-difference simulations*

Γ/ν	r_c/b	$\Gamma[\frac{m^2}{s}]$	λ/b	$\theta[^\circ]$	mesh	$L_x[m]$	$L_y = L_z[m]$
$1.67 \cdot 10^3$	0.20	2.5	8.0	45°	$64 \times 128 \times 128$	$8.0 b$	$8.0 b$
$1.67 \cdot 10^3$	0.20	2.5	8.5	45°	$64 \times 128 \times 128$	$8.5 b$	$8.0 b$
$1.67 \cdot 10^4$	0.20	2.5	8.0	45°	$64 \times 128 \times 128$	$8.0 b$	$8.0 b$
$1.67 \cdot 10^4$	0.20	2.5	8.5	45°	$64 \times 128 \times 128$	$8.5 b$	$8.0 b$
$1.67 \cdot 10^4$	0.20	2.5	8.0	45°	$128 \times 128 \times 128$	$8.0 b$	$8.0 b$
$1.67 \cdot 10^4$	0.20	2.5	8.5	45°	$128 \times 128 \times 128$	$8.5 b$	$8.0 b$

field.

Tables 5.1 and 5.2 indicate that in the present study, the lowest Reynolds number simulations have a Reynolds number ($O(10^3)$) that is comparable to that used in the numerical studies of Garten et al. (2001) and Robins and Delisi (1997), see section 5.1. Furthermore, this Reynolds number is comparable to that of the experimental study of Leweke and Williamson (1998). The spacing of the vortices is chosen such that the ratio r_c/b matches that of this experimental study. This allows a direct comparison of the results of the lowest Reynolds number simulations with the results of the the experimental study of Leweke and Williamson (1998).

The simulations at higher Reynolds numbers are performed to highlight the Reynolds number dependence of the temporal evolution of the Crow instability. This is a requirement to relate the present results to the trailing-vortex wake of an aircraft in cruise flight, with a typical Reynolds number based on circulation of $O(10^7)$.

The spatial resolution of the simulations listed in table 5.1 is such that there are 2.0 and 3.025 mesh points per vortex core radius for the 81^3 mesh and the 121^3 mesh, respectively. For the simulations summarized in table 5.2 there are 3.2 mesh points per vortex core radius. Thus, the spatial resolution used in this chapter is comparable to that of Robins and Delisi (1997).

In table 5.1, α_f denotes the filter coefficient of the high-order accurate low-pass filter, that is

applied to the flow field after each time-step. This filter operation is applied in both numerical methods for the Navier-Stokes equations. In this chapter, both Navier-Stokes solvers employ a 10th-order accurate symmetric filter stencil, given by equation (3.12) in section 3.3. In both cases, a formulation in multiple spatial directions is used, described in section 3.5 for the parallel method and in section 3.6 for the hybrid method. For the simulations listed in table 5.2, the filter coefficient $\alpha_f = 0.25$.

As indicated in tables 5.1 and 5.2, this chapter studies the dependence of the evolution of the long-wavelength instability on a number of parameters:

- Reynolds number $Re_\Gamma = \Gamma/\nu$. The range of $1.67 \cdot 10^3$ to $6.7 \cdot 10^5$ is covered by the various simulations discussed in this chapter,
- spatial resolution. The numerical simulations listed in table 5.1 study the resolution properties of the high-order accurate compact-difference discretization methods. Based on these results, the mesh size in the two non-periodic directions of the simulations presented in table 5.2 was chosen. The simulations using the hybrid method investigate the effect of spatial resolution in the periodic direction,
- spatial filtering. Effects of numerical dissipation by the compact-difference low-pass filter were studied in the simulations using the Navier-Stokes method based on compact-difference discretization methods for all three coordinate directions,
- prescribed wavelength of the instability mode. The initialization of the flow field uses results from linear stability theory to determine the wavelength of the most amplified instability mode. The sensitivity of the numerical results to this wavelength was studied by varying the wavelength in the batch of numerical simulations shown in table 5.2.

The numerical simulations were performed on multi-processor SGI Origin 200/2000 machines with either SGI R10K or SGI R12K processors. The parallel simulations described here used 4 processors, as shown in table 5.1. The simulations using the hybrid method were performed on a single processor.

5.3 Determination of initial condition

The initial condition consists of a pair of counter-rotating vortices with a small sinusoidal perturbation of the vortex axes, symmetric with respect to the vertical plane. The situation is sketched in figure 5.5. The bold lines show the perturbed vortex axes. The perturbation is periodic in the axial direction, which corresponds with the x -coordinate. The spacing of the vortices in the unperturbed situation is denoted by b . Both vortices are perturbed with perturbation $\underline{r}(x, t)$, in an inclined plane. The inclination angle with respect to the horizontal plane of both planes is identical and denoted by θ . In each of the (y, z) -planes, the flow is two-dimensional. A pair of Lamb-Oseen vortices is prescribed with the vortex centres shifted from the unperturbed situation by the perturbation $\underline{r}(x, t)$. The Lamb-Oseen vortex was introduced in section 1.1 and is characterized by a Gaussian azimuthal velocity profile. The vortex has a viscous core region of radius r_c , at which the maximum of the azimuthal velocity occurs.

With this choice of initialization, the velocity field is prescribed as follows:

$$\begin{aligned}
u(x, y, z) &= 0 \\
v(x, y, z) &= +[z - z_{c,L}(x)] \frac{\Gamma}{2\pi r_L^2} \left[1 - \exp(-\gamma r_L^2/r_c^2)\right] \\
&\quad - [z - z_{c,R}(x)] \frac{\Gamma}{2\pi r_R^2} \left[1 - \exp(-\gamma r_R^2/r_c^2)\right] \\
w(x, y, z) &= -[y - y_{c,L}(x)] \frac{\Gamma}{2\pi r_L^2} \left[1 - \exp(-\gamma r_L^2/r_c^2)\right] \\
&\quad + [y - y_{c,R}(x)] \frac{\Gamma}{2\pi r_R^2} \left[1 - \exp(-\gamma r_R^2/r_c^2)\right]
\end{aligned} \tag{5.1}$$

with Γ the strength of the vortices. The constant γ in the exponential function is chosen to position the maximum of the azimuthal velocity at r_c (this leads to the constraint $(2\gamma + 1)e^{-\gamma} = 1 \rightarrow \gamma \cong 1.256$).

The vortex centers of the left and right vortex are $(y_{c,L}, z_{c,L})$ and $(y_{c,R}, z_{c,R})$, respectively. The distances from these vortex centers are computed from:

$$\begin{aligned}
r_L(x) &= \sqrt{(y - y_{c,L}(x))^2 + (z - z_{c,L}(x))^2} \\
r_R(x) &= \sqrt{(y - y_{c,R}(x))^2 + (z - z_{c,R}(x))^2}
\end{aligned} \tag{5.2}$$

and

$$\begin{aligned}
y_{c,L}(x) &= 0.5L_y - \frac{b}{2} - A \cos\left(\frac{2\pi x}{L_x}\right) \cos(\theta) \\
y_{c,R}(x) &= 0.5L_y + \frac{b}{2} + A \cos\left(\frac{2\pi x}{L_x}\right) \cos(\theta) \\
z_{c,L}(x) &= 0.5L_z + A \cos\left(\frac{2\pi x}{L_x}\right) \sin(\theta) \\
z_{c,R}(x) &= 0.5L_z + A \cos\left(\frac{2\pi x}{L_x}\right) \sin(\theta)
\end{aligned} \tag{5.3}$$

with A the amplitude of the initial perturbation, which is typically around 5 per cent of b , or $0.25 r_c$. As a result of the velocity that is induced by the vortices on one another, the vortex pair will translate downwards with a constant velocity. In the initial flow field, a constant upward velocity, of $\Gamma/2\pi b$, is superposed on the flow field (5.1) to prevent the vortex pair from translating out of the computational domain.

The initial pressure field is prescribed as a constant pressure field. In the numerical simulations, this pressure field quickly adjusts to one consistent with the velocity field. This sudden transition did not produce problems in the present long-wavelength instability simulations.

5.4 Numerical study of linear stage of the Crow instability

This section describes numerical results for the *linear* stage of the development of the Crow instability. This stage is dominated by the exponential growth predicted by the linear stability theory for a counter-rotating vortex pair. A remarkable feature of the Crow instability

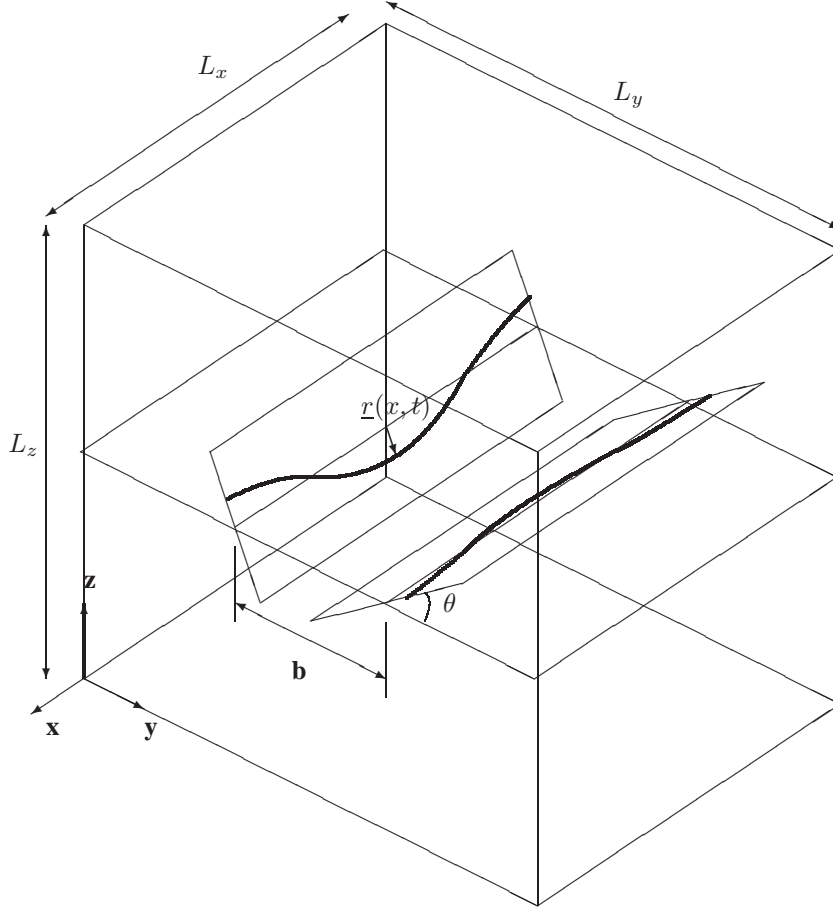


FIGURE 5.5: *Geometrical description of vortex pair, with spacing b , with a sinusoidal perturbation located in rectangular computational domain, of dimension $[0, L_x] \times [0, L_y] \times [0, L_z]$*

is that even after the instability reaches large amplitudes, i.e. outside the linear regime, the growth continues to be roughly exponential, even up to the time at which the two vortices touch one another, see for example Garten et al. (2001). This effect was first described by Moore (1972).

This exponential growth of the perturbation amplitude is studied, for the various numerical simulations, in section 5.4.1. Another noticeable feature of this stage of the development of the Crow instability is the increasing inclination angle of the plane of perturbations of the vortices. Linear stability predicts an inclination angle for the plane in which infinitesimal perturbations grow, of around 45° . Both numerical studies discussed in more detail in section 5.1, i.e. Garten et al. (2001) and Robins and Delisi (1997), predict a gradual increase of the inclination angle up to around 60° - 65° at the time of commencement of the vortex-reconnection process. In Garten et al. (2001), this effect was shown for the unstratified situation for three different Reynolds numbers. The dependence of the increase in inclination angle on Reynolds number was shown to be small for the considered range of Reynolds numbers. This suggests that the increase of the inclination angle is a predominantly inviscid process. The change in

inclination angle is studied in section 5.4.2 using the present numerical results.

5.4.1 Exponential growth of perturbations

In this section, the amplitude growth of the perturbation is studied using the numerical simulations of table 5.1. The amplitude growth is computed using the difference in location of the vortex centers in planes perpendicular to the axial direction (cross-flow planes) at the point of closest and furthest separation. The vortex-center location in these planes is determined by searching for the pressure minimum. Typically, meshes are used with a mesh spacing of around 1/5th of the vortex core radius for the 81^3 mesh and about 1/8th of the vortex core radius for the 121^3 mesh. This spatial resolution renders the process of determining the location of the vortex center somewhat sensitive to errors. Especially on the coarse mesh and for small amplitudes, this effect can be expected to lead to a significant error margin on the derived amplitude growth.

Figure 5.6 shows the normalized amplitude of the perturbation (normalization using the amplitude of the perturbation in the initial flow field) versus non-dimensional time for the high Reynolds number simulation on the coarse 81^3 mesh. Results for two values of the filter coefficient α_f are compared with the exponential growth rate predicted by linear stability theory. Here, the theory of Widnall et al. (1970) is used to determine this theoretical growth rate.

For the coarse mesh, figure 5.6 shows that the numerical diffusion by the spatial filter has a significant influence on the amplitude growth. A high-order accurate filter is used (here, a 10th-order filter) that introduces a noticeable damping only in the upper half of the wavenumber spectrum, see section 3.3. This shows that the flow field is coarsely-resolved for this mesh. Furthermore, it can be observed that excessive numerical dissipation for this test case, with $\alpha_f = 0.10$, leads to an over-prediction of the growth rate. The results obtained on the coarse mesh for the least dissipative filter, i.e. $\alpha_f = 0.25$, agree quite well with both the asymptotic prediction and the results obtained on the finer mesh (121^3), shown in figure 5.7. As

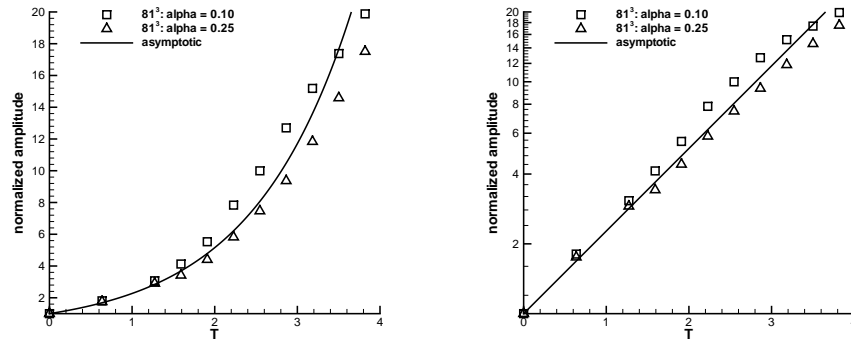


FIGURE 5.6: *Effect of spatial filtering on the growth rate: $Re_\Gamma = 6.7 \cdot 10^5$, 81^3 mesh (linear scale (left) and log-scale (right))*

in figure 5.6, figure 5.7 compares numerical results for two values of the filter coefficient α_f with the exponential growth rate from linear stability theory. In this case, the differ-

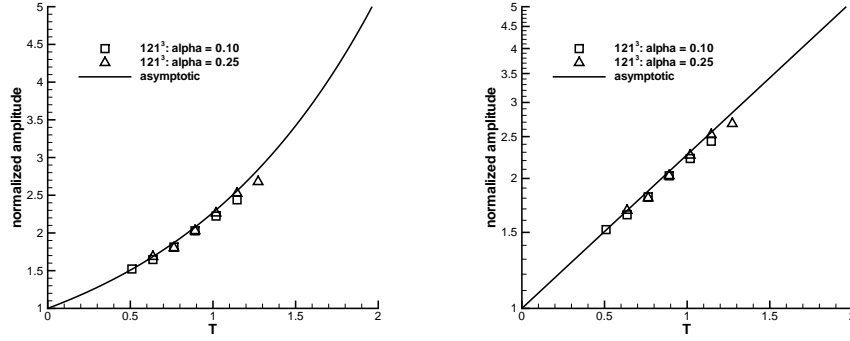


FIGURE 5.7: *Effect of spatial filtering on the growth rate: $Re_\Gamma = 6.7 \cdot 10^5$, 121^3 mesh (linear scale (left) and log-scale (right))*

ence between the results of the two simulations is very small. This indicates that the linear stage of the Crow instability is well-resolved on the fine mesh. Both results agree very well with the exponential-growth curve predicted by linear stability theory. The over-prediction of the growth rate for excessive numerical dissipation can be explained by the smearing of the vorticity of the vortices, i.e. the peak of the Gaussian distribution is reduced and the base is broader as a result of the numerical viscosity. For the simulation on the 81^3 mesh and $\alpha_f = 0.10$, this appears to lead to an artificial increase of the circulation compared to better-resolved simulations. The circulation of each of the vortices is related to the vorticity field of the vortex by equation (1.2) of section 1.1.

Figure 5.8 shows results for the amplitude growth for the two Reynolds numbers considered in the results of table 5.1. For both numerical results, the filter coefficient $\alpha_f = 0.25$. As expected, the higher viscous dissipation in the lower Reynolds number simulation leads to a reduction of the growth rate of the perturbation amplitude. The dependence on Reynolds number found here, is consistent with the results by Garten et al. (2001), shown in figure 5.1. In this chapter, the Reynolds number is changed by modification of the kinematic viscosity ν , the strength of the vortices is left unaltered.

From the results presented here, a number of conclusions can be drawn:

- the growth of the perturbation amplitude shows an exponential behaviour up to amplitudes at which nonlinear effects can be expected to be significant. This observation is in agreement with the findings of Moore (1972).
- for the parameters chosen in table 5.1, the flow field is well-resolved for the fine 121^3 mesh. On the 81^3 mesh, satisfactory results are obtained with spatial filtering coefficients $\alpha_f \geq 0.25$. For lower values of α_f , the numerical results are significantly influenced by numerical dissipation.
- Viscous dissipation leads to a reduction of the growth rate of the perturbation amplitude. This effect is more pronounced at later stages of the development of the instability. In figure 5.8, the numerical results for different Reynolds numbers show a marked deviation for non-dimensional time $T > 2$.

- Comparing results obtained on different meshes and for different values of the filter coefficient, it can be observed that for the present test case, excessive numerical dissipation leads to an over-prediction of the growth rate. This excessive numerical dissipation can be caused by either a too coarse mesh or the application of the spatial filter with a coefficient α_f that is too low.

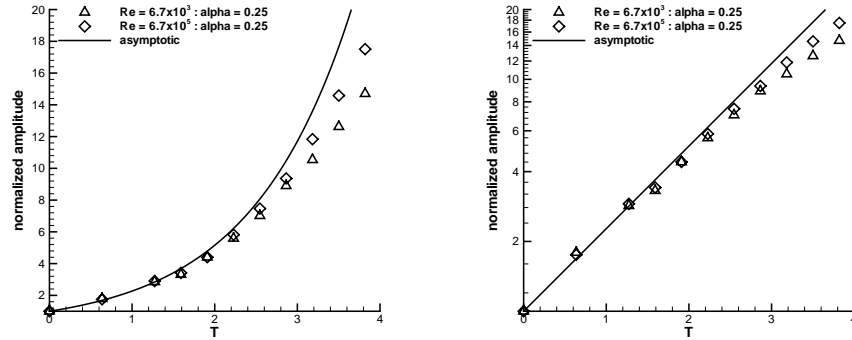


FIGURE 5.8: *Effect of Reynolds number on the growth rate: $\alpha_f = 0.25$, 81^3 mesh (linear scale (left) and log-scale (right))*

5.4.2 Rotational motion of perturbations

A noticeable feature of the results of Garten et al. (2001) and Robins and Delisi (1997) is the rotational motion of the perturbations of the vortices with respect to the plane of the perturbations that is predicted by the linear stability theory, i.e. a plane inclined approximately 45° with respect to the horizontal plane. The inclination angle, denoted by θ in figure 5.5, showed a marked increase as time progresses. In Garten et al. (2001), the effect of viscosity, i.e. the increase of the vortex core radius by viscous diffusion, was thought to be contributing to this effect. Figure 5.2 shows how the inclusion of the viscous vortex-core growth into the theoretical predictions of Crow (1970) can improve the agreement with the numerically computed inclination-angle. This analysis by Garten et al. (2001) therefore appears to highlight one of the underlying mechanisms of the rotational motion of the perturbations of the vortices. However, the results discussed in this study appear to rule out the underlying mechanism discussed by Garten et al. (2001). The effect of Reynolds number on the increase of the inclination angle is shown in figure 5.9. This figure shows the evolution of the inclination angle for $\lambda/b = 8.0$ at $Re_\Gamma = 1.67 \cdot 10^3$ and $Re_\Gamma = 1.67 \cdot 10^4$. For both Reynolds numbers, a gradual increase to around 60° is observed. In the case of $Re_\Gamma = 1.67 \cdot 10^4$, this angle is attained somewhat faster as a result of the faster rate at which the Crow instability develops for a higher Reynolds number. For the two Reynolds numbers considered here, which are an order of magnitude different, a mechanism driven by viscous dissipation, such as the mechanism discussed by Garten et al. (2001), can be expected to lead to a more pronounced increase of the inclination angle for the lowest Reynolds number. In figure 5.9, the opposite

effect can be observed. Therefore, an inviscid non-linear mechanism appears to be a more likely explanation of the rotational motion of the perturbations.

In this section, another possible mechanism is studied: the effect of restricting the wavelength of the instability mode throughout the evolution to that predicted by the linear stability theory. This effect is discussed using the numerical simulations summarized in table 5.2. Figure 5.10 compares the rotational motion for simulations with $\lambda/b = 8.0$ and $\lambda/b = 8.5$ at the lower Reynolds number, $Re_\Gamma = 1.67 \cdot 10^3$. The figure shows a projection of the iso-surface $|\underline{\omega}| = 300 \text{ s}^{-1}$ onto the cross-flow plane at different instances in time. Comparison of the results for the case $\lambda/b = 8.0$ and $\lambda/b = 8.5$, shows that the difference between the results of the two simulations is negligible. Therefore, the effect of restricting the wavelength to the wavelength predicted by the linear stability theory, appears to be unimportant in the mechanism of the rotational motion of the perturbations.

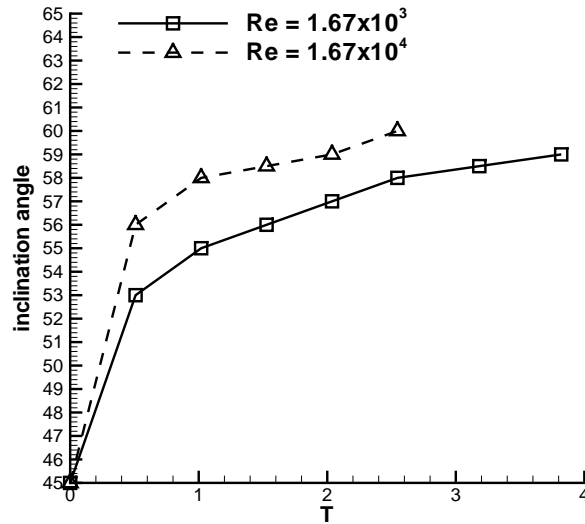


FIGURE 5.9: *Inclination angle versus non-dimensional time: $\lambda/b = 8.0$, $Re_\Gamma = 1.67 \cdot 10^3$ ($64 \times 128 \times 128$ mesh) and $Re_\Gamma = 1.67 \cdot 10^4$ ($128 \times 128 \times 128$ mesh).*

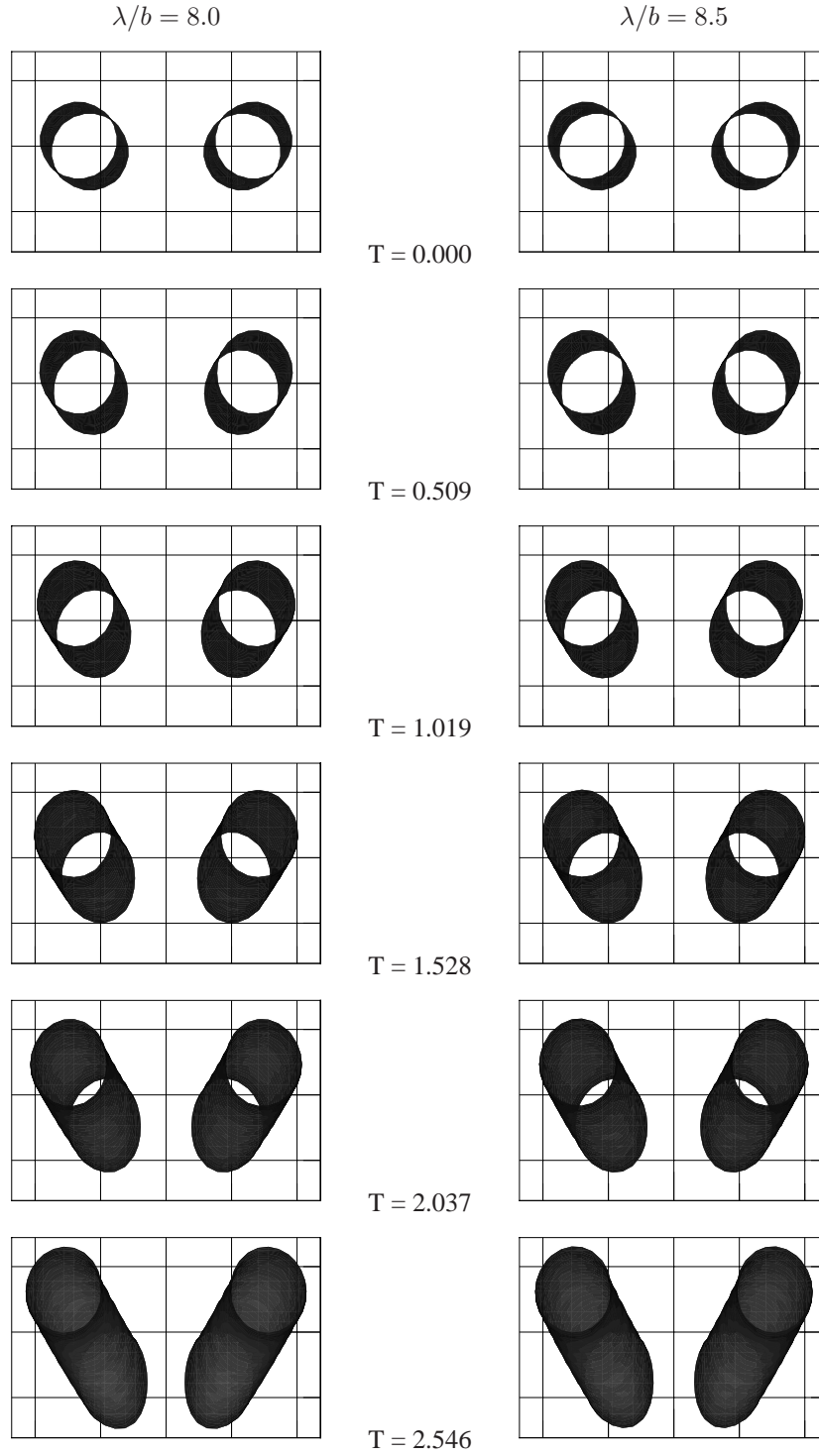


FIGURE 5.10: Iso-vorticity surface (300 s^{-1}): $Re_{\Gamma} = 1.67 \cdot 10^3$, $64 \times 128 \times 128$ mesh.

5.5 Nonlinear stage of the Crow instability

This section describes the characteristic features of the later stages of the long-wavelength Crow instability in a counter-rotating vortex pair. Some of the features were shown in figure 1.1 of chapter 1. The figure shows water vapour entrained in the trailing vortices. Even this crude visualization clearly shows the formation of ring-like structures at the later stages. The formation of these ring-like structures is preceded by a process characterized by a rapid growth of sinusoidal perturbations of the two counter-rotating vortices. At a certain instance in time, the perturbation amplitude has increased far enough to create a strong interaction of the left and right vortices, leading to the formation of the vortex rings. The process described here, is commonly known as *vortex reconnection*.

In this section, the vortex-reconnection phase of the Crow instability is discussed in detail using numerical results from a simulation on a fine mesh (128^3 mesh) for Reynolds number $Re_\Gamma = 1.67 \cdot 10^4$. The simulation was performed using the hybrid Navier-Stokes method. Figure 5.12 shows a typical numerical result. The formation of vortex rings can clearly be observed from a sequence of plots of iso-surfaces of the vorticity magnitude at successive non-dimensional times. The flow field was initialized as described in section 5.3, thus with a constant upward velocity superposed on the flow field, equal to the self-induced translational motion of the undisturbed counter-rotating vortex pair. This prevents the vortices from advecting out of the computational domain during the simulation. A detailed discussion based on these numerical results is presented in subsection 5.5.2. A detailed qualitative description of vortex reconnection process was presented by Kida and Takaoka (1994). This qualitative description is discussed in section 5.5.1.

5.5.1 Theoretical analysis by Kida and Takaoka (1994)

The analysis by Kida and Takaoka (1994) provides an explanation of vortex reconnection, both for colliding vortex rings and for interacting vortex tubes. Experimental studies of vortex reconnection typically involve visualization using a passive scalar, such as dye or smoke. Numerical studies usually employ iso-surfaces of vorticity magnitude for the visualization of the vortical flow field. Interpretation of the results of either experimental or numerical studies requires care, since the dynamics of a scalar field and that of the vorticity field are quite different. Furthermore, iso-surfaces of vorticity magnitude are not, in general, vortex tubes. This means that, in general, vorticity vectors on the tube formed by the iso-surfaces are not aligned with the iso-surface. As a result of this distinction, Kida and Takaoka (1994) distinguish three types of reconnection: *scalar*, *vortex* and *vorticity* reconnection. Vorticity reconnection involves the change of the topology of vorticity lines. The theoretical study by Kida and Takaoka (1994) explains the characteristic features of vortex reconnection by studying the changes in the topology of vorticity lines.

Figure 5.11 shows a series of sketches of this topology at different stages of the reconnection process. The left plot of this figure shows the situation of the two counter-rotating vortices when the vortex cores are in close proximity in an interaction zone, deforming while being forced to move towards each other and meeting in the (vertical) plane of symmetry. At this plane of symmetry the vorticity must be zero or the vorticity vector normal to this plane. This stage corresponds to the situation shown in the first plot of figure 5.12. The hatched area represents this interaction zone. In this zone closely spaced regions with opposite-signed vorticity induce a velocity field with large gradients, implying a significant level of viscous

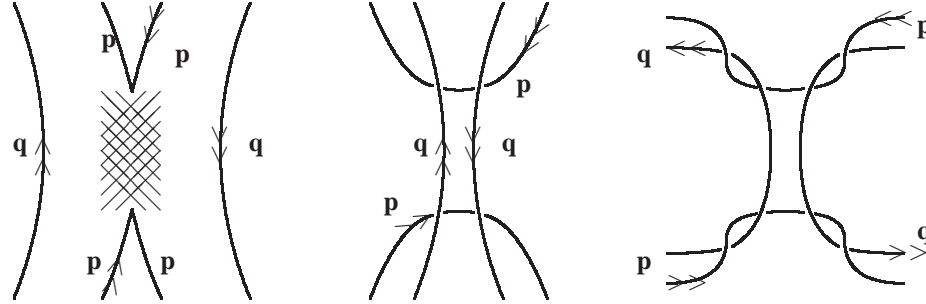


FIGURE 5.11: *Bridging process during vorticity reconnection, as described by Kida and Takaoka (1994). Double arrows indicate direction of vorticity lines. Viscous cancellation is taking place in hatched area.*

dissipation, leading to a reduction of velocity gradients and consequently reducing the vorticity. This process is commonly referred to as *viscous cancellation* of opposite-signed vorticity. In figure 5.11, four vortex lines are shown, two per vortex. The lines **p** represent the vorticity lines closest to one another. The vorticity lines furthest from one another are denoted by **q**. Note that the vorticity magnitude does not need to be constant along vortex lines, similar to the non-constant velocity magnitude along a streamline. The "viscous cancellation" creates a connection of the vorticity lines **p** at both ends of the viscous interaction zone in a cusp, i.e. in the region where the vorticity will have a vanishing magnitude. The vorticity lines rotate around each other in both vortex cores. The flattening of the vortex cores in the region of the interaction zone causes a smaller angular velocity of the vorticity lines in this region. As explained in Kida and Takaoka (1994), the vorticity lines **p** and **q** must be tangled at the ends of the interaction zone. As a result, the vorticity lines are strongly twisted in the vicinity of the ends of the interaction zone. This process is sketched in the middle and right plots of figure 5.11. It was further noted by Kida and Takaoka (1994) that during the reconnection, the interaction zone is bent in the direction perpendicular to the plane of figure 5.11, this because of the high curvature dependent self-induced velocity. This bending deformation is clearly present in the numerical results shown in figure 5.12. The portions of vorticity lines **p** that link the two interacting vortices are called *bridges* by Kida and Takaoka (1994), the described process of cross-linking of vorticity lines is referred to as *bridging*. The process described here, can only occur in a viscous flow. In an inviscid flow, vorticity lines are advected as passive elements by the velocity field. Furthermore, in the absence of viscosity, the Kelvin-Helmholtz theorems preclude the cross-linking of vorticity lines.

5.5.2 Numerical analysis of vortex reconnection

In figure 5.12, a perspective view of the vortex pair is shown on the left-hand side and a top view on the right-hand side. Shown is a sequence of plots of iso-surfaces of the vorticity magnitude at successive non-dimensional times. The vorticity magnitude $|\underline{\omega}| = 500 \text{ s}^{-1}$ is shown, since this level highlights many of the details of the vortical flow field. Note that iso-surfaces of $|\underline{\omega}|$ do not indicate a stream surface of a vortex tube. In figure 5.12, non-dimensional time advances from 3.183 to 4.456. The sequence of plots of figure 5.12 starts at an instance in time, at which the sinusoidal deformation of the vortices has grown to an amplitude such that the vortices nearly touch in a region around $x = 0.5 L_x$. This region

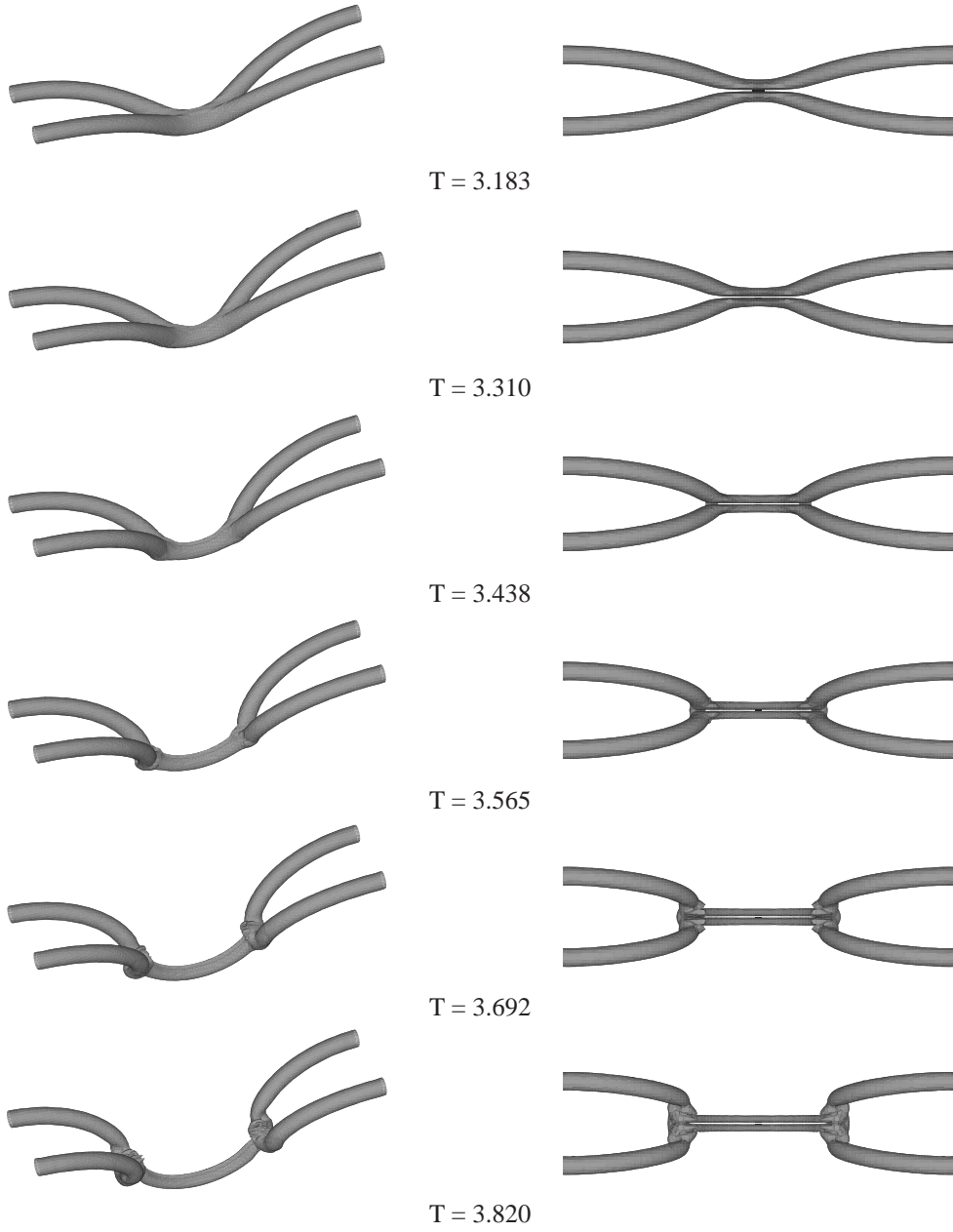
is the interaction zone, introduced in subsection 5.5.1. In this interaction zone, a significant flattening of the cross-flow plane shape of the vortices occurs as a result of the strain field induced on one another. In subsequent stages of the development, the length of the interaction zone increases, i.e. the two vortices are in close proximity for an increasing part of the wavelength, forming a dipole-like structure. The "viscous cancellation" of opposite-signed vorticity in the ends of this interaction zone leads to the cross-linking of vorticity lines. The bridging creates vortex-ring structures and a tube-like structure that connects these ring-like structures, shown as iso-surfaces of vorticity magnitude in figure 5.12.

Note that the vortex-ring structure is not a flat vortex ring but is a non-planar deforming structure.

The bridging process is studied using computed vorticity lines in figures 5.13 and 5.14 for the first four time levels of figure 5.12. In each of these plots, six vorticity lines belonging to the right vortex are considered. Note that the sequence of plots does not show the temporal evolution of these vorticity lines, since in each of the plots six vorticity lines are shown starting at corresponding locations in the vortex core region. In figures 5.13 and 5.14, the two counter-rotating vortices are shown using two iso-surfaces of magnitude of vorticity. At the earliest time shown, i.e. $T = 3.183$, just one of the computed vorticity lines, i.e. the one initially closest to the plane of symmetry, reaches the plane of symmetry in a cusp, at which location $|\omega|$ vanishes, and continues into the left vortex. At later time levels, it can be observed that an increasing number of the computed vorticity lines make this "cross-over". Furthermore, it can be noted that the tangling and twisting of the vorticity lines, indicated in the sketches of figure 5.11, does occur in the simulated flow field. The structure of the vortex-tube connecting the vortex rings can be seen from figure 5.15. For the first six time levels shown in figure 5.12, an cross-flow plane intersection of the flow field at $x = 0.50$, i.e. at half distance in the periodic direction, is presented. For these six time levels, figure 5.15 shows the cross-flow plane streamline pattern within the the cross-section on the left-hand side and the iso-surfaces of the axial component of the vorticity vector on the right-hand side. It can clearly be seen that the vortex tube is a dipole, formed from the interacting counter-rotating vortices. During this dipole formation, viscous effects play an important role. This can be seen from the decreasing extrema in the iso-surfaces of the axial component of the vorticity vector. Furthermore, some vorticity is shed by this tube-like dipole structure. Despite the viscous decay of the dipole structure, its self-induced motion can be seen to exceed that of the original vortex pair, i.e. the dipole structure shown in figure 5.15 moves downward as time progresses.

An interesting feature of the flow field at this stage of the development, is that the self-induced translational motion of the ring-like structures is very similar to the sink velocity of the original unperturbed counter-rotating vortex pair, i.e. the ring-like structures remain in the middle of the computational domain.

With the self-induced downward velocity of the dipolar tube-like structure exceeding the self-induced motion of these vortex rings, a noticeable bending deformation of the tube results. An interesting flow pattern is present at the junction of the dipole tube and the vortex rings. In the plots of figure 5.11, a notable tangling and twisting of vorticity lines is present in the vicinity of this junction. The direction of the rotational motion of the vortex rings is such that the tube-like structure is 'pulled' into the ring-like structures. This latter effect and the bending deformation lead to a significant elongation and stretching of the dipole tube, which



can be observed in the top views shown on the right-hand side of figure 5.12.

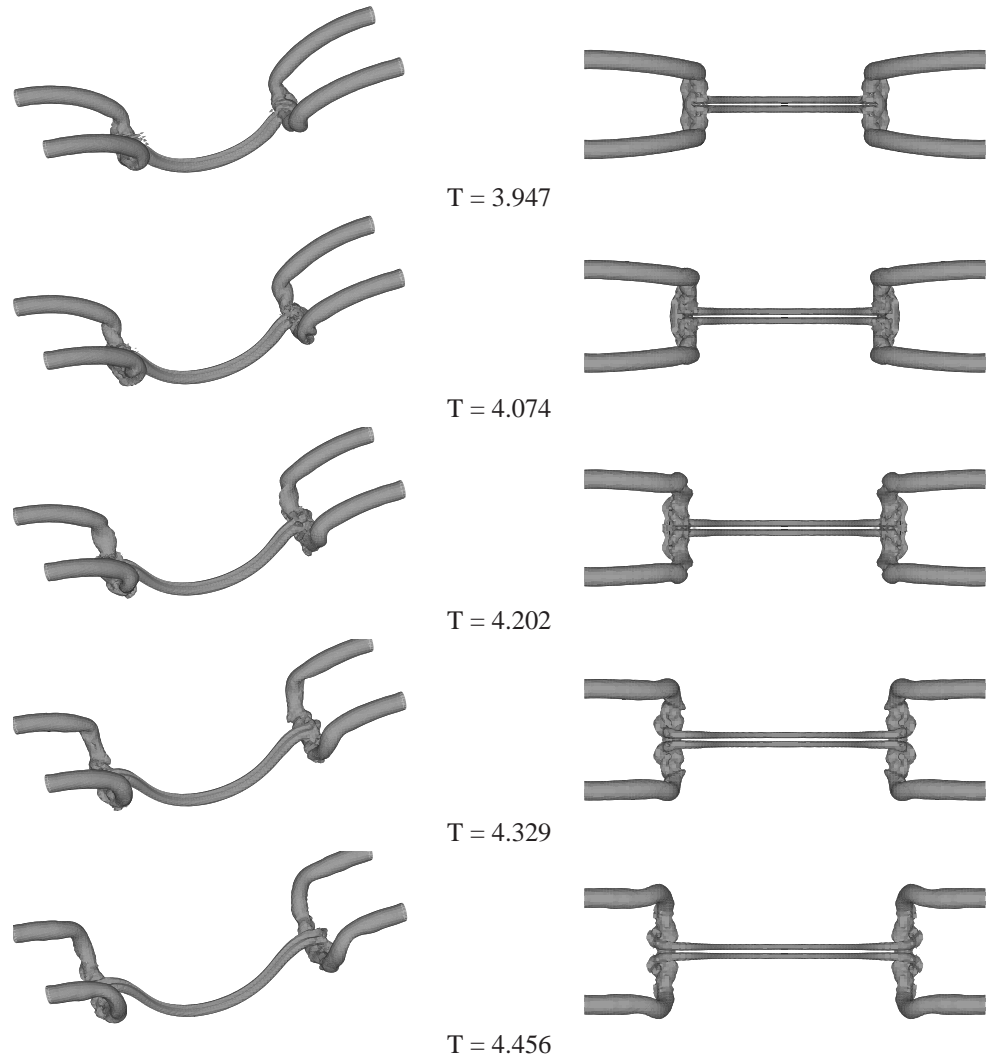
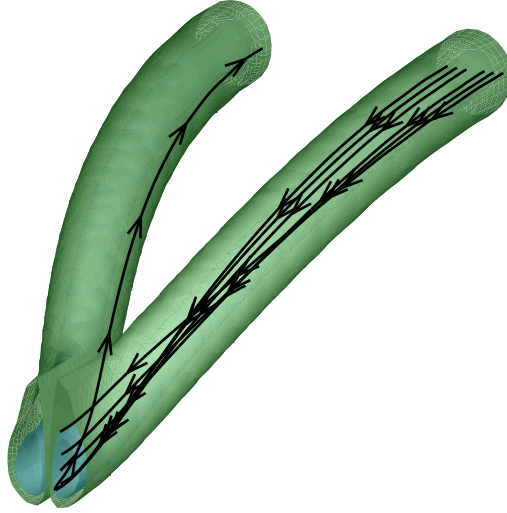


FIGURE 5.12: *Formation of vortex-ring structures: $Re_\Gamma = 1.67 \cdot 10^4$, 128^3 mesh, $r_c/b = 0.2$, $\lambda/b = 8.0$, $|\underline{\omega}| = 500 \text{ s}^{-1}$*

T = 3.183



T = 3.310

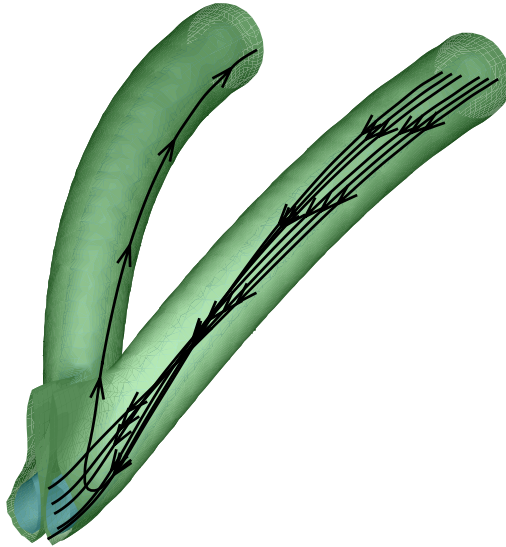


FIGURE 5.13: *Cross-over of vortex lines. Vortex tubes shown as iso-surfaces $|\underline{\omega}| = 300 \text{ s}^{-1}$ and 900 s^{-1} . $Re_{\Gamma} = 1.67 \cdot 10^4$ simulation on 128^3 mesh.*

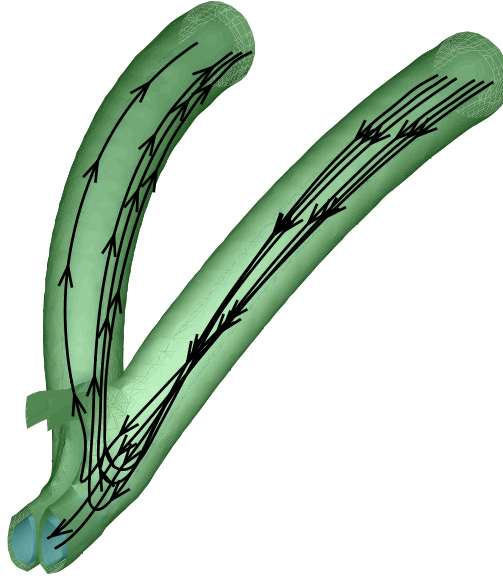
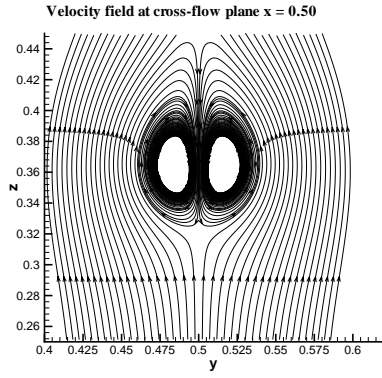
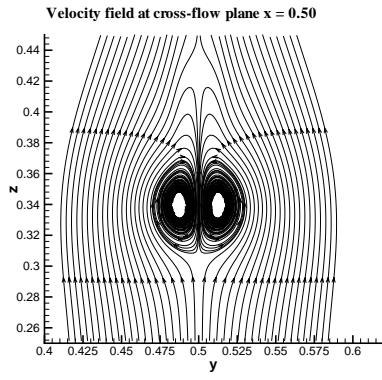
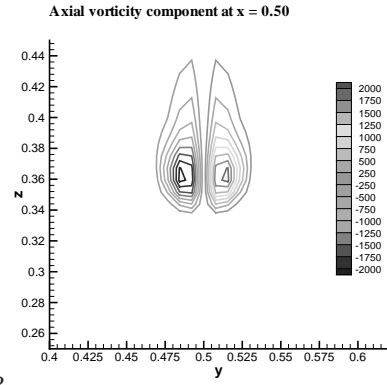
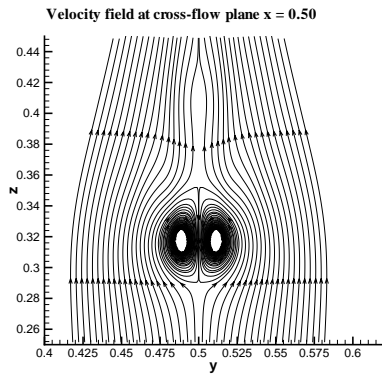
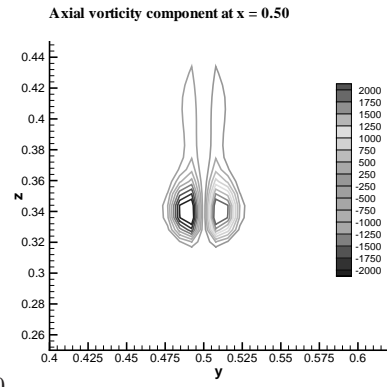
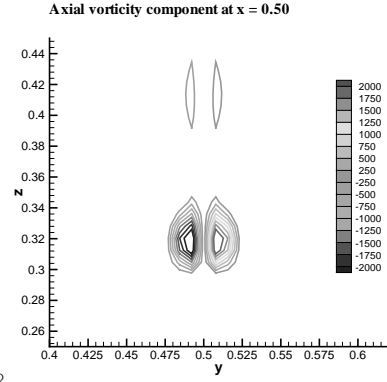
T = 3.438**T = 3.565**

FIGURE 5.14: *Cross-over of vortex lines. Vortex tubes shown as iso-surfaces $|\underline{\omega}| = 300 \text{ s}^{-1}$ and 900 s^{-1} . $Re_{\Gamma} = 1.67 \cdot 10^4$ simulation on 128^3 mesh.*


 $T = 3.183$

 $T = 3.310$

 $T = 3.438$


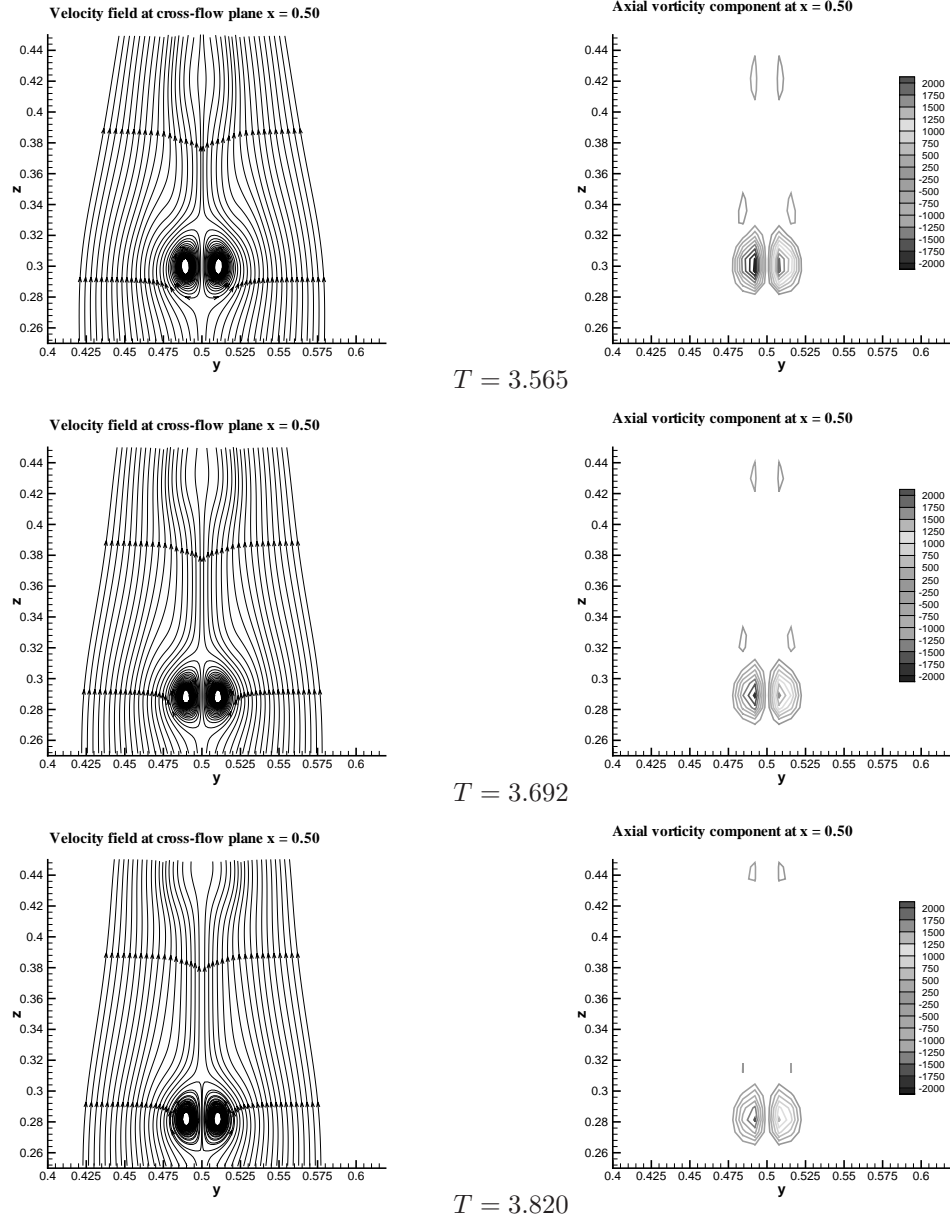


FIGURE 5.15: Cross section of dipole structure: $Re_\Gamma = 1.67 \cdot 10^4$, 128^3 mesh, $T = 3.183$ to $T = 3.820$.

5.6 Numerical study of the nonlinear stage of the Crow instability

The characteristic features of the nonlinear stage of the Crow instability were described in section 5.5, showing the formation of vortex-ring structures and a dipole-tube structure connecting these rings. Numerical results were described for $Re_\Gamma = 1.67 \cdot 10^4$ computed on a 128^3 mesh, see table 5.2. Iso-surfaces of the magnitude of vorticity were shown at various instances in time.

In this section, the dependence of this nonlinear evolution on Reynolds number and spatial resolution is investigated. The results for both Reynolds numbers and meshes considered in table 5.2, are discussed and compared to the numerical results described in section 5.5.

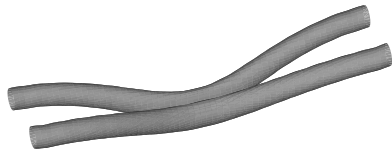
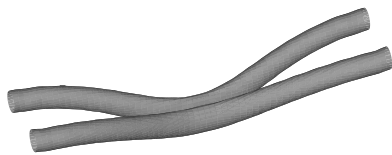
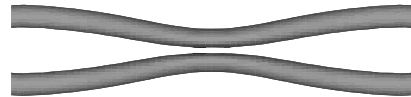
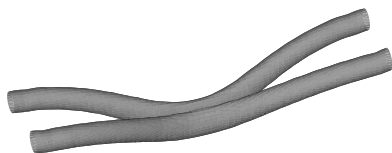
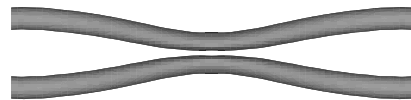
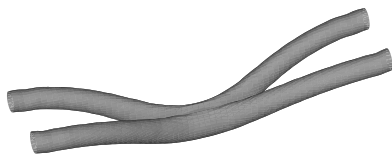
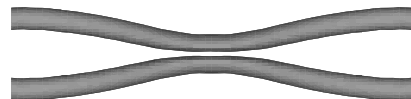
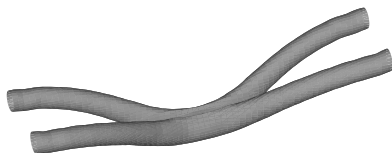
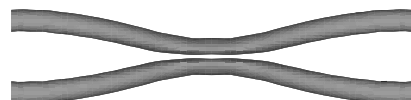
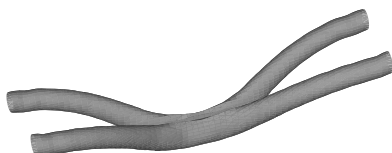
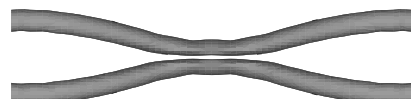
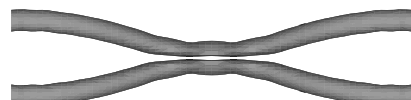
Figure 5.16 shows the evolution of the Crow instability for $Re_\Gamma = 1.67 \cdot 10^3$ computed on a $64 \times 128 \times 128$ mesh. The figures show the evolution of an iso-surface of the magnitude of vorticity. For this Reynolds number, the iso-surface $|\underline{\omega}| = 300 \text{ s}^{-1}$ is shown, in contrast to figure 5.12, which shows the evolution of the iso-surface $|\underline{\omega}| = 500 \text{ s}^{-1}$. This lower value of $|\underline{\omega}|$ was chosen to take into account the stronger viscous dissipation at the lower Reynolds. The iso-surface $|\underline{\omega}| = 300 \text{ s}^{-1}$ was found to highlight the most striking features of the Crow instability.

Comparing the sequence of plots of figure 5.16 with the higher Reynolds number results of figure 5.12, a number of differences can be observed:

- at the first time instance shown, i.e. $T = 3.183$, the growth of the Crow instability has progressed further for the high Reynolds number simulation than for the simulation with the lower Reynolds number. This can be attributed to the reduced growth rate in the linear stage of the evolution for lower Reynolds numbers, see for example figure 5.8;
- due to this reduced growth rate in the linear stage for lower Reynolds numbers, the vortex-reconnection process commences later than for higher Reynolds numbers;
- the vortex-reconnection process proceeds faster for the high Reynolds number simulation. This faster vortex-reconnection process for higher Reynolds numbers was predicted by Garten et al. (2001). Based on numerical simulations, these researchers predict a characteristic time-scale t_R of vortex reconnection depending on Reynolds number as: $t_R \sim 1/Re$. The numerical results of the present study indicate a similar dependence of this characteristic time-scale.

The numerical simulations of Garten et al. (2001) considered the range of Reynolds numbers from $Re_\Gamma = 628$ to 1260 , which is lower than the Reynolds numbers considered in the present study. Based on their simulations, Garten et al. (2001) predicted a delay of commencement of the vortex-reconnection process for higher Reynolds numbers. This effect is not observed here. Here, the difference in Reynolds number between the low Reynolds number simulation and the high Reynolds number simulation is larger than in Garten et al. (2001). As a result, the effect of the reduced growth rate of the linear stage for the low Reynolds number simulation, can be expected to have a more pronounced effect.

Figure 5.17 shows the evolution of the Crow instability for $Re_\Gamma = 1.67 \cdot 10^4$ computed on a $64 \times 128 \times 128$ mesh. Comparing these results with the results for this Reynolds number computed on the 128^3 mesh, it can be observed that the smallest structures of the flow at later instances in time, are not fully-resolved for the $64 \times 128 \times 128$ mesh. Also, on the 128^3 mesh, the dipole-like structure connecting the vortex rings does not form the smaller vortex-ring structure observed in the simulations on the $64 \times 128 \times 128$ mesh. The formation of this extra vortex-ring structure can therefore be attributed to the under-resolution of the flow field on this coarser mesh. The spatial resolution of the Crow instability in the nonlinear stage of the development is discussed in more detail in the next section.

 $T = 3.183$  $T = 3.310$  $T = 3.438$  $T = 3.565$  $T = 3.692$  $T = 3.820$ 

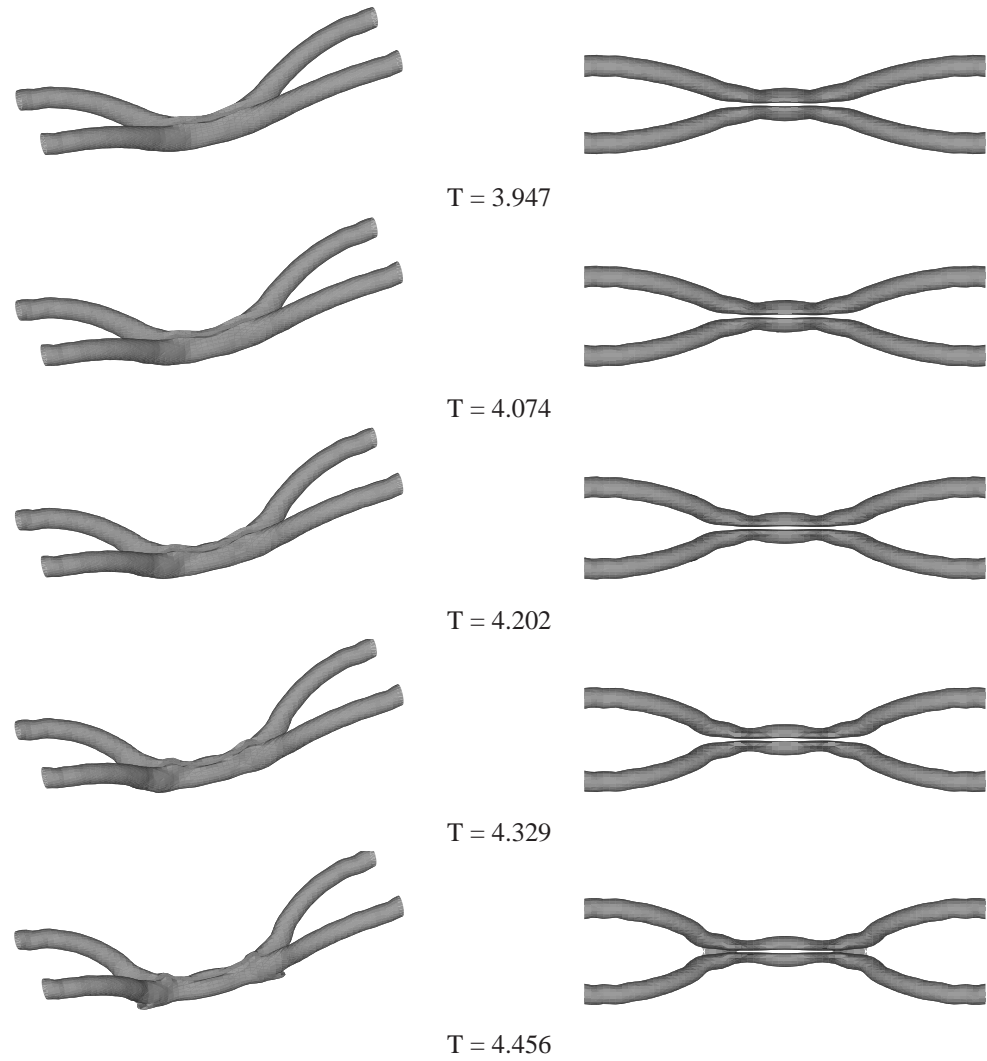
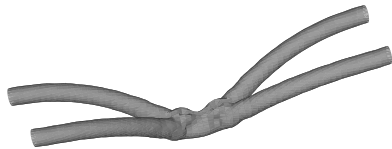
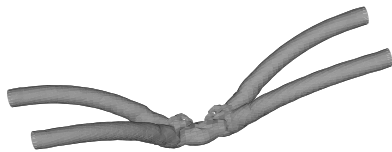
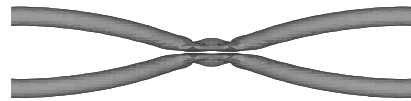
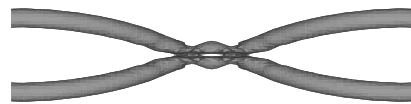
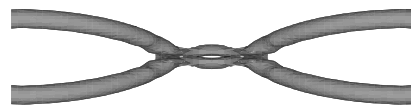
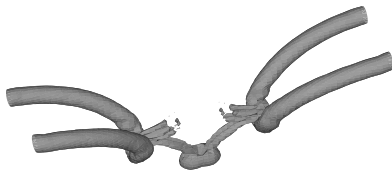
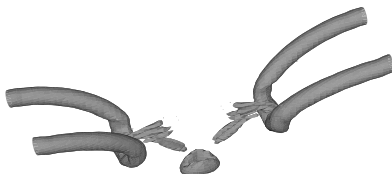
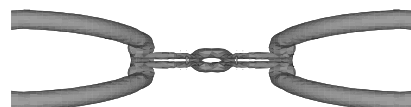


FIGURE 5.16: *Formation of vortex-ring structures: $Re_{\Gamma} = 1.67 \cdot 10^3$, $64 \times 128 \times 128$ mesh, $r_c/b = 0.2$, $\lambda/b = 8.0$, $|\underline{\omega}| = 300 \text{ s}^{-1}$*

 $T = 3.183$  $T = 3.310$  $T = 3.438$  $T = 3.565$  $T = 3.692$  $T = 3.820$



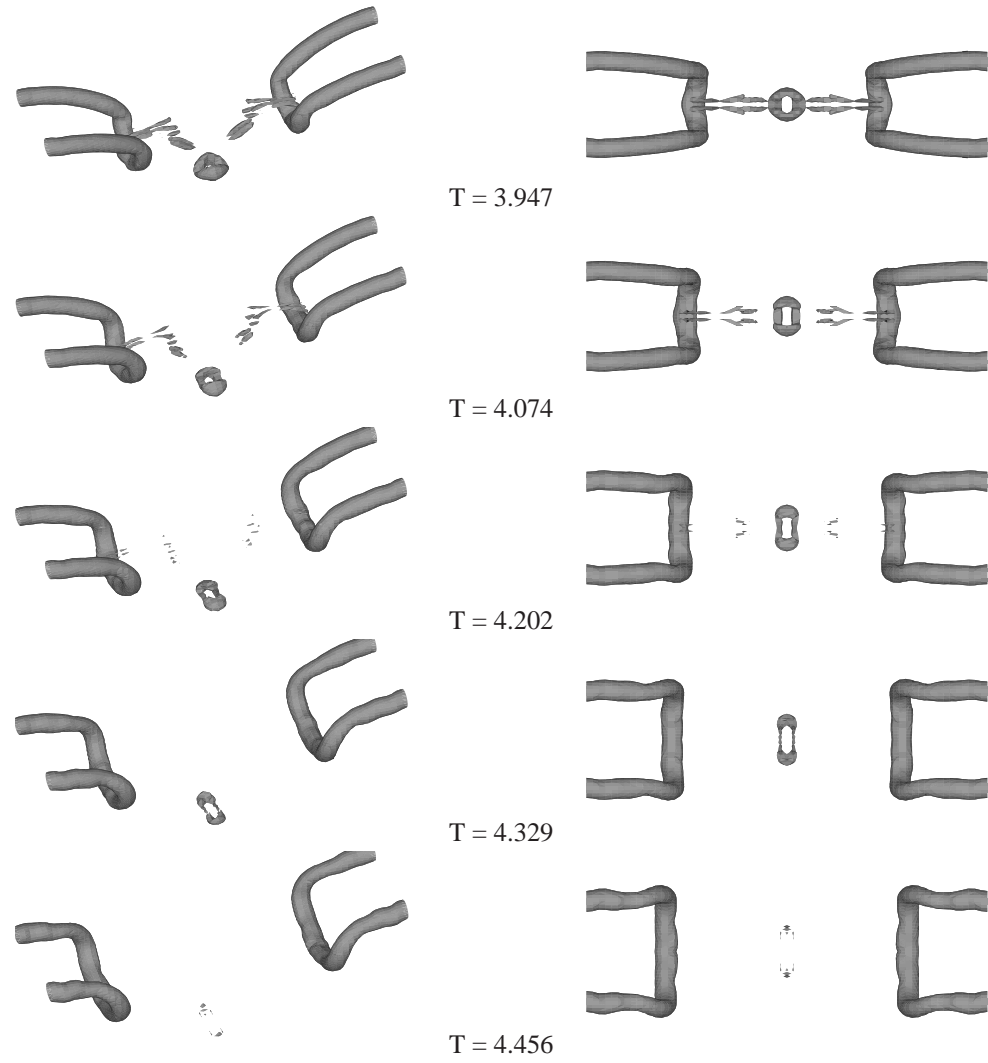


FIGURE 5.17: *Formation of vortex-ring structures: $Re_{\Gamma} = 1.67 \cdot 10^4$, $64 \times 128 \times 128$ mesh, $r_c/b = 0.2$, $\lambda/b = 8.0$, $|\underline{\omega}| = 500 \text{ s}^{-1}$*

5.7 Analysis of kinetic energy spectra

In this section the evolution of the long-wavelength instability is analyzed using kinetic energy spectra. These spectra are obtained by computing the Fast Cosine Transform in the periodic direction of the kinetic energy, scaled by the number of mesh points in the cross-flow planes, i.e. the Fast Cosine Transform is computed employing the discrete quantity:

$$E_k = \frac{1}{(N_J + 1)(N_K + 1)} \sum_{i=0}^{N_J} \sum_{j=0}^{N_K} \frac{1}{2} \left(u_{i,j,k}^2 + v_{i,j,k}^2 + w_{i,j,k}^2 \right) \quad (5.4)$$

with k denoting the wave number in the axial direction, which coincides with the x -coordinate direction. The coefficients of this Fast Cosine Transform represent the amount of kinetic energy contained in modes at the various wavelengths in the periodic direction. The Fast Cosine Transform used here gives coefficients for wave numbers $k \in [0, N_I]$, with $N_I + 1$ the number of mesh points in the periodic direction. As a result of the prescribed boundary conditions and the choice for a single instability mode in the computational domain, only the coefficients of even wave numbers k are non-zero. Wavenumber $k = 0$ represents the average in the periodic direction. Therefore, E_0 represents a measure for the total kinetic energy per unit of volume averaged over the computational domain. The time-dependence of this quantity is studied in subsection 5.7.1.

Wave number $k = 2$ corresponds to the wavelength of the instability mode, or the length of the computational domain in the axial direction. The distribution of the kinetic energy over the range of wave numbers represents a measure for the spatial resolution of the numerical simulations. The mode corresponding to $k = N_I$ represents the shortest resolvable mode in the periodic direction of the computational domain. The discretization methods used here, can be shown to have a poor resolution for short wavelengths with a wave number close to $k = N_I$. Therefore, for a well-resolved simulation it is required that the energy contained at these short wavelengths is small throughout the evolution of the instability. Kinetic energy spectra at various stages of the evolution of the Crow instability are discussed in subsection 5.7.2.

In this section, results from three simulations of the evolving Crow instability are discussed, obtained using the hybrid Navier-Stokes method: results for $Re_\Gamma = 1.67 \cdot 10^3$ on the $64 \times 128 \times 128$ mesh and for $Re_\Gamma = 1.67 \cdot 10^4$ on both the $64 \times 128 \times 128$ and $128 \times 128 \times 128$ meshes. For these three simulations, $\lambda/b = 8.0$ and $L_x = L_y = L_z = 8.0 b$. These three simulations are part of the group of simulations shown in table 5.2 of section 5.2.

5.7.1 Decay of kinetic energy of vortex pair

For $Re_\Gamma = 1.67 \cdot 10^4$, the averaged kinetic energy E_0 at wave number $k = 0$ is plotted as a function of non-dimensional time in figure 5.18. The averaged kinetic energy is normalized by the value of this quantity at $T = 0$. Results are compared for the two different meshes. For the $64 \times 128 \times 128$ mesh, the evolution of the Crow instability was shown in figure 5.17 of section 5.6. The results for the $128 \times 128 \times 128$ mesh was shown in figure 5.12 of section 5.5. These figures clearly showed the reconnection process of the vortices and the formation of the vortex rings and the 'bridges' connecting these rings from $T \approx 3$ onwards. This reconnection process coincides with a steepening of the energy decay in figure 5.18. This shows that the Crow instability enhances the energy decay of a counter-rotating vortex pair compared to viscous diffusion of the vortex cores, which leads to a growing vortex core

radius and a decrease of the azimuthal velocity. This energy decay mechanism dominates the earlier stage of the development, with a significantly smaller slope of the total kinetic energy curve.

A notable feature of figure 5.18 is the small difference in computed energy decay for the two meshes. Comparing figures 5.12 and 5.17, a notable difference can be observed in the resolution of the small-scale vortical structures at the later stages of the development. From the comparison shown in figure 5.18, it can be concluded that the kinetic energy contained in these structures is very small and that the majority of the kinetic energy is contained in the vortex rings. The effect of Reynolds number on the kinetic energy decay is shown

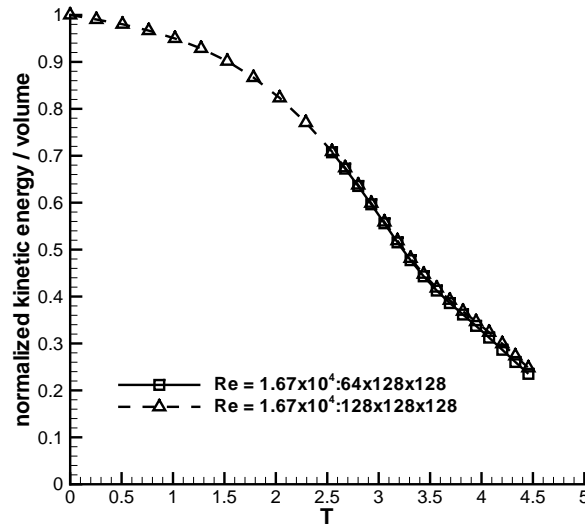


FIGURE 5.18: *Decay of normalized kinetic energy E_0 : effect of mesh resolution*

in figure 5.19. These figures show a nearly constant decay of the kinetic energy for the lower Reynolds number. The energy decay in the early stages is more pronounced for the lower Reynolds number, as a result of the larger viscous diffusion of the vortex cores. The evolution of the Crow instability for this lower Reynolds number was shown in figure 5.16 of section 5.6. A significantly slower evolution of the reconnection process can be observed for this lower Reynolds number. This reduced rate of the reconnection process and the increased contribution of the viscous diffusion of the vortices in the energy decay process, explain the absence of the steepening of the decay curve, as observed for the higher Reynolds number. A notable features is that the remaining kinetic energy remaining is higher at the later stages for the lower Reynolds number situation than for the higher Reynolds number. This shows the importance of the Crow instability in the energy decay process.

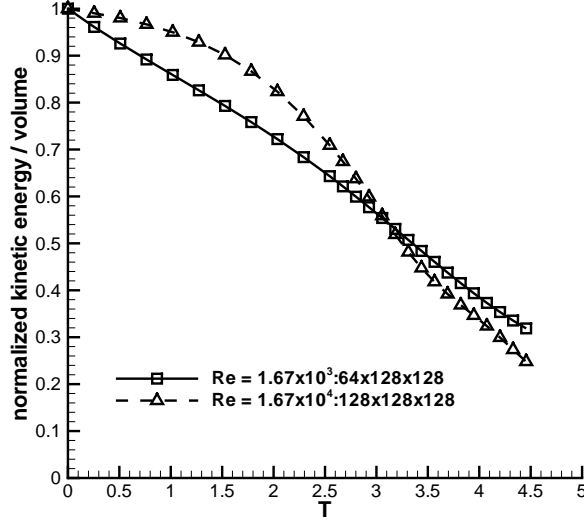


FIGURE 5.19: *Decay of normalized kinetic energy E_0 : effect of Reynolds number*

5.7.2 Kinetic energy spectra for nonlinear stage

For the three simulations considered in this section, the kinetic energy spectra are shown in figures 5.20, 5.21 and 5.22 for the later stages of the long-wavelength instability. Non-dimensional time T advances from 3.183 to 4.456. As an illustration of the temporal evolution of the kinetic energy spectra, figure 5.20 shows the spectrum for $T = 1.273$, which corresponds to an early stage of the development.

The numerical errors of the various finite-difference approximations used in the Navier-Stokes method will be significant at the highest wave numbers in these spectra, at wave numbers close to that of the shortest resolvable mode. Therefore, a low kinetic energy content at these high wave numbers is a requirement for a well-resolved simulation. The energy contained in the shortest-resolvable mode is therefore a useful measure for the spatial resolution of the numerical simulation.

Figure 5.20 shows the spectra for $Re_\Gamma = 1.67 \cdot 10^3$ and the $64 \times 128 \times 128$ mesh. The horizontal axis starts at $k = 2$, corresponding to the instability mode at the most amplified wavelength. The figure shows that most of the kinetic energy is contained at the lower wave numbers. The kinetic energy at the wave number corresponding to the shortest resolvable wavelength is about 5 orders of magnitude smaller than that at the wavelength of the instability.

Figure 5.20 shows that kinetic energy is transferred to ever smaller wavelengths as time advances. The situation at $T = 1.273$ is shown to illustrate the shape of the kinetic energy spectrum at an early stage of the evolution of the instability.

The transfer of kinetic energy to ever smaller wavelengths corresponds to the formation of the

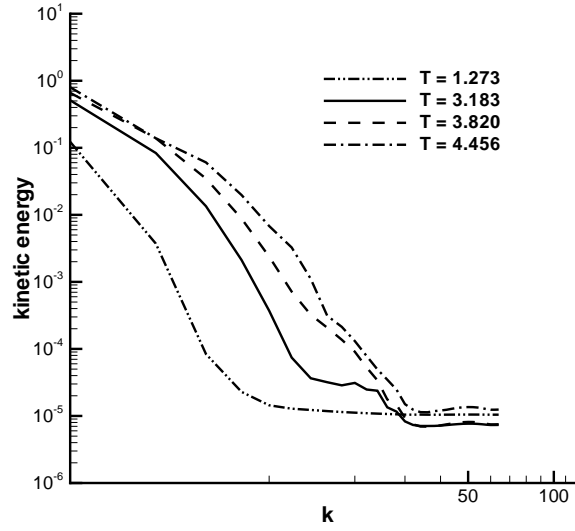


FIGURE 5.20: *Kinetic energy spectrum of simulation shown in figure 5.16 : $Re_{\Gamma} = 1.67 \cdot 10^3$, $64 \times 128 \times 128$ mesh*

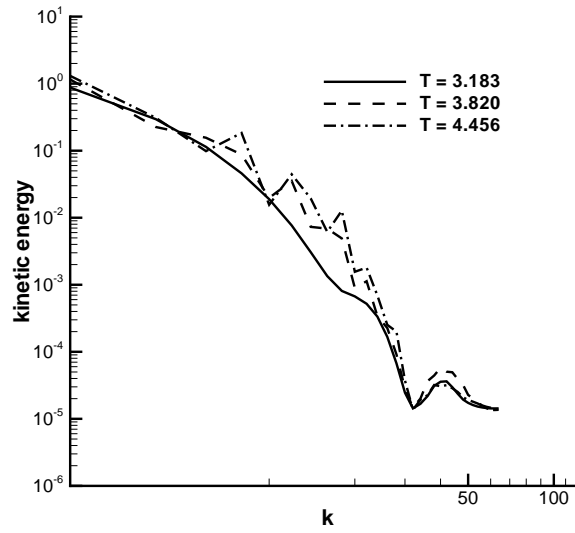


FIGURE 5.21: *Kinetic energy spectrum of simulation shown in figure 5.17 : $Re_{\Gamma} = 1.67 \cdot 10^4$, $64 \times 128 \times 128$ mesh*

smaller scale vortical structures typical of the later stages of the development, i.e. the vortex-ring structures and the dipolar 'bridges' linking the two vortex rings. For this Reynolds number, the mesh appears to be sufficient for a good resolution of the flow field: the kinetic energy content at the smallest wavelengths remains low throughout the simulation.

Figure 5.21 shows a similar results for a higher Reynolds number, $Re_\Gamma = 1.67 \cdot 10^4$. At this higher Reynolds number, more kinetic energy is contained at the smaller wavelengths. As expected the spatial resolution is less than at the lower Reynolds. The time-dependence of the spectra is equivalent with that of figure 5.20, with a transfer of energy to smaller length-scales.

The small 'bump' in the energy spectra is a result of the suppressed energy build-up at the under-resolved wavelengths. Without application of the low-pass compact-difference filter, this build-up would continue, leading to significant numerical errors at the later stages. Finally, figure 5.22 shows results for the same Reynolds number at the finer 128^3 mesh. The

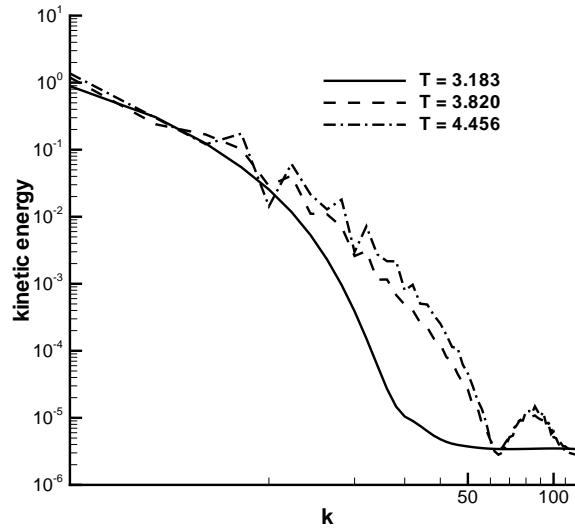


FIGURE 5.22: *Kinetic energy spectrum of simulation shown in figure 5.12 : $Re_\Gamma = 1.67 \cdot 10^4$, $128 \times 128 \times 128$ mesh*

figure shows that less energy is contained at the smallest wavelengths than for the coarser mesh. Furthermore, the formation of the small 'bump' in the energy spectra is delayed to later times.

Figures 5.20 and 5.22 show that a sufficient resolution of the long-wavelength instability at the different Reynolds numbers is obtained using the chosen meshes.

SHORT-WAVELENGTH INSTABILITY



This chapter presents a numerical study of the short-wavelength instability in a counter-rotating vortex pair. Theoretical results for vortices immersed in a strain field are used for the determination of the initial conditions of the time-accurate numerical simulations based on the Navier-Stokes equations and in the discussion of the numerical results. Furthermore, the numerical results are compared with the results from an experimental study by Leweke and Williamson (1998) of a closely-spaced vortex pair generated in a water tank.

Some general characteristics of the short-wavelength instability were discussed earlier in section 1.3. Cooperative instabilities in vortex pairs result from the velocity field the vortices induce on one another. For the short-wavelength branch of the cooperative instabilities, the strain field created by the induced velocity causes a flattening of the vortex core regions. This leads to finite regions with elliptical streamlines in the cross-flow planes of the vortices. Three-dimensional flows which are initially constant in one of the three coordinate directions and contain finite regions with elliptical streamlines in the two other coordinate directions are known to develop three-dimensional instabilities which are periodic in the initially constant coordinate direction, see for example Waleffe (1990) and Pierrehumbert (1986). These three-dimensional instabilities are commonly known as *elliptic instabilities*. General features of these elliptic instabilities are that the center of the elliptical flow region is displaced in the direction of the maximum stretching of the applied strain field and that the disturbance of the flow in inner and outer parts of the finite elliptical region are displaced in opposite radial directions. Both features are characteristic of the short-wavelength instability modes in strained vortices, such as those in vortex pairs. This short-wavelength instability can be treated as a manifestation of an elliptic instability of the vortex cores, see Leweke and Williamson (1998).

In this chapter, the temporal evolution of the short-wavelength instability in a counter-rotating vortex pair and its dependence on a number of parameters is studied. Results from linear stability theory show that the short-wavelength instability in a vortex pair occurs in a number of branches around increasingly higher wave numbers in the periodic direction. Recently, the linear stability of a pair of Lamb-Oseen vortices was studied by Sipp et al. (1998) using a matrix-eigenvalue method. The longest-wavelength branch of the short-wavelength instability typically corresponds to a most unstable wavelength of the order of the vortex core radius. The subsequent branches correspond to ever smaller wavelengths. The analysis presented by Sipp et al. (1998) included three of these short-wavelength branches. Instability modes at even higher wave numbers were not considered.

Numerical simulations of time-dependent flows require the prescription of a physically meaningful initial flow field. For the short-wavelength instability in a vortex pair this proves to be more complicated than for the long-wavelength Crow instability. In the case of the Crow instability, it is general practice to initialize the flow field with a vortex pair consisting of nearly straight vortices with a small sinusoidal displacement of the vortex centers in planes perpendicular to the periodic direction and using a two-dimensional flow field in these planes. Typically, the displacement of the vortex centers has a sinusoidal dependence in the periodic direction with a wavelength equal to the wavelength of the most amplified unstable mode as found from linear stability theory.

The short-wavelength instability is characterized by a strong deformation of the vortices within the vortex cores. An initialization method similar to that for the Crow instability will not initiate many of the important features of the instability. Therefore, a more elaborate method to compute the initial condition is used in the present study. This method is described in detail in section 6.1. The method is based on a normal mode analysis of the linearized Euler equations in cylindrical coordinates for a Lamb-Oseen vortex. The normal modes represent the radial dependence of Kelvin modes on this vortex. The short-wavelength instabilities studied here, are assumed to occur as a result of a resonance effect between the straining field and two stationary Kelvin waves, one with azimuthal wavenumber $m = -1$ and the other with $m = +1$. This mechanism was described in for example Tsai and Widnall (1976) and Sipp (2000). The computed spatial structure for these specific Kelvin modes can then be used to create the perturbations for the two vortices of the vortex pair. This method for the computation of the initial flow field can be used for the different branches of the short-wavelength instability.

The numerical results discussed in this chapter were obtained using the hybrid Fourier/compact-difference Navier-Stokes method described in chapter 3. The effect of various parameters on the evolution of the instability is studied. The theoretical work by Sipp (2000) predicts a weakly non-linear saturation phenomenon for the short-wavelength instability, i.e. the perturbation shows an initial exponential growth until a certain amplitude is reached. In the subsequent stages of the development, the growth is predicted to terminate and a rotational motion of the perturbation sets in. Analyzing this saturation phenomenon is the major objective of the present chapter. Numerical results are presented and discussed in section 6.2.

6.1 Determination of initial condition

The determination of the initial conditions to be used in the time-dependent simulations is based on the computation of specific Kelvin modes of a Lamb-Oseen vortex. Following the analyses by Tsai and Widnall (1976) and Sipp (2000), the stationary Kelvin modes with azimuthal wavenumber $|m| = 1$ are considered. The initial perturbation of the vortices in the vortex pairs is assumed to be a linear combination of these Kelvin modes. In this section, the axial direction of the vortex coincides with the z -coordinate direction. In a cylindrical

coordinate system this can be written as:

$$\underline{u}(r, \theta, z) = A_{-1} \begin{bmatrix} \tilde{u}_r \\ \tilde{u}_\theta \\ \tilde{u}_z \\ \tilde{p} \end{bmatrix}_{m=-1} e^{-i\theta} e^{ikz} + A_{+1} \begin{bmatrix} \tilde{u}_r \\ \tilde{u}_\theta \\ \tilde{u}_z \\ \tilde{p} \end{bmatrix}_{m=+1} e^{+i\theta} e^{ikz} + \text{c.c.} \quad (6.1)$$

where A_{-1} and A_{+1} are the complex amplitudes, which are taken as complex conjugates

$$A_{-1} = Ae^{-i\phi} \quad \text{and} \quad A_{+1} = Ae^{+i\phi} \quad (6.2)$$

with ϕ an arbitrary angle and A the real-valued amplitude of the disturbance. In equation (6.1), \tilde{u}_r , \tilde{u}_θ , \tilde{u}_z and \tilde{p} are functions of the radial coordinate r and c.c denotes the complex conjugate of the preceding complex expression. These functions can be obtained from a normal mode analysis of the linearized Euler equations for a base flow consisting of a Lamb-Oseen vortex, as described in sections 6.1.1, 6.1.2, 6.1.3 and 6.1.4. The method used here is based on the method of Sipp (2000). With these normal modes known, the initial perturbation of the counter-rotating vortex pair is computed in section 6.1.5.

6.1.1 Normal modes of linearized equations for Lamb-Oseen vortex

Consider the three-dimensional flow consisting of a vortex column with a Lamb-Oseen azimuthal velocity profile. Assume that the axial direction coincides with the z -coordinate direction. The azimuthal velocity profile of a Lamb-Oseen is given by:

$$u_\theta(r) = \frac{\Gamma}{2\pi} \frac{[1 - \exp(-\gamma r^2/r_c^2)]}{r} \quad (6.3)$$

where r_c represents the vortex core radius.

The constant γ in the exponential function is chosen to position the maximum of azimuthal velocity at r_c (this leads to the constraint $(2\gamma + 1)e^{-\gamma} = 1 \rightarrow \gamma \cong 1.256$).

In the remainder of this section, non-dimensional quantities are used, with velocity components scaled by $\Gamma\sqrt{\gamma}/2\pi r_c$ and the r and z coordinates by $r_c/\sqrt{\gamma}$.

In a cylindrical coordinate system (r, θ, z) , this flow field has velocity components

$$u_r(r, \theta, z) = 0, \quad u_\theta(r, \theta, z) = r\Omega(r), \quad u_z(r, \theta, z) = 0 \quad (6.4)$$

with the angular velocity $\Omega(r)$ given by

$$\Omega(r) = (1 - e^{-r^2})/r^2 \quad (6.5)$$

Consider small perturbations that are periodic in both azimuthal and axial directions, as in equation (6.1). Assuming a steady inviscid flow, the linearized Euler equations in a cylindrical coordinate system for small perturbations $\tilde{u}_r(r)$, $\tilde{u}_\theta(r)$ and $\tilde{u}_z(r)$ become

$$im\Omega\tilde{u}_r - 2\Omega\tilde{u}_\theta = -\frac{d\tilde{p}}{dr} \quad (6.6)$$

$$im\Omega\tilde{u}_\theta + \tilde{u}_r\left(2\Omega + r\frac{d\Omega}{dr}\right) = -i\frac{m\tilde{p}}{r} \quad (6.7)$$

$$im\Omega\tilde{u}_z = -ik\tilde{p} \quad (6.8)$$

$$\frac{d\tilde{u}_r}{dr} + \frac{\tilde{u}_r}{r} + \frac{im}{r}\tilde{u}_\theta + ik\tilde{u}_z = 0 \quad (6.9)$$

with the pressure perturbation \tilde{p} scaled with the constant density of the fluid. The system of equations (6.6), (6.7) and (6.8) can be rewritten in matrix notation as

$$\begin{bmatrix} im\Omega & -2\Omega & 0 \\ 2\Omega + r\frac{d\Omega}{dr} & im\Omega & 0 \\ 0 & 0 & im\Omega \end{bmatrix} \begin{bmatrix} \tilde{u}_r \\ \tilde{u}_\theta \\ \tilde{u}_z \end{bmatrix} = - \begin{bmatrix} \frac{d\tilde{p}}{dr} \\ im\frac{d\tilde{p}}{dr} \\ ik\tilde{p} \end{bmatrix} \quad (6.10)$$

The first two equations of system (6.10) give for the two unknowns \tilde{u}_r and \tilde{u}_θ :

$$\begin{aligned} \tilde{u}_r(r) &= \left[-im\left(\Omega\frac{d\tilde{p}}{dr} + 2\frac{\tilde{p}}{r}\right) \right] / \left[(4-m^2)\Omega^2 + 2\Omega r\frac{d\Omega}{dr} \right] \\ \tilde{u}_\theta(r) &= \left[(2\Omega + r\frac{d\Omega}{dr})\frac{d\tilde{p}}{dr} + m^2\frac{\tilde{p}}{r} \right] / \left[(4-m^2)\Omega^2 + 2\Omega r\frac{d\Omega}{dr} \right] \end{aligned} \quad (6.11)$$

and for the unknown \tilde{u}_z system (6.10) gives:

$$\tilde{u}_z(r) = -\frac{k}{m\Omega}\tilde{p} \quad (6.12)$$

Equations (6.11) and (6.12) show that the radial structure functions \tilde{u}_r , \tilde{u}_θ , \tilde{u}_z and \tilde{p} for azimuthal wave numbers $|m| = 1$ have the following form

$$\begin{bmatrix} \tilde{u}_r \\ \tilde{u}_\theta \\ \tilde{u}_z \\ \tilde{p} \end{bmatrix}_{m=-1} = \begin{bmatrix} iu_{\pm 1} \\ v_{\pm 1} \\ w_{\pm 1} \\ p_{\pm 1} \end{bmatrix} \quad \text{and} \quad \begin{bmatrix} \tilde{u}_r \\ \tilde{u}_\theta \\ \tilde{u}_z \\ \tilde{p} \end{bmatrix}_{m=+1} = \begin{bmatrix} -iu_{\pm 1} \\ v_{\pm 1} \\ -w_{\pm 1} \\ p_{\pm 1} \end{bmatrix} \quad (6.13)$$

with $u_{\pm 1}$, $v_{\pm 1}$, $w_{\pm 1}$ and $p_{\pm 1}$ real-valued functions of r . Equation (6.13) is identical to the equivalent equation (2.145) of section 2.7.1. For azimuthal wavenumber $m = -1$, system of equations (6.10) can be transformed into the following system

$$\frac{d}{dr} \begin{bmatrix} u_{\pm 1} \\ p_{\pm 1} \end{bmatrix} = \begin{bmatrix} -\frac{1}{r} + \frac{2\Omega + r\frac{d\Omega}{dr}}{r\Omega} & -\frac{k^2 + 1/r^2}{\Omega} \\ -\Omega + 2\left(2\Omega + r\frac{d\Omega}{dr}\right) & -\frac{2}{r} \end{bmatrix} \begin{bmatrix} u_{\pm 1} \\ p_{\pm 1} \end{bmatrix} \quad (6.14)$$

$$v_{\pm 1} = \frac{(2\Omega + r\frac{d\Omega}{dr})u_{\pm 1} - p_{\pm 1}/r}{\Omega} \quad (6.15)$$

$$w_{\pm 1} = \frac{kp_{\pm 1}}{\Omega} \quad (6.16)$$

The normal modes of the linearized Euler equations for the Lamb-Oseen vortex are computed from the coupled set of equations (6.14). The other two components of these modes can then be computed from relations (6.15) and (6.16). For the computation of the normal modes, boundary conditions need to be prescribed for system (6.14). The determination of these boundary conditions is described in section 6.1.2.

System (6.14) is a homogeneous system of linear equations, which has non-trivial solutions only for specific axial wave numbers k . The discretization of system of equations (6.14) is based on a Chebyshev collocation method described in section 6.1.3. The discretization matrix is a singular matrix for the axial wave numbers of interest here. The procedure to find these wave numbers k uses *LU* decomposition on the resulting matrix and checks the pivot of the last row. The procedure searches for the value of k for which this pivot is identically zero.

6.1.2 Boundary value problem for pressure

From the system of equations (6.10), a boundary value problem for the pressure can be derived. Substitution of equation (6.13) in equation (6.11) gives expressions for the real-valued functions $u_{\pm 1}$ and $v_{\pm 1}$ in terms of the pressure perturbation:

$$\begin{bmatrix} u_{\pm 1} \\ v_{\pm 1} \end{bmatrix} = \frac{1}{\Delta} \begin{bmatrix} -m\Omega \frac{dp_{\pm 1}}{dr} - 2\frac{m}{r}\Omega p_{\pm 1} \\ (2\Omega + r\frac{d\Omega}{dr})\frac{dp_{\pm 1}}{dr} + \Omega\frac{m^2}{r}p_{\pm 1} \end{bmatrix} \quad (6.17)$$

where $\Delta = (4 - m^2)\Omega^2 + 2\Omega r\frac{d\Omega}{dr}$. From equation (6.12) follows

$$w_{\pm 1} = -\frac{k}{m\Omega}p_{\pm 1} \quad (6.18)$$

Substitution of expressions (6.17) and (6.18) in the continuity equation (6.9) gives

$$-m\left(\frac{d}{dr} + \frac{1}{r}\right) \left\{ \frac{\Omega \frac{dp_{\pm 1}}{dr} + 2\Omega \frac{p_{\pm 1}}{r}}{\Delta} \right\} + \frac{m}{r} \left\{ \frac{(2\Omega + r\frac{d\Omega}{dr})\frac{dp_{\pm 1}}{dr} + \Omega\frac{m^2}{r}p_{\pm 1}}{\Delta} \right\} - \frac{k^2}{m\Omega}p_{\pm 1} = 0 \quad (6.19)$$

This can be rewritten as

$$\begin{aligned} \frac{m\Omega}{\Delta} \frac{d^2 p_{\pm 1}}{dr^2} + \frac{m}{\Delta} \left\{ \frac{\Omega}{r} - \frac{\Omega}{\Delta} \frac{d\Delta}{dr} \right\} \frac{dp_{\pm 1}}{dr} + \\ \frac{m}{\Delta} \left\{ \frac{2}{r} \frac{d\Omega}{dr} - \frac{m^2\Omega}{r^2} - 2\frac{\Omega}{\Delta r} \frac{d\Delta}{dr} + \Delta \frac{k^2}{m^2\Omega} \right\} p_{\pm 1} = 0 \end{aligned} \quad (6.20)$$

Finally, the governing equation for the pressure component of normal modes of a Lamb-Oseen vortex can be written as

$$\frac{d^2 p_{\pm 1}}{dr^2} + \left(\frac{1}{r} - \frac{1}{\Delta} \frac{d\Delta}{dr} \right) \frac{dp_{\pm 1}}{dr} + \left(\frac{2}{\Omega r} \left(\frac{d\Omega}{dr} - \frac{\Omega}{\Delta} \frac{d\Delta}{dr} \right) + \frac{\Delta k^2}{m^2\Omega^2} - \frac{m^2}{r^2} \right) p_{\pm 1} = 0 \quad (6.21)$$

Equation (6.21) is identical to the corresponding equation given in Saffman (1992).

The boundary conditions for the normal modes of system of equations (6.14) can now be derived from studying the behaviour of equation (6.21) in the vicinity of $r = 0$. Developing the coefficient of $\frac{dp_{\pm 1}}{dr}$ in equation (6.21) for vanishing r gives

$$\begin{aligned} \frac{1}{r} - \frac{1}{\Delta} \frac{d\Delta}{dr} &= \frac{1}{r} - \frac{1}{(4 - m^2)\Omega^2 + 2\Omega r\frac{d\Omega}{dr}} \frac{d}{dr} \left\{ (4 - m^2)\Omega^2 + 2\Omega r\frac{d\Omega}{dr} \right\} \\ &= \frac{1}{r} - \frac{2(5 - m^2)\Omega \frac{d\Omega}{dr} + 2\Omega r\frac{d^2\Omega}{dr^2} + 2r\left(\frac{d\Omega}{dr}\right)^2}{(4 - m^2)\Omega^2 + 2\Omega r\frac{d\Omega}{dr}} \\ &\approx \frac{1}{r} - \frac{(2m^2 - 12)r + O(r^3)}{(4 - m^2) + O(r^2)} \quad \text{for } r \ll 1 \\ &\approx \frac{1}{r} \quad \text{for } r \ll 1 \end{aligned} \quad (6.22)$$

And similarly for the coefficient of $p_{\pm 1}$ in equation (6.21)

$$\begin{aligned} \frac{2}{\Omega r} \left(\frac{d\Omega}{dr} - \frac{\Omega}{\Delta} \frac{d\Delta}{dr} \right) + \frac{\Delta k^2}{m^2\Omega^2} - \frac{m^2}{r^2} &\approx (22 - 4m^2) + O(r^2) \\ &\quad + \frac{k^2}{m^2} \left\{ (4 - m^2) + O(r^2) \right\} \\ &\quad - \frac{m^2}{r^2} \approx -\frac{m^2}{r^2} \quad \text{for } r \ll 1 \end{aligned} \quad (6.23)$$

With expansions (6.22) and (6.23), equation (6.21) can be written, for vanishing r , as

$$\frac{d^2 p_{\pm 1}}{dr^2} + \frac{1}{r} \frac{dp_{\pm 1}}{dr} - \frac{m^2}{r^2} p_{\pm 1} = 0 \quad (6.24)$$

For $|m| = 1$, equation (6.24) has the solution $p_{\pm 1}(r) = r$. This leads to the following boundary conditions at the origin for system (6.14):

$$\begin{aligned} \frac{dp_{\pm 1}}{dr}(0) &= 1 \\ u_{\pm 1}(0) &= -m \end{aligned} \quad (6.25)$$

for $|m| = 1$. For $r \rightarrow \infty$ it is prescribed that the perturbations $u_{\pm 1}$, $v_{\pm 1}$, $w_{\pm 1}$ and $p_{\pm 1}$ vanish.

6.1.3 Chebyshev collocation discretization method

The system of equations (6.14) is discretized using a Chebyshev collocation method. The perturbations $p_{\pm 1}$ and $u_{\pm 1}$ are expanded in terms of Chebyshev polynomials T_k

$$f(r_i) = \left[\sum_{k=0}^N c_k T_k(r_i) \right] - \frac{1}{2} c_0 \quad (6.26)$$

which are exact on the $N + 1$ Gauss collocation points r_i :

$$r_i = \cos \left(\frac{2i+1}{2N+2} \pi \right), \quad i = 0, \dots, N \quad (6.27)$$

In equations (6.26), T_k are the Chebyshev polynomials

$$T_k(x) = \cos \left(k \cos^{-1}(x) \right) \quad (6.28)$$

First derivatives of the variables are approximated similarly as

$$\frac{df}{dr}(r_i) = \left[\sum_{k=0}^N c'_k T_k(r_i) \right] - \frac{1}{2} c'_0 \quad (6.29)$$

The coefficients in (6.29) and (6.26) are related through the recurrence relation

$$c'_{k-1} = c'_{k+1} + 2kc_k, \quad k = N, \dots, 1, \quad c'_0 = 0 \quad (6.30)$$

For the spatial discretization of the system of equations, a relation between the values of quantity f and the derivative of f in the collocation points (6.27) is required.

$$\begin{bmatrix} \frac{df}{dr}(r_0) \\ \frac{df}{dr}(r_1) \\ \vdots \\ \frac{df}{dr}(r_N) \end{bmatrix} = D^{(1)} \begin{bmatrix} f(r_0) \\ f(r_1) \\ \vdots \\ f(r_N) \end{bmatrix} \quad (6.31)$$

with the derivative matrix $D^{(1)}$ computed using recurrence relation (6.30).

6.1.4 Computed Kelvin modes for Lamb-Oseen vortex

Using the search method described in section 6.1.1, the first three normal modes for a Lamb-Oseen vortex are computed. This vortex has an azimuthal velocity profile given by equation (6.3). The first three normal modes occur at (scaled) axial wave numbers $k = 2.261$, $k = 3.958$ and $k = 5.612$.

This corresponds to wavelengths of $2.512 r_c$, $1.416 r_c$ and $0.999 r_c$, respectively. For these three modes, the components $u_{\pm 1}$, $v_{\pm 1}$, $w_{\pm 1}$ and $p_{\pm 1}$ are plotted, for azimuthal wavenumber $m = -1$, in figures 6.1, 6.2 and 6.3. For all three axial wave numbers, radial velocity

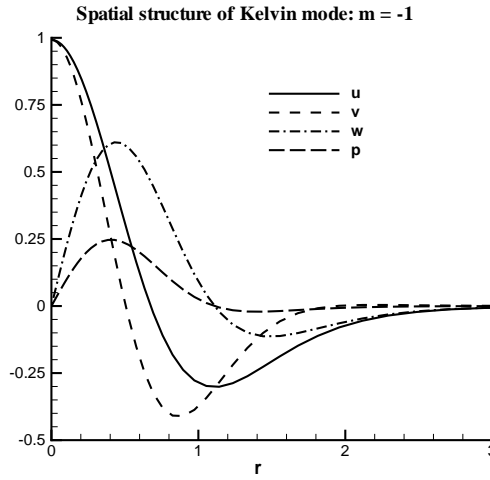


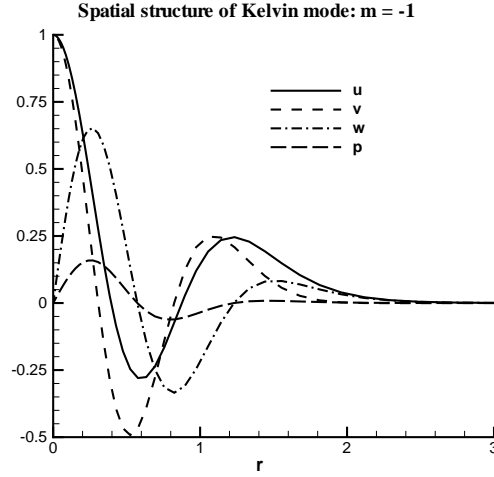
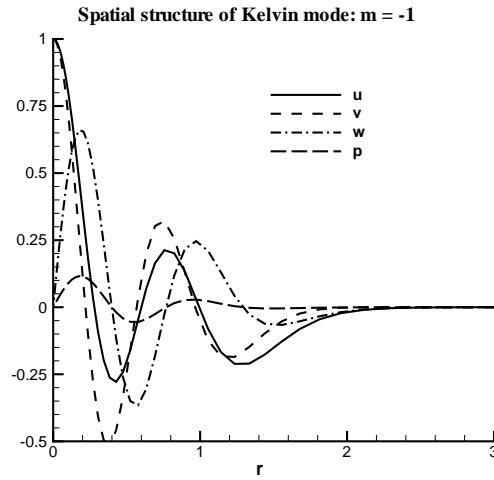
FIGURE 6.1: Normal mode: $m = -1$, $k = 2.261$.

component $u_{\pm 1}$ and azimuthal velocity component $v_{\pm 1}$ do not vanish at the origin. Furthermore, it can be observed that for increasing axial wave numbers, thus for smaller-wavelength modes, the perturbations show a more rapid variation in the radial direction and an increasing number of oscillations. Thus, the modes with smaller wavelengths in the axial direction are characterized by smaller length scales in the radial direction.

6.1.5 Initial perturbation of the vortex pair

With assumption (6.2) and equation (6.13), the perturbation for each vortex, given by equation (6.1), can be written as

$$\begin{aligned}
 \underline{u}(r, \theta, z) &= A e^{i\phi} e^{-i\theta} e^{ikz} \begin{bmatrix} iu_{\pm 1} \\ v_{\pm 1} \\ w_{\pm 1} \\ p_{\pm 1} \end{bmatrix} + A e^{-i\phi} e^{+i\theta} e^{ikz} \begin{bmatrix} -iu_{\pm 1} \\ v_{\pm 1} \\ -w_{\pm 1} \\ p_{\pm 1} \end{bmatrix} + \text{c.c.} \\
 &= 4A \begin{bmatrix} u_{\pm 1} \sin(\theta - \phi) \cos(kz) \\ v_{\pm 1} \cos(\theta - \phi) \cos(kz) \\ w_{\pm 1} \sin(\theta - \phi) \sin(kz) \\ p_{\pm 1} \cos(\theta - \phi) \cos(kz) \end{bmatrix} \quad (6.32)
 \end{aligned}$$

FIGURE 6.2: Normal mode: $m = -1$, $k = 3.958$.FIGURE 6.3: Normal mode: $m = -1$, $k = 5.612$.

with $u_{\pm 1}$, $v_{\pm 1}$, $w_{\pm 1}$ and $p_{\pm 1}$ the real functions of r computed in the previous sections. Perturbations on the basic flow field of the form (6.32) induce a distortion of the vortex core region, with the deformation being more pronounced near the vortex axis.

The next step in the computation of the initial perturbation of the vortex pair, is the determination of the angle ϕ . For an isolated vortex, this angle is arbitrary. In the vortex pair, ϕ determines the phase-relation of the perturbation of the two vortices. Here, the phase-relation is

chosen to match that observed in the water-tank visualizations of Leweke and Williamson (1998), described in section 1.3.3.

For the short-wavelength instability at the largest axial-wavelength, the initial vorticity field is presented in figure 6.4. The qualitative behaviour of the disturbance is in good agreement with the observed short-wavelength instabilities of Leweke and Williamson (1998).

6.2 Numerical results

Table 6.1 summarizes the parameters of the numerical simulations that were performed for the short-wavelength instability. In all cases, the magnitude of the circulation of the vortices is taken as $2.5 \text{ m}^2/\text{s}$. The temporal development of two axial wavelengths is considered. For the longest wavelength situation, the effect of spacing of the vortex pair and effects of viscosity are studied. The effect of the spacing is expected to be particularly important, since the spacing of the vortex pair determines the strength of the effective strain field in which both vortices are immersed. The effect on the strain on the vortex cores is the underlying mechanism of the short-wavelength instability. The theoretical work of Sipp (2000) predicts that the amplitude of the perturbation of the vortices, at which the growth of the instability saturates, is directly proportional to the strength of the strain field. In this section, time is non-

TABLE 6.1: *Parameters of short-wavelength instability simulations*

k	r_c/b	Γ/ν	mesh	$\delta t[s]$	$L_x = 2\lambda[m]$	$L_y = L_z[m]$
2.261	0.20	$1.67 \cdot 10^4$	$64 \times 128 \times 128$	$5.0 \cdot 10^{-5}$	$5.024 r_c$	$8.0 b$
2.261	0.20	$1.67 \cdot 10^5$	$64 \times 128 \times 128$	$5.0 \cdot 10^{-5}$	$5.024 r_c$	$8.0 b$
2.261	0.15	$1.67 \cdot 10^4$	$64 \times 128 \times 128$	$8.9 \cdot 10^{-5}$	$5.024 r_c$	$8.0 b$
3.958	0.20	$1.67 \cdot 10^4$	$64 \times 128 \times 128$	$5.0 \cdot 10^{-5}$	$2.832 r_c$	$8.0 b$

dimensionalized using $\Gamma/2\pi b^2$. Here b is the spacing of the vortex pair. The time-step in the simulation of the vortex pair with the larger separation is adjusted, such that non-dimensional times after a specific number of time-steps correspond to those for the simulation of the closer-spaced vortex pairs

6.2.1 Results for $k = 2.261$

This section describes the simulations that were performed for the branch of short-wavelength instabilities with the longest wavelength. The length of the computational domain in the axial direction of the vortex pair, L_x in table 6.1, is chosen to fit two modes of the instability. The wavelength λ of the instability with $k = 2.261$ is $2.512 r_c$.

For this branch of instabilities, the following effects are studied:

- aspect ratio r_c/b of the vortex pair. This ratio determines the strength of the effective strain field in which the vortices are located. To adjust this ratio, the spacing b is changed and the core radius r_c is kept constant;

- viscous effects. The Reynolds number based on circulation Γ/ν is changed by adjusting the kinematic viscosity ν . Here, $\nu = 1.5 \cdot 10^{-4} \text{ m}^2/\text{s}$ for the low Reynolds number simulations and $1.5 \cdot 10^{-5} \text{ m}^2/\text{s}$ for the highest Reynolds number case.

The initial condition used for the simulations with $r_c/b = 0.20$ is shown in figure 6.4. For simulations with $r_c/b = 0.15$, the parameters are identical except for the spacing b of the pair. Results for the low Reynolds simulation for $r_c/b = 0.20$ are shown in figure 6.5.

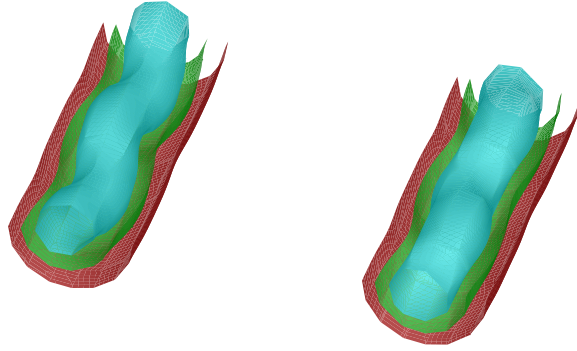


FIGURE 6.4: *Short-wavelength instability: $k = 2.261$, $r_c/b = 0.20$, initial condition, iso-surfaces $|\underline{\omega}| = 600, 900$ and 1200 s^{-1} .*

Iso-surfaces of vorticity ($|\underline{\omega}| = 600 \text{ s}^{-1}$, 900 s^{-1} and 1200 s^{-1}) are shown at three time-levels, i.e. after 500, 1000 and 1500 time-steps. The corresponding non-dimensional times are presented in the figure. Initially, the disturbances in both vortices can be seen to grow while maintaining the pattern of the initial condition of figure 6.4. Thus, disturbances in inner regions of the vortex are in opposite direction to those in outer regions of the vortex. Furthermore, the inclination angle of the inner region with respect to the horizontal plane remains around 45° . At later stages, this inclination angle can be seen to change significantly. Detailed analysis shows that a rotation of the disturbance sets in. This finding is consistent with the saturation phenomenon predicted by Sipp (2000). At later stages, the disturbances in the outer part of the vortices lose the organized pattern of the initial stages and more complicated, small-scale vortical structures are produced. To study the effect of the spacing of the vortex pair, a simulation was performed with $r_c/b = 0.15$. Figure 6.6 shows similar results as figure 6.5 for this case. Results are presented at identical non-dimensional times, to enable a direct comparison with the $r_c/b = 0.20$ case. From this sequence of plots it can be seen that the behaviour is qualitatively similar to that of the closer-spaced vortex pair. However, the amplitude of the disturbances is somewhat smaller and the rotational motion sets in at an earlier stage of the development. This dependence of the saturation process on the strength of the strain field on the vortices, which is proportional to the spacing of the vortices in the present vortex pair, is in agreement with the theoretical predictions by Sipp (2000). The development of the vorticity field for both spacings is compared in figure 6.7. This figure shows a top view of the vortex pairs, with $r_c/b = 0.20$ shown on

the left and $r_c/b = 0.15$ and the right-hand side of the figure. The Reynolds number dependence of development of the short-wavelength instability is studied by considering two different Reynolds numbers. Decreasing the kinematic viscosity from $1.5 \cdot 10^{-4} \text{ m}^2/\text{s}$ to $1.5 \cdot 10^{-5} \text{ m}^2/\text{s}$ leads to results that for the initial stages of the development are indiscernible and are not reproduced here. The iso-vorticity surfaces are shown for this higher Reynolds number in figure 6.8 for $T = 1.909$. Comparing this figure with the corresponding plot in figure 6.5 shows that the formation of small-scale structures in the outer regions of the vortices is slightly more pronounced for the higher Reynolds number simulation. However, this study shows that the Reynolds number dependence of the flow considered here is very limited.

6.2.2 Results for $k = 3.958$

This section describes the simulation that was performed for the second branch of short-wavelength instabilities, i.e. at a shorter wavelength than that considered in the preceding section. Again, the length of the computational domain in the axial direction of the vortex pair is chosen to fit two modes of the instability. Now, the wavelength λ of the instability with $k = 3.958$ is $1.416 r_c$. The initial condition for the simulation is shown in figure 6.9. The amplitude of the disturbances imposed on the vortices is identical to that used for the simulations described in the previous section. The disturbances for this wavelength are even more concentrated in the inner regions of the vortices than for the mode with $k = 2.261$. This can be attributed to the stronger radial dependence of the normal mode for this wavelength, shown in figure 6.2, than for the mode with $k = 2.261$, depicted in figure 6.1. Figure 6.10 shows iso-surfaces of vorticity for different stages of the development. As in the previous section, the results are those after 500, 1000 and 1500 time-steps. The striking feature of figure 6.10 is that the initiated instability mode at $k = 3.958$ is not attenuated. Instead, an instability occurs at a wavelength equal to the length of the computational domain in the axial direction. This wavelength is very similar to the wavelength corresponding to the instability mode with $k = 2.261$. This simulation indicates that the short-wavelength instability at the longest wavelength, i.e. the instability branch around $k = 2.261$, is the preferred short-wavelength instability for this type of flows. This is consistent with the findings of Leweke and Williamson (1998). These researchers repeatedly found short-wavelength instabilities in an unforced vortex-pair, in a series of experiments in a quiescent water tank, corresponding to the branch around $k = 2.261$. An explanation of this phenomenon can be the effect of viscosity, which at the length scales representative for these short-wavelength instabilities, can have a significant effect. Theoretical studies concerning three-dimensional elliptic instabilities, such as Waleffe (1990), show that the exponential growth rate σ of the occurring three-dimensional instability is of the form

$$\sigma = \frac{9}{16}\epsilon - \nu k^2 \quad (6.33)$$

with k the wavenumber of the instability mode, ν the kinematic viscosity and ϵ a measure of the ellipticity of the streamlines in planes perpendicular to the periodic coordinate direction. Using the fundamental relation (6.33), the effect of viscosity can be expected to favour longer-wavelength instability modes over modes corresponding to shorter-wavelength branches.

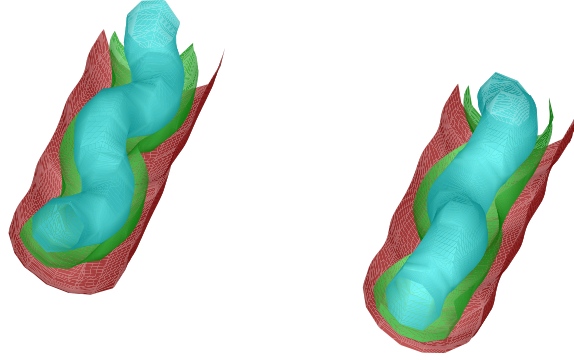
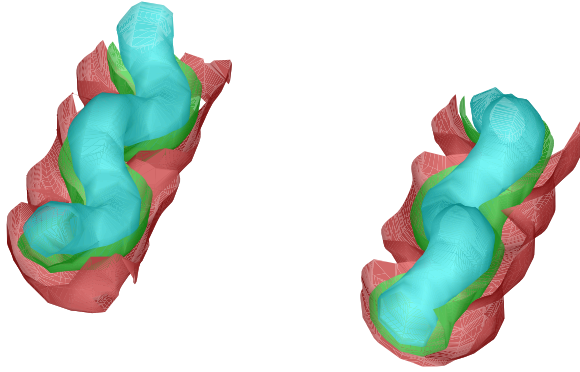
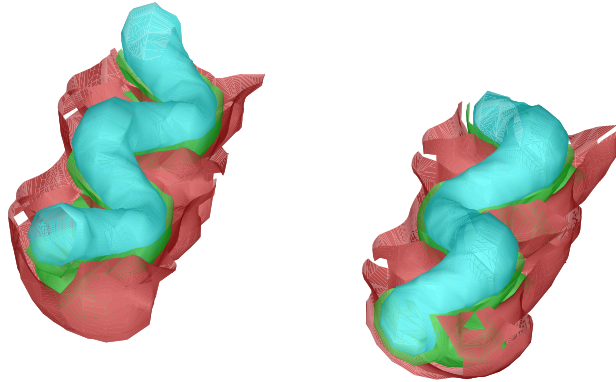

 $T = 0.637$

 $T = 1.273$

 $T = 1.909$

FIGURE 6.5: *Short-wavelength instability: $k = 2.261$, $r_c/b = 0.20$, $Re_\Gamma = 1.67 \cdot 10^4$, iso-surfaces $|\underline{\omega}| = 600, 900$ and 1200 s^{-1}*

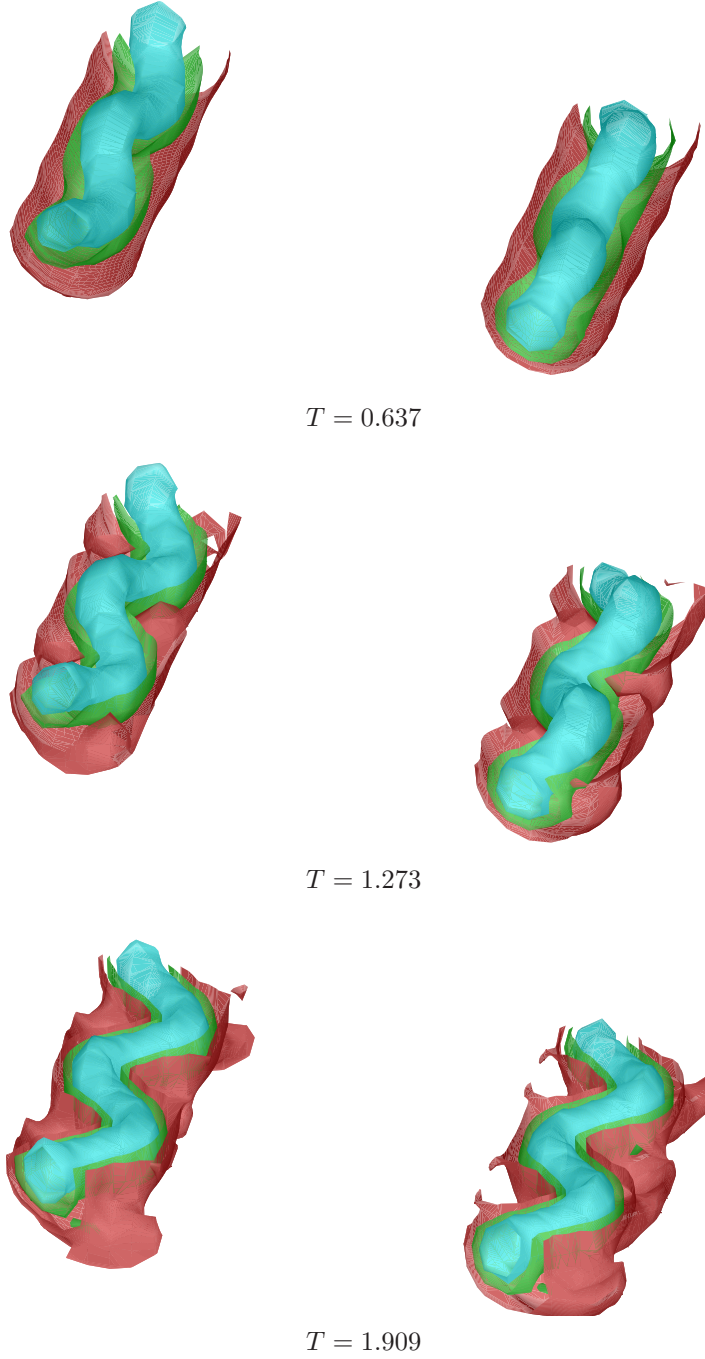


FIGURE 6.6: *Short-wavelength instability: $k = 2.261$, $r_c/b = 0.15$, $Re_\Gamma = 1.67 \cdot 10^4$, iso-surfaces $|\underline{\omega}| = 600, 900$ and 1200 s^{-1}*

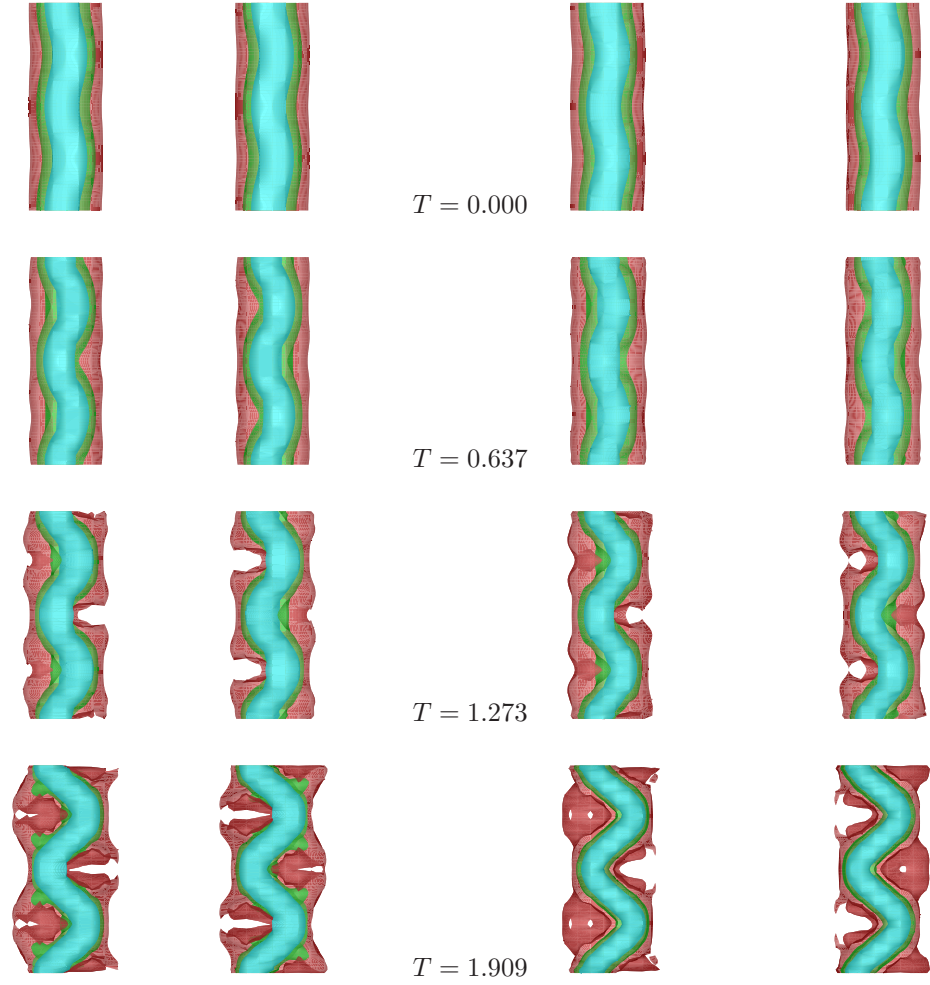
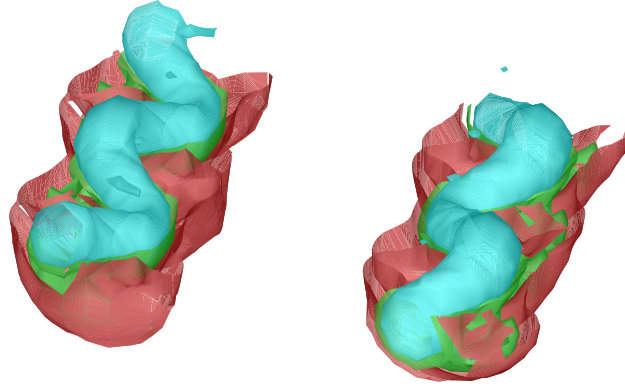


FIGURE 6.7: *Short-wavelength instability: $k = 2.261$, $Re_\Gamma = 1.67 \cdot 10^4$, $r_c/b = 0.20$ (left) and $r_c/b = 0.15$ (right), iso-surfaces $|\underline{\omega}| = 600, 900$ and 1200 s^{-1}*



$T = 1.909$

FIGURE 6.8: *Short-wavelength instability: $k = 2.261$, $r_c/b = 0.20$, $Re_\Gamma = 1.67 \cdot 10^5$, iso-surfaces $|\underline{\omega}| = 600, 900$ and 1200 s^{-1}*

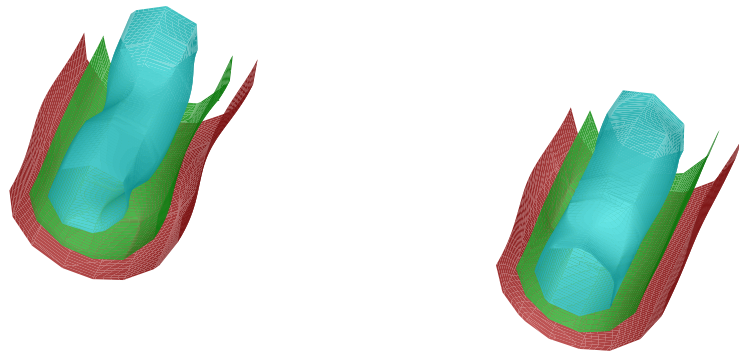
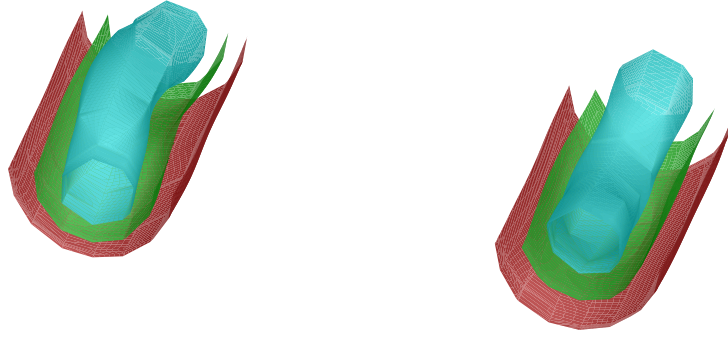
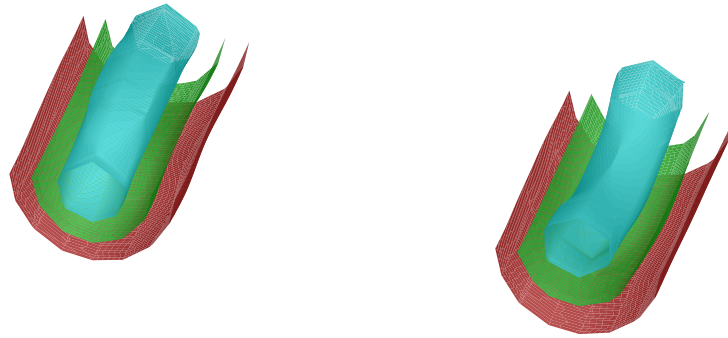
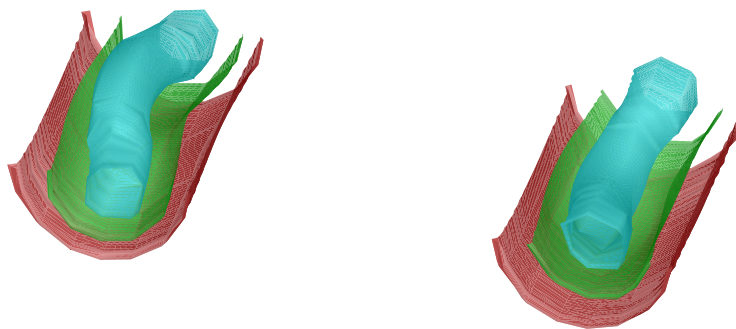


FIGURE 6.9: *Short-wavelength instability: $k = 3.958$, $r_c/b = 0.20$, iso-surfaces $|\underline{\omega}| = 600, 900$ and 1200 s^{-1} ; initial condition*



$$T = 0.637$$


$$T = 1.273$$


$$T = 1.909$$

FIGURE 6.10: *Short-wavelength instability: $k = 3.958$, $r_c/b = 0.20$, $Re_\Gamma = 1.67 \cdot 10^4$, iso-surfaces $|\underline{\omega}| = 600, 900$ and 1200 s^{-1}*

VORTEX-PAIR REBOUND FROM SOLID WALL



This chapter presents a numerical study of the rebound process of a counter-rotating vortex pair when it approaches a solid wall. The study is performed for the two-dimensional situation. Thus, effects of three-dimensional cooperative instabilities are excluded.

Numerical studies similar to the one discussed in this chapter have been performed in the past by various researchers. Here, this two-dimensional study is included as an illustration of the additional complexities that occur when a counter-rotating vortex pair interacts with a solid surface.

In case the vortices are point vortices in a potential flow, this interaction is easily understood. Figure 7.1 presents a sketch of a vortex-pair interacting with a solid wall at two instances in time. Below the solid surface, shown as the hatched area in the plots, two *mirror* vortices are present. These mirror vortices enforce the flow along the solid surface to be tangential. This is a well-known method of imposing boundary conditions in a potential flow.

In this inviscid flow, the counter-rotating vortex pair descending towards the solid wall, will experience a gradually decreasing sink rate as it approaches the solid surface. At the same time, the vortex-separation distance will increase. This separation distance is denoted with b in figure 7.1 and is a function of time. In section 7.3, the trajectory of the point vortices in potential flow is analyzed, showing that the trajectory is a hyperbola-like curve. In the immediate vicinity of the wall, the vortices will travel nearly parallel to the surface in opposite directions.

Translating this model problem to the situation that occurs near an airport runway, with the counter-rotating vortex pair representing the trailing vortex wake of an aircraft in either landing or take-off configuration, the conclusion could be drawn that these vortices quickly move away from the runway, the stronger the vortex the quicker, reducing the threat to following aircraft. However, in a viscous flow, the interaction process of a counter-rotating vortex pair with a solid surface is significantly more complicated. Upon approaching the solid surface, the descending vortices will induce a boundary layer along the surface as a result of the zero-slip velocity boundary condition pertinent to viscous flow. The pressure field of the vortices interacting with the wall involves low-pressure regions underneath the vortices. This results in the situation that the flow in the boundary layer will experience an adverse pressure gradient in certain parts of this layer. The adverse pressure gradient leads to boundary-layer separation, producing a separating shear layer. The vorticity of the free shear layer, commonly called *secondary* vorticity, interacts with the primary vortex, causing a major deviation of its trajectory from that of the inviscid situation. Of particular interest is the re-bouncing of the vortices from the solid surface. In contrast to the monotonic downward motion in the

inviscid situation, the vortex-pair will develop an upward motion as a result of the interaction of the primary vortices with the separating shear layers. Furthermore, the vortices will stay at a location close to the runway center much longer than in an inviscid flow. These effects combined create a serious threat to following aircraft. In this chapter, the rebound process is studied using Navier-Stokes simulations for various Reynolds numbers and spatial resolutions.

7.1 Numerical method for two-dimensional flow

The numerical method used for the two-dimensional flow simulations is based on the fourth-order accurate direct solver for the Helmholtz/Poisson equations in two dimensions. This solver is based on the compact-finite difference stencil presented in section 4.4. The direct solution method is described in detail in section 4.6. The Navier-Stokes method used in this chapter, employs the fractional time-stepping method of Kim and Moin (1985), presented in section 3.2. Here, the two-dimensional equivalents of equations (3.7), (3.8) and (3.9) are discretized using the same compact finite-difference methods of fourth-order and sixth-order accuracy as in the two Navier-Stokes methods for three-dimensional flows described in sections 3.5 and 3.6.

The boundary condition for the pressure on the solid surface is a Neumann boundary condition. Assuming that the solid surface corresponds to the line $y = 0$, as is shown in figure 7.1, the gradient of the pressure can be computed from the momentum conservation equation in the y -coordinate direction, given as:

$$\frac{\partial v}{\partial t} + u \frac{\partial v}{\partial x} + v \frac{\partial v}{\partial y} = -\frac{1}{\rho} \frac{\partial p}{\partial y} + \nu \Delta v \quad (7.1)$$

with $\Delta = \frac{\partial^2}{\partial x^2} + \frac{\partial^2}{\partial y^2}$. On the solid surface, the velocity component v in the y -coordinate direction is zero at any instance in time. Therefore, the terms $\frac{\partial v}{\partial t}$, $u \frac{\partial v}{\partial x}$, $v \frac{\partial v}{\partial y}$ and $\frac{\partial^2 v}{\partial x^2}$ vanish from equation (7.1) at $y = 0$. The remaining identity at $y = 0$ is:

$$\frac{\partial p}{\partial y} = \rho \nu \frac{\partial^2 v}{\partial y^2} \quad (7.2)$$

With this Neumann boundary condition imposed on the edge $y = 0$ and a Dirichlet boundary condition on the remaining edges, the pressure Poisson equation (3.8) is solved.

7.2 Summary of performed simulations

The numerical simulations carried out for the present vortex-pair rebound test case are listed in table 7.1. The first two columns of table 7.1 show the Reynolds number based on circulation, i.e. $Re_\Gamma = \Gamma/\nu$, and ratio of vortex-core radius r_c over the initial vortex separation distance b . Both circulation and vortex radius of the prescribed initial flow field are kept constant in this study. The Reynolds number is adjusted by changes in kinematic viscosity ν . The range of Reynolds numbers $1.67 \cdot 10^3$ to $6.7 \cdot 10^5$ is covered by the various simulations discussed in this chapter.

Two meshes were considered to study the spatial resolution of the computed flow fields. Both meshes span 10 initial vortex-pair separation distances in the vertical direction and 40 initial

TABLE 7.1: *Parameters of 2D simulations*

Γ/ν	r_c/b	$\Gamma[m^2/s]$	mesh	r_c/h	$\delta t[s]$	$L_x[m]$	$L_y[m]$
$1.67 \cdot 10^3$	0.25	2.5	512×128	3.2	$2.5 \cdot 10^{-5}$	$40.0 b$	$10.0 b$
$1.67 \cdot 10^4$	0.25	2.5	512×128	3.2	$2.5 \cdot 10^{-5}$	$40.0 b$	$10.0 b$
$1.67 \cdot 10^5$	0.25	2.5	512×128	3.2	$2.5 \cdot 10^{-5}$	$40.0 b$	$10.0 b$
$1.67 \cdot 10^4$	0.25	2.5	1024×256	6.4	$2.5 \cdot 10^{-5}$	$40.0 b$	$10.0 b$
$1.67 \cdot 10^5$	0.25	2.5	1024×256	6.4	$2.5 \cdot 10^{-5}$	$40.0 b$	$10.0 b$

vortex-pair separation distances in the horizontal direction. For both meshes, the mesh width in the two spatial directions is identical and constant throughout the domain. The quantity r_c/h in table 7.1 shows the ratio of the vortex core radius of the vortices in the initial flow field over the uniform mesh spacing of the Cartesian mesh. This ratio provides a measure for the spatial resolution of the primary vortices of the vortex-pair during the rebound process. Another important aspect is the spatial resolution of the boundary layer induced along the solid wall. The spatial resolution of this separating boundary layer is discussed later. In this chapter, time is non-dimensionalized using $\Gamma/2\pi b^2$.

7.3 Vortex-pair interaction with wall in potential flow

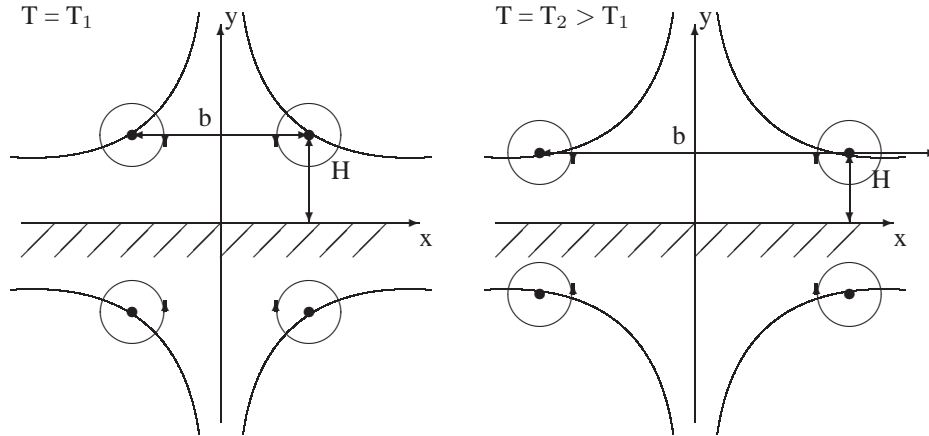


FIGURE 7.1: *Interaction of a pair of point-vortices with a solid wall in potential flow. Mirror vortices are introduced to enforce a zero-normal velocity boundary condition. The trajectory of the vortices is a hyperbola-like curve.*

Figure 7.1 shows the interaction process of a pair of point-vortices with a solid wall in potential flow. A number of quantities are defined in figure 7.1: the time-dependent separation distance b and the time-dependent height H of the vortex pair above the solid wall. The time-dependence of these quantities can be derived by studying the velocity field generated by the four vortices, i.e. the primary vortex pair and the mirror vortex pair. Assuming that these

vortices are point-vortices of strength Γ , the velocity components are given by:

$$u(x, y) = \frac{\Gamma}{2\pi} \left[\frac{(y-H)}{(x+b/2)^2 + (y-H)^2} - \frac{(y-H)}{(x-b/2)^2 + (y-H)^2} - \frac{(y+H)}{(x+b/2)^2 + (y+H)^2} + \frac{(y+H)}{(x-b/2)^2 + (y+H)^2} \right] \quad (7.3)$$

$$v(x, y) = \frac{\Gamma}{2\pi} \left[\frac{-(x+b/2)}{(x+b/2)^2 + (y-H)^2} + \frac{(x-b/2)}{(x-b/2)^2 + (y-H)^2} + \frac{(x+b/2)}{(x+b/2)^2 + (y+H)^2} - \frac{(x-b/2)}{(x-b/2)^2 + (y+H)^2} \right] \quad (7.4)$$

The velocity components at the location of the right primary vortex can be evaluated as:

$$u(\frac{b}{2}, H) = \frac{\Gamma}{2\pi} \left[\frac{b^2}{2H(b^2 + 4H^2)} \right] \quad ; \quad v(\frac{b}{2}, H) = \frac{\Gamma}{2\pi} \left[\frac{-4H^2}{b(b^2 + 4H^2)} \right] \quad (7.5)$$

From the symmetry of the vortex system, it follows that the separation distance b and the height H of the primary vortex pair above the wall obey the following relations:

$$\frac{db}{dt} = \frac{\Gamma}{2\pi} \left[\frac{b^2}{H(b^2 + 4H^2)} \right] \quad ; \quad \frac{dH}{dt} = \frac{\Gamma}{2\pi} \left[\frac{-4H^2}{b(b^2 + 4H^2)} \right] \quad (7.6)$$

From equation (7.6), it follows that the trajectory of the right primary vortex is a hyperbola-like curve

$$\frac{1}{b(t)^2} + \frac{1}{4H(t)^2} = \text{constant} \quad (7.7)$$

The trajectory analysis for the other vortices can be performed equivalently, leading to similar hyperbola-like trajectories.

7.4 Numerical results for vortex-pair rebound

Figure 7.2 shows iso-vorticity contours for numerical results obtained on the 512×128 mesh at five time-levels, progressing from $T = 3.979$ to $T = 7.958$. Results are compared for $Re_\Gamma = 1.67 \cdot 10^3$ and $Re_\Gamma = 1.67 \cdot 10^5$. For both Reynolds numbers, identical contour levels are shown. Figure 7.2 shows that viscous decay reduces the strength of the vortices at a significantly faster rate for the lowest Reynolds number than for the higher Reynolds number. This more rapid reduction in strength of the vortices for the simulation at $Re_\Gamma = 1.67 \cdot 10^3$ leads to a marked time-lag of the rebound process compared to the $Re_\Gamma = 1.67 \cdot 10^5$ simulation. Apart from the retardation of the rebound process, a notable feature of the results shown in figure 7.2 is that for lower Reynolds numbers, the secondary vorticity magnitude is relatively closer to the strength of the primary vortices than for higher Reynolds numbers. This leads to a stronger deformation of the primary vortices for lower Reynolds numbers.

Figure 7.3 shows a similar comparison of the results for two different Reynolds numbers obtained on the finer 1024×256 mesh. In this figure, results are compared for $Re_\Gamma =$

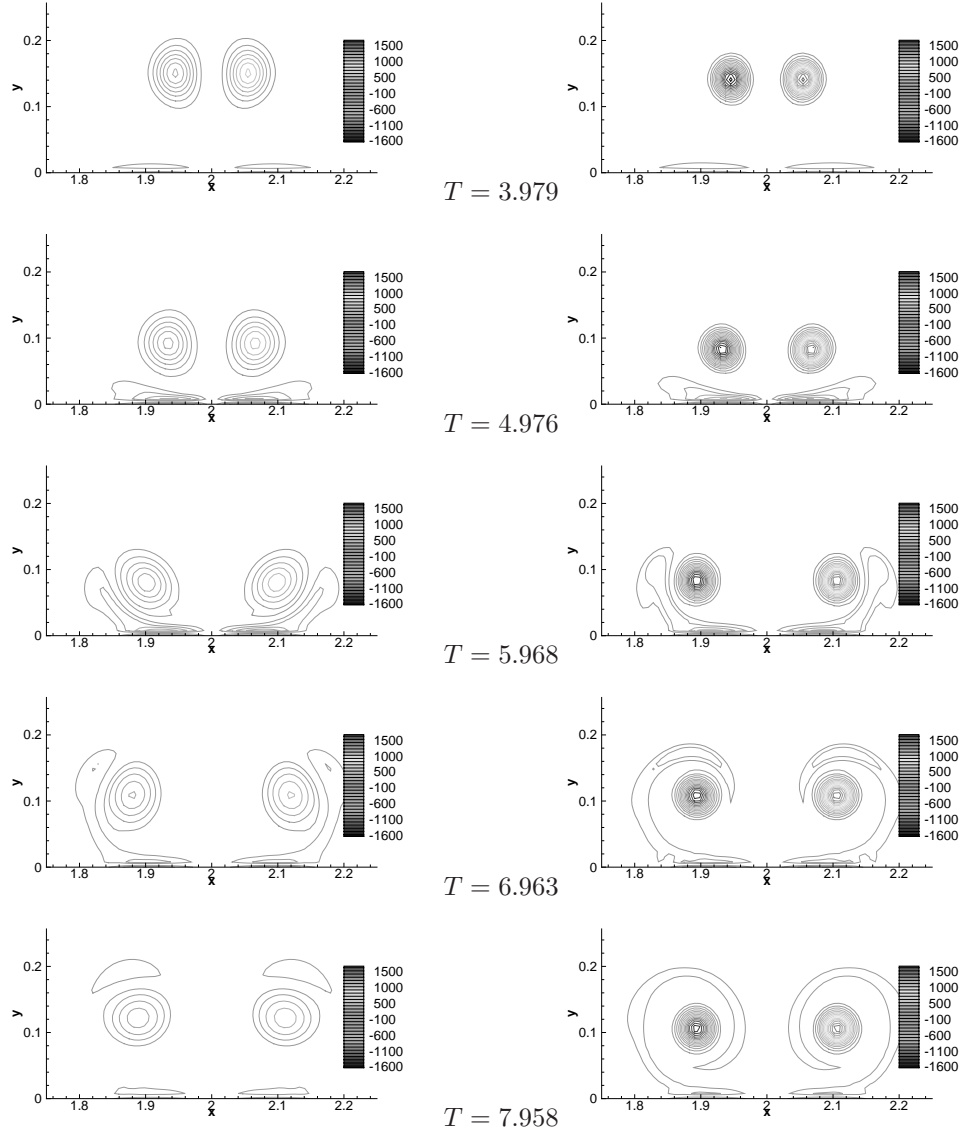


FIGURE 7.2: Iso-vorticity contours for vortex pair rebound from wall: 512×128 mesh, Reynolds number $\Gamma/\nu = 1.67 \cdot 10^3$ (left) and 1.67×10^5 (right).

$1.67 \cdot 10^4$ and $Re_\Gamma = 1.67 \cdot 10^5$. As in figure 7.2, the lower-Reynolds number situation leads to a more pronounced viscous decay of the vortices. For the Reynolds numbers shown in figure 7.3 the flow field patterns are qualitatively very similar for both Reynolds numbers. Comparing figure 7.2 with figure 7.3, it can be seen that the 512×128 mesh is not sufficiently fine to resolve the boundary layer induced along the wall. For Reynolds number $Re_\Gamma = 1.67 \cdot 10^5$, the simulations on the two different meshes are significantly different, specifically with

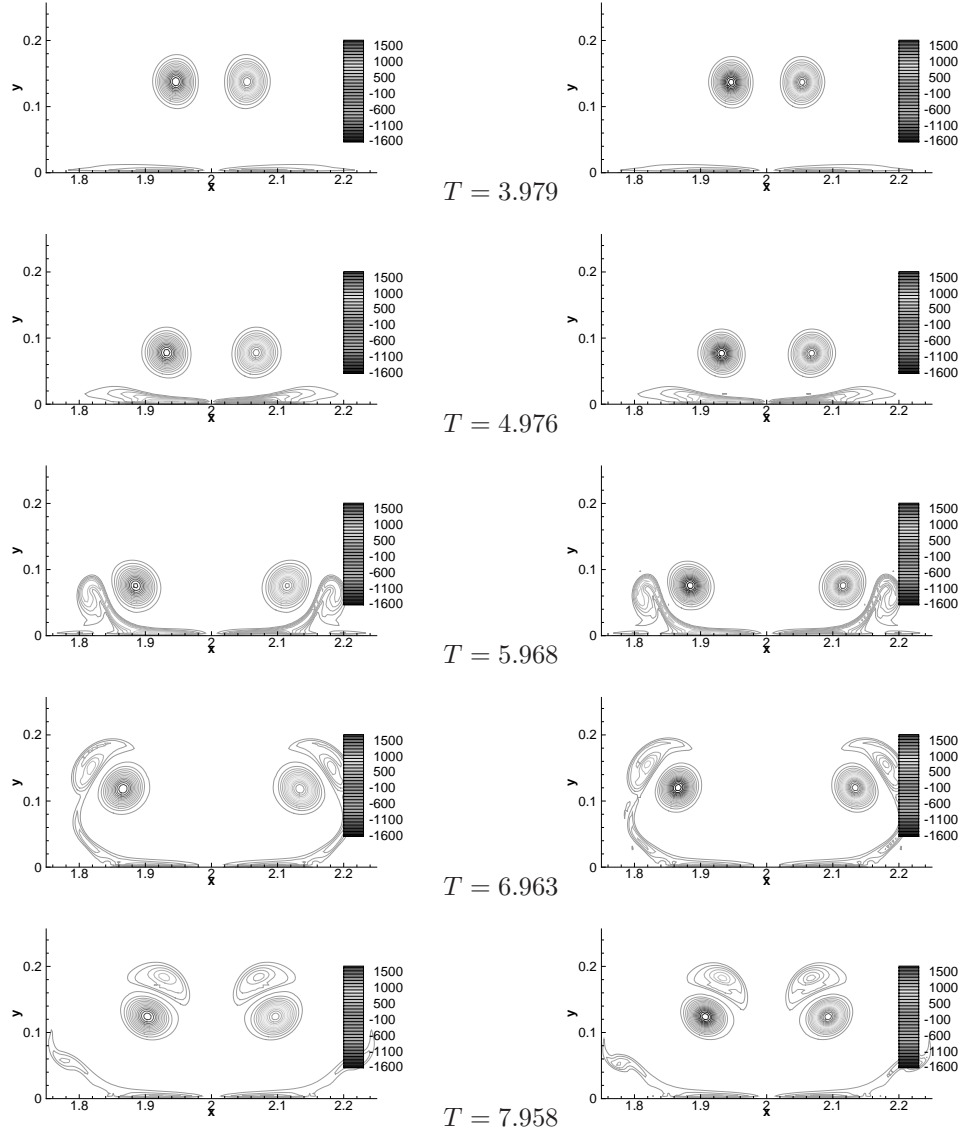


FIGURE 7.3: Iso-vorticity contours for vortex pair rebound from wall: 1024×256 mesh, Reynolds number $\Gamma/\nu = 1.67 \cdot 10^4$ (left) and $1.67 \cdot 10^5$ (right).

respect to the induced secondary vorticity and the compactness of the secondary vortex core. The simulations on the finest mesh clearly show the generation of a dipole-like structure, formed by the primary and secondary vortices.

In all the simulations discussed in this chapter, the effect of the separating boundary layer along the wall is to create a significant deviation of the trajectory of the vortices from the hyperbola-like trajectory of an equivalent point-vortex pair in potential flow. On either side

of the centerline, i.e. $x = 2.0$ in the test case considered here, the majority of the secondary vorticity is of opposite sign compared to the vorticity of the primary vortex. The interaction of the vortical structures of opposite signs causes the primary vortices to rebound from the wall and remain in the vicinity of the centerline of the domain. This situation is particularly dangerous in the presence of a cross-wind. Since the vortices remain close to the runway for a long time, a situation can easily occur in which the vortices advect to a position along the runway used by a following during take-off or landing.

Figure 7.4 compares the computed trajectory with the point-vortex trajectory for simulations obtained on the fine mesh. The figure shows that the computed trajectories for different Reynolds numbers are fairly similar. For both Reynolds numbers considered, the deviation of the computed trajectory from the point-vortex trajectory is large in the vicinity of the wall. Figure 7.5 shows the effect of spatial resolution on the computed trajectories for $Re_\Gamma = 1.67 \cdot 10^5$. This figure highlights the under-resolution of the induced boundary layer for the 512×128 mesh. Figures 7.6 and 7.7 show a close up of the velocity field in the boundary

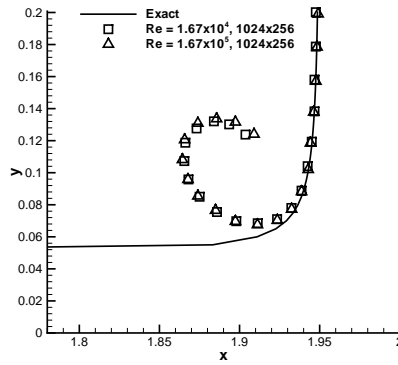


FIGURE 7.4: Comparison of computed trajectory of left primary vortex with hyperbolic trajectory for point-vortices: effect of Reynolds number

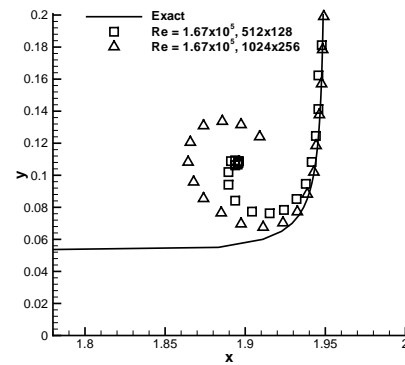


FIGURE 7.5: Comparison of computed trajectory of left primary vortex with hyperbolic trajectory for point-vortices: effect of spatial resolution

layer generated along the solid wall by the presence of the left vortex. Profiles are shown for four horizontal locations in the separation region. The figures show the situation at two different instances in the development of the separated shear layer, with a region of reverse flow developing close to the wall. The velocity profiles clearly show the spatial resolution of the induced boundary layer on the fine mesh. The part of the boundary layer developing profiles typical for adverse pressure gradients, is resolved by around 10 grid points in the direction normal to the wall.

Figures 7.8, 7.9 and 7.10 show a close-up of the streamline pattern in the vicinity of the left primary vortex. The results are from a simulation on the 1024×256 mesh for $Re_\Gamma = 1.67 \cdot 10^4$. The three time-levels correspond to those of the last three plots of figure 7.3. The figures show computed streamlines on top of iso-vorticity contours. The formation of a

shear layer, resulting from boundary layer separation, can clearly be seen from these figures. The induced vortical structures form a dipole-like structure, with significant differences in vorticity magnitudes at the centers of vorticity. Since the primary vortex remains close to the wall during this rebound-process, the production of vorticity in the separating boundary layer continues.

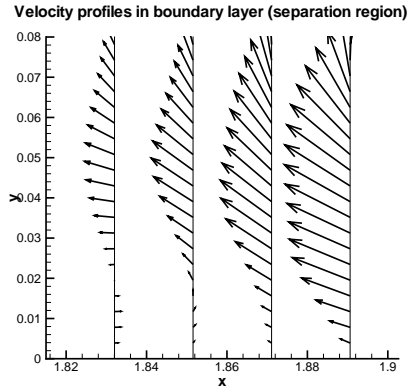


FIGURE 7.6: *Velocity profiles in boundary layer induced by left vortex: $Re_\Gamma = 1.67 \cdot 10^4$, 1024×256 mesh, $T = 5.472$*

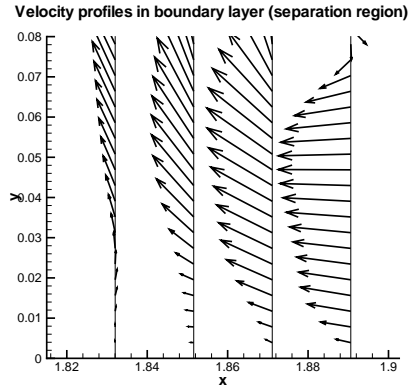


FIGURE 7.7: *Velocity profiles in boundary layer induced by left vortex: $Re_\Gamma = 1.67 \cdot 10^4$, 1024×256 mesh, $T = 5.968$*

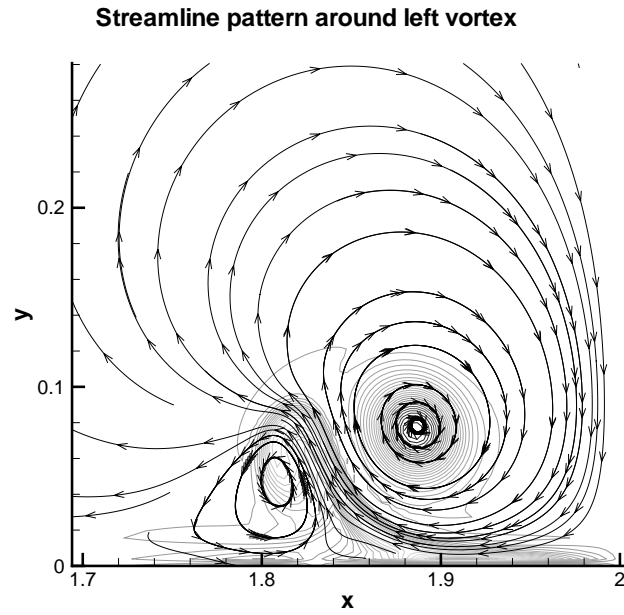


FIGURE 7.8: *Streamline pattern around left vortex: $Re_\Gamma = 1.67 \cdot 10^4$, 1024×256 mesh, $T = 5.968$*

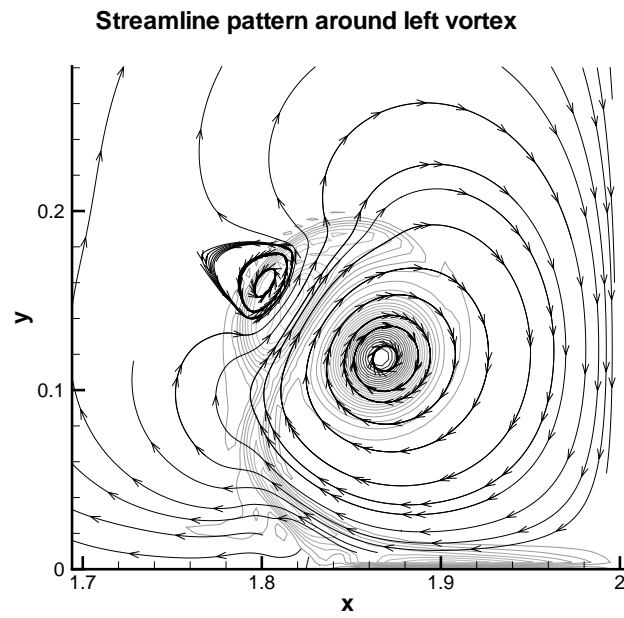


FIGURE 7.9: *Streamline pattern around left vortex: $Re_\Gamma = 1.67 \cdot 10^4$, 1024×256 mesh, $T = 6.963$*

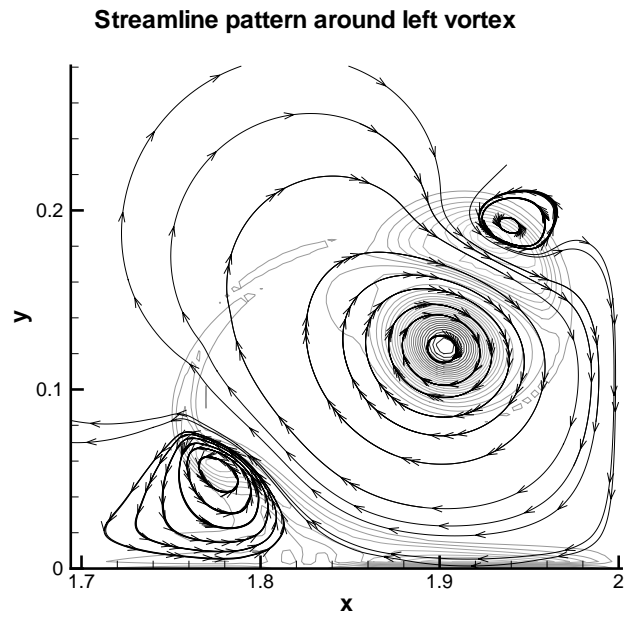


FIGURE 7.10: *Streamline pattern around left vortex:* $Re_{\Gamma} = 1.67 \cdot 10^4$, 1024×256 mesh, $T = 7.958$

CONCLUDING REMARKS



In the present study, long-wavelength and short-wavelength instabilities in counter-rotating vortex pairs have been studied employing high-order accurate computational methods for the Navier-Stokes equations governing three-dimensional incompressible flows. Even with high-order accurate spatial discretization techniques and the use of modern multi-processor computers, the vortex pairs considered in the simulations have a Reynolds number based on circulation which is at least two orders of magnitude lower than that of the trailing vortex pair in the wake of a large aircraft, which features a Reynolds number of $O(10^7)$. In the present study, vortex pairs at a range of Reynolds numbers from $O(10^3)$ to $O(10^5)$ are studied. This practical limitation has previously motivated various researchers to study vortex pairs at similar low Reynolds numbers. The present study has not been aiming for an extension of the achievable Reynolds number. Instead, the focus has been on studying details of the evolution of both long-wavelength and short-wavelength instabilities at later stages, at which complicated flow features occur.

In the course of the present study, two simulation methods have been developed for the Navier-Stokes equations governing incompressible three-dimensional flows: a parallel method based on compact finite-difference discretization methods and a "hybrid" method, which combines compact finite-difference methods and a Fourier collocation method. The computational methods are new developments of the present study. The design, development and verification of the computational methods formed a significant part of the present study.

The conclusions of the present study concerning the development of both methods are presented in section 8.1. The findings of the numerical studies of both long-wavelength and short-wavelength instabilities are presented in sections 8.2 and 8.3, respectively.

In section 8.4 the results of the present study are discussed in relation to the wake vortex hazard, since this is the problem that motivated the present research effort. In contrast to the time-dependent three-dimensional flows discussed in chapters 5 and 6, chapter 7 describes a numerical study of the time-dependent two-dimensional flow of a vortex-pair rebound from a solid wall. This chapter was included in the present study to highlight the complexities that occur when counter-rotating vortex pairs approach a solid wall. Chapter 7 showed that the interaction with the ground leads to a situation in which the vortices remain close to the center of the domain, i.e. the centerline of a runway in the case of an aircraft during take-off or landing, for much longer periods of time than predicted by simple inviscid theories. Results of chapter 7 will not be discussed any further here.

Section 8.5 concludes this chapter with recommendations for further study.

8.1 Development of Navier-Stokes methods

For the three-dimensional time-accurate flow simulations, two different methods have been developed, described in detail in chapter 3. The two methods use compact finite-difference methods for the spatial discretization. The decision to use compact finite-difference discretization techniques was motivated by the higher accuracy these methods provide compared to that provided by more traditional finite-difference methods. For the same order of the truncation error, compact finite-difference methods are designed to have a smaller constant in the leading order term of the truncation error. Furthermore, these methods can be formulated to have a higher-order truncation error for a given stencil width than traditional central-difference schemes.

The present numerical study involved simulations of flows in a simple rectangular domain. For these simple geometries, spectral methods can be formulated to lead to an even better spatial resolution for a given number of degrees of freedom (or mesh points). Spectral methods were discussed in detail by Canuto et al. (1987). However, spectral methods are restricted in the type of boundary conditions that can be imposed on the computational domain. This restriction does not occur for compact finite-difference methods. The combination of higher accuracy than traditional finite-difference methods and the greater flexibility in the prescription of boundary conditions compared to spectral methods, formed the motivation for the choice of compact finite-difference methods.

The test cases studied here are characterized by the periodicity of the flow field in the axial direction of the vortex pair. This periodicity formed the motivation to design a version of the compact finite-difference Navier-Stokes solver that uses a Fourier expansion of the flow field in the axial direction. The development of this hybrid method was pursued after the development of the parallel Navier-Stokes method, based on compact finite-difference discretization methods in all three spatial directions was completed. Therefore, this hybrid Navier-Stokes method uses many of the spatial discretization techniques of the parallel method. The discretization methods used in the two Navier-Stokes simulation tools are described in detail in chapter 4.

Both methods have been successfully applied in simulations of three-dimensional instabilities in vortex pairs. From the simulations that have been performed, a number of conclusions can be drawn:

- the compact finite-difference methods give sufficiently accurate results when the mesh width is chosen such that a vortex core diameter is covered with approximately 7 or more mesh points;
 - both methods require a very limited amount of computer memory. The implementation of both methods takes advantage of the uniformity of the used Cartesian meshes by not storing any mesh related variables. Furthermore, storage of the discretization matrix of the Helmholtz/Poisson equations is not required because these coefficients are constant for each of the mesh points;
 - computing times of several days on 4 processors were required to perform simulations with the parallel Navier-Stokes method on the finest mesh considered, i.e. 121^3 , for the initial stages of the Crow instability;
 - the parallel method showed a nearly linear scaling of the performance with respect to
-

the number of processors used in the simulations. The method was tested on up to 16 processors. However, practical limitations on available computer resources resulted in the use of 4 processors for the majority of the parallel simulations discussed in chapter 5. Typically, a speed-up of around 3.9 was achieved for simulations running on 4 processors;

- for the present test cases, the hybrid method is significantly more efficient as a result of the Fourier expansion in the periodic direction. The gain in efficiency is such that the hybrid method requires a similar computing time to perform a time-step on a single processor as the parallel Navier-Stokes method running on 4 processors;
- the domain decomposition method used in the parallel method introduces an extra restriction on the maximum time-step that can be used compared to the one possible in the hybrid method;

The last two findings make the hybrid method the preferred method for long-time simulations of the vortex-pair instabilities.

8.2 Numerical study of long-wavelength instability

The initial stage of the evolution of the Crow instability is dominated by the (nearly) exponential growth of sinusoidal perturbations of the vortices. The dynamics of the instability at this stage are well-studied and allow a validation of the developed numerical methods, by comparing the obtained results for this stage with both theoretical results from linear stability theory and with numerical results presented by various authors for similar test cases. Section 5.4 discussed the numerical results obtained for this stage of the development of the instability. The comparison with linear stability and with numerical results from other authors provides confidence in the developed numerical methods and highlights some characteristics of this stage of the Crow instability: the dependence of the growth rate on the Reynolds number and the increase of the inclination angle of the perturbations with respect to the horizontal plane. The rotational motion of the perturbations and the physical background of this effect have not received much attention by researchers in the past. In section 5.4, this feature is discussed in some detail, but the underlying mechanism of the increasing inclination angle of the perturbations can not be isolated from the numerical results discussed here. A mechanism was proposed by Garten et al. (2001) as a possible underlying mechanism for the phenomenon, in which the increase of vortex core size due to viscous diffusion leads to larger inclination angles for the growing instability mode. The simulations performed at different Reynolds numbers, however, appear to rule out the mechanism discussed by Garten et al. (2001). In the present simulations, covering a wider range of Reynolds number than that in Garten et al. (2001), show that, for the ratio $r_c/b = 0.2$, the inclination angle increases to a value of around 60° , independent of the Reynolds numbers. For higher Reynolds numbers, the increase of inclination angle can be observed to occur faster than for lower Reynolds numbers. The results of the simulations appear to show that an inviscid non-linear mechanism causes the increasing inclination angle of the perturbations. The inclination angle at any instance during the linear stage of the development of the Crow instability appears to be directly related to the amplitude of the perturbations at that instance. The later stage of the Crow instability is of greater practical relevance for the wake-vortex

hazard. This stage of the evolution is characterized by the vortex-reconnection process, leading to the formation of vortex rings. In section 5.5.2, the reconnection process is analyzed in detail using highly-accurate numerical results obtained in the present study. A comparison is made between the topology of the computed vortex lines and the pattern discussed by Kida and Takaoka (1994), discussed in section 5.5.1. The pattern of the computed vortex lines was shown to agree very well with the pattern given by Kida and Takaoka (1994). Section 5.6 presented a numerical study of this later stage of the Crow instability. The discussion focuses on the spatial resolution requirements for simulations of the Crow instability in the nonlinear stage and the effect of the Reynolds number on the evolution of the vortex-reconnection process. Studying the sensitivity of the dynamics of the Crow instability with respect to the Reynolds number is an important aspect of a computational study, since an extrapolation of the numerical results to higher Reynolds number is required to draw any conclusions on the evolution of the Crow instability in trailing vortices for flight conditions.

Section 1.3.1 describes the important role of the Crow instability in the wake-vortex decay as one of the characteristic features of this instability. The decay of kinetic energy was studied in detail in section 5.7. The analysis in that section shows that the occurrence of the Crow instability leads to a higher decay rate compared to the situation in which the vortex decays as a result of molecular viscosity alone. This decay-enhancing effect is more pronounced for higher Reynolds numbers for which the viscous decay is slower. The results shown in section 5.6 indicate that the vortex-reconnection process in the evolution of the Crow instability proceeds faster for higher Reynolds numbers. A notable result from section 5.7 was that for the two Reynolds numbers considered, the retardation of the vortex-reconnection process in the lower Reynolds number situation was such that at the latest times considered, the remaining kinetic energy was higher for the lower Reynolds number simulation than for the higher Reynolds number simulation. Considering the larger kinematic viscosity in the lower Reynolds number situation, this result shows the important role of the vortex-reconnection process in the reduction of the hazard a trailing vortex wake poses to a following aircraft.

8.3 Numerical study of short-wavelength instability

Certain aspects of the short-wavelength instability, such as the non-linear saturation of the growth of the perturbation and the complicated dynamics at later stages of the development, are not fully understood. Increasing the understanding of these aspects of the short-wavelength vortex-pair instability formed the motivation for the numerical study of the short-wavelength instability in the present work.

The formulation of a physically meaningful initial flow field formed an interesting part of the numerical study. A method was devised based on the method used in the theoretical study of Sipp (2000). The method used here assumes that the short-wavelength instability mode can be treated as the result of the interaction of an imposed strain field with two Kelvin modes, with azimuthal wavenumber $|m| = 1$. In the vortex pair studied here, the strain field results from the velocity field induced by the vortices on one another. Kelvin modes with $|m| = 1$ occur at a range of increasingly higher axial wave numbers. In this study, the spatial structure of these modes at the first three axial wave numbers is computed from a normal mode analysis of the linearized Euler equations in cylindrical coordinates, showing that the perturbation

of the vortex is progressively more concentrated to the region close to the vortex axis when the axial wave number increases.

For the first two axial wave numbers, three-dimensional simulations were performed using the initial flow field computed from the normal mode analysis.

From these simulations, the following conclusions can be drawn:

- for both axial wave numbers, a smooth transient phase occurs in which the pressure adjusts to the prescribed velocity field. This shows that the prescribed initial velocity field is a good approximation to a solution of the Navier-Stokes equations;
 - the short-wavelength perturbations show a rapid growth in planes inclined around 45° with respect to the horizontal plane in the initial stages of the evolution. Thus, the inclination does not show a rapid increase in the initial stages as in the case of the Crow instability;
 - the results of the numerical simulations at the lowest wave number of the short-wavelength modes show a rapid initial growth of the perturbations of the vortices. As the perturbation amplitude reaches a magnitude of about 20 to 25 per cent of the initial vortex spacing, the growth rate shows a sudden decrease in combination with the onset of a rotational motion of the perturbations. This process is a manifestation of the non-linear saturation predicted by Sipp (2000);
 - The effect of vortex-pair separation distance was studied for the lowest wave number. Comparison of the results for the two vortex spacings considered, shows that a larger vortex-pair separation leads to a smaller saturation amplitude and an earlier onset of the rotational motion of the perturbation of the vortices. This finding confirms the predictions of the theoretical work by Sipp (2000);
 - the effect of the Reynolds number on the evolution of the short-wavelength instability was similarly studied for the lowest wave number of the two that were considered. For the time-scales and range of Reynolds numbers studied here, the obtained results show that the Reynolds number does not appear to play a significant role;
 - at the later stages of the evolution of the short-wavelength instability, the development of very complicated small-scale flow features can be observed. The development of these small-scale structures can be attributed to (linear) instabilities of the flow field at these later stages. The development of these small-scale structures indicates the transition to a turbulent flow field. The possibility of these additional instabilities was pointed out by Sipp (2000) as a complicating factor when translating the results of his theoretical study to the developing short-wavelength instability in a vortex pair. The numerical results obtained here, confirm this prediction;
 - the simulation of the short-wavelength instability at the higher axial wave number considered, shows that the vortex pair develops a longer wavelength instability than the initialized instability mode. The growing mode can be considered as a manifestation of the lowest wave number branch of the short-wavelength instability. The preference for the longest-wavelength branch of the short-wavelength instability can be attributed to the stronger viscous damping of the growth-rate of higher wave number modes.
-

The numerical study of the short-wavelength instability has been mainly qualitative in nature and has confirmed the theoretical predictions of Sipp (2000). The wavelength of the lowest wave number branch of the short-wavelength instability is in good agreement with that of the anti-symmetric short-wavelength mode observed in the visualization of a counter-rotating vortex pair in a water-tank experiment by Leweke and Williamson (1998). The selection of this wavelength can be seen from the simulations obtained in the present study.

The simulations of the short-wavelength instability have given insight in some of the characteristics of the evolution of this instability at later stages. Section 1.4 described some of the proposed methods to enhance trailing-vortex decay, based on excitation of short-wavelength instability modes in the trailing vortices. Improving the understanding of the characteristics of the dynamics of the short-wavelength instability is therefore of great relevance for the development and application of these decay enhancing methods.

8.4 Discussion

The present computational study of both the long-wavelength and short-wavelength instability considered a counter-rotating vortex pair as a model for the trailing vortex wake of an aircraft in cruise flight. The dynamics of three-dimensional instabilities in such a vortex pair are driven by the velocity field that the vortices induce on one another. This property leads to the introduction of a non-dimensionalization of time with a characteristic time-scale of $2\pi b^2/\Gamma$, with Γ the strength of the vortices of the vortex pair and b the spacing between the vortices.

In section 1.5, the example of a Boeing 747-400 in cruise flight was discussed. Characteristic values for the circulation Γ of the vortex pair, the spacing of the vortex pair and Reynolds number based on circulation were derived. The estimated Reynolds number for the cruise flight was $O(10^7)$, i.e. two orders of magnitude higher than the highest Reynolds number considered in the numerical simulations performed in the present study. Therefore, the vortex-reconnection process in the nonlinear stage of the Crow instability can be expected to proceed even faster than in the simulation at the highest Reynolds number considered, i.e. $O(10^5)$. Furthermore, in the evolution of the trailing vortex pair, the Crow instability can be expected to have a significant effect on the decay of the kinetic energy of the flow, since it was shown in the present study, that the decay enhancing effect of the Crow instability is more pronounced for higher Reynolds numbers.

8.5 Recommendations for further study

Chapter 1 reviewed some of the previous research work on vortex pair instabilities related to the dynamics of aircraft trailing vortex wakes. The present study aimed at increasing the understanding of some of the aspects that are not fully understood. However, a number of aspects of the dynamics of counter-rotating vortex pairs remain to be investigated. The most prominent of these aspects are:

- the interaction of the long-wavelength and short-wavelength instability when these two types of instability occur simultaneously. Section 1.3.3 described the situation of a counter-rotating vortex pair developing both the long-wavelength and short-wavelength

instability at the same time. A significant interaction between the two types was described with a long-term evolution which is markedly different from the situation with just the long-wavelength instability. The interaction of the different types of instability was predicted to lead to a higher kinetic energy decay rate as a result of the development of structures at much smaller length scales. For a future computational study, a detailed study of the interaction between these two types of instability, including an analysis of the kinetic energy spectrum, is therefore worthwhile;

- the effect of the prescribed type of vortex. The numerical simulations discussed in the present study use Lamb-Oseen vortices as initial vorticity fields. This type of vortex has been used extensively in the past by researchers to model trailing vortices in the far wake of a lift generating wing. The Lamb-Oseen vortex has a smooth transition region between the vortex core region and the outer part of the vortex, with the " $1/r$ " dependence of the velocity on the radial coordinate r . Accurate measurements of the velocity profile in trailing vortices are extremely difficult for the full-scale flight conditions, and as a result, not much is known about the details of the velocity distribution, or even the radius of the core region, of trailing vortices. Recently, wind-tunnel measurements have been performed, at both ONERA and DLR, focusing on the wake of an aircraft model. Due to the requirement to measure at a number of wing spans behind the aircraft model to get a reasonably developed vortex wake, the model needs to be at a fairly small scale (typically around $1/70$). As a result, the measurements give a rather coarse resolution of the velocity field in the wake of the aircraft model and the Reynolds number is orders of magnitude different from the flight conditions. Measurements of this type seem to indicate that the velocity profile has a regime with a " $1/\sqrt{r}$ " dependence of the velocity in between the vortex core region and the outer region. More work is certainly necessary to get a better understanding of the velocity profile in aircraft trailing vortices. An interesting aspect of a future computational study would be a sensitivity study of the dynamics of the three-dimensional cooperative instabilities with respect to the prescribed velocity profiles of the vortices;
 - multiple-vortex systems. The instability of a double trailing-vortex pair was analyzed by Crouch (1997), using a linearized eigenvalue formulation. Such a multiple trailing-vortex pair can be used as a model for the far-wake of an aircraft in take-off and landing configurations. The additional trailing vortices are formed at the edges of deflected trailing-edge flaps. The interaction of these additional vortices with the wing-tip vortices can lead to a faster growth of cooperative instabilities on the trailing vortices. The dynamics of the short-wavelength instability were shown in chapter 6 to have a strong dependence of the imposed strain field on a vortex. In the trailing vortex wake of an aircraft in either take-off or landing configuration, the relatively close proximity of the trailing vortices could lead to a more pronounced effect of short-wavelength instabilities compared to the situation in the wake of an aircraft in cruise flight.
-

REFERENCES

- BATCHELOR, G. K. (1964). Axial flow in trailing line vortices. *J. Fluid Mech.*, 20:645–658.
- BAYLY, B. J. (1986). Three-dimensional instability of elliptic flow. *Phys. Rev. Lett.*, 57(17):2160–2163.
- BRIGHAM, E. O. (1974). *The Fast Fourier Transform*. Prentice-Hall, Englewood Cliffs, N.J.
- CANUTO, C., HUSSAINI, M., QUARTERONI, A., AND ZANG, T. (1987). *Spectral methods in fluid dynamics*. Springer Verlag, New York.
- CHORIN, A. J. (1967). A numerical method for solving incompressible viscous flow problems. *J. Comp. Phys.*, 2:12–26.
- CORJON, A., DARRACQ, D., CHAMPAGNEUX, S., AND LAPORTE, F. (1999). On wake vortex far field evaluation prediction. In Elsenaar (1999).
- COTTET, G. H., SBALZARINI, I., MÜLLER, S., AND KOUMOUTSAKOS, P. (2000). Optimization of trailing vortex destruction by evolution strategies. Technical Report Summer Program 2000, Center for Turbulence Research.
- CROUCH, J. D. (1997). Instability and transient growth for two trailing-vortex pairs. *J. Fluid Mech.*, 350:311–330.
- CROW, S. C. (1970). Stability theory for a pair of trailing vortices. *AIAA Journal*, 8(12):2172–2179.
- DARACQ, D., MOET, H., AND CORJON, A. (1999). The effects of atmospheric conditions on aircraft trailing vortices. In Elsenaar (1999).
- DE BRUIN, A. C., HEGEN, G. H., ROHNE, P. B., AND SPALART, P. R. (1996). Flow field survey in trailing vortex system behind a civil aircraft model at high lift. Technical Report TP 96284, National Aerospace Laboratory.
- DONOHUE, S. R. (1996). *Vortex flow and vortex breakdown above a delta wing in high subsonic flow: an experimental investigation*. PhD thesis, Delft University of Technology, Delft, The Netherlands.
- Elsenaar, A., editor (1999). *2nd Workshop of Wakenet on prediction of far field vortex location and decay*, BriteEuram 4th Framework Programme, Oberpfaffenhofen, Germany.
- FREUND, R. W. AND NACHTIGAL, N. (1991). QMR: A quasi-minimal residual method for non-hermitean linear systems. *Numer. Math.*, 60:315–339.
- GARTEN, J. F., WERNE, J., FRITTS, D. C., AND ARENDT, S. (2001). Direct numerical simulations of the Crow instability and subsequent vortex reconnection in a stratified fluid. *J. Fluid Mech.*, 426:1–45.
-

- GEIST, A., BEGUELIN, A., DONGARRA, J., JIANG, W., MANCHEK, R., AND SUNDERAM, V. (1993). PVM 3 user's guide and reference manual. Technical report, ONRL/TM - 12187.
- GOLUB, G. H. AND VAN LOAN, C. F. (1996). *Matrix computations*. Johns Hopkins studies in the mathematical sciences. The Johns Hopkins University Press, Baltimore, MD, third edition.
- GRUNE, D., BAL, H. E., JACOBS, C. J. H., AND LANGENDOEN, K. G. (2000). *Modern compiler design*. Worldwide series in computer science. John Wiley and sons, Chichester, U.K.
- HARLOW, F. H. AND WELCH, J. E. (1965). Numerical calculation of time-dependent viscous incompressible flow of fluid with a free surface. *Phys. Fluids*, 8(12):2181.
- HESTENES, M. R. AND STIEFEL, E. (1952). Methods of conjugate gradients for solving linear systems. *J. Res. Nat. Bur. Stand.*, 49:409–436.
- HIRSCH, H. (1988). *Numerical computation of internal and external flows*. Wiley series in numerical methods in engineering. John Wiley and sons.
- HOEIJMAKERS, H. W. M. (1989). Computational aerodynamics of ordered vortex flows. Technical Report NLR TR-88088 U, National Aerospace Laboratory.
- HOLZÄPFEL, F. (1999). Weather effects on wake vortices - simulations versus simple models & simulated LIDAR observations. In Elsenaar (1999).
- KIDA, S. AND TAKAOKA, M. (1994). Vortex reconnection. *Annu. Rev. Fluid Mech.*, 26:169–189.
- KIM, J. AND MOIN, P. (1985). Application of a fractional-step method to incompressible Navier-Stokes equations. *J. Comp. Phys.*, 59:308–323.
- LAPORTE, F. AND CORJON, A. (2000). Direct numerical simulations of the elliptic instability of a vortex pair. *Phys. Fluids*, 12(5):1016–1031.
- LELE, S. K. (1992). Compact finite difference schemes with spectral-like resolution. *J. Comp. Phys.*, 103:16–42.
- LEWEKE, T. AND WILLIAMSON, C. H. K. (1998). Cooperative elliptic instability of a vortex pair. *J. Fluid Mech.*, 360:85–119.
- LOCKARD, D. P. AND MORRIS, P. J. (1998). Wing-tip vortex calculations using a high-accuracy scheme. *J. Aircraft*, 35(5):728–738.
- MESSAGE PASSING FORUM (1994). MPI: A message passing interface standard. *Intl. J. Supercomputing appl.*, 8(3/4).
- MOORE, D. W. (1972). Finite amplitude waves on aircraft trailing vortices. *Aero Q.*, 19:307.
- MOORE, D. W. AND SAFFMAN, P. G. (1973). Axial flow in laminar trailing vortices. *Proc. R. Soc. Lond. A.*, 333:491–508.
- MOORE, D. W. AND SAFFMAN, P. G. (1975). The instability of a straight vortex filament in a strain field. *Proc. R. Soc. Lond. A.*, 346:413–425.
- OPENMP (1998). OpenMP C and C++ application program interface. Technical Report 004-2229-001, OpenMP Architecture Review Board, <http://www.openmp.org>.
- ORLANDI, P., CARNEVALE, G. F., LELE, S. K., AND SHARIFF, K. (1998). DNS study of stability of trailing vortices. Technical Report Summer Program 1998, Center for Turbulence Research.
- PECKHAM, D. H. AND ATKINSON, S. A. (1957). Preliminary results of low speed wind tunnel tests on a gothic wing of aspect ratio 1.0. Technical Report CP 508, ARC.
-

- PIERREHUMBERT, R. T. (1986). Universal short-wave instability of two-dimensional eddies in an inviscid fluid. *Phys. Rev. Lett.*, 57(17):2157–2159.
- PRESS, W. H., TEUKOLSKY, S. A., VETTERLING, W. T., AND FLANNERY, B. P. (1994). *Numerical Recipes in C: The Art of Scientific Computing*. Cambridge University Press, Cambridge, U.K.
- PROCTOR, F. H. (1996). Numerical simulations of wake vortices measured during the Idaho Falls and Memphis field programs. *AIAA Paper 96-2496*.
- REID, J. K. (1971). On the method of conjugate gradients for the solution of large sparse systems of linear equations. In Reid, J. K., editor, *Large sparse sets of linear equations*, pages 231–254, New York. Academic Press.
- RENNICH, S. C. AND LELE, S. K. (1998). A method for accelerating the destruction of aircraft wake vortices. *AIAA Paper 98-0667*.
- RISSE, F., CORJON, A., AND STOESSEL, A. (1997). Direct numerical simulations of wake vortices in intense homogeneous turbulence. *AIAA Journal*, 35(6):1030–1040.
- ROBINS, R. E. AND DELISI, D. P. (1997). Numerical simulations of three-dimensional trailing vortex evolution. *AIAA Journal*, 35(9):1552–1555.
- ROBINS, R. E. AND DELISI, D. P. (1998). Numerical simulations of three-dimensional trailing vortex evolution in stratified fluid. *AIAA Journal*, 36(6):981–985.
- ROBINSON, A. C. AND SAFFMAN, P. G. (1984). Three-dimensional stability of an elliptic vortex in a straining field. *J. Fluid Mech.*, 142:451–466.
- ROSSOW, V. J. AND JAMES, K. D. (2000). Overview of wake-vortex hazards during cruise. *J. Aircraft*, 37(6):960–975.
- SAAD, Y. AND SCHULZ, M. (1986). GMRES: A generalized minimal residual algorithm for solving non-symmetric linear systems. *SIAM J. Scientific and Statistical Computing*, 7:856–869.
- SAFFMAN, P. G. (1992). *Vortex dynamics*. Cambridge Monographs on Mechanics and applied Mathematics. Cambridge University Press, Cambridge, U.K.
- SARPKAYA, T. (1998). Decay of wake vortices of large aircraft. *AIAA Paper 98-0592*.
- SARPKAYA, T. (2000). New model for vortex decay in the atmosphere. *J. Aircraft*, 37(1):53–61.
- SIPP, D. (2000). Weakly nonlinear saturation of short-wave instabilities in a strained Lamb-Oseen vortex. *Phys. Fluids*, 12(7):1715–1729.
- SIPP, D., COPPENS, F., AND JACQUIN, L. (1998). Theoretical and numerical analysis of wake vortices. In Giovanini, A. et al., editors, *Third International Workshop on Vortex Flows and Related Numerical Methods*, volume 7 of *ESAIM Proceedings*, pages 397–407, Toulouse, France.
- SPALART, P. R. (1998). Airplane trailing vortices. *Annu. Rev. Fluid Mech.*, 30:107–138.
- STROUSTRUP, B. (1986). *The C++ programming language*. Addison-Wesley, Reading, Mass., U.S.A.
- SUN, X.-H. AND ZHUANG, Y. (1997). A high-order direct solver for helmholtz equations with neumann boundary conditions. Technical Report 97-11, ICASE.
- THOMAS, P. J. AND AUERBACH, D. (1994). The observation of the simultaneous development of a long- and a short-wave instability mode on a vortex pair. *J. Fluid Mech.*, 265:289–302.
-

- TSAI, C. Y. AND WIDNALL, S. E. (1976). The stability of short waves on a straight vortex in a weak externally imposed strain field. *J. Fluid Mech.*, 73:721–733.
- VAN NOORDENBURG, M. B. H. (1999). *On leading-edge vortex flow and vortex breakdown*. PhD thesis, University of Twente, Enschede, The Netherlands.
- VERHAAGEN, N. G. AND VAN RANSBEECK, P. (1990). Experimental and numerical investigation of the flow in the core of a leading-edge vortex. *AIAA Paper 90-0384*.
- VICROY, D. D., VIJGEN, P. M., REIMER, H. M., GALLEGOS, J. L., AND SPALART, P. R. (1998). Recent NASA wake-vortex flight tests, flow-physics database and wake-development analysis. *AIAA Paper 98-5592*.
- VISBAL, M. R. (1996). Computed unsteady structure of spiral vortex breakdown on delta wings. *AIAA Paper 96-2074*.
- VISBAL, M. R. AND GAITONDE, D. V. (1998). High-order accurate methods for unsteady vortical flows on curvilinear meshes. *AIAA Paper 98-0131*.
- WALEFFE, F. (1990). On the three-dimensional instability of strained vortices. *Phys. Fluids A*, 2(1):76–80.
- WHITE, F. M. (1974). *Viscous fluid flow*. McGraw-Hill.
- WIDNALL, S. E., BLISS, D., AND ZALAY, A. (1970). Theoretical and experimental study of the stability of a vortex pair. In J. H. Olsen, A. G. and Rogers, M., editors, *Aircraft wake turbulence and its detection*, pages 305–329, Seattle, WA.
- WIDNALL, S. E., BLISS, D. B., AND TSAI, C. Y. (1974). The instability of short waves on a vortex ring. *J. Fluid Mech.*, 66:35–47.
-

SUMMARY

At large distance behind an aircraft in cruise, i.e. one or more kilometers, the trailing wake can be treated as a counter-rotating vortex pair. The temporal evolution of such a vortex pair, including the development of three-dimensional instabilities, is the subject of this thesis. The vortex pair in the wake far behind an aircraft is formed by the roll-up of the vortex sheet that emanates from the trailing-edge of a lift-generating wing. The formation of this vortex pair is a direct consequence of the generation of lift by a wing with finite-span. The resulting vortex pair forms a hazard to following aircraft and its strength depends linearly on the weight of the aircraft generating the wake. Depending on the way an aircraft encounters the wake vortex pair generated by another aircraft, a number of situations can occur: the aircraft experiences a series of strong vertical accelerations, when the vortex wake is traversed from the side; the aircraft experiences a strong loss of lift when flying through the down-wash velocity field between the two vortices; or, the following aircraft experiences a rolling moment, when one of the trailing vortices is entered. The hazard is particularly severe in the landing phase of the flight and when the aircraft is significantly lighter than the wake-generating aircraft. In air traffic control, the wake vortex problem is dealt with by prescribing minimum separation distances between leading and following aircraft, that depend on the relative weights of the aircraft. A more complete understanding of the dynamics of the trailing wake vortices could lead to a system of less conservative separation distances, and as a result, to a larger capacity of airports and air corridors.

In this thesis, three-dimensional instabilities that can occur in counter-rotating vortex pairs, are studied, as is the role of these instabilities in the decay process of the vortex pair. The occurrence of these instabilities in trailing vortices can often be seen as growing sinusoidal perturbations on the condensation trails behind an aircraft in cruise. These condensation trails are formed by condensing water vapor entrained from the exhaust gases into the trailing vortices.

In the present study, time-accurate numerical simulations of a vortex pair in an incompressible medium are discussed, as a model of a trailing vortex wake. Effects of ambient turbulence and stratification are neglected. A major part of the present study has been the development of suitable numerical methods for the vortex-pair simulations based on the three-dimensional Navier-Stokes equations. The developed methods are based on higher-order accurate spatial discretization techniques, some of which are new developments of this study and are described in detail in this thesis.

Two types of three-dimensional instabilities can be distinguished: long-wavelength and short-wavelength instabilities. The long-wavelength instability is better known as *Crow* instability,

while the short-wavelength instability is frequently called *elliptic* or *Widnall* instability. In this thesis, linear stability theory is used to determine characteristic quantities of both types of instability. This data is subsequently used in the prescription of the initial flow field from which time-accurate numerical simulations start. The Crow instability has a characteristic wavelength of approximately eight times the spacing of the vortex pair in the unperturbed situation. The short-wavelength instability has a characteristic wavelength which is of the order of the diameter of the vortex cores. For both types of instability, results from detailed time-accurate numerical simulations are discussed.

In the numerical analysis of the Crow instability, the emphasis is on the vortex reconnection phase and the subsequent vortex-ring formation. A detailed analysis of the simulated flow field in this phase of the development clearly shows the underlying physical mechanism. Furthermore, the spectra of kinetic energy are studied, highlighting the important role of the Crow instability in the decay of the vortex pair. The analysis shows how much kinetic energy is dissipated at each stage of the evolution of the instability and the dependence of this decay on Reynolds number.

A number of characteristics of the temporal development of the short-wavelength instability are not fully understood, e.g. the non-linear saturation of the amplitude growth and the onset of small-scale instabilities in the outer part of the vortex cores. The present numerical simulations show these features in detail. The obtained results are consistent with results from theoretical analyses of these non-linear phenomena. In the numerical study of the short-wavelength instability, the dependence on a number of parameters is studied: Reynolds number, spacing of the vortex pair and the axial wavelength of the initial perturbation. The saturation amplitude is shown to have a direct dependence on the spacing of the vortex pair: a large spacing between the vortices results in a small saturation amplitude. For a typical aircraft wake vortex pair, the spacing of the vortices is such that the saturation amplitude can be expected to be very small. Therefore, the role of this type of instability in the decay of the vortex pair is thought to be less prominent than that of the Crow instability. However, for the future development of devices that enhance the wake vortex decay, a thorough understanding of the short-wavelength instability is relevant, since many of these devices are based on the (active) excitation of the short-wavelength instability.

SAMENVATTING

Op grote afstand achter een vliegtuig in kruisvlucht, enkele kilometers of meer, kan het zog beschouwd worden als twee wervels met tegengestelde draairichting. De ontwikkeling van een dergelijk wervelpaar in tijd en, met name, de ontwikkeling van drie-dimensionale instabiliteiten in dit wervelpaar, vormen het onderwerp van dit proefschrift.

Het wervelpaar in het zog ver achter een vliegtuig wordt gevormd door het oprollen van een wervelvlak dat aan de achterrand van een draagkracht genererende vleugel ontstaat. De vorming van een dergelijk wervelpaar is inherent verbonden aan het opwekken van draagkracht door een vleugel met een eindige spanwijdte. Dit wervelpaar vormt een serieus gevaar voor volgende vliegtuigen. Het gevaar neemt toe met de sterkte van de wervelpaar, welke rechtevenredig is met het gewicht van het vliegtuig dat het zog genereert. Afhankelijk van de manier waarop een vliegtuig een zogwervelpaar tegenkomt dat door een ander vliegtuig is opgewekt, kunnen verschillende situaties ontstaan: het vliegtuig ondervindt een reeks sterke verticale versnellingen wanneer het zog in dwarsrichting doervlogen wordt; het vliegtuig verliest draagkracht wanneer het te dicht recht achter een vliegtuig vliegt en daardoor in het gebied met sterke neerstroming tussen de twee wervels terecht komt; of, het vliegtuig ondergaat een sterke, rollende beweging wanneer er in een van de wervels wordt gevlogen. Deze gevaren zijn met name ernstig tijdens de landingsfase van de vlucht en wanneer het vliegtuig veel lichter is dan het vliegtuig dat het zog veroorzaakt. In de praktijk wordt met dit zogprobleem rekening gehouden door het voorschrijven van een minimale afstand tussen twee opeenvolgende vliegtuigen, waarbij deze afstand afhangt van het gewicht van beide vliegtuigen. Een verbeterd inzicht in de dynamica van de wervelparen in het zog van vliegtuigen kan ertoe leiden dat in de toekomst deze afstanden minder behoudend worden voorgeschreven en daarmee de capaciteit van vliegvelden en vliegroutes wordt vergroot.

In dit proefschrift worden drie-dimensionale instabiliteiten, die in een dergelijk wervelpaar kunnen optreden, bestudeerd en wordt er bekeken hoe deze instabiliteiten het wervelpaar opbreken. In de praktijk is het optreden van deze instabiliteiten in een wervelpaar zichtbaar wanneer condenserende waterdamp uit de uitlaatgassen van de motoren in de wervels terecht komt. De wervels worden zichtbaar als twee condensstrepen en vertonen groeiende sinusvormige verstoringen.

Dit proefschrift beschrijft tijdsnauwkeurige numerieke simulaties van een wervelpaar in een onsamendrukbaar medium, als model voor het wervelzog ver achter een vliegtuig. Effecten van turbulentie en dichtheidsgradiënten in de omringende atmosfeer worden niet meegenomen in de simulaties.

De ontwikkeling van geschikte numerieke methodes voor de simulatie van de wervelstro-

mingen vormde een belangrijk deel van het in dit proefschrift beschreven onderzoek. De numerieke methodes zijn gebaseerd op een aantal nieuw ontwikkelde technieken voor een nauwkeurige ruimtelijke discretizatie van de Navier-Stokes vergelijkingen. Deze technieken worden dan ook in dit proefschrift in detail beschreven.

Twee soorten driedimensionale instabiliteiten kunnen worden onderscheiden:

de lange-golflengte instabiliteit en de korte-golflengte instabiliteit. De lange-golflengte instabiliteit is beter bekend als *Crow* instabiliteit, terwijl de korte-golflengte instabiliteit veelal als *elliptische* ofwel *Widnall* instabiliteit wordt aangeduid. In dit proefschrift worden van beide type instabiliteit en met behulp van lineaire stabiliteitstheorie karakteristieke grootheden bepaald. Deze worden vervolgens gebruikt voor de berekening van het initiële stromingsveld nodig voor de start van de tijdsnauwkeurige numerieke simulaties. De karakteristieke golflengte van de *Crow* instabiliteit bedraagt ongeveer acht keer de afstand tussen de wervels in het onverstoorde wervelpaar. Voor de korte-golflengte instabiliteit is de karakteristieke golflengte van dezelfde orde van grootte als de diameter van de wervelkernen. Zowel de lange-golflengte als de korte-golflengte instabiliteit worden in dit proefschrift bestudeerd met behulp van gedetailleerde numerieke simulaties.

Bij de *Crow* instabiliteit gaat de aandacht vooral uit naar de vorming van de verbinding tussen de wervels en de daaropvolgende vorming van wervelringen. Een gedetailleerde analyse van het gesimuleerde stromingsveld onthult het mechanisme van de wervelringvorming. Verder wordt het spectrum van kinetische energie in detail bestudeerd, waaruit de belangrijke rol die de *Crow* instabiliteit speelt in de dissipatie van het wervelpaar duidelijk naar voren komt. De hier beschreven studie van het energiespectrum toont aan hoeveel kinetische energie er op ieder moment tijdens de evolutie van de instabiliteit nog over is, en hoeveel inmiddels is gedissipeerd. De invloed van het Reynolds getal op het proces wordt bestudeerd.

De korte-golflengte instabiliteit in een wervelpaar vertoont een aantal eigenschappen die tot op heden niet volledig worden begrepen, zoals het optreden van een saturatieproces van de amplitudegroei en de vorming van kleinschalige instabiliteiten in de wervels. De numerieke simulaties die in dit proefschrift worden besproken, laten deze verschijnselen duidelijk zien. De resultaten van de tijdens de huidige studie uitgevoerde simulaties zijn in grote mate consistent met theoretische voorspellingen die recent zijn gepubliceerd in de literatuur. Verder wordt de afhankelijkheid bestudeerd van parameters als Reynolds getal, de afstand tussen de wervels en de opgelegde golflengte. De amplitude waarbij saturatie optreedt, blijkt direct afhankelijk te zijn van de afstand tussen de wervels: bij een grote afstand tussen de wervels is deze amplitude kleiner dan bij een wervelpaar met een kleinere afstand tussen de wervels. Voor een typisch vliegtuigzog is deze afstand zodanig groot dat een relatief kleine maximale amplitude van de korte-golflengte instabiliteit resulteert. De rol van deze instabiliteit in de dynamica van zogwervels is daarmee veel minder prominent dan die van de *Crow* instabiliteit. Deze korte-golflengte instabiliteit kan in de toekomst wel een belangrijkere rol gaan spelen wanneer methoden ontwikkeld worden die van deze korte-golflengte instabiliteit gebruik maken om het wervelzog van een vliegtuig sneller te laten opbreken. Het beter begrijpen van de mechanismen van de korte-golflengte instabiliteit is dan ook van groot belang voor de ontwikkeling van deze, al dan niet, actieve methoden.

ACKNOWLEDGMENT

This thesis is the result of research work carried out in the past four years. During this period, many people have made a contribution to this work. I owe thanks to them for their involvement. A number of people have been particularly important in the completion of this work. I would like to thank them here.

First, I would like to express my gratitude to Harry Hoeijmakers for the support, guidance and advice over the past four years. Your enthusiasm for (computational) fluid dynamics in general, and for flows involving vortices in particular, has been essential for the completion of this thesis. The enjoyable discussions and your sincere interest in many things outside the scope of my research work are greatly appreciated.

The work presented in this thesis could not have been achieved without the financial support from the foundation Fundamenteel Onderzoek der Materie (FOM) through grant 97-PR-1598 'Dynamics of aircraft wake vortices in the atmosphere'. This support is gratefully acknowledged.

I would like to thank prof. A. Leonard of the Graduate Aeronautical Laboratories (GALCIT) at the California Institute of Technology for the opportunity to work in his group as visiting researcher for three months. The stimulating atmosphere in the laboratory and the 'alternative' view provided by prof. Leonard and other members of GALCIT is greatly appreciated. I would like to thank staff, fellow PhD candidates and students of the Engineering Fluid Dynamics group at the University of Twente for providing an enjoyable working environment and for their direct or indirect contribution to this thesis. Special thanks go to Wouter den Breeijen for his efforts in keeping the computer network running and to the (former) secretaries of the group.

Finally, I would like to thank my parents and brothers for their support and understanding.

ABOUT THE AUTHOR

René Steijl was born on July 29, 1974 in Rotterdam, the Netherlands. He lived in Geervliet, a small town in the vicinity of Rotterdam, and attended secondary school in nearby Spijkenisse. After finishing secondary school in 1992, he studied Aerospace Engineering at the Delft University of Technology. During the fourth year of this study, he had an internship at ESCTEC in Noordwijk, the technical center of the European Space Agency. During this internship and the following thesis work, the author worked on modeling and numerical simulation of hypersonic reentry flows and flows involving condensation effects. In September 1997, he graduated cum laude in the section High Speed Aerodynamics of the department of Aerospace Engineering of Delft University of Technology.

The work on computational fluid mechanics during the last phase of the study in Delft had raised enough interest and enthusiasm in this subject to start the PhD project described in this thesis. In December 1997, this research on aircraft wake vortex dynamics started under the guidance of prof. dr. ir. H.W.M. Hoeijmakers in the section Theoretical Aerodynamics of the department of Aerospace Engineering in Delft. From February 1998 to December 2001, he worked on this PhD project in the section Engineering Fluid Dynamics of the department of Mechanical Engineering at the University of Twente, chaired by prof. Hoeijmakers.

From October 2000 to January 2001, the author worked as visiting researcher in the Graduate Aeronautical Laboratory (GALCIT) of the California Institute of Technology. There, he continued work on his thesis subject under the supervision of prof. A. Leonard.

In his spare time, the author likes playing squash, biking and watching sports.
